THE UNIVERSITY OF
SYDNEY

Biophysical determinants of the behaviour of human myelinated axons

James Howells

A thesis presented to

The Faculty of Medicine

in fulfilment of the requirements

for the degree of

Doctor of Philosophy

December 2013

THE UNIVERSITY OF SYDNEY

When you can measure what you are speaking about, and express it in numbers, you know something about it; but when you cannot measure it, when you cannot express it in numbers, your knowledge is of a meagre and unsatisfactory kind.

— Lord Kelvin

Certificate of Originality

I hereby declare that this submission is my own work and to the best of my knowledge it contains no materials previously published or written by another person, or substantial proportions of material which have been accepted for the award of any other degree or diploma at The University of Sydney or any other educational institution, except where due acknowledgement is made in the thesis. Any contribution made to the research by others, with whom I have worked at The University of Sydney or elsewhere, is explicitly acknowledged in the thesis. I also declare that the intellectual content of this thesis is the product of my own work, except to the extent that assistance from others in the project's design and conception or in style, presentation and linguistic expression is acknowledged.

James Howells

12 December 2013

Abstract

This thesis investigates the role of the *hyperpolarization-activated* current, I_h, on the excitability of human axons. It exploits the unique characteristics of the underlying hyperpolarization-activated cyclic-nucleotide-gated (HCN) channels to improve existing and create new techniques for studying I_h. An isolated amplifier with low-noise and high common-mode rejection was developed, and threshold tracking techniques were modified to allow the measurement of the excitability of low-threshold sensory axons and of cutaneous afferents close to their receptors. These developments open up the possibility of studying changes in polyneuropathies, where symptoms and possibly the underlying pathology are more apparent distally in the limbs. Strong and long-lasting hyperpolarization was used to open more HCN channels and to examine their contribution to the excitability of motor and sensory axons. A mathematical model of myelinated motor axons was adapted to account for the response to strong and long-lasting hyperpolarization. Without structural changes the model was then modified to fit the observed excitability of sensory axons. Changes in the excitability and safety margin during focal hyperthermia were studied in both motor and sensory axons of the median nerve, and the underlying mechanisms were explored using the new mathematical model. Finally, the involvement of I_h in the frequency preference of oscillation in human axons was investigated by developing resonance techniques that have hitherto never been used to study axonal function.

Acknowledgements

I would first like to thank my supervisor and mentor Professor David Burke. I am indeed fortunate to have been one of your students. Thank you for all that you have taught me and for your patience and wisdom. Thank you for giving me the freedom to think outside the box and for knowing precisely when to reel me back in. Thank you for allowing the contest of ideas, and perhaps most of all thank you for *encouraging* me to write! I only wish I had met you much earlier.

I would like to thank Professor Hugh Bostock, a close friend and mentor who has provided the foundations that underpin this area of research. Thank you Hugh for your insights, generosity and for providing me the opportunity to contribute to Qtrac.

Thank you to my friends and colleagues particularly Dr. Dirk Czesnik from Germany, and at The University of Sydney, Dr. Craig Campbell, Dr. Stacey Jankelowitz, Dr. Karl Ng, Dr. Ángeles Sánchez-Pérez, Ms Mary Sweet and Dr. Susie Tomlinson.

A special thank you to my close friend and colleague Louise Trevillion, who introduced me to this area and has helped me immensely throughout this endeavour.

Thank you to all those volunteers who have made this thesis possible, and the National Health and Medical Research Council which provided a postgraduate research scholarship to support this project.

Lastly I would like to thank all of my friends and family, for the sacrifices they have made and the support they have given. Thank you Hans and Leonard for your valuable discussions, and thank you Tillie for being the glue that makes it all happen.

Thank you Adelle for everything. Thank you for your belief in me and for your enduring love and support.

Thank you Bastiaan and Felix. Tickle Trap!

Abbreviations

4AP	4-Aminopyridine
cAMP	Cyclic adenosine monophosphate, or cyclic-AMP
CAP	Compound action potential
CM	Membrane capacitance
CMAP	Compound muscle action potential
CNS	Central nervous system
CSAP	Compound sensory action potential
E_K	Potassium equilibrium potential
G_H	Hyperpolarization-activated conductance
G_{Ks}, G_{Kf}	Slow- and fast-potassium conductances
HCN	Hyperpolarization-activated cyclic-nucleotide gated channels (HCN1, HCN2, ...)
H1, H2	Hyperpolarization phases induced by trains of stimuli
I_{AR}	Anomalous rectifier current (earlier name for I_f and I_h)
I_f	Funny current (as observed in the cardiac system)
I_h	Hyperpolarization-activated current
I_{Kf}	Fast potassium current
I_{Ks}	Slow potassium current
I_{NaP}	Persistent sodium current
I_q	Queer current (earlier name for I_f or I_h)
I_{rh}	Rheobasic current
IV	Current-threshold relationship
JPN	Juxtaparanode
KCNQ	Gene family that encodes slow-potassium channels (e.g. KCNQ2, KCNQ3, ...)
KCNA	Gene family that encodes fast-potassium channels

K_f	Fast potassium channel
K_s	Slow potassium channel
K_v	Voltage-gated potassium channel (e.g. $K_v1.1$, $K_v7.2$, ...)
K_{IR}	Classical inward rectifier conductance
K_{2P}	Two-pore domain potassium channels
$[K^+]_o$	Extracellular potassium ion concentration
Na_v	Voltage-gated sodium channel (e.g. $Na_v1.6$, ...)
PIP_2	Phosphatidylinositol-4,5-bisphosphate
PNS	Peripheral nervous system
PS	Paranodal segment
Q10	Temperature coefficient of 10 °C
QT	Charge-duration relationship
RC	Recovery cycle
RM	Membrane resistance
RMP	Resting membrane potential
RRP	Relative refractory period
SDTC	Strength-duration time constant (τ_{SD})
SNAP	Sensory nerve action potential
SR	Stimulus-response curve/relationship
STX	Saxitoxin
TE	Threshold electrotonus (TEd - depolarizing; TEh - hyperpolarizing)
TEA	Tetraethylammonium
TTX	Tetrodotoxin
$V_{0.5}$	Half-maximal activation potential
ZAP	Impedance(Z) Amplitude Profile

Table of Contents

Certificate of Originality ..... *i*

Abstract ..... *ii*

Acknowledgements ..... *iii*

Abbreviations ..... *iv*

Chapter 1 Literature Review **1**

Introduction 2

Nervous system overview 3

Axons 4

Axon structure 4

Unmyelinated axons 5

Myelinated axons 6

Function 9

Electrotonic conduction 9

Saltatory conduction 9

Ion channels and transporters 11

Voltage-gated ion channels in the peripheral nervous system 13

General structure and function 14

Na^+ channels 15

K^+ channels 19

HCN channels 22

'Leak' currents 29

Ion pumps and transporters 30

Na^+/K^+ pump 30

Na^+/Ca^{2+} exchanger 31

Axonal excitability 31
Threshold tracking 32
Threshold / Recruitment order 34
Strength-duration properties 36
Recovery cycle 38
Threshold Electrotonus and the current-threshold relationship 41
Modelling 43
Lipid bilayer 43
The Hodgkin-Huxley model 45
Model description 46
Modelled behaviour 48
Model evolution 49
The 'Bostock' model 50
Chapter 2 Methodology 52
Recording setup 53
Electrodes 53
Skin preparation, grounding, noise and stimulus artefact 55
Temperature 55
Excitability testing 57
Excitability protocols 57
Unconditioned measures 58
Responses to subthreshold conditioning 59
Excitability following activation 60
Axonal excitability recording 61
Analysis of axonal excitability 61

Chapter 3 Tracking small sensory nerve action potentials in studies of axonal excitability in human subjects 65

Summary 66

Introduction 67

Methods 69

Preamplifier design 69

Preamplifier performance (test bench) 71

Electrodes and skin preparation 71

Excitability testing 73

Tracking small, noisy action potentials 74

Post-digitisation signal conditioning 75

Measuring the amplitude of biphasic and triphasic action potentials 75

Results 77

Amplifier performance 77

Recovery from stimulus artefact during CSAP recruitment 77

Signal-to-noise measurements *in vivo* 80

Threshold tracking 2-µV sensory action potentials 80

Repeatability of small-target recordings 83

Orthodromic measurement of distal excitability properties 86

Discussion 88

Axonal excitability close to the electrode noise floor 88

Physiological implications and clinical applications 90

Chapter 4 The voltage dependence of I_h in human myelinated axons: a new model of human sensory and motor axons 92

Summary 93

Introduction 94

Methods 95

Excitability protocols 97

Mathematical modelling 98

Results 102

Sensory excitability 103

Accommodation to hyperpolarization 103

The recovery cycle 106

Strength-duration time constant 106

Comparison with conventional sensory recordings 106

Motor excitability 106

Accommodation to hyperpolarization 110

Excitability measures sensitive to membrane potential 110

Other excitability measures 111

Modelling 111

Model equations 111

Motor axons 114

Sensory axons 114

Can the differences between sensory and motor axons be explained by the consequences of changing a single parameter? 118

Discussion 118

Technical issues 119

Insights from mathematical modelling 119

Other mechanisms that influence the action potential and the depolarizing afterpotential 122

Functional implications 123

Chapter 5 Excitability and the safety margin in human axons during hyperthermia 125

Summary 126

Introduction 127

Methods 129

Excitability protocols 131

Routine axonal excitability assessment 131

Polarized recovery cycles 132

Mathematical modelling 133

Statistical analysis 134

Results 134

CMAP recruitment 134

Threshold electrotonus and current-threshold relationship in motor axons 137

The recovery cycle of motor axons 139

Reproducibility 139

Excitability of sensory axons 143

Polarized recovery cycles 143

Modelling 146

Discussion 151

Mechanisms underlying hyperthermia-induced changes in excitability 152

Resting membrane potential 152

The recovery cycle 153

Accommodation to long-lasting depolarization 156

The hyperpolarization-activated cation conductance, I_h 156

The role of K^+ channels in hyperthermia 157

Variability of hyperpolarizing threshold electrotonus measures 158

Clinical implications 158

Chapter 6 I_h and resonance in human axons 161

Summary 162

Introduction 163

Methods 165

'Threshold ZAP' protocol 166

Analysis of Frequency-response curves 171

Modelling 173

Excitability clamping 173

Results 174

In vivo measurement of frequency response in human axons 174

Frequency-response curves 174

Computational Model 179

Assessment of the mathematical models in the frequency domain 179

The voltage dependence of the frequency response 181

The contribution of slowly-rectifying conductances to the frequency response. 183

Conductances that alter the magnitude of the frequency response 186

Discussion 189

Comparison with the current-threshold relationship. 189

Verification of the motor and sensory axon models 190

Factors contributing to resonance in motor and sensory axons 190

Low-frequency attenuation 191

High-frequency attenuation 191

Amplifiers and suppressors of resonance 191

Differences between motor and sensory axons. 192

Functional consequences 192

Conclusions 196

Chapter 7 Summary and Conclusions..... 197

The study of small amplitude sensory nerve action potentials..... 198

New models of human motor and sensory axons..... 199

The impact of focal hyperthermia on axonal excitability..... 200

Subthreshold oscillations and resonance in human axons 201

Future Work 203

References 204

Chapter 1

Literature Review

Introduction

The safe passage of an impulse along an axon is critically dependent upon the distribution and properties of a class of membrane-bound proteins known as voltage-gated ion channels. Changes in the function of voltage-gated ion channels have profound effects on the excitability of an axon.

This thesis examines the contribution of hyperpolarization-activated cyclic-nucleotide-gated (HCN) channels to the normal function of large myelinated axons in the human peripheral nervous system. HCN channels are unusual in the wider family of voltage-gated ion channels, in the sense that they open during hyperpolarization, not depolarization, of the axonal membrane, and pass a slowly activating depolarizing current (I_h) carried by both Na^+ and K^+ ions. HCN channels influence axonal excitability by contributing to resting membrane potential, and the 'inward rectification' produced by their activity acts as a brake on long-term hyperpolarization.

I_h has a role in many of the excitability changes observed in both healthy and diseased axons of the peripheral nervous system. Normal sensory axons appear to have greater inward rectification than motor, and this has been attributed to greater expression of HCN channels. Altered inward rectification has been observed in the peripheral nervous system in many diseases, both primarily peripheral and primarily central, including porphyria, stroke, and diabetes mellitus, and has been implicated in epilepsy and pain. Consequences of the differences in membrane potential (see Chapter 4) and of the activity of I_h and the persistent Na^+ current (I_{Nap}) are that sensory axons are more protected from conduction block than motor axons for the same impulse load, but at a price of a greater susceptibility to become ectopically active (Burke *et al.*, 1997).

Nervous system overview

The nervous system of vertebrates has two major divisions: the brain and spinal cord form the central nervous system (CNS); and together with muscle, axons, ganglia, receptors and synapses distal to the spinal cord form the peripheral nervous system (PNS).

The peripheral nervous system is further divided into the autonomic, otherwise known as the involuntary or visceral, and the somatic nervous systems. The large myelinated fibres of the somatic nervous system are readily accessible to external stimulation and it is these axons that will be examined in this thesis, though the results may equally be applicable to both central and peripheral axons, because their functional properties are similar, if not identical (Ritchie, 1995).

Upper motor neurons in the motor cortex of the brain descend down through the ventral column to the anterior horn where they synapse with lower motor neurons, referred to as α motor neurons (α-MNs). The axons of α-MNs ('efferent' axons) exit the spinal cord through the ventral root and extend toward the target muscle. In the vicinity of the target muscle the motor axon branches many times, and the axon terminals innervate single muscle fibres (approximately 100-300 muscle fibres/motor axon for abductor pollicis brevis; Buchthal & Schmalbruch, 1980; Gandevia & Burke, 2004). This arborisation is normally efficient in terms of the space and energy demands placed on the axon: i.e., the security of impulse conduction is normally high all the way from the α-MN, along the parent axon through its branching, across the neuromuscular junction to the innervated muscle fibres. Chapter 5 will discuss the effects of hyperthermia, as occurs in febrile illnesses, on the security of transmission through this pathway.

Sensory fibres ('afferent' axons) pass information from the periphery to the central nervous system. The peripheral process ascends from receptors toward the dorsal root ganglion where the cell bodies are located. The central process has local effects within the spinal cord and projections to supraspinal centres.

Axons

An axon serves only one function: to transmit impulses faithfully, and can be viewed as the neural analogue of a transmission cable in a feedback control system. Its sole purpose is to convey signals efficiently and reliably to and from the cell body, or soma, of a neuron, and its properties appear to be regulated to do so with minimal expenditure of energy. Given that discharge patterns and discharge rates vary for afferent and efferent axons, it is not unexpected that their biophysical properties will differ, as explored in Chapter 4. Axons are long thin projections of a neuron which begin in the cell body at the axon hillock and continue to either synapses or sensory receptors. Afferent fibres relay sensory input gathered at distal receptor sites toward the central nervous system, and efferent fibres transmit neural commands to multiple muscle fibres within the same motor unit.

Axon structure

Axonal structure is intimately related to its function and location within the nervous system. The two key inter-related structural attributes of axons which have an impact on function, and in particular on the speed of transmission, are: the presence or absence of myelination; and axonal diameter.

Myelination reduces the internodal capacitance and to a limited degree insulates the underlying axon. Myelin ensheathes nearly the entire axonal surface with narrow gaps (nodes of Ranvier; which are described below) occurring at regular intervals.

Concentrating the need for action potential generation at these narrow openings reduces axonal energy expenditure and myelination of the internodal region reduces the capacitive load on nodes of Ranvier, facilitating saltatory conduction which is both efficient and rapid (Lillie, 1925; Tasaki, 1939; Huxley & Stämpfli, 1949; Ritchie, 1995).

In the peripheral nervous system, axonal calibre varies from approximately 1 to 20 µm for myelinated axons and from 0.1 to 2 µm for unmyelinated axons (Berthold & Rydmark, 1995). It has long been observed that the speed of propagation of action potentials for both unmyelinated and myelinated fibres increases as a function of axonal diameter (Gasser & Grundfest, 1939; Hursh, 1939), and Rushton (1951) theorised that the conduction velocity of an axon should be proportional to the axonal diameter for myelinated fibres and to the square root of axonal diameter for unmyelinated fibres.

The axons studied in this thesis are both myelinated and large. Large myelinated cutaneous afferents (Aα/β) of the median nerve innervate four types of mechanoreceptive units in the glabrous skin of the human hand and are typically between 7 and 15 µm in calibre with a peak in the distribution around 10 – 12 µm (Johansson & Vallbo, 1983). In contrast, motor axons of the median nerve have relatively homogeneous properties, innervating the intrinsic muscles of the hand. Motor axons are probably of similar size to large myelinated cutaneous afferents but have slightly slower conduction velocities.

Unmyelinated axons

The majority of somatic axons are unmyelinated and of small calibre, propagating action potentials electrotonically at speeds of less than 2 ms^{-1}. Given the space and metabolic constraints that myelinated and unmyelinated axons impose, this distribution probably reflects a trade-off between functions such as motor control and

reflex which require fast transmission for coordination and control and the need for sensory detail which requires further integration in the central nervous system (Rushton, 1951).

Myelinated axons

Glial cells, such as oligodendrocytes in the central nervous system and Schwann cells in the peripheral nervous system are essential non-neuronal accessory cells that support and sustain nervous function. Unlike the central nervous system, where individual oligodendrocytes wrap multiple neighbouring axons simultaneously; myelination in the peripheral nervous system is achieved with arrays of Schwann cells that each myelinate single axonal segments or internodes.

During the initial stages of development Schwann cells contain a fairly homogeneous population of axons, which are not differentiated on the basis of myelination (Ochoa, 1971; Kleitman & Bunge, 1995; Webster, 2005). As Schwann cells divide, the axons are radially sorted into smaller and smaller groups until the axons ultimately destined for myelination form a one-to-one relationship with Schwann cells, with the largest axons likely to begin myelination first (Cravioto, 1965; Ochoa, 1971; Webster, 2005). As the axon grows in diameter, the close apposition of axon and Schwann cell is thought to stimulate the myelination process (Ochoa, 1971; Webster *et al.*, 1973).

In healthy somatic axons this tightly-packed myelination continues uniformly from the axon initial segment right through to the neuromuscular junction or receptive field. These tightly abutting myelinations are separated by narrow gaps, or nodes of Ranvier, which are dense in Na^+ channels essential for action potential generation.

The myelin sheath continues to grow longitudinally and transversely to accommodate the growing axon and the internodal length increases with maturation until the second decade (Jacobs & Love, 1985; Farrar *et al.*, 2013).

Nodes of Ranvier

Inextricably linked with myelination are the periodic interruptions in the myelin sheath first discovered by Louis Ranvier in 1875. These nodes of Ranvier are typically only 1 µm wide and occur approximately every 1 - 1.5 mm in mature large myelinated axons (Nilsson & Berthold, 1988; Berthold & Rydmark, 1995), thereby representing < 0.1% of the entire length of an axon.

Protein interactions at the axo-glial interface (formed by the contact of paranodal loops of the myelin sheath and the axon) contribute to the highly specific expression of ion channels on either side of the myelin sheath attachment (Arroyo *et al.*, 1999; Debanne *et al.*, 2011).

Voltage-gated Na^+ channels ($Na_v1.6$) are expressed at high density on the mature nodal axolemma (Caldwell *et al.*, 2000). Current- and voltage- clamp studies of the human node of Ranvier have found a large and transient Na^+ current and small slow and fast K^+ conductances. Blocking the K^+ currents did not appreciably alter action potential repolarization (Schwarz *et al.*, 1995). Persistent Na^+ current (described below) has been recorded in large rat dorsal root ganglion neurons (Baker & Bostock, 1997), and is likely to be active at the nodes of Ranvier, contributing to differences in latent addition between motor and sensory axons (Bostock & Rothwell, 1997) and to threshold behaviour (Hales *et al.*, 2004; Bostock *et al.*, 2005).

Fine structure

The stereotypical internode covers more than 95% of the length of a myelinated axon, and apart from a small protuberance where the Schwann cell nucleus is located, the fibre and axonal diameters are constant until they approach the internodal end regions (as shown in Fig. 1.1).

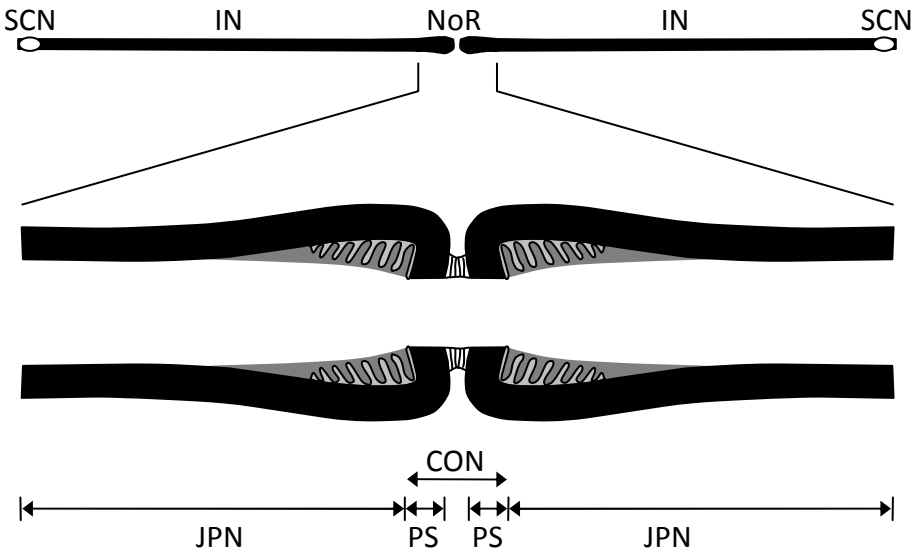

Figure 1.1. Fine structure of the node-paranode region (modified from Berthold et al. (2005), p. 43). Key morphological features of the internodal end regions of myelinated axons. The node of Ranvier (NoR) is flanked by paranodal segments (PS) and together they form the constricted region (CON) where the cross-sectional area of the axon is ~25% of that at the internode (and for matter >95% of the axon). The Schwann cell nucleus (SCN) is typically located at the middle of the internode (IN). The axon diameter begins tapering in the juxtaparanode (JPN) as it approaches the paranodal loops or myelin sheath attachment.

This morphologically complex end region has a fundamental impact on nodal excitability and was revealed in detail by ultrastructural studies of large feline spinal root fibres by Berthold and Rydmark (1983) using electron microscopy. The internodal end region is typically 50 – 80 µm for large fibres and consists of: the juxtaparanode (JPN) and the paranodal segment (PS) which is where the myelin sheath turns toward and forms an attachment or tight junction with the underlying axon (which is approximately 3 – 5 µm wide independent of fibre size). Along the juxtaparanode the axonal diameter tapers as it progresses toward the paranodal segment, where the axon is constricted to approximately half its internodal diameter (Rydmark, 1981; Berthold & Rydmark, 1983). At the same time the fibre diameter increases as it

approaches the nodes of Ranvier producing the bulges seen in light microscopy (Berthold & Rydmark, 1983).

Function

Electrotonic conduction

Electrotonic conduction of neural information proceeds according to cable theory which was developed by Lord Kelvin to describe telegraphic transmission in a leaky submarine cable. This 'passive' spread of an impulse decays exponentially and is a form of graded or analogue transmission. By combining neural inputs temporally or spatially, electrotonic conduction provides an integrative capability essential for neural computation.

As a consequence of this electrotonic decay unmyelinated axons require Na^+ and K^+ channels distributed along their entire length to propagate impulses safely. This form of signalling is slower and metabolically more expensive than in myelinated axons, additionally requiring wider distribution and greater expression of Na^+/K^+-ATPase pumps to maintain ionic gradients.

Saltatory conduction

By 1912 the principle of 'all-or-none' propagation had been demonstrated in frog muscle fibres (Lucas, 1909), and then in the sciatic nerve of frog (Adrian, 1912). Kato (1924) demonstrated "decrementless" conduction through a narcotized region of the sciatic nerve of Japanese toads, countering the strongly held and prevailing view that electrical disturbances suffered a decrement of intensity and velocity through such "abnormal" regions (Kato, 1970). Kato surmised that this "decrementless" conduction could only occur if the region traversed contained a local supply of energy. Lillie (1925) devised an analogue of a myelinated nerve, in which an iron wire enclosed by a regularly interrupted glass tube is immersed in ferric acid. This preparation showed a

dramatic increase in the speed of transmission over that with a non-interrupted glass tube or bare wire, and Lillie first proposed that this type of saltatory conduction could explain the faster transmission of impulses in myelinated than non-myelinated nerve. Support for Lillie's hypothesis was later found in nerve by Tasaki (1939) who demonstrated that action currents could actually jump a few inexcitable nodes of Ranvier. Perhaps the most clear demonstration of saltatory conduction was performed by Huxley and Stämpfli (1949) who (unaware of the study by Tasaki) showed in frog fibres discrete jumps in action currents as each node of Ranvier was crossed.

Saltatory conduction relies upon the insulative properties of the myelin sheath, but perhaps more importantly on the reduction of the internodal capacitance due to the increased charge separation afforded by the dielectric properties of the tightly wrapped myelin lamellae (Blight, 1985; Ritchie, 1995). A reduced internodal capacitance allows more rapid charging of the internodal axolemma, speeding up action potential generation. In rat ventral roots Rasminsky and Sears (1972) measured an internodal conduction time of 20 μs for internodes of 0.75 to 1.45 mm in length, corresponding to a range of conduction velocities of 38 to 73 ms^{-1}. When these fibres were demyelinated using diphtheria toxin, conduction slowed, most likely due to an increased internodal capacitance and decreased resistance across the myelin sheath.

The safe transmission of impulses in myelinated fibres requires a certain degree of redundancy. Following the studies of Hodgkin (1937), Tasaki (1939) observed that the nodal action current was larger than the threshold current required for excitation and estimated the safety factor of transmission to be ~8 – 10. This is particularly important: where morphological changes degrade transmission, such as at

branchpoints (which only form at nodes of Ranvier, (Quick *et al.*, 1979)), in demyelinating diseases, and during hyperthermia (which is the subject of Chapter 5).

For high-speed impulse propagation, saltatory conduction is efficient in terms of both metabolic and space constraints. For fibres greater than about 1 µm a myelinated fibre will conduct more rapidly than an unmyelinated fibre of the same diameter. Conversely, for the same conduction velocity a myelinated fibre will be thinner than an unmyelinated fibre. Saltatory conduction allows a reduced overall expression of Na^+ and K^+ channels (concentrating Na^+ and K_s channels at the nodes of Ranvier), and is believed to be metabolically less expensive in terms of the requisite Na^+/K^+-ATPase pump activity required to restore ion gradients.

Ion channels and transporters

The transport of ions between the cytoplasm and extracellular fluid is essential not only for signalling in excitable tissue but also for the maintenance of cell volume and viability in all cells. Sydney Ringer determined that an isotonic solution composed of the right ratio of sodium, potassium and calcium (serendipitously) salts was essential for the continued beating of a frog's heart (Hille, 1992; Miller, 2004).

The protective membrane of cells consists of phospholipids arranged in a tightly packed double layer. Each phospholipid has a hydrophilic head and two hydrophobic (and lipophilic) tails. These lipids spontaneously assemble in self-sealing planar arrays with the polar heads of one layer facing the extracellular fluid and the heads of the other layer the cytoplasm. The tails of apposing layers face each other, providing a hydrophobic interior which is energetically unfavourable for the permeation of ions which are electrostatically bound to water molecules.

The cell's membrane provides a relatively impermeable barrier to ions, which can be overcome by the incorporation of highly specialised proteins into the lipid bilayer for the transport of ions into and out of the cell. Ion channels, which are essentially, water filled pores with ion selectivity and gating mechanisms achieve the high rates of transfer of ions (10^6 ions/s) down their electrochemical gradients necessary for signal transduction. In contrast to ion channels which reduce electrical and concentration gradients by rapid diffusion, ion transporters slowly establish and maintain these gradients with the consumption of energy in the form of (i) ATP for the Na^+/K^+-ATPase pump and (ii) the Na^+ gradient for the Na^+/Ca^{2+} exchanger.

The landmark studies by Hodgkin and Huxley (1952a, b, c, d) and Hodgkin, Huxley and Katz (1952) correctly inferred many of the fundamental properties of ion channels (though this term was not in use for at least another decade) using voltage clamp and ion substitution techniques, despite a complete lack of knowledge of the underlying molecular basis of the Na^+ and K^+ conductances. Although they established the 'independence principle' for Na^+ and K^+ currents, it was not clear at the time what the mechanism was that allowed Na^+ and K^+ to flow independently. Subsequent pharmacological and patch clamp studies have provided compelling evidence for separate ionic pathways or channels through the membrane (Narahashi *et al.*, 1964; Hille, 1967; Sigworth & Neher, 1980).

Following on from those early studies of Na^+ and K^+ channels in the squid giant axon, a vast array of ion channels have been discovered. Ion channels can be categorised on the basis of their gating mechanism and fall in to three main groups: (i) voltage-gated, such as Na^+, K^+, Ca^{2+},Cl^- and HCN channels; (ii) ligand-gated which are activated by chemical stimuli; and (iii) other gating mechanisms in which the channels are responsive to stimuli such as light, temperature, stretch and pressure. This division is

based on the principal form of gating, but the principal form of gating may in turn be modulated by one of the other forms of gating (e.g. modulation of HCN channels by cyclic AMP [cAMP], phosphatidylinositol-4,5-bisphospate [PIP2], pH, etc). Additionally there are K^+ background 'leak' channels, which are relatively voltage insensitive and, electrically speaking, approximate the behaviour of an ohmic conductor.

Signalling can theoretically proceed with only Na^+ channels, but in reality the diversity of nervous system function is achieved by the finely tuned contributions of other ion channels and ion transporters. An imbalance in the expression and or function of ion channels and their associated transporters is a contributing factor in the pathophysiology of many neurological disorders, and therefore makes ion channels suitable targets for pharmacological intervention (Krishnan *et al.*, 2009; Cregg *et al.*, 2010; Mantegazza *et al.*, 2010; Postea & Biel, 2011).

Voltage-gated ion channels in the peripheral nervous system

In the large myelinated fibres of the peripheral nervous system, movement of ions across the membrane is principally mediated by voltage-gated channels (Na^+, K^+, and HCN), the K^+ leak channels, and the ion transporters, such as the Na^+/K^+-ATPase pump and Na^+/Ca^{2+} exchanger.

Interactions of proteins at the septate-like junction between Schwann cells and axon regulate the distribution of both Na^+ and K^+ channels, with Na^+ channels clustered in high density in the nodal gap and fast K^+ channels localised to the juxtaparanodal region (Rosenbluth, 1976; Dupree *et al.*, 1999; Poliak & Peles, 2003). Disruptions of the paranodal proteins of the axo-glial interface lead to altered ion channel expression and localisation and contribute to the symptoms associated with dysmyelination (Bray *et al.*, 1981; Rosenbluth, 1990; Dupree *et al.*, 1999).

The excitability of the nodal membrane is tempered by the action of slow K^+ ($K_v7.2$ and $K_v7.3$) and fast K^+ ($K_v1.1$ and $K_v1.2$) channels which are expressed on the nodal and juxtaparanodal axolemmas, respectively (Debanne *et al.*, 2011). Physiological and pharmacological studies suggest that HCN channels are located at the internode (Baker *et al.*, 1987). HCN channels mediate the hyperpolarization-activated cation current (I_h) which contributes to the determination of resting membrane potential, thereby influencing axonal excitability (Kaupp & Seifert, 2001; Robinson & Siegelbaum, 2003; DiFrancesco, 2006).

Calcium channels are not present at the node of Ranvier of the large myelinated axons studied in this thesis. The role of chloride channels in these same axons has received little attention, and therefore both of these voltage-gated ion channels will not be discussed further.

General structure and function

Ion channels are integral membrane proteins with a hydrophilic pore which conducts ions across the membrane and a lipophilic face which seals against the membrane bilayer. Voltage-gated ion channels have the same basic structure of four α-subunits or four subunit domains arranged around an aqueous ion conducting pore (Yu *et al.*, 2005). Voltage-gated Na^+ (and Ca^{2+}) channels consist of one α-subunit with four domains, while voltage-gated K^+ and HCN channels occur as tetramers of α-subunits (each resembling a Na^+ channel domain). The domains or subunits of voltage-gated ion channels consist of six transmembrane segments (S1-S6) and a pore loop (P) with the segments S5, S6 and the pore loop between them forming the selectivity filter and ion conducting pore (Bezanilla, 2005; Yu *et al.*, 2005). The transmembrane segments S1 to S4 provide the voltage sensing apparatus for both depolarization and hyperpolarization activated conductances (Männikkö *et al.*, 2002; Yu *et al.*, 2005;

Börjesson & Elinder, 2008). Auxiliary nonpore-forming subunits are able to modify the basic function of ion channels by altering cellular adhesion and expression, and modulating activation and inactivation (Bezanilla, 2005; Yu *et al.*, 2005).

The diffusion of ions through voltage-gated ion channels is rapid but highly selective. The mechanism of selectivity differs between channel types, but is principally due to pore configuration and electrostatic interactions in the pore lining, which Hodgkin and Huxley predicted (Hodgkin & Huxley, 1952d; Hille, 1972; Doyle *et al.*, 1998; Siegelbaum & Koester, 2000).

Na^+ channels

Hodgkin and Huxley (1952b) identified Na^+ ions as responsible for the inward current during the initial phase of depolarization of an action potential. Despite the fact that these early studies were performed on *unmyelinated* giant axons of squid the characterisation of Na^+ channels was and still is directly applicable to the fast saltatory conduction seen in human myelinated fibres, in large part due to the highly conserved nature of Na^+ channels across species. Using voltage clamping and manipulation of the ionic milieu, elucidation of the functional detail followed, with a thorough description of the voltage dependence and kinetics of the independent processes of activation and inactivation underlying voltage-dependent gating (Hodgkin & Huxley, 1952b, c, d). As with other ion channels, progress in Na^+ channel research proceeded rapidly with the introduction of new techniques such as: the application of specific toxins, blockers and modulators of function; patch-clamping; heterologous expression; and mutagenesis.

Beginning with the introduction of tetrodotoxin (TTX; Narahashi *et al.,* 1964) a range of pharmacological agents have been used to study Na^+ channels, all of which act on α-subunit receptor sites (Catterall *et al.*, 2005). These neurotoxins have a variety of effects which include: pore blocking, enhancement of activation, reduction of

activation to inactivation coupling, and a slowing of inactivation (Bostock *et al.*, 1978; Cestèle & Catterall, 2000; Catterall *et al.*, 2005).

The highly selective channel blocker, saxitoxin (STX) was used by Ritchie and colleagues to measure the density of Na^+ channels in unmyelinated and myelinated nerve. The binding of tritium-labelled STX in rabbit vagus nerve gave a specific Na^+ channel expression of 100 channels / μm^2 (Ritchie *et al.*, 1976), though a later study using the rat cervical sympathetic trunk (which is purely unmyelinated) yielded a figure of 200 channels / μm^2 (Pellegrino *et al.*, 1984). Ritchie and Rogart (1977) found that the binding of radio-labelled STX was only marginally greater in the homogenized sciatic nerve of rabbit than in the intact nerve, which allowed them to estimate the Na^+ channel density at the node of Ranvier to be between 1000 and 2000 channels / μm^2, and under the myelin sheath to be no greater than about 25 channels / μm^2. Despite the concentration of Na^+ channels at the node, there are probably more Na^+ channels on the internode, simply due to its much larger area. In fact, in axons segmentally demyelinated with diphtheria toxin Bostock and Sears (1978) showed continuous conduction is still possible, albeit slowed, for up to 1 ½ times the internodal length, though this was seen only in small axons and at a low temperature.

There are nine members of the voltage-gated Na^+ channel family ($Na_v1.1$ to $Na_v1.9$), with the isoforms $Na_v1.2$ (*SCN2A)* and $Na_v1.6$ (*SCN8A*) occurring in the large myelinated fibres of the peripheral nervous system. $Na_v1.2$ and $Na_v1.6$ are expressed at the site of action potential initiation, the axon initial segment (Hu *et al.*, 2009b), and $Na_v1.2$ is expressed at the developing node of Ranvier, but is replaced by $Na_v1.6$ once myelination begins (Caldwell *et al.*, 2000; Lai & Jan, 2006). In fact, in mice with motor endplate disease, action potentials could be recorded during development, but the

disease was fatal at around three weeks (Duchen & Stefani, 1971). Motor endplate disease was later attributed to a mutation of $Na_v1.6$ channels (Burgess *et al.*, 1995).

Fast (transient) Na^+ current

The rapidly activating (and inactivating) Na^+ current underlying action potential initiation in the unmyelinated squid axon has also been observed at the mammalian node of Ranvier with voltage- and current-clamp protocols in single myelinated fibres of rabbit, rat, cat and human (Chiu *et al.*, 1979; Brismar, 1980; Schwarz & Eikhof, 1987; Schwarz *et al.*, 1995). For fast Na^+ currents, the channel open probability is the product of two processes, activation and inactivation. This means that in addition to channel blocking, alterations in the molecular mechanisms responsible for activation and inactivation can disrupt action potential initiation and propagation. Na^+ channel inactivation is more sensitive to temperature than activation, and this difference is believed to underlie the increased refractoriness observed with cooling (Burke *et al.*, 1999; Kiernan *et al.*, 2001a). With heating, as occurs in fever, it is commonly believed that changes in the time course of the sodium current are responsible for conduction block in axons with an impaired safety margin for action potential generation, a belief explored in Chapter 5.

Persistent (late) Na^+ current

Chandler and Meves (1970a, b) found evidence for two types of Na^+ conductance in the squid giant axon; the first rapidly activates and inactivates in accordance with the Hodgkin-Huxley model; and the second was maintained conductance due to the incomplete inactivation of Na^+ channels. Voltage-clamp studies in frog myelinated fibres also revealed a 'non-inactivatable' current at the node of Ranvier which was greater in sensory than in motor fibres (Dubois & Bergman, 1975; Benoit & Dubois, 1987).

The persistent sodium current (I_{NaP}) is a depolarizing current that shows little (or at the least very slow) inactivation and activates with depolarization (i.e. it is regenerative), activates more slowly and at membrane potentials closer to resting membrane potential than transient Na^+ channels (French *et al.*, 1990; Schwindt & Crill, 1995; Kay *et al.*, 1998).

In the central nervous system it is likely that I_{NaP} aids repetitive activity with sustained depolarization (French *et al.*, 1990; Kay *et al.*, 1998). In the peripheral nervous system, I_{NaP} may account for the TTX-sensitivity of resting membrane potential (Baker & Bostock, 1997) and a greater I_{NaP} in sensory axons than motor may underlie their greater propensity for ectopic activity than motor (Erlanger & Blair, 1938; Mogyoros *et al.*, 2000). The role of this current is examined in Chapters 4 and 6.

There have been a number of theories as to the molecular mechanism underlying I_{NaP} , including: a window current due to the m-h (activation-inactivation) overlap, a mode change of transient Na^+ channels, and a separate Na^+ channel isoform (Alzheimer *et al.*, 1993; Catterall *et al.*, 2005; Kiss, 2008). The determination of the molecular basis of I_{NaP} has been hampered by the lack of isoform specific blockers of Na^+ channels. Recent studies point toward the facilitation of persistent currents by the co-expression of α and β-subunits, though the precise contribution of auxiliary β-subunits appears to be tissue specific (Qu *et al.*, 2001; Aman *et al.*, 2009).

Non-invasive threshold tracking studies are well suited to the study of the functional properties of I_{Nap} in axons of different modality, in disease, and in response to therapeutic agents. The longer strength duration time constant and greater threshold change in latent addition in sensory axons than motor suggests a larger I_{NaP} in sensory axons (Mogyoros *et al.*, 1996; Bostock & Rothwell, 1997; Bostock *et al.*, 1998), though

this may not necessarily be due to an increased fraction of channels acting in a persistent mode (which is discussed in Chapter 4).

K^+ channels

In addition to the inward current carried by Na^+ ions, Hodgkin and Huxley (1952b) found in the squid giant axon a late outward current which was unaffected by the concentration of Na^+ in the external fluid. The underlying K^+ conductance had a slower time-course than that of Na^+ and did not show appreciable inactivation.

At the node of Ranvier in frog, Dubois (1981) found evidence for three types of K^+ channels, a slow non-inactivating conductance (K_s) which was insensitive to 4-AP (4-aminopyridine), and two fast 4-AP-sensitive conductances (K_{f1} and K_{f2}) which inactivated very slowly. Similarly, recordings of acutely demyelinated frog nerve fibres, revealed the same three K^+ currents (G_{Ks}, G_{Kf1} and G_{Kf2}) at the internode, though in differing proportions (Grissmer, 1986). In myelinated rat nerve fibres, Baker and colleagues (1987) deduced that a slow outward rectifier was present at the nodes and probably the internodes, and that the fast outward rectifiers were primarily internodally located, a view supported by Röper and Schwarz (1989), who found the density of K_s and K_f channels to be maximal on the nodal and paranodal membranes, respectively. In the first study of action potentials and currents at the human node of Ranvier, Schwarz and colleagues (1995) recorded similar K^+ currents to those in rat axons, but concluded that the second form of K_f, G_{Kf2} was small in human axons. Patch clamp recordings in human axons have shown that at least five types of voltage-dependent K^+ channels underlie the macroscopic K_s and K_f currents (Reid *et al.*, 1999).

Potassium channels form the largest ion channel family, and the 40 voltage-gated K^+ (K_v) channels represent the largest voltage-gated ion channel family (Gutman *et al.*, 2005; Wulff *et al.*, 2009). These K_v channels are further divided into 12 sub-families,

with additional functional diversity resulting from the heteromeric assembly of K^+ channel α-subunits and the co-assembly of auxiliary β-subunits. In fact K_v5 and K_v6 subunits are not functional on their own, but when co-assembled with K_v2 serve to modify or silence channel function (Gutman *et al.*, 2005).

The K_v1 and K_v7 families are present on the large myelinated axons of the peripheral nervous system and are responsible for the macroscopic K_f and K_s currents affecting axonal excitability in health and disease (Arroyo *et al.*, 1999; Devaux *et al.*, 2004; Schwarz *et al.*, 2006).

Slow K^+ current

The slowly gated K^+ current (I_{Ks}) dampens the growth of excitability in response to sustained depolarization. For long-lasting depolarizations, this outwardly rectifying current limits the extent of excitability increases, a process known as accommodation (Bostock, 1995). In apparent opposition, the persistent Na^+ current, I_{NaP}, facilitates repetitive action potentials. However the gating of these two currents act on different timescales, so that while I_{NaP} may assist in the initiation of bursting, the ratcheting of the K_s conductance with each action potential serves to limit the number and rate of action potentials within a burst. Similarly, I_{Ks} reduces the excitability following an action potential as seen in the recovery cycle, with the slow deactivation of K_s channels the major factor in the period of late subexcitability (Baker *et al.*, 1987; Bostock *et al.*, 1998). The role of I_{Ks} in the changes of excitability during hyperthermia is examined in Chapter 5.

Although Hille (1967) demonstrated selective block of nodal K^+ currents using TEA (tetraethylammonium) in frog nerve, it was not until Dubois (1981) applied the selective inhibitor 4-AP to a similar preparation, that slow K^+ currents could be decomposed from the overall 'nodal' K^+ current.

Assisted by a revised model of a myelinated axon (Barrett & Barrett, 1982), an examination of slow outward rectification in myelinated spinal root axons of rat using electrophysiological techniques and various blocking agents deduced that K_s channels were located at the node of Ranvier and probably also at the internode (Baker *et al.*, 1987). A view later supported by the observation that resting membrane potential is sensitive to TEA, and that this sensitivity develops slowly over 10 – 15 minutes (Barrett *et al.*, 1988). Molecular localisation studies identified the clustering of *KCNQ*2 (and to a lesser extent *KCNQ*3) at the nodes of Ranvier in both the peripheral and central nervous system, and in combination with the effects of the channel modulators suggest that *KCNQ* channels mediate I_{Ks} (Devaux *et al.*, 2004; Schwarz *et al.*, 2006).

Fast K^+ current

The delayed rectification observed by Hodgkin and Huxley (1952b) in giant squid axons, which they modelled as a single outward K^+ current, corresponds most closely to the fast K^+ current recorded in mammalian myelinated fibres. The application of selective K^+ channel blockers and demyelinating agents used to study the various voltage-gated K^+ currents not only shed light on the different forms of K^+ current and their location, but also on the role of fast K^+ channels in the excitability of premyelinated, dysmyelinated and demyelinated axons.

Of the five types of K^+ channels identified in patch-clamp studies of myelinated nerve fibres (Jonas *et al.*, 1989; Safronov *et al.*, 1993; Reid *et al.*, 1999), the channel with intermediate kinetics (I; denoted K_{f1} by Dubois, 1981) is likely to be primarily responsible for the macroscopically recorded fast K^+ current in human peripheral axon (Schwarz *et al.*, 1995).

Underlying fast K^+ currents is the K_v1 voltage-gated K^+ channel subfamily (Gutman *et al.*, 2005). K_v1 channels are also known as *Shaker* potassium channels because of the

observed effect caused by mutations of the encoding gene (*KCNA)* in *Drosophila* (Papazian *et al.*, 1987; Tempel *et al.*, 1987). Similarly, mutations of *KCNA1* in humans can lead to dysfunction of $K_v1.1$ channels as has been observed with nerve excitability studies in patients with the episodic ataxia type 1 channelopathy (Tomlinson *et al.*, 2010b).

Unlike the situation in unmyelinated fibres, the fast K^+ current (I_{Kf}) does not appreciably contribute to the repolarization of an action potential in mature myelinated fibres (Kocsis *et al.*, 1982; Schwarz & Eikhof, 1987). It is likely that the strategic placement of K_f channels at the paranode, or more specifically the juxtaparanode serves to limit the re-excitation of the nodal membrane following a single stimulus (Chiu & Ritchie, 1981; Kocsis *et al.*, 1982; Baker *et al.*, 1987; Poliak & Peles, 2003).

There is no clear measure attributable solely to fast K^+ conductances in studies of axonal excitability. However differences in the activation of K_f can be observed with modest depolarization as seen early in depolarizing threshold electrotonus, and in the supernormal period following the strong depolarization of an action potential (Tomlinson *et al.*, 2010b; Ng *et al.*, 2013).

HCN channels

Unlike most other voltage-dependent channels, HCN channels are *activated by hyperpolarization*. The peculiar nature of the underlying current has lead to various names such as the anomalous rectifier (I_{AR}), the queer (I_q) or funny current (I_f), or the hyperpolarization-activated current (I_h). I_h is a mixed cationic current passing both Na^+ and K^+ ions, and marginally selective for K^+ over Na^+, with a selectivity (P_{Na}/P_K) of 0.2 to 0.4 , giving a reversal potential for HCN channels greater than about -50 mV (Pape, 1996; Biel *et al.*, 2009). Under physiological conditions, this results in a net inward

current of Na^+ ions at rest, thereby contributing to the determination of resting membrane potential. Although I_h is primarily carried by Na^+ ions, I_h is dependent on the extracellular concentration of K^+ ions ($[K^+]_o$), with small increases in $[K^+]_o$ greatly enhancing I_h (Mayer & Westbrook, 1983; Ludwig *et al.*, 1998). Indeed this $[K^+]_o$ sensitivity may influence axonal excitability during hyperkalaemia (Kiernan *et al.*, 2002; Krishnan *et al.*, 2005b; Krishnan *et al.*, 2006), increasing I_h currents and depolarizing resting membrane potential.

I_h is a *depolarizing* current which produces 'inward rectification' that lessens the extent of hyperpolarization, thereby acting as a brake on long term changes in resting membrane potential. This negative feedback enables I_h to act as a high-pass filter blocking low-frequency inputs and contributing to the frequency preference mechanism in neural tissue, actions that may underlie spontaneous oscillations (Puil *et al.*, 1994; Hutcheon *et al.*, 1996a, b; Hutcheon & Yarom, 2000), and will be examined in Chapter 6.

I_h has slow kinetics and is activated more powerfully the greater the hyperpolarization (DiFrancesco, 1981; Pape, 1996; Biel *et al.*, 2009). In the heart, the analogous current I_f, contributes to repolarization and is essential for triggering the next systole (Brown *et al.*, 1979; Pape, 1996; DiFrancesco, 2006). Similarly, in some neurones, I_h creates a threshold overshoot in the recovery from the post-discharge after-hyperpolarization, so that it plays a pacemaker role (McCormick & Pape, 1990; Hutcheon *et al.*, 1996b; Biel *et al.*, 2009).

Voltage clamp experiments on mouse dorsal root ganglions have revealed an inward (or anomalous) rectification that differed from the classical inward rectifier (K_{IR}) in that it increased with $[K^+]_o$, was greatly reduced in Na^+-free solution, and was blocked by Cs^+ but only slightly by Ba^{2+} (Mayer & Westbrook, 1983). Using selective blockers,

Baker and colleagues (1987) observed a Cs^+-sensitive 'upwards sag' in response to hyperpolarizing currents in the myelinated axons of dorsal and ventral roots of rat, which they were able to attribute to a mixed Na^+/K^+ inward rectification located at the internode. Additionally, Baker and colleagues (1987) found that Cs^+ increased the post-tetanic depression associated with the Na^+/K^+-ATPase pump hyperpolarization. The time-course, voltage dependence and relative insensitivity to block by Ba^{2+} suggest that K_{IR} is not responsible for the observed inward rectification in mammalian myelinated axons (Mayer & Westbrook, 1983; Baker *et al.*, 1987).

Unmyelinated C fibres are more sensitive to activity-dependent conduction slowing and block than myelinated axons, and Grafe and colleagues (1997) demonstrated a Cs^+-sensitive inward rectification in response to long-lasting hyperpolarization in isolated rat vagus and human sural nerve. Type 4 C-fibres (probably sympathetic efferents) have a distinctive slowing profile in response to repetitive activity when compared to other cutaneous C-fibre types, and this has attributed to the role of I_h in these units (Campero *et al.*, 2004; George *et al.*, 2007).

Isoforms, subunit composition and molecular detail

The channels underlying I_h are the HCN channel family (Kaupp & Seifert, 2001; Robinson & Siegelbaum, 2003; DiFrancesco, 2006). Functional HCN channels are composed of four subunits and four different isoforms are present in mammals, encoded by a multigene family (Biel *et al.*, 2009). All four channels (HCN1-4) are present in the mammalian nervous system, and *in vitro*, stable channel complexes of more than one isoform (heterotetramers) can form (e.g. HCN1/2; Much *et al.* 2003). If heteromerization occurs *in vivo*, then it may confer greater diversity of function with fewer subunit types, and may also provide a regulatory mechanism for the function or dysfunction of I_h (Ulens & Tytgat, 2001; Altomare *et al.*, 2003; Much *et al.*, 2003).

Indeed, Brewster and colleagues (2005) found that developmental seizures promoted the co-assembly of HCN1 & HCN2 subunits in the rat hippocampus.

The members of the HCN family are ordered by their activation rates, with HCN1 being the fastest, followed by HCN2, HCN3 and HCN4. Activation rates are dependent on experimental conditions, and Moosmang and colleagues (2001) have reported the following activation rates for individually transfected HEK293 cells at -140 mV and room temperature: HCN1, 30 ms; HCN2, 184 ms; HCN3, 265 ms; HCN4, 461 ms.

HCN channels follow a sigmoidal activation with increasing hyperpolarization and do not inactivate. The voltage dependence of HCN channels and their macroscopic pacemaker currents varies widely with tissue type, subunit composition and regulation (particularly by intracellular modulators). Half-maximal activation ($V_{0.5}$) values have been reported to lie between approximately -70 to -100 mV, with $V_{0.5}$ for HCN1 typically more positive than the other isoforms (Moosmang *et al.*, 2001; Altomare *et al.*, 2003; Biel *et al.*, 2009).

Like other voltage-gated ion channels the transmembrane segment S4 is largely responsible for the voltage sensing of HCN channels. Surprisingly however, site-directed mutagenesis studies in *Xenopis laevis* oocytes have revealed that the voltage sensor mechanism is conserved between depolarizing and hyperpolarizing channels, suggesting that the coupling between the sensor and activation gate (namely the loop linking S4 and S5) is responsible for the anomalous behaviour (Männikkö *et al.*, 2002; Börjesson & Elinder, 2008).

Modulation

The role of I_h varies dependent on the functional requirements of the excitable membrane on which it is expressed. This is achieved by the specific expression of

homomeric (or possibly heteromeric) HCN channels which each have a unique profile of voltage dependence, activation kinetics and modulation.

The activation of I_h is upregulated by a number of modulators which can depolarize the voltage dependence, bringing otherwise quiescent channels into the physiological range.

Facilitation of HCN channels by cyclic nucleotides, in particular cyclic AMP act by removing tonic inhibition, which in the presence of intracellular cyclic AMP results in depolarizing shifts of the half-activation voltage ($V_{0.5}$) by: for HCN1, ~ +5 mV; HCN2 and HCN4, ~ +20 mV, whilst human HCN3 is unaffected by intracellular cAMP (Chen *et al.*, 2001b; Hofmann *et al.*, 2005).

Critically, in the cardiac system cyclic AMP modulation is involved in autonomic control of heart rate (DiFrancesco, 2006). β-adrenergic stimulation increases cyclic AMP and consequently I_h leading to faster diastolic (pacemaker) depolarization and heart rate. In opposition, vagal stimulation decreases cyclic AMP levels, and I_h activation, slowing depolarization and heart rate (Baruscotti *et al.*, 2005). Perhaps unsurprisingly then, the voltage dependence of the dominant cardiac isoform, HCN4, is modulated more by cyclic AMP than other isoforms.

In the nervous system where HCN1 is more widely expressed, the more positive voltage dependence, faster activation kinetics and ability of HCN1 to act without cAMP facilitation suggests that HCN1 channels are able to participate in changes in axonal excitability in a more rapid and energetically favourable way than the slower isoforms.

Independent of the effects of cyclic AMP, the voltage activation curve of HCN can be depolarized by 15 - 20 mV by the ubiquitous phospholipid, phosphatidylinositol 4,5-bisphosphate (PIP_2), suggesting that PIP_2 functions to bring the voltage dependence of

HCN channels to the pacemaking range (Pian *et al.*, 2006; Zolles *et al.*, 2006; Pian *et al.*, 2007).

HCN channels are sensitive to both intracellular and extracellular pH and therefore activity, with an acidic intracellular pH of 6 hyperpolarizing the $V_{0.5}$ of HCN channels by 10 mV, and an alkaline intracellular pH of 9 depolarizing $V_{0.5}$ by 10 mV (Munsch & Pape, 1999; Stevens *et al.*, 2001; Zong *et al.*, 2001).

As with other voltage-gated ion channels, the kinetics of HCN channels are quite sensitive to temperature changes, with temperature coefficients over 10°C (Q10) of between 4 and 6.3 (Ishii *et al.*, 2001; Robinson & Siegelbaum, 2003). The temperature effects of raised temperature are explored in Chapter 5.

Distribution

HCN4 is the dominant isoform of the heart; at the sinoatrial node HCN4 accounts for approximately 80% of I_h , with HCN2 making up the remainder in humans (Moosmang *et al.*, 2001; Biel *et al.*, 2009).

Physiological and pharmacological studies in spinal root myelinated axons of the rat provide evidence that I_h is internodal (Baker *et al.*, 1987), but there is as yet, no morphological confirmation of this. *In situ* hybridisation and immunohistochemical experiments in rodent dorsal root ganglia (DRG) suggest that (i) HCN1 and HCN2 are expressed on large neurons (i.e. those responsive to tactile and proprioceptive stimuli), (ii) HCN2 and possibly HCN3 are expressed on small neurons (typically responsive to nociceptive and thermal stimuli), and (iii) HCN4 is expressed at very low levels or not at all (Moosmang *et al.*, 2001; Tu *et al.*, 2004; Kouranova *et al.*, 2008). HCN1, 2 and 3 have also been identified immunohistochemically in anterior horn motoneurons in rat spinal cord (Tu *et al.*, 2004). However what is expressed on neurons in the DRG (sensory) and anterior horn (motor) is not necessarily active in axons, and knowledge

of HCN expression on axons is limited. HCN2 has been identified in rat sciatic nerve fibres (Jiang *et al.*, 2008b), and HCN1 and 2 identified in the pre-terminal portion of central axonal membranes (Notomi & Shigemoto, 2004). To date, HCN channel expression has not been examined in human peripheral nerve tissue.

In response to bright light, retinal photoreceptors hyperpolarize, activating I_h to depolarize membrane potential back to 'dark' levels (Hille, 1992). The only isoform expressed in murine photoreceptors is HCN1, where it is expressed at high levels (Moosmang *et al.*, 2001).

Dysfunction

In humans, physiological evidence for HCN channel dysfunction, or dysregulation has been reported in a wide range of neurological disorders (Krishnan *et al.*, 2009), including diabetes mellitus (Horn *et al.*, 1996; Yang *et al.*, 2001; Krishnan & Kiernan, 2005), porphyria (Lin *et al.*, 2008), stroke (Jankelowitz *et al.*, 2007a) and probably in epilepsy and SUDEP (sudden unexplained death in epilepsy).

In animals there is mounting evidence that I_h is involved in neuropathic pain (Chaplan *et al.*, 2003; Jiang *et al.*, 2008a; Jiang *et al.*, 2008b; Momin *et al.*, 2008; Momin & McNaughton, 2009; Emery *et al.*, 2011; Moldovan *et al.*, 2013) and epilepsy (Chen *et al.*, 2001a).

Molecular targets

A number of early bradycardic agents such as ZD7288, have been used to block I_h experimentally, but have had limited success therapeutically because they are not isoform-specific and side-effects are not uncommon (BoSmith *et al.*, 1993; Moosmang *et al.*, 2001). Ivabradine is a more recent and selective blocker of I_h that does not cross the blood-brain and presumably blood-nerve barriers (Bucchi *et al.*, 2006; Descoeur *et al.*, 2011; Postea & Biel, 2011). Ivabradine has been approved for the treatment of

stable angina pectoris in patients unable to use beta blockers, as it blocks open HCN4 and closed HCN1 channels yielding fewer visual disturbances (Swedberg *et al.*, 2010), and subtle modification of its structure may yield further specificity for HCN4 (Melchiorre *et al.*, 2010).

HCN1 and to a lesser extent HCN2 contribute to the spontaneous discharge of medium to large myelinated fibres of the peripheral nervous system and can be blocked using ZD7288 (Moosmang *et al.*, 2001; Chaplan *et al.*, 2003). The differential distribution of HCN isoforms in neuronal, visual and cardiac systems and differential sensitivity to blockers will be important if HCN function is to be a therapeutic target for neuropathic pain or epilepsy without unintended side-effects in the cardiac system (Maher *et al.*, 2009; Wickenden *et al.*, 2009; McClure *et al.*, 2011).

'Leak' currents

Background K^+-selective leak currents influence resting membrane potential and as a consequence axonal excitability. Though a background leak of K^+ ions has been long proposed (Hodgkin & Huxley, 1947, 1952d) the underlying channels have only recently been identified (Goldstein *et al.*, 2005; Enyedi & Czirják, 2010).

Potassium leak, or two-pore domain K^+ channels (K_{2P}) channels, consist of two pore-forming P-domains and four transmembrane segments. Unlike voltage-gated ion channels however, K^+ leak channels are composed of only the ion conducting elements of a voltage-gated ion channel, namely the transmembrane segments, M1 and M2 (which are analogous to S5 and S6 in voltage-gated ion channels), rendering the channels relatively insensitive to voltage (Goldstein *et al.*, 2001; Yu & Catterall, 2004; Goldstein *et al.*, 2005; Yu *et al.*, 2005; Enyedi & Czirják, 2010).

K^+ leak channels are resistant to most K^+ channel blockers, but are modulated by a number of environmental factors such as pH and mechanical stress, and probably contribute to the hyperpolarization of resting membrane potential by volatile anaesthetics (Enyedi & Czirják, 2010).

Tonic currents due to K_{2P} channels, Na^+/K^+-ATPase pump and slower forms of I_h are difficult to resolve using existing axonal excitability methods, and as such model interpretation is unable to separate out the various components underlying the modelled pump currents and leak conductances. This is relevant to the insights gained in Chapters 4 and 5, and to other studies performed during the course of this thesis (Trevillion *et al.*, 2010; Arnold *et al.*, 2013).

Ion pumps and transporters

In contrast to the rapid and passive diffusion of ions through ion channels, ion pumps and transporters actively transport at most 100 ions / second consuming energy in the process.

Na^+/K^+ pump

The Na^+/K^+-ATPase pump opposes the influx of Na^+ and efflux K^+ ions by pumping 3 Na^+ ions out of and 2 K^+ ions into the cell per pump cycle (Skou & Esmann, 1992). This process is electrogenic, it hyperpolarizes membrane potential, and is the primary driver of post-tetanic hyperpolarization (Bergmans, 1970; Bostock & Grafe, 1985; Applegate & Burke, 1989; Bostock & Bergmans, 1994), which in turn is countered by the activation of I_h. Activity-dependent hyperpolarization is more pronounced in unmyelinated fibres (Ritchie, 1995), in which conduction slows greatly as the stimulation frequency is increased (Grafe *et al.*, 1997).

Ouabain, strophanthidin and Li^+ all block Na^+/K^+-ATPase, which Gordon and colleagues (1990) used to abolish post-train afterhyperpolarization in rat optic nerve. Na^+/K^+-ATPase pump activity increases with extracellular K^+ and intracellular Na^+ concentrations. The literature is scant in regard to the effect of heating on Na^+/K^+-ATPase pump activity, but it is likely that pump transactions are facilitated by heating, and this possibility is discussed in Chapter 5.

Na^+/Ca^{2+} exchanger

The Na^+/Ca^{2+} exchanger is important for the maintenance of cytoplasmic Ca^{2+} levels. In the forward mode intracellular Ca^{2+} ions are exchanged for extracellular Na^+ ions using the Na^+ gradient (established by Na^+/K^+-ATPase), though the stoichiometry and therefore the electrogenicity of such a transaction has not been clearly established (Eisner & Lederer, 1985). A reduction in the Na^+ gradient can lead to the Na^+/Ca^{2+} exchanger running in reverse, increasing intracellular Ca^{2+}, triggering a cascade of events that contribute to axonal degeneration (Craner *et al.*, 2004).

Axonal excitability

The ability of an axon to conduct an action potential is dependent on a number of finely tuned and interrelated factors. In addition to the passive or morphological properties affecting axonal excitability, the recent history of membrane potential and the currents that alter it are major determinants of the preparedness of an axon to trigger an action potential. The complex coupling between membrane potential and voltage-gated, leak and pump currents permits axonal specialization, but at the same time provides a mechanism for dysfunction.

Changes in membrane potential occur whenever there is a net current flowing through ion channels and transporters. Conversely, the current through voltage-gated ion

channels is dependent on membrane potential, doubly so: first, as the name suggests, the conductance is controlled by membrane potential (and its recent history), and secondly by the electrochemical driving force or difference between membrane potential and the channel's reversal potential.

Much of the current understanding of the ionic determinants of axonal excitability is based on *ex vivo* measurements. In these artificial environments the cell membranes and the precise intra- and extracellular environments surrounding them can be manipulated as desired or according to the experimental paradigm. Threshold tracking on the other hand provides a rapid and non-invasive technique for studying the axonal excitability of *in vivo* preparations (Bostock *et al.*, 1998; Kiernan *et al.*, 2000; Kiernan *et al.*, 2001b). Threshold-tracking studies give insight into the underlying complex mechanisms of the intact organism as it functions, in health, during disease and in response to manipulation, by for example ischaemia, temperature and pharmacological agents (Krishnan *et al.*, 2009; Moldovan *et al.*, 2013). Threshold-tracking studies are a complementary tool, which do not replace *in vitro* or animal studies, but rather depend upon them for interpretation, and extend their applicability to humans.

Threshold tracking

The study of excitability or 'irritability' of excitable tissue predates voltage-clamp studies and the concept of an ion channel. Indeed, Georges Weiss was commissioned to examine the comparability of stimulation devices for muscle and nerve in the latter part of the 19th century, culminating in his treatise 'Fundamental Law of Electrostimulation' (Weiss, 1901; Irnich, 2002). Axonal excitability studies have traditionally focussed on three main approaches to electrophysiology: first, observations of the stimulus characteristics that determine threshold at rest; secondly,

the effect of long-lasting subthreshold polarization; and thirdly, excitability changes following activation.

Adrian (1917) applied strength-duration techniques to the testing of the denervation and reinnervation of human muscle, a question of contemporary importance with the nerve injury from gunshot wounds during the first world war.

The first excitability studies in human axons were probably those of Kugelberg (1944) and Kugelberg and Skoglund (1946), who used linear and exponentially rising stimulus ramps to examine the accommodative properties of peripheral nerve. Gilliatt and Willison (1963) measured the refractory and supernormal periods of human median nerve at the elbow using pairs of independently variable condenser discharges at the wrist. They normalised their excitability data to the unconditioned stimulus intensity, much as is done in modern threshold tracking studies.

The first comprehensive study of excitability in human axons was performed by Joseph Bergmans who tracked the threshold of activation of single units in response to a number of manoeuvres such as activation and ischaemia. These studies constituted his thesis (Bergmans, 1970) and were methodical and painstaking, requiring the manual adjustment of the stimulus intensity with threshold defined as the appearance of an action potential in response to three out of five successive stimuli.

Raymond used a 'threshold hunter' device to record the excitability following an impulse in frog sciatic nerve (Raymond, 1979). The threshold hunter adjusted the charge contained in a test stimulus to 'hunt' a single fibre response by automatically varying the width of the test pulse between 40 and 300 μs. Bostock and colleagues (1983) used a tripolar electrode and a purpose-built constant-current stimulator to measure membrane currents and thresholds for activation simultaneously in exposed rat spinal roots. The output current of the stimulator followed a computer controlled

command signal, which tracked the threshold for activation as the electrode advanced along the nerve.

The first automated threshold tracking studies in humans were those of Bostock and Baker (1988), who developed the technique of threshold electrotonus as a non-invasive equivalent of the measurement of the electrotonic response to long subthreshold currents. The technique of threshold tracking was then applied in humans to the study of post-ischemic paraesthesiae (Bostock *et al.*, 1991a; Bostock *et al.*, 1991b), strength-duration properties (Mogyoros *et al.*, 1996), the recovery of excitability following an impulse (Kiernan *et al.*, 1996), and latent addition in motor and sensory fibres (Bostock & Rothwell, 1997).

Key elements of these early threshold tracking techniques were incorporated into a standard protocol of axonal excitability, and the participants of a summer course of 'Clinical Axonal Electrophysiology' in Trondheim, Norway (1999) had their excitability tested using this new '*TROND*' protocol (Kiernan *et al.*, 2000). This cohort provided the normative data for motor axons and was soon followed by a complementary study in sensory nerve (Kiernan *et al.*, 2001b). Essential for the interpretation of subsequent studies were studies on the effects of membrane polarization, ischaemia and temperature (Kiernan & Bostock, 2000; Kiernan *et al.*, 2001a). Since its introduction this rapid and non-invasive protocol has been used to study changes in axonal excitability in many neurological and neuromuscular disorders (for reviews see Nodera & Kaji, 2006; Krishnan *et al.*, 2009).

Threshold / Recruitment order

The absolute threshold for recruitment is dependent on a number of factors including the stimulation setup, proximity to nerve and pulse parameters. The studies in this thesis focus on the large myelinated fibres of the median nerve which, at the wrist, are

superficially located. Large axons typically have the lowest thresholds because their lower axial resistances allow greater current densities which means the largest fibres are activated first (Rattay, 1989). This sequence is the opposite of normal physiological recruitment (Henneman & Olson, 1965; Henneman *et al.*, 1965).

Activation threshold is sensitive to membrane potential, which in turn is sensitive to alterations in ion channels or pumps active at rest and the extracellular and cytoplasmic environments. The unconditioned threshold forms the control for axonal excitability studies, and threshold changes in response to various forms of conditioning are normalised to it.

Single motor units have been an attractive preparation for axonal excitability studies because they represent a single axon and their threshold is simply defined as the stimulus intensity at which an 'all-or-none' response occurs (ie. in response to 50% of the stimuli; Kugelberg & Skoglund, 1946; Bergmans, 1970; Bostock & Baker, 1988; Trevillion *et al.*, 2010). In comparison to compound action potentials (CAPs) however, single motor units, have smaller potentials, are often difficult to isolate *in vivo*, are slower to track, and provide information about only the lowest threshold axons. This would not matter if the properties of axons of different threshold were the same: unfortunately, as mentioned below, they are not (Shibuta *et al.*, 2010; Trevillion *et al.*, 2010; Nodera & Rutkove, 2012a).

These difficulties are overcome by tracking CAPs that are a fixed fraction (typically 30 – 50%) of the maximal response. Initial observations have suggested that threshold tracking studies using CAPs yields quicker but equivalent results to those using single motor units. Recent studies have however found that there are differences in the excitability of axons activated at different thresholds (Shibuta *et al.*, 2010; Trevillion *et al.*, 2010; Nodera & Rutkove, 2012a). In our study, we suggested that the threshold for

activation is reduced by a greater activity of I_h in low-threshold axons (Trevillion *et al.*, 2010).

The size of a compound action potential grows sigmoidally in response to increasing electrical stimulation. In healthy nerve, most motor axons are recruited between 80 and 120% of the stimulus for a half-maximal CMAP (Kiernan *et al.*, 2000), and most sensory axons between 70 and 130% (Kiernan *et al.*, 2001b). Typically a fraction of the CAP is tracked and this usually corresponds to the steepest part of the Stimulus-response (SR) curve (~40% of the maximal CAP) or a pre-defined fraction of 40 or 50% of the maximal CAP. The common wisdom is that tracking a fractional CAP actually reflects the properties of the last axons recruited into the CAP. If the target axon is recruited at the steepest part of the SR curve then it is likely that axons with very similar properties will be recruited around the same stimulus intensity. Indeed interpretation of axonal excitability studies generally assumes that the recruitment order is not altered substantially by the various excitability tests.

Finally, it must be said that, although excitability studies test properties of axons at the stimulus site, axonal excitability studies require the faithful transmission of an action potential from the stimulus site to the recording site. The recordings therefore test only the axons that are able to conduct. Additionally motor axons require secure transmission across the neuromuscular junction and along muscle fibres.

Strength-duration properties

Using the discharge from capacitors of different sizes, Hoorweg (1892) measured the threshold voltage required for stimulation of nerve, effectively generating the first strength-duration curves (Geddes, 1994).

The generation of narrow square pulses was solved by Weiss (1901) who used a rifle to cut two wires in rapid succession, the first cut interrupted a short circuit which allowed a current to flow, and the second cut generated an open circuit thereby terminating the current pulse. The distance between the wires and the velocity of the rifle determined the pulse width. Using this technique, Weiss found empirically that the key characteristic of a threshold stimulus was not the shape of a pulse, but rather its charge, and that the charge increased linearly with pulse duration. Weiss formulated his law of stimulation as $Q = a + b \cdot d$, where Q is the stimulus charge, d is the pulse width and a and b are constants.

Lapicque (1909) recognised that the current-duration plot was of a hyperbolic nature and that as the pulse width increased the current decreased to a minimum, which he termed rheobase. He also defined chronaxie as the pulse width corresponding to a threshold current twice that of rheobase, and summarised these findings in his formula: $I = b \cdot (1 + c/d)$, where I is the threshold current, b is rheobase (corresponding to the slope of the line in Weiss' equation), c is chronaxie (which is equal to the strength-duration time constant [τ_{SD}] when Weiss' law applies) and d is again the pulse width.

Adrian (1917) observed that normal (innervated) muscle had a short chronaxie, and that denervated muscle had a long chronaxie, consistent with earlier observations that muscle responded to galvanic (long), and nerve to faradic (short) stimulation. Adrian's observations of chronaxie provided a clinically useful tool for assessing the state of innervation of muscle.

Despite more complicated equations proposed later by Lapicque (1907) and Hill (1936), several studies have found that Weiss's equation (and Lapicque's re-expression of it in terms of rheobase and chronaxie) has provided the simplest and most accurate

fit of the experimental data (Bostock, 1983; Bostock *et al.*, 1983; Mogyoros *et al.*, 1996).

Geddes and Bourland (1985a, b) made the interesting observation that the energy in a rectangular stimulus pulse is at a minimum when the pulse width is equal to chronaxie.

Depolarization and ischaemia both increase τ_{SD}, while hyperpolarization and the release of ischaemia decrease τ_{SD} (Bostock & Bergmans, 1994; Mogyoros *et al.*, 1996; Bostock & Rothwell, 1997; Mogyoros *et al.*, 1998; Kiernan & Bostock, 2000).

Strength-duration properties depend on both passive and active properties of the fibre. Demyelinated fibres have longer strength-duration time constants, which Bostock and colleagues (1983) have attributed to the increase in electrotonic time constant due to a greater nodal area. Bostock (1983) modelled the changes to τ_{SD} due to changes in active and passive parameters, and found that for the active parameters, τ_{SD} was most sensitive to the kinetics of sodium activation.

Using the method of latent addition, Bostock and Rothwell (1997), found that the recovery from brief (60 μs) hyperpolarizing and depolarizing stimuli in human axons could be modelled by the inclusion of a persistent sodium conductance. They found that the slower recovery of sensory axons to both hyperpolarizing and depolarizing stimuli than motor could be adequately modelled by a greater maximum Na_p conductance (though they did mention that a greater I_{NaP} may be achieved by depolarization). This possibility is supported by the data in Chapter 4.

Recovery cycle

A characteristic pattern of excitability follows in the wake of an action potential. Using paired pulses to the sciatic nerve of frog Gotch and Burch (1899) observed a reduction in excitability immediately following a propagated disturbance, and Boycott (1899)

demonstrated that this period of reduced excitability was prolonged with cooling. Adrian and Lucas (1912) made the further distinction between the initial period of inexcitability and the subsequent period of reduced excitability, which they termed the absolute and relative refractory periods, respectively. Adrian and Lucas (1912) also examined the period of supernormality which follows refractoriness while seeking "... to obtain a clearer understanding of the fact that of two like stimuli sent into an excitable tissue the first may often produce no apparent effect whereas the second will provoke an obvious response". The period of depressed excitability following the supernormal period was given the analogous name of late subnormality (Graham, 1935).

Gilliatt and Willison (1963) recorded the refractory period and supernormality in human median nerve, and observed that ischaemia prolonged the refractory period and abolished supernormality.

Bergmans (1970) recorded the complete recovery cycle of single human motor axons, and with trains of stimuli induced two phases of hyperpolarization which he called H1 and H2. The first phase, H1, was in response to short trains of suitably-timed stimuli (~250 Hz) which Bergmans postulated was due to a slow K^+ conductance (a decade earlier than the first experiments demonstrating the existence of a slow K^+ conductance). Bergmans provided convincing evidence that the second phase, H2 was due to enhanced activation of the electrogenic Na^+/K^+-ATPase pump, and in contrast to H1, H2 is long-lasting continues to develop with subsequent stimuli in long trains. H2 is believed to contribute to the excitability changes following high-frequency stimulation of cutaneous afferents (Applegate & Burke, 1989; Burke & Applegate, 1989; Kiernan *et al.*, 1997a; Kiernan *et al.*, 1997b).

The recovery of excitability following activation is underpinned by interdependent and finely tuned active and passive mechanisms. In their quantitative description of action potential initiation in squid axons, Hodgkin and Huxley (1952d) attributed refractoriness primarily to the inactivation of Na^+ channels, and the relative refractory period to the recovery from inactivation. Elucidation of the mechanism for supernormality came with a study of the associated depolarizing afterpotential in myelinated lizard axons (Barrett & Barrett, 1982). Barrett and Barrett proposed a new model of excitability at the node of Ranvier, which involved the charging and then discharging of the capacitance of the internodal axolemma during and after an action potential. Stys and Waxman (1994) postulated that the activation of slow K^+ channels during the action potential could be responsible for afterhyperpolarization and the late subnormal period. This view was supported by later studies of rat sural nerve where the application of the K_v7 activator flupirtine enhanced and prolonged late subexcitability, while the blocker XE991 decreased late subexcitability (Schwarz *et al.*, 2006; Sittl *et al.*, 2010).

The first automated measurements of recovery cycles in humans were made using custom circuitry under computer control, in which Stys and Ashby (1990) measured the threshold crossings of the response to paired stimuli in sensory nerve. By varying the interstimulus interval, this allowed them to construct recovery cycles measuring the small shifts in latency. Threshold tracking studies using the *TROND* protocol require less demanding hardware, can be applied to both motor and sensory nerve, and provide multiple measures of excitability (Bostock *et al.*, 1998; Kiernan *et al.*, 2000; Kiernan *et al.*, 2001b).

The same pattern of excitability changes in the recovery from activation is seen in both motor and sensory axons, though the extents of superexcitability and subexcitability

are smaller in sensory axons than motor (Kiernan *et al.*, 1996; differences in the excitability of motor and sensory axons are examined in Chapter 3). Recovery cycles recorded using single motor units and different target response levels are not significantly different (Kiernan *et al.*, 1996; Shibuta *et al.*, 2010; Trevillion *et al.*, 2010; Nodera & Rutkove, 2012a), perhaps suggesting that the mechanisms underlying the recovery cycle do not change with target level, and that other factors are responsible for the differential activation of axons to graded electrical stimuli.

Threshold Electrotonus and the current-threshold relationship

Following Galvani's discovery of the rheoscopic frog (or more familiarly, the frog sciatic-gastrocnemius preparation), long lasting polarizing pulses using battery piles were employed in the study of "animal electricity" (du Bois-Reymond, 1849). Pflüger's thesis (1859) examined the electrotonic behaviour of excitability in the frog and found that the source of excitation was at the cathode on make (beginning) and at the anode on break (end) of galvanic stimulation. During subthreshold depolarization a slow process (termed accommodation by Nernst, 1908) counters the excitatory effect of polarization, thereby limiting action potential initiation at the cathode to the onset of the pulse. Erlanger and Blair (1938) found a characteristic of sensory fibres was their increased repetitiousness in response to constant current stimulation when compared to motor fibres, and that this was as they had expected, accompanied by less accommodation in sensory fibres. This difference is examined further in Chapter 4. Lorente de Nó (1947b, a) applied long-lasting depolarizing and hyperpolarizing currents to frog-sciatic nerve and observed that the "nerve reaction" (accommodation of excitability) mirrored the slow changes in membrane potential (Bostock, 1995).

Though Hodgkin and Huxley (1952d) did not specifically make measurements of accommodation (in the excitability sense) they did record membrane potential

changes in response to 15-ms wide polarizing currents and their quantitative description, based on voltage-clamp measurements alone, demonstrated comparable accommodation of membrane potential.

Mayer and Westbrook (1983) used the electrotonic responses to long-lasting currents to study inward rectification in mouse DRG neurones. Baker and colleagues (1987) argued that in order to study the rectifying properties of myelinated axons, techniques other than the nodal voltage clamp, which could access the channels located under the myelin sheath, were required. By studying the electrotonic response of rat spinal roots in combination with various channel blockers, Baker and colleagues were able to identify: an internodally-located inward rectification (I_h); a slow outward rectification I_{Ks} (predominantly nodal); and an internodally located fast outward rectification (I_{Kf}).

Bostock and Baker (1988) developed a non-invasive technique "threshold electrotonus" to study the electrotonic properties of human axons *in vivo*. Threshold electrotonus measures the threshold changes before, during, and after long-lasting conditioning currents. Bostock and Baker observed that threshold electrotonus (when plotted as threshold reduction versus delay) mirrors the electrotonic changes seen in intact and current-clamped axons. From a theoretical standpoint, the mirroring of membrane potential by threshold changes is reasonable because the fast electrotonic properties of myelinated axons are nearly linear (at least for narrow pulses; Baker *et al.*, 1987; Bostock *et al.*, 1991a).

In a similar manner, the current-threshold relationship ("threshold I/V") was introduced as an analogue of the traditional current-voltage plots, and measures the threshold reduction at the end of long (typically 200 ms) depolarizing and hyperpolarizing pulses (Kiernan *et al.*, 2000). The current-threshold relationship

measures the rectifying properties of both the nodal and internodal axolemma, and its slope provides the threshold analogue of input conductance.

Since their introduction, threshold electrotonus and current-threshold techniques have been deployed in myelinated and unmyelinated fibres of human, mouse and rat nerve. In unmyelinated axons, Grafe and colleagues (1997) used threshold electrotonus to demonstrate the importance of inward rectification in action potential conduction and resting membrane potential. Threshold electrotonus and current-threshold studies in axons of different electrical threshold have revealed a greater inward rectification in low-threshold axons (Shibuta *et al.*, 2010; Trevillion *et al.*, 2010; Nodera & Rutkove, 2012a). Alterations in threshold electrotonus and the current-threshold relationship and therefore the rectifying properties of human axons have been observed in numerous diseases, including stroke, porphyria and diabetes (reviewed in Krishnan *et al.*, 2009).

Modelling

Mathematical modelling of excitable tissue has provided great insight into the molecular and physiological mechanisms underlying action potential initiation and propagation. Careful and insightful application of modelling techniques allowed Hodgkin and Huxley (1952d) to predict the presence of ion channels and many of their key features, and in doing so provide the framework for our understanding of axonal excitability.

Lipid bilayer

The impedance of most cell membranes can be modelled by an equivalent circuit consisting of the parallel combination of a capacitance and resistance (see Fig. 1.2 below; Fricke, 1923; Fricke, 1925; Cole, 1933; Cole & Curtis, 1936).

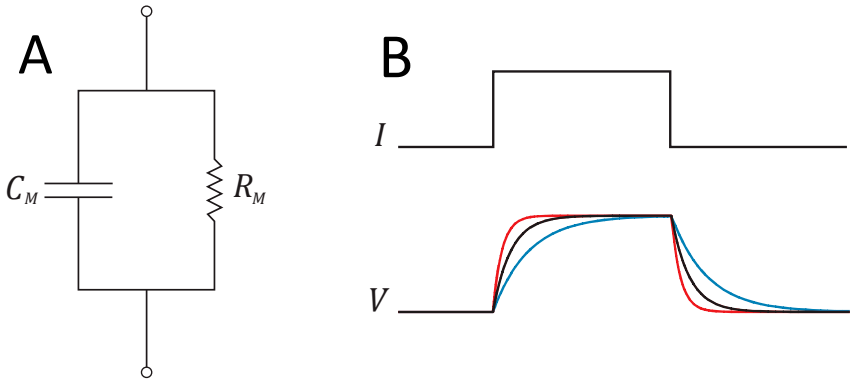

Figure 1.2. A. Equivalent circuit for biological membrane, with a capacitance (C_M) and resistance (R_M) in parallel. **B.** Membrane Potential (V) in response to square current pulse (I) across membranes with progressively longer time constants (red shortest, blue longest).

Electrically this circuit functions as a low pass filter, and the membrane time constant can be derived simply by considering that the membrane capacitance (C_M) relates the charge (Q) stored on the plates of a capacitor (the lipid bilayer) to the voltage (V) across its terminals:

$$Q = C_M V$$

If one rearranges the equation, differentiates it with respect to time, recognises the definition of current and applies Ohm's law one obtains:

$$\frac{dV}{dt} = \frac{1}{C_M}\frac{dQ}{dt} = \frac{1}{C_M} I = \frac{V}{R_M C_M}$$

which is a first order differential equation, describing exponential growth or decay, and has the solution:

$$V = V_0 e^{\pm t/R_M C_M}, \text{ where } V = V_0 \text{ at } t = 0$$

The product $R_M C_M$ is the membrane time constant, and effectively limits the rate at which the membrane potential can be varied. Myelination creates a narrow nodal gap with low capacitance and combined with a high resting conductance speeds up membrane potential changes and action potential propagation. The inclusion of

voltage-dependent ion channels changes the properties of the nodal membrane and therefore contributes to the relatively long strength duration time constant. The membrane time constant can be estimated in human subjects using the method of latent addition, and is of the order of 45 – 50 μs (Bostock & Rothwell, 1997).

Cole and Curtis (1939) measured the impedance during activity and found the resistance to be highly variable and, rather unexpectedly, that the capacitance remained constant, setting the scene for later voltage-clamp studies of the ionic basis of these conductance changes. Not only does the membrane capacitance vary little during an action potential, but it also varies little (~ 1 $\mu F/cm^2$) across biological membranes (Hille, 1992), thereby allowing fine control of membrane dynamics by changes in the input conductance.

Electrically this circuit is the classic low-pass RC filter, and in combination with the high-pass filtering provided by I_h provides the prerequisites for resonant activity which is the subject of Chapter 6.

The Hodgkin-Huxley model

Hodgkin and Huxley's (1952d) quantitative description of the nature of membrane permeability changes was based on several key observations from their voltage-clamp studies of the squid giant axon. First, the ionic and capacitive currents are independent and the membrane capacitance is constant, confirming the earlier findings of Cole and Curtis (1939). Second, permeability changes of the Na^+ and K^+ currents are independent. Third, and perhaps most importantly, the permeability is dependent on voltage rather than current.

Model description

The Hodgkin-Huxley model began with a dissection of the membrane conductance in the circuit description above (denoted as R_M [its reciprocal] in the circuit of Fig 1.2). The overall current across the membrane is made up of the ion impermeable (capacitive) and ion permeable (ionic) currents as follows:

$$I = C_M \frac{dV}{dt} + I_{ion}$$

where the ionic current, I_{ion} flows through voltage-gated conductances. The voltage-clamping studies were predicated on the fact that once the initial membrane potential transient decays sufficiently ($\frac{dV}{dt} = 0$) the observed current is I_{ion}.

Hodgkin and Huxley found that the ionic current is composed primarily of a rapidly activating and inactivating inward Na^+ current (I_{Na}), a slow outward K^+ current (I_K), and a background leak of K^+ ions (I_{Lk}). In this model the individual currents are described using Ohm's law as the product of a conductance (g; which for Na^+ and K^+ is voltage-gated) and the electrochemical driving force (which is the difference between membrane potential and the Nernst potential for the ion):

$$I_{Na} = g_{Na}(E - E_{Na})$$
$$I_K = g_K(E - E_K)$$
$$I_{Lk} = g_{Lk}(E - E_{Lk})$$

The equivalent electrical circuit is composed of the simple combination of a capacitor, resistors and voltage sources as in Fig 1.3.

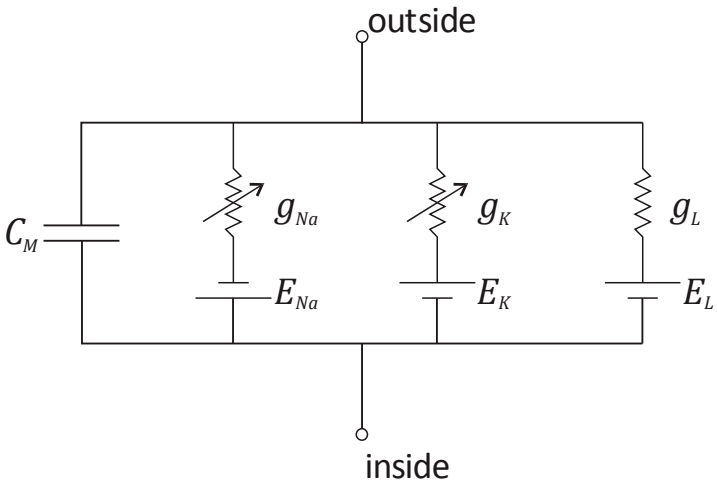

Figure 1.3. Equivalent circuit for the Hodgkin-Huxley model. The membrane is represented by the membrane capacitance, C_M, in parallel with Na^+, K^+ and an ohmic leak conductance (g_{Na}, g_K and g_L respectively). The reversal potentials of these conductances are shown as E_{Na}, E_K and E_L, respectively.

Na^+ conductance

Hodgkin and Huxley modelled the Na^+ conductance as the product of independent and reversible activation and inactivation processes:

$$g_{Na} = \bar{g}_{Na} m^3 h \qquad (1-m) \underset{\beta_m}{\overset{\alpha_m}{\rightleftharpoons}} m \qquad (1-h) \underset{\beta_h}{\overset{\alpha_h}{\rightleftharpoons}} h$$

where $\bar{g}_{Na}$ is the maximum Na^+ conductance and m and h are the activation and inactivation variables, respectively. α_m and β_m are the voltage-dependent forward and backward rate constants between the de-activated $(1-m)$ and activated (m) states. The inactivation variable h however represents the probability that a Na^+ channel is *not* inactivated. The rate constants are described by the first-order differential equations:

$$\frac{dm}{dt} = \alpha_m(1-m) - \beta_m m \qquad \frac{dh}{dt} = \alpha_h(1-h) - \beta_h h$$

K^+ conductance

Hodgkin and Huxley described the K^+ conductance, without inactivation, as:

$$g_K = \bar{g}_K n^4 \qquad (1-n) \underset{\beta_n}{\overset{\alpha_n}{\rightleftharpoons}} n \qquad \frac{dn}{dt} = \alpha_n(1-n) - \beta_n n$$

where n is the K^+ activation variable, and α_n and β_n are the voltage-dependent forward and backward rate constants for activation.

Leak conductance (and Na^+ extrusion)

The background leak of K^+ ions was modelled as a constant ohmic conductance (g_{Lk}) which was not voltage-dependent. Hodgkin and Huxley acknowledged that the resting potential could be modified by reducing the leak conductance and incorporating a small current which might represent the extrusion of Na^+ ions. They postulated that "... some additional process must take place in a nerve in the living animal to maintain the ionic gradients which are the immediate source of the energy used in impulse conduction".

Modelled behaviour

Hodgkin and Huxley's model was based on the supposition that, under the influence of an electric field the movement of charged particles at particular sites in the membrane may indeed control ionic permeability. A supposition that was later supported by the molecular characterisation of the voltage sensor of ion channels. It is remarkable that this simple and empirically derived model is able to account for the range of phenomena that it does, including the form of an action potential in response to depolarization, absolute and relative refractoriness, accommodation and anode break excitation, and the effects of temperature. With the inclusion of the cable properties of the fibre, spatial measurements such as the conduction velocity and the form of propagated action potentials were also accurately modelled.

Model evolution

From this watershed moment in the modelling of excitable tissue, many researchers have adapted the Hodgkin-Huxley model to gain insight into: new ion channels, isoforms, and modes of action; the excitability of different tissues and different species; drug action; and disease mechanisms.

The axonal excitability studies contained in this thesis focus on the ionic determinants of excitability which is measured at the node but is also influenced by internodal properties. Studies on superficially-located nerves using relatively large electrodes permit the use of a two-compartment space-clamped model to test nodal excitability, and this obviates the need for multi-compartment models with greater morphological complexity. The following description will focus on some of the developments which led to the 'Bostock' model of a human motor axon.

Based on the observations of Dodge and Frankenhaeuser (1958) that the nodal currents in the frog axon resembled those of the squid axon, Fitzhugh (1962) created a model of the myelinated frog fibre using Hodgkin-Huxley kinetics for nodal excitability. He found good agreement with experimental evidence on action potential initiation and saltatory conduction.

Frankenhaeuser and Huxley (1964) calculated membrane action potentials and ionic currents based on voltage-clamp recordings of myelinated nerve fibres of *Xenopus laevis*. Goldman and Albus (1968) used the myelinated model of Fitzhugh with the nodal membrane described by the Frankenhaeuser-Huxley equations to calculate propagated impulses and their results were in good agreement with Rushton's (1951) theory and the experimental findings of several investigators that the conduction velocity is proportional to fiber diameter in myelinated axons.

Koles and Rasminsky (1972) used a model similar to that of Goldman and Albus to examine the effects of partial demyelination. Their model showed that, for the same increase in conductance and capacitance, paranodal demyelination was more effective at blocking conduction than uniform demyelination of an entire internode.

Bostock (1983) examined the effects of changes in model membrane parameters on the strength-duration behaviour using the Goldman and Albus model. Bostock found that the strength-duration time constant depended on the electrotonic time constant and the kinetics of sodium activation, and the computed charge-duration data was best fit by Weiss' law.

The 'Bostock' model

The 'Bostock' model was first published in a study that examined the causes of post-ischaemic fasciculations (Bostock *et al.*, 1991b), and has its origins in the revised model of a myelinated axon of Barrett and Barrett (1982). The active and passive components were adapted from the best available mammalian data. Three types of rectification (I_{Ks}, I_{Kf} and I_h) were incorporated into the nodal and internodal description as described for rat fibres by Baker and colleagues (1987). The paper by Schwarz and Eikhof (1987) provided the kinetics for the Na^+ and K_f conductances. The model evolved to include: better detail for Na^+ currents from voltage- and current-clamp recordings of human axons (Schwarz *et al.*, 1995); and the incorporation of persistent Na^+ behaviour as inferred by Bostock and Rothwell (1997). Further minor adjustments were made to fit the recordings of the excitability of healthy human motor axons, and this model has been used to describe the pathophysiology of changes due to tetrodotoxin poisoning, porphyria, stroke and multiple sclerosis (Kiernan *et al.*, 2005; Jankelowitz *et al.*, 2007a; Lin *et al.*, 2008; Ng *et al.*, 2008). This model has also given insight into mechanisms underlying maturation and ageing (Jankelowitz *et al.*, 2007b;

Farrar *et al.*, 2013), and basis of differences in axons recruited at different electrical thresholds (Trevillion *et al.*, 2010).

The 'Bostock' model exchanges morphological complexity for ionic detail and this trade-off is well suited to assist the interpretation of recordings of axonal excitability. This model is described in detail and developed further in Chapter 3, which also presents for the first time, a model of the excitability of the human sensory axon.

Chapter 2

Methodology

The studies presented in this thesis were performed with the QtracS threshold tracking software (© Prof Hugh Bostock, Institute of Neurology, UCL, UK) on the median nerve of healthy human subjects using a recording arrangement similar to the one illustrated in Fig. 2.1 and with excitability equipment as illustrated in Fig 2.2. Apart from the compound sensory action potentials (CSAPs) recorded orthodromically in Chapter 3, the excitability of both motor and sensory axons of the median nerve was tested at the wrist.

Recording setup

Electrodes

Axonal excitability studies test the excitability at the site of stimulation (i.e. underneath the cathode). Figure 2.1 illustrates the typical recording arrangement for testing the excitability of the median nerve. Disposable 'non-polarisable' Ag/AgCl ECG electrodes were used for stimulation, with the cathode placed in line with the median nerve at the proximal wrist crease and the anode approximately 10 cm proximal on the radial edge of the forearm. For the most sensitive measurements the optimal cathode location was sought with a saline-soaked, gauze-covered Ag/AgCl electrode.

Compound muscle action potentials (CMAPs) were measured using disposable ECG electrodes with the active electrode over the thenar eminence and the reference electrode over the proximal phalanx of digit one. CSAPs were recorded with self-adhesive disposable Ag/AgCl ring electrodes, with the active electrode at the proximal end of digit two and the reference 4 cm distal.

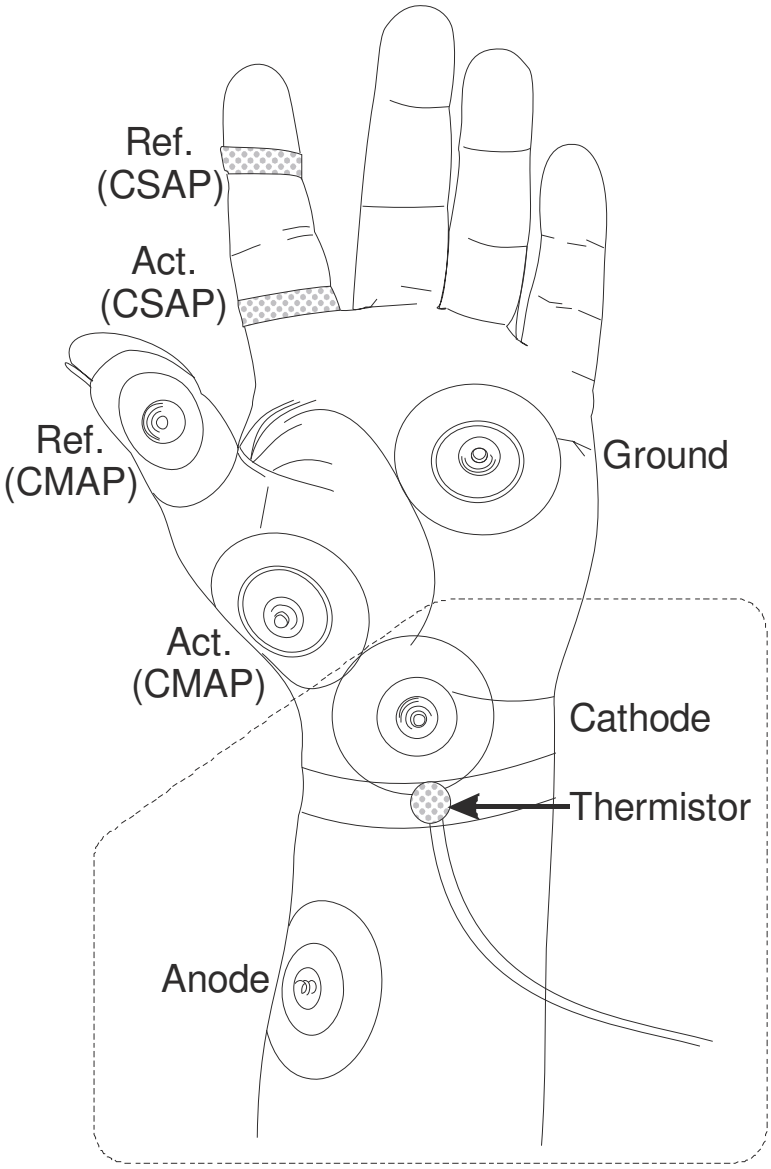

Figure 2.1. Typical recording arrangement. Stimuli delivered at the wrist (cathode) using Ag/AgCl electrodes with the anode 10 cm proximal on radial edge of the forearm. CMAPs are recorded over the thenar eminence, with the reference electrode on the proximal phalanx of the thumb. CSAPs were recorded using disposable Ag/AgCl ring electrodes on digit 2. The same ground was used for both motor and sensory recordings.

A thermistor records the temperature close to the site of stimulation (cathode).

The dotted lines indicate the area where the heat pads were applied for the hyperthermia experiments (Chapter 5).

Improvements were made to the grounding arrangement during the course of the studies. Initial studies used a disposable ECG electrode on the palm of the hand, and this was subsequently replaced with a large electrosurgical plate and electrolyte cream, the best performance however was achieved using an ECG electrode on the dorsum of the hand. The improvement was presumably due to lower skin impedance on the dorsum and for the most sensitive measurements this could be further optimised with gentle skin abrasion and searching for the optimal location.

Skin preparation, grounding, noise and stimulus artefact

The measurement of small sensory action potentials recorded with non-invasive surface electrodes is hampered by noise and stimulus artefact, and the development of a low-noise amplifier and techniques to overcome such issues are dealt with in detail in Chapter 3. Briefly, the use of low-impedance electrodes at the optimal location with good skin-surface preparation can have a major impact on the ability of a recording system to resolve tiny potentials in the presence of noise. Optimally located stimulus electrodes with good skin-surface preparation require lower compliance voltages to deliver the requested current (generating lower stimulus artefacts). Similarly, optimally placed and prepared recording electrodes will have greater signal-to-noise ratios.

Temperature

The control and measurement of temperature is critical for most axonal excitability studies (Burke *et al.*, 1999; Kiernan *et al.*, 2001a). The skin surface temperature was measured and recorded continuously with a 'banjo' style thermistor (YSI 409B) close to the site of stimulation. The forearm was wrapped in a towel, and studies commenced only when the temperature was stable and greater than 32°C.

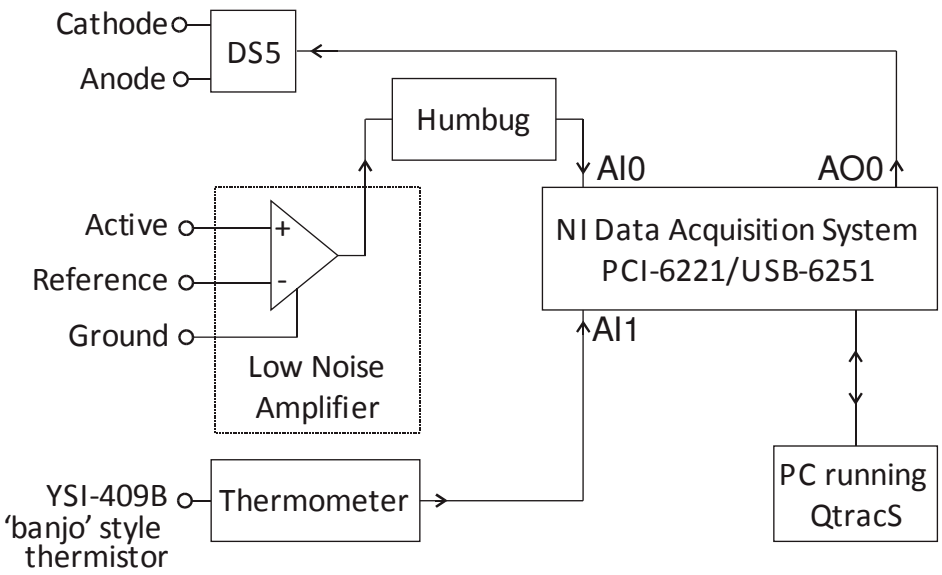

Figure 2.2. Axonal excitability recording system. The QtracS threshold tracking software runs on a personal computer installed with a National instruments data acquisition system (either as an internal PCI card with shielded cable and connector, or as a USB-device). QtracS provides the stimulus waveform for each test, which the data acquisition system digitises as a voltage waveform and the DS5 converts into a corresponding stimulus waveform which is applied to the subject through the cathode and anode. Synchronised with the stimulus waveform is the acquisition of the response waveform, which is fed back to QtracS for online analysis. The low-noise AC-coupled amplifier has any residual mains frequency noise removed with a Humbug 50/60 Hz Noise Eliminator. A skin-surface thermistor is connected to a thermometer which outputs 10 mV/°C which is sampled before the response data acquisition.

Excitability testing

Axonal excitability was tested using new and modified excitability protocols within QtracS which controlled both the data acquisition and stimulation via a 16-bit data acquisition system (National Instruments; USB-based NI-USB6251 or PCI-based PCI-6221; see Fig 2.2).

Current waveforms were delivered with a DS5 isolated bipolar constant current stimulator (Digitimer, Welwyn Garden City, UK) which followed the real-time command voltage generated by QtracS.

The CMAPs and CSAPs were amplified (x200 or x250 for motor; x10k for sensory) and bandpass filtered (2 Hz – 2 kHz) using the purpose-built, battery-powered isolated amplifier (or a prototype) with low noise and high common mode rejection developed in Chapter 3. Mains frequency noise was removed using a HumBug 50/60 Hz Noise Eliminator which subtracts the synchronous line frequency noise and its harmonics without the usual distortion associated with a notch filter. The amplified signals were then digitised with the data acquisition system, and returned to QtracS for online measurement.

Excitability protocols

Apart from the studies in Chapter 6, axonal excitability was tested using customised versions of the *TROND* protocol. The *TROND* protocol is a suite of excitability tests which tracks changes in the stimulus current (threshold) required to recruit a fixed proportion of the maximal response (typically 40-50%; Kiernan *et al.*, 2000; Kiernan *et al.*, 2001b). Once the threshold target is established, a control threshold is tracked throughout the measurement, and this control threshold sets the conditioning levels and is used to normalise excitability changes.

Unconditioned measures

The first task of all threshold tracking experiments is to record the ***stimulus-response curve*** (Fig. 2.3), by recording the response to stimuli which are gradually increased (or decreased) in strength. The stimulus-response characteristics then determine the threshold tracking target (indicated by the red vertical arrow) and optimise proportional tracking for the rest of the experiment.

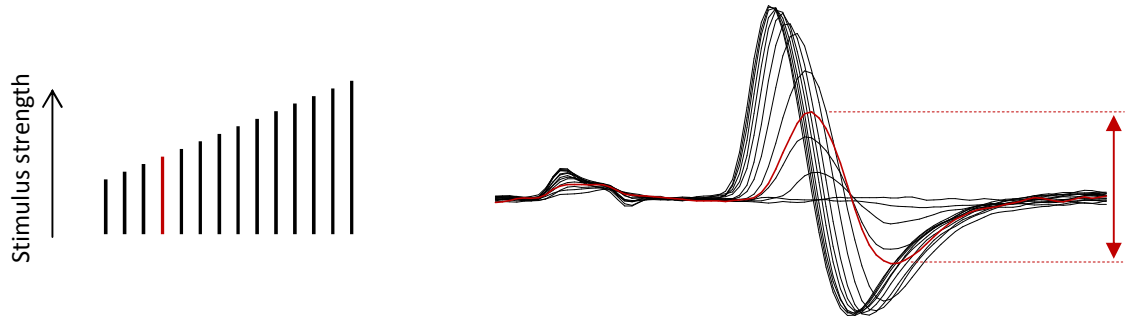

Figure 2.3. Stimulus-response test protocol. The stimulus-response characteristics are obtained by recording the response amplitudes (shown on the right) to stimuli of progressively increasing strength (shown on the left). The target response and its corresponding threshold stimulus (unconditioned control threshold) are shown in red. The target is generally ~40% of maximum but in later experiments it was set to 50% because recent studies have shown differences in axons recruited at difference thresholds (Shibuta *et al.*, 2010; Trevillion *et al.*, 2010).

The ***strength-duration properties*** are measured by tracking the thresholds (to the target response determined above) of stimuli of varying width (Fig 2.4). For CMAPs the thresholds are tested with pulse widths of: 1, 0.8, 0.6, 0.4 and 0.2 ms. To avoid errors caused by dispersion, CSAP measurements test the narrower pulse widths of 0.5, 0.4, 0.3, 0.2, 0.1 ms. The strength-duration plot is typically hyperbolic. The stimulus charge (strength x width) is linearly related to the stimulus duration with the slope representing rheobase (I_{rh}) , and the negative X-axis intercept the strength-duration time constant (τ_{SD}; Weiss' law; Mogyoros *et al.*, 1996).

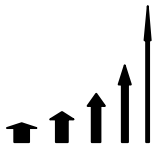

Figure 2.4 Strength-duration protocol. The stimulus thresholds for the target response of pulses of different widths (1, 0.8, 0.6, 0.4, 0.2 ms for motor and 0.5, 0.4, 0.3, 0.2, 0.1 ms for sensory) are tested, and typically follow a hyperbolic distribution.

Responses to subthreshold conditioning

Threshold electrotonus and the current-threshold relationship examine the accommodative properties of the axonal membrane by polarizing membrane potential with long-lasting subthreshold pulses.

Threshold electrotonus probes time-course of accommodation. In the standard protocol, the threshold is measured before, during and after 100-ms conditioning pulses of +40 and -40% of the unconditioned test threshold strength (red and green conditioning pulses in Fig 2.5, respectively).

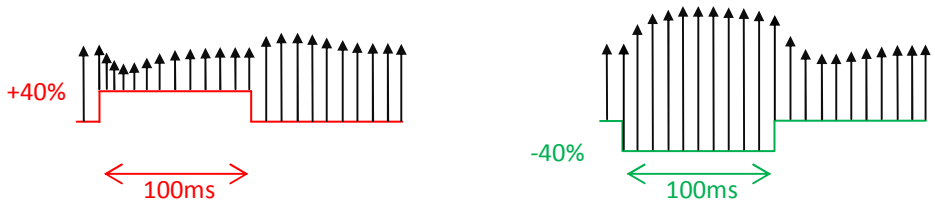

Figure 2.5. Threshold electrotonus protocol. Thresholds are tested before during and after 100-ms subthreshold pulses of +40% (red) and -40% (green) of the unconditioned thresholds. The intensity of the tracked stimulus is indicated by the height of the vertical arrows. The time-course of the threshold changes are dependent on a number of factors, including membrane polarization and the rectifying currents I_{Ks} and I_h.

Unintended activation often accompanies 40% depolarizing threshold electrotonus producing a 'notch', particularly with sensory axons and in pathology (Burke *et al.*, 2007; Trevillion *et al.*, 2007). In studies where such activation is anticipated, depolarization levels of ±20% (or even ±30% as in Figs 2.8 & 2.9) are used. The extended protocol used in this thesis also adds longer hyperpolarization pulses of 70% (for 200 ms) and 100% (for 300 ms).

The ***current-threshold relationship*** tests the axonal excitability 200 ms after the onset of long-lasting conditioning pulses which are graded in strength from +50% to -100% of the unconditioned threshold. Depolarization levels (+10 to +50%) provide a measure of outward rectification due to K_s channels, and hyperpolarization reflects the closing of K_s channels and the opening of HCN channels (inward rectification).

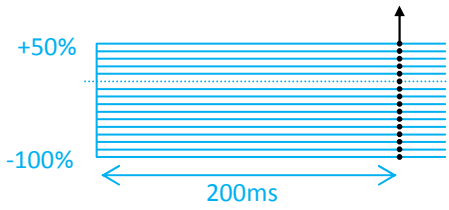

Figure 2.6. Current-threshold protocol. Excitability is tested 200 ms after the onset of conditioning pulses (indicated by arrow and filled black circles) which are reduced in 10% steps from +50% to -100% of the unconditioned control threshold. The results are plotted as current versus threshold reduction to mirror traditional 'IV' plots.

Excitability following activation

The recovery of excitability following activation was studied by testing the threshold following supramaximal stimulation (Fig. 2.7). The 18 conditioning-test intervals followed an approximately logarithmic sequence from 2 to 200 ms (though they are measured in the reverse order), reflecting the time-course of the periods of refractoriness, superexcitability and late subexcitability.

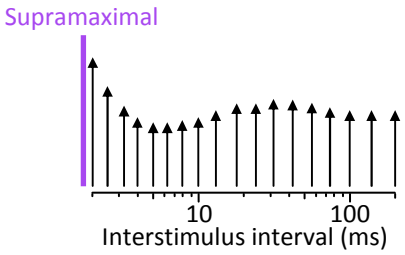

Figure 2.7. Recovery cycle protocol. Excitability is tested at 18 conditioning-test intervals following supramaximal stimulation (indicated by purple bar). The height of the vertical arrows reflects the test stimulus strength (threshold).

Axonal excitability recording

Figure 2.8 illustrates an excitability recording of sensory axons using the modified protocol of Chapter 4. Even with extended measures and the tracking of sensory axons, the study was completed in less than 25 minutes (*cf.* a standard motor recording < 10 mins). The stimulus-response relationship (SR section in Fig. 2.8) records the peak-to-peak response amplitudes (Fig. 2.8C) to linearly increasing stimuli (Fig. 2.8B). From the maximal response obtained (~130 μV in Fig. 2.8B) the target amplitude is set and then tracked for all subsequent measures. QtracS automatically adjusts (tracks) the test stimulus for each test condition. When the tracking is acceptable on a predetermined number of occasions, QtracS advances to the next test. Averaging and signal conditioning are also employed to increase the signal-to-noise ratio (and this is dealt with in more detail in Chapter 3). The use of proportional tracking accelerates the tracking process, as can be seen by the rapid return to the target response each time the test condition is changed (Fig 2.8C).

Analysis of axonal excitability

The analysis of excitability was performed off-line using the QtracP software. For each test condition, the tracked thresholds are extracted and averaged. For threshold electrotonus (TE) and the current-threshold relationship (IV) the threshold change is normalised as a threshold reduction.

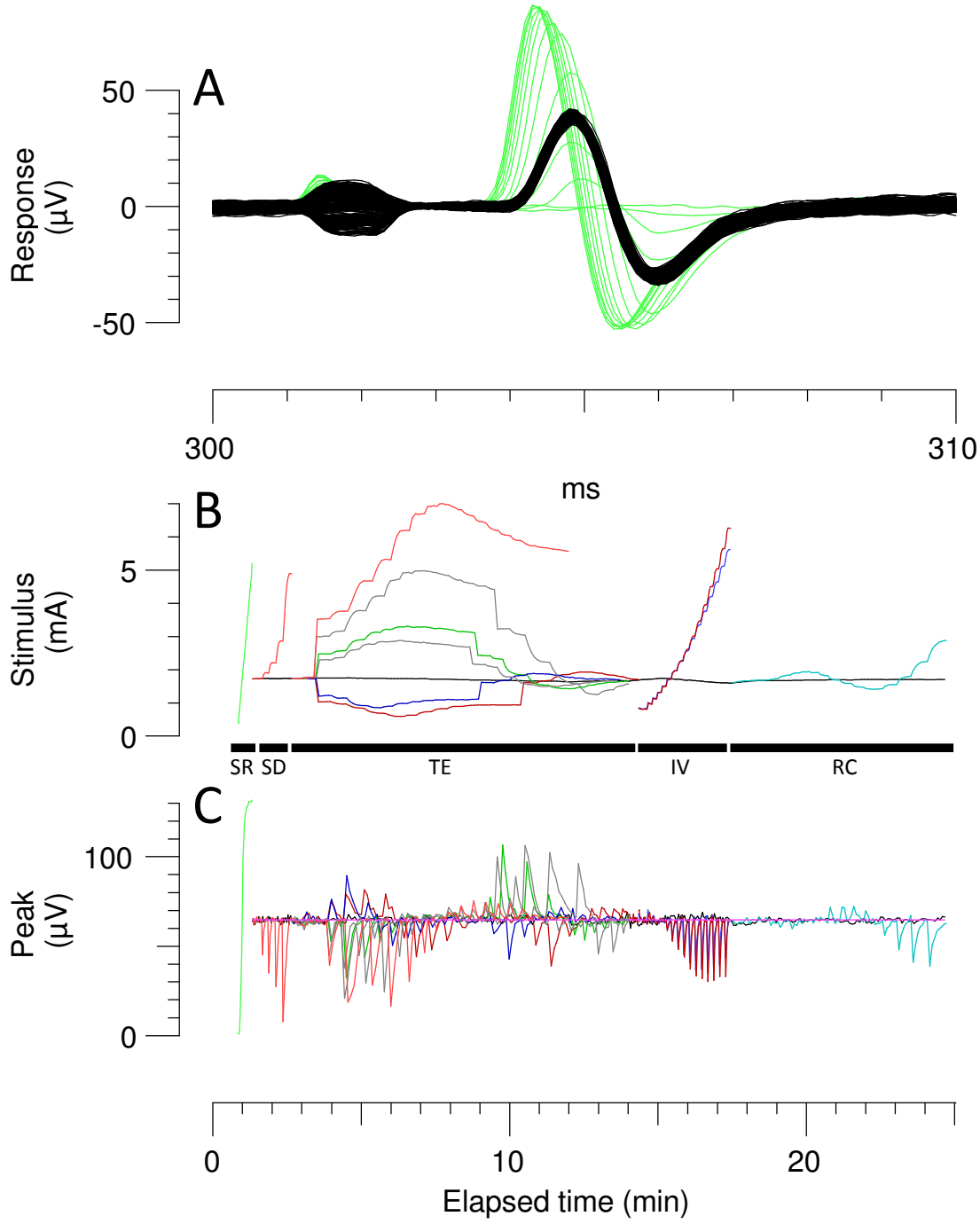

Figure 2.8. Threshold tracking recording. **A.** Responses for the stimulus-response measurement (green) and the unconditioned control stimulus (black). **B.** Tracked thresholds for: stimulus-response (SR), strength-duration (SD), threshold electrotonus (TE), current-threshold (IV) and the recovery cycle (RC) and the unconditioned test (black line throughout). **C.** Peak-to-peak amplitudes as the protocol tracks the target response (~65 µV; pink line). Note the rapidity of proportional tracking with conditioning stimulus changes.

The TE data are plotted against the conditioning-test (C-T) interval (Fig 2.9B), and the IV data are plotted as normalised current against threshold reduction (Fig 2.9C; note in this recording threshold was tested at 2 intervals, 100 & 200 ms). Similarly the recovery cycle data were normalised (as a threshold change) and plotted against C-T interval (Fig. 2.9D). Statistical analysis and plotting of group data was also performed primarily with QtracP (as outlined in each study).

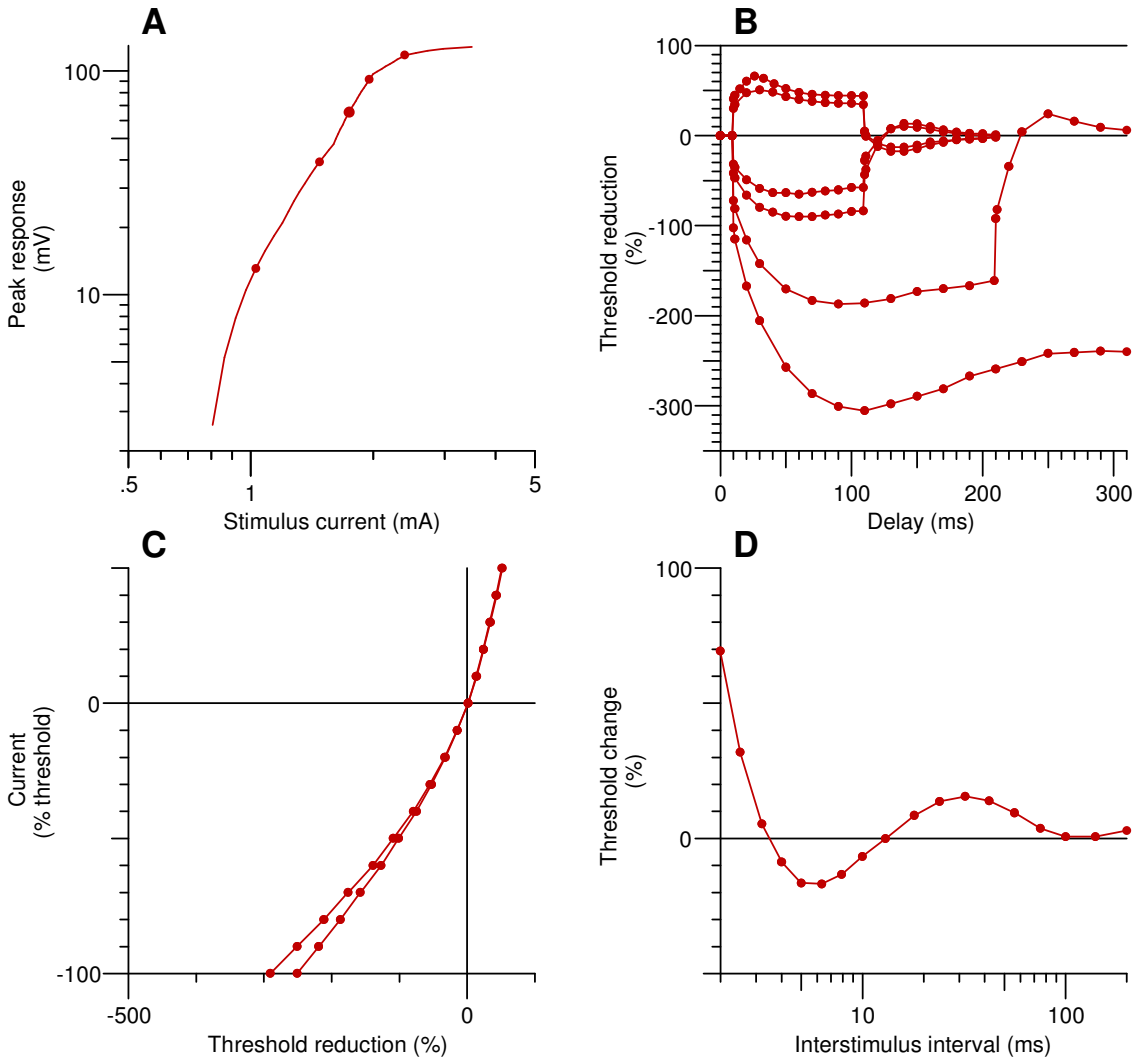

Figure 2.9. Axonal excitability measures derived from the recording in presented in Fig. 2.8. **A.** The stimulus-response curve plots the sigmoidal growth of the response (peak-to-peak amplitude) to stimuli of increasing intensity. **B.** Threshold electrotonus plots the decrease in threshold upwards ('threshold reduction'; equivalent to an increase in excitability) so that the traces resemble traditional electrotonic waveforms. Note that this is in the opposite direction to that shown in *D*. **C.** Current-threshold relationship plots the threshold reduction (X-axis) versus the current strength (Y-axis). **D.** The recovery cycle shows the recovery of excitability following activation with periods of refractoriness, superexcitability and then late subexcitability.

Chapter 3

Tracking small sensory nerve action potentials in studies of axonal excitability in human subjects

Summary

Excitability studies on normal and diseased human axons *in vivo* have been greatly enhanced by fast threshold-tracking techniques, using surface stimulation and recording. Although sensory axons are often more affected in disease, most studies to date have been on motor axons, because of technical difficulties in resolving small nerve volleys in the presence of noise and stimulus artefact. This study describes techniques for tracking low-amplitude compound action potentials, using a battery-powered, isolated preamplifier of simple construction with high common mode rejection (>125 dB [balanced inputs]) and low noise (<0.4 μV referred to input [shorted]). The amplifier allows the tracking of targets as small as 2 μV for a full range of excitability measurements without the usual distortion due to residual stimulus artefact and without the need for clamping, additional filtering or ensemble averaging. The findings suggest that the properties of low-threshold cutaneous axons, like those of low-threshold motor axons, differ from those of higher threshold. The results present the first axonal excitability recordings of afferents distal to the wrist, using orthodromic stimulation, and demonstrate that excitability properties of the same axons differ at the wrist and digit. Based on measurements of stimulus artefact distortion, noise and the performance in experiments, it is concluded that the techniques described here will facilitate the study of diseased axons for which the sensory potentials may be only a few microvolts in amplitude and have high thresholds. In addition, these techniques make it possible to study sensory axons closer to their extremities, where the symptoms of neuropathy usually start. This amplifier and the recording techniques were essential for the subsequent chapters.

Introduction

As discussed in Chapter 1 non-invasive threshold tracking techniques have been applied to the study of the underlying mechanisms of a wide range of neuropathologies (reviewed in: Krarup & Moldovan, 2009; Krishnan *et al.*, 2009). As a rapid *in vivo* method, threshold tracking is able to examine the action of a variety of drugs and toxins in human and animal subjects in real time (Kiernan *et al.*, 2005; Krishnan *et al.*, 2005a; Kuwabara & Misawa, 2008; Park *et al.*, 2009b, 2011; Nodera & Rutkove, 2012b).

In contrast to fixed stimulus studies, where the intensity of both conditioning and test stimuli are set and then kept constant, threshold tracking tests the effect of a conditioning stimulus by automatically adjusting the test stimulus intensity to maintain a response at a pre-determined fraction of the maximal compound action potential.

Even in subjects with only a few surviving motor units, the size and latency of the compound muscle action potential (CMAP) are sufficient to allow a clean and artefact-free recording. In the study that introduced the technique for the rapid measurement of multiple measures of axonal excitability, and established normative data for clinical testing (Kiernan *et al.*, 2000), the maximal CMAP of thenar muscles to the median nerve stimulation was, on average, 8.4 mV (baseline to peak) and, in a recent report of nerve conduction studies on a larger cohort of healthy individuals, it was 9.1 mV with a latency of onset of ~3.6 ms (Benatar *et al.*, 2009).

In contrast excitability studies on sensory axons are technically challenging, primarily because they depend on recording nerve action potentials which are much smaller and have shorter latencies (Krarup, 2004). The compound sensory nerve action potential (CSAP or SNAP) is measured in microvolts and recorded antidromically from the surface with lower limits of 26 μV (Kiernan *et al.*, 2001b) and 18.1 μV (Chapter 4),

when measured peak to peak. However, in 100 normal subjects, Benatar and colleagues (2009) reported the maximal median sensory CSAPs of 3.1 to 86 μV, dependent on age, though the measurement was baseline to peak. In threshold tracking, the target potential is submaximal, on the fast rising phase of the stimulus-response curve, typically 40 – 50% of the maximal CSAP, so that adequate signal-to-noise ratios may not be achieved even in normal subjects.

Currently there is no commercially available system for electromyography and nerve conduction studies (EMG/NCS) with a real time analogue output suitable for threshold tracking studies. Indeed, few have near real-time output capability and, because they are designed for a different purpose (comprehensive EMG/NCS neurodiagnostics), those that do are prohibitively expensive and of excessive size when their sole purpose in axonal excitability studies is amplification. Furthermore, these systems typically have significant and sometimes variable delays in the analogue output (presumably due to the signal path, isolation, digital signal processing and reconstruction of the analogue signal). Whilst the synchronisation between stimulation and recording may be recovered post-hoc for latency purposes, it complicates on-line procedures, such as the tracking of small target potentials.

In order to track small CSAPs efficiently, the preamplifier requires low noise and high common mode rejection (CMR). In addition, for small CSAPs close to the noise level, the threshold tracking strategy needs to take account of the fact that a 'response' may be due to noise alone. This study shows how a preamplifier of simple construction can be used to track microvolt potentials just above the noise floor established by the recording electrodes, without significant intrusion of the stimulus artefact into the recording. Its potential is illustrated in studies of the most excitable sensory axons, and of the excitability properties at more distal sites than have previously been

described, and the amplifier and techniques developed here were used in studies reported in Chapters 4 – 6.

Methods

To assess the feasibility of recording axonal excitability with small CSAPs, 14 experiments were performed on three healthy subjects with the approval of The University of Sydney's Human Research Ethics Committee, and in conformity with the *Declaration of Helsinki*.

Preamplifier design

The preamplifier used in this study is illustrated in Fig. 3.1 and broadly consists of an input and output stage galvanically separated by an isolation amplifier (ISO124, Burr Brown). The instrumentation amplifier IC (AD8221BR) has exceptional common mode rejection and low noise characteristics and the inputs are protected against 1 kV 'human body model' electrostatic discharge (AD8221 datasheet, Analog Devices). High-pass filtering of electrode offsets is achieved by bootstrapping the output by tying the instrumentation amplifier reference pin to the low-pass output, thereby preserving the high common mode rejection. Universal active filters (UAF42, Texas Instruments) are used to simplify the filter design; the first UAF is configured as a two-pole high-pass (0.2 Hz) Butterworth filter which also provides the low-pass reference signal for the instrumentation amplifier. The second UAF is a two-pole high-pass (2 Hz) Butterworth filter to remove motion artefact. The final pair of UAFs is configured as a four-pole low-pass (2 kHz) Bessel filter, which has superior step response characteristics and is

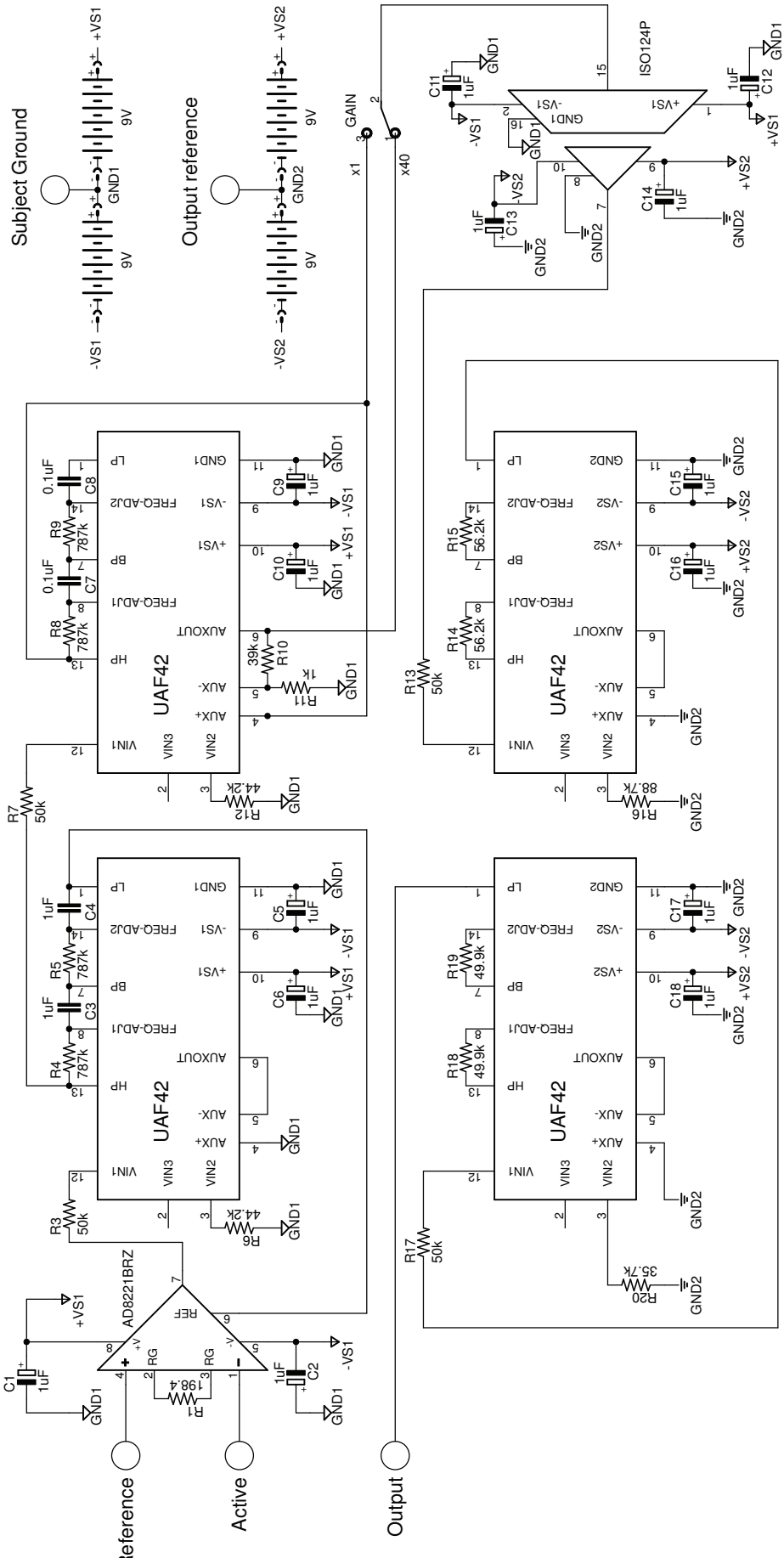

Figure 3.1. Circuit schematic for a battery-powered isolated preamplifier for small sensory potentials. The circuit is powered by two pairs of 9V 'transistor' batteries and the subject is galvanically isolated from the data acquisition system by the isolation amplifier (ISO124P). The subject ground is tied to the midpoint (GND1) of the pair of batteries on the subject's side of the isolation amplifier, whereas the amplifier's output is referenced to the midpoint (GND2) of the pair of batteries on the data acquisition side of the isolation amplifier. The instrumentation amplifier (AD8221BRZ) provides the critical first stage of amplification and is set to a gain of x250 with a 1% 200Ω resistor (matched as close as possible to 198.4Ω). The first active filter chip decouples any dc-offset potentials. The second active filter is a 2-pole Butterworth high-pass filter (f_c = 2 Hz) for the removal of motion artefact. The 3rd and 4th active filter chips combined provide a 4-pole low-pass Bessel filter (f_c = 2 kHz) to limit the measurement bandwidth.

positioned so as to additionally remove the ripple due to the modulation / demodulation carrier frequency of the isolation amplifier.

The instrumentation amplifier is configured with a fixed gain of 250 which is suitable for amplification of CMAPs while still achieving good CMR for sensory potentials. Additional gain (x40) for CSAPs is achieved using the auxiliary amplifier of the second UAF. The input and output stages are each powered by a pair of 9V 'transistor' (PP3) batteries, and the integrated circuits (ICs) are placed so that the current drain is balanced on either side of the isolation. The preamplifier was easily constructed on a single-sided circuit board (100x100 mm; Fig. 3.2) with socketable ICs (apart from the surface mount instrumentation amplifier) and through-hole passive components.

Preamplifier performance (test bench)

The frequency response was tested by applying a 0.5-mV sinusoidal signal to the preamplifier's inputs and measuring the peak response as a function of frequency between 0.2 Hz and 10 kHz.

The common mode rejection between 10 Hz and 10 kHz was determined by measuring the amplitude of a sinusoidal signal between the preamplifier's inputs (differential-mode, A_{diff}) required to give the same output response as a large sinusoidal signal at both inputs (common-mode, A_{cm}). The common mode rejection ratio (CMRR) is calculated as:

$CMRR = -20 * \log_{10}(A_{diff}/A_{cm})$.

Electrodes and skin preparation

Skin impedance was lowered at both the recording and stimulation sites by abrasion of the skin surface (3M Trace Prep, 3M, Ontario, Canada), followed by cleaning with an isopropyl alcohol swab. Sensory potentials were first recorded antidromically from

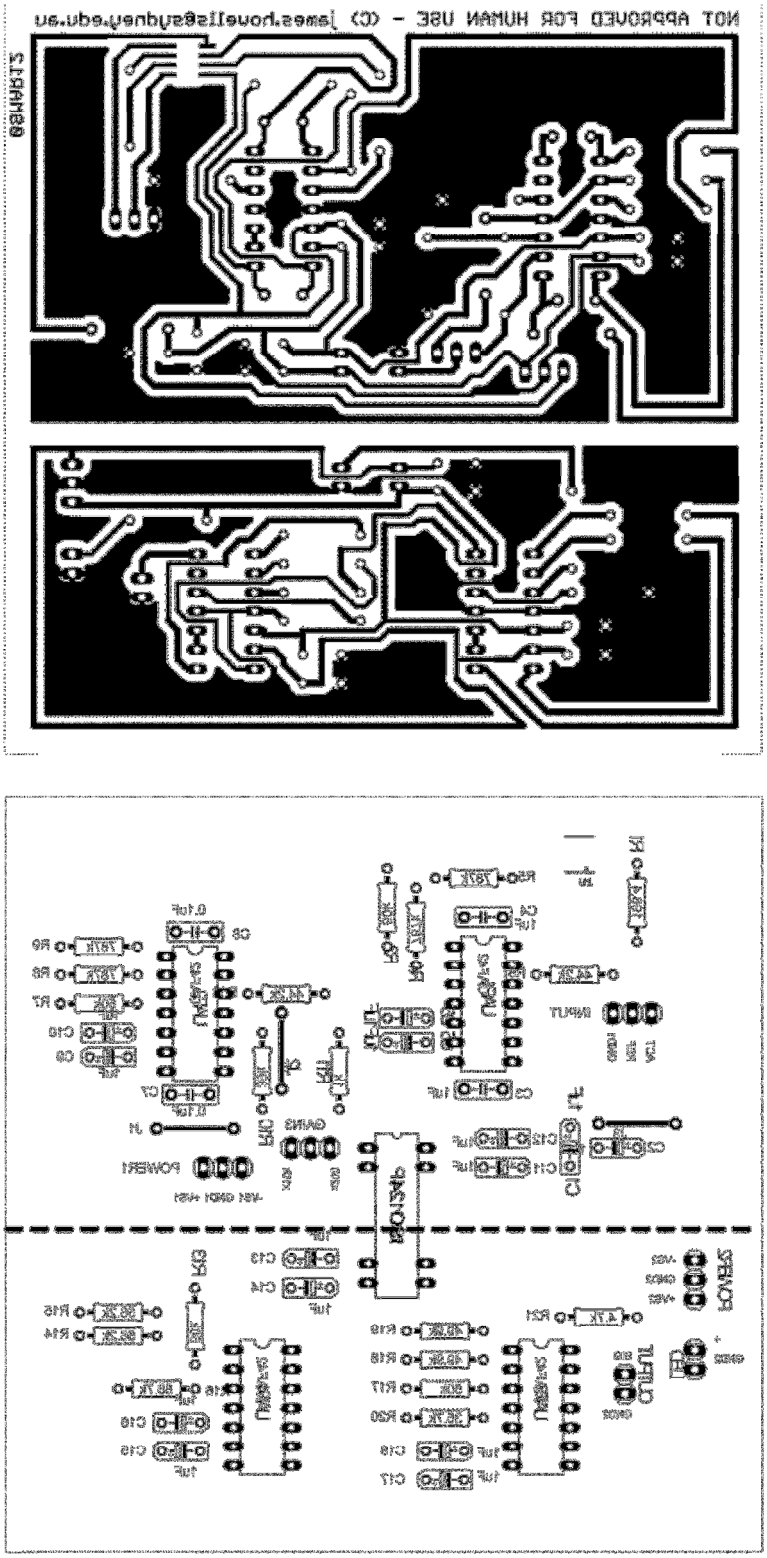

Figure 3.2. Circuit implementation

Upper image. Circuit board mirror image for etching.

Lower image. Silkscreen mirror image for component placement.

digit 2 using disposable Ag/AgCl ring electrodes (RE-D, The Electrode Store, Enumclaw, WA, USA), with two ring electrodes 4 cm apart (Eduardo & Burke, 1988), with the more proximal electrode around the proximal phalanx. The cathode, anode and ground electrodes were of the disposable Ag/AgCl ECG type (1010M & 4620M, Unilect, Unomedical, Stonehouse, UK). The ground electrode was placed on the dorsal aspect of the hand. The cathode was located at the wrist crease with the anode 10 cm proximally, towards the radial edge of the forearm. The location of the cathode was adjusted to obtain the minimum threshold current so reducing further the stimulus artefact. For the orthodromic recordings the stimulation and recording sites were reversed. The leads (from the stimulator) to the cathode and anode were swapped with the leads (from the amplifier) to the proximal and distal ring electrodes respectively.

Excitability testing

Axonal excitability was tested using the described refinements of the protocols described in Chapter 2, and specifically the stimulus-response paradigm which controlled both the stimulation and recording through a 16-bit multifunction data acquisition device (NI USB-6251).

The stimuli were delivered by an isolated bipolar constant current stimulator (DS5, Digitimer, Welwyn Garden City, UK) which followed a real-time command voltage which was synchronised with the recording sweep. The compound action potentials were amplified by the preamplifier (gain x10k) and bandpass filtered (2 Hz to 2 kHz). The amplified waveform had any residual mains frequency noise removed with a HumBug 50/60 Hz Noise Eliminator (Quest Scientific, North Vancouver, BC, CA) before being digitised at a sampling frequency of 10 kHz.

As described in Chapter 2 the *TROND* protocol cycles through five measures of axonal excitability: stimulus-response (SR) curve, strength-duration relationship (plotted as charge-duration [QT]), threshold electrotonus (TE), current-threshold (IV) relationship and a recovery cycle (RC). Earlier studies (Trevillion *et al.*, 2010; Nodera & Rutkove, 2012a) have suggested that the hyperpolarization-activated cation conductance I_h may play a role in the excitability of low threshold motor axons, and it is for this reason that we have also included an extended measurement of the hyperpolarizing threshold electrotonus, namely a 200-ms long hyperpolarization with an amplitude of 70% of the control threshold.

Tracking small, noisy action potentials

For most of the CSAPs recorded, the maximal CSAP and the signal to noise ratio (SNR) were sufficient to allow 'proportional tracking' (as in the usual TROND protocol; Kiernan *et al.*, 2000; Kiernan *et al.*, 2001b). Proportional tracking adjusts the stimulus step size in proportion to the error between the actual and target responses, allowing fast tracking when the stimulus conditions change rapidly and finer tracking control of the stimulus for slow events. For the smallest CSAPs and noisier recordings, a different tracking strategy was adopted, since the lower SNR meant that proportional tracking would have resulted in excessive oscillations about the target response. A more conservative approach was taken where the basic stimulus step size was a fixed percentage (Δ) of the current stimulus. If successive responses fell on the same side of the target then, the step size was increased by Δ, 2Δ, 3Δ and 4Δ% of the current stimulus until the target was met (and *vice versa*). On the other hand, when successive responses fell on opposite sides of the target, the step size was halved until it returned to the basic step size of Δ. This method is referred to as 'arithmetic/geometric tracking'.

Post-digitisation signal conditioning

Two passes of a 1-2-1 binomial smoothing filter (Marchand & Marmet, 1983) were applied to the digitised data in order to remove high-frequency noise acquired after amplification or as a result of the digitisation process. The transfer function for this low-pass Gaussian filter is $H(f) = \cos^4(\frac{\pi}{2}\frac{f}{f_N})$, where f_N is the Nyquist frequency. Initial observations of the digitised waveforms showed that the stimulus artefacts were small and the return to baseline was nearly complete before the onset of the CSAP. As such, previously required 'clamping' techniques were unnecessary, and the measurement window could be shortened (see Discussion).

Measuring the amplitude of biphasic and triphasic action potentials

Two additional peak-to-peak measurement options were programmed to reduce further the effects of noise. For the low SNR recordings the peak-to-peak measurement accuracy of the biphasic CSAPs was improved by requiring the positive peak to precede the negative peak (i.e. peak[+]-to-peak[-]; Fig. 3.3A). Initial observations of the orthodromic recordings showed a predominantly triphasic response, with variable negative peaks occurring on both sides of the positive peak. A new triphasic peak-to-peak measurement was defined as the difference in amplitude between the positive peak and the interpolated negative peak (Fig. 3.3B). The interpolated negative peak amplitude was determined by linear interpolation between the two negative peaks to the time corresponding to the positive peak. Both of these improvements to peak-to-peak measurements are discussed later.

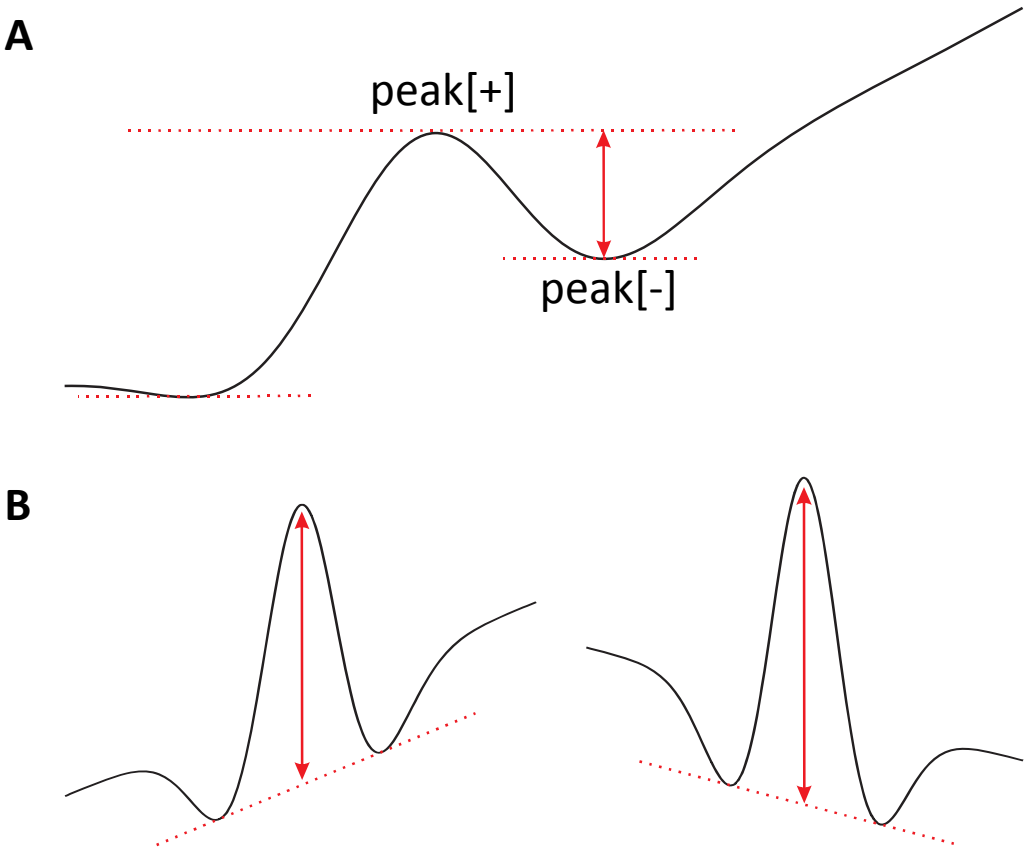

Figure 3.3. New measurements of biphasic and triphasic action potentials.

A. Biphasic measurement requiring positive peak (peak[+]) to precede the negative peak (peak[-]). The red arrow indicates the peak[+]-to-peak[-] measurement.

B. Two examples of triphasic measurement between positive peak and the interpolated negative peak, with the measured amplitude indicated by the red arrows.

Results

Amplifier performance

With the preamplifier's inputs shorted and the gain set to x10k the output of the preamplifier was measured with a true RMS multimeter (34401A, Agilent) to be 3.85 mV, or 0.385 µV when referred to the amplifier's inputs (RTI).

There was no appreciable attenuation in the frequency response of the amplifier between 5 and 1000 Hz (Fig. 3.4A). Beyond 5 kHz the filter roll-off was 22.3 dB/octave. The high-pass filter has an attenuation of 11 dB/octave below 1 Hz but steepens to 14.9 dB below 0.5 Hz due to the ac-coupling arrangement. The equivalent 'noise bandwidth' was calculated from the frequency response (Fig. 3.4A) and was 2.4 kHz which gives a noise density of 7.9 nV/√Hz (RTI), in close agreement with the figure in the manufacturer's datasheet.

With balanced inputs the common mode rejection was greater than 136 dB below 500 Hz and had a minimum value of 125 dB (Fig. 3.4B) over the bandwidth of the amplifier (2 kHz).

Recovery from stimulus artefact during CSAP recruitment

Figure 3.5 illustrates the recovery from stimulus artefact during the recruitment of sensory fibres by gradually increasing stimulus strengths. Subject #1 had higher recruitment thresholds (right column) and from the greater stimulus artefact and background noise, most probably a greater skin surface-electrode impedance.

The peak deflections due to stimulus artefact were 8.5, 5.2 and 2.2 µV for Subjects #1, 2 and 3 respectively. In all three recordings the stimulus artefact had decayed to a negligible value before the CSAP onset.

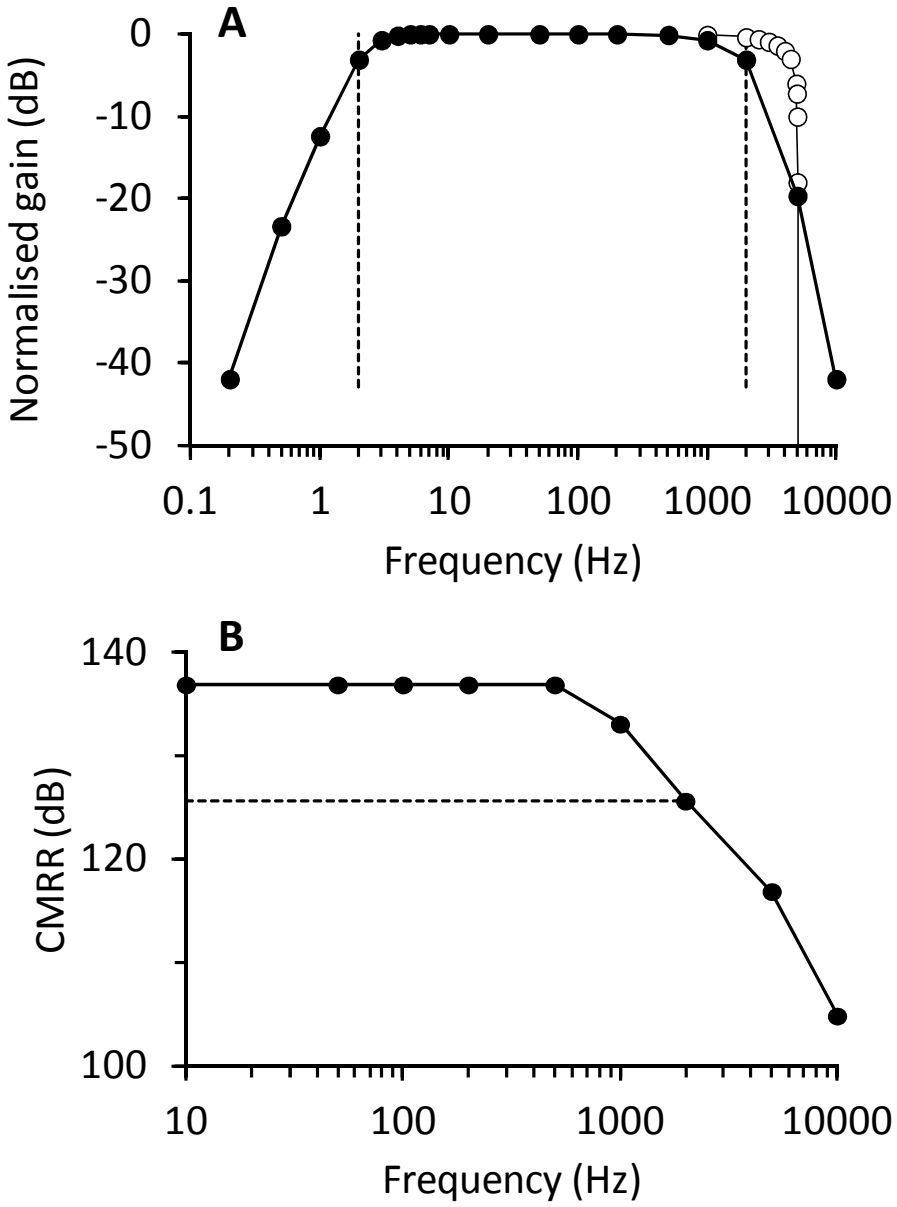

Figure 3.4. Amplifier performance. A. Normalised frequency response measured with a 0.5-mV sine wave. The gain is normalised to the maximal bandpass response. The dotted lines indicate the band-pass (2 Hz to 2 kHz). The open circles indicate the low-pass filter characteristics of two applications of a 1-2-1 Gaussian filter for data sampled at 10 kHz. **B.** Common mode rejection vs. frequency. The dotted line corresponds to the -3 dB frequency of the low pass filter, and shows a minimal CMRR of 125 dB over the amplifier's bandwidth.

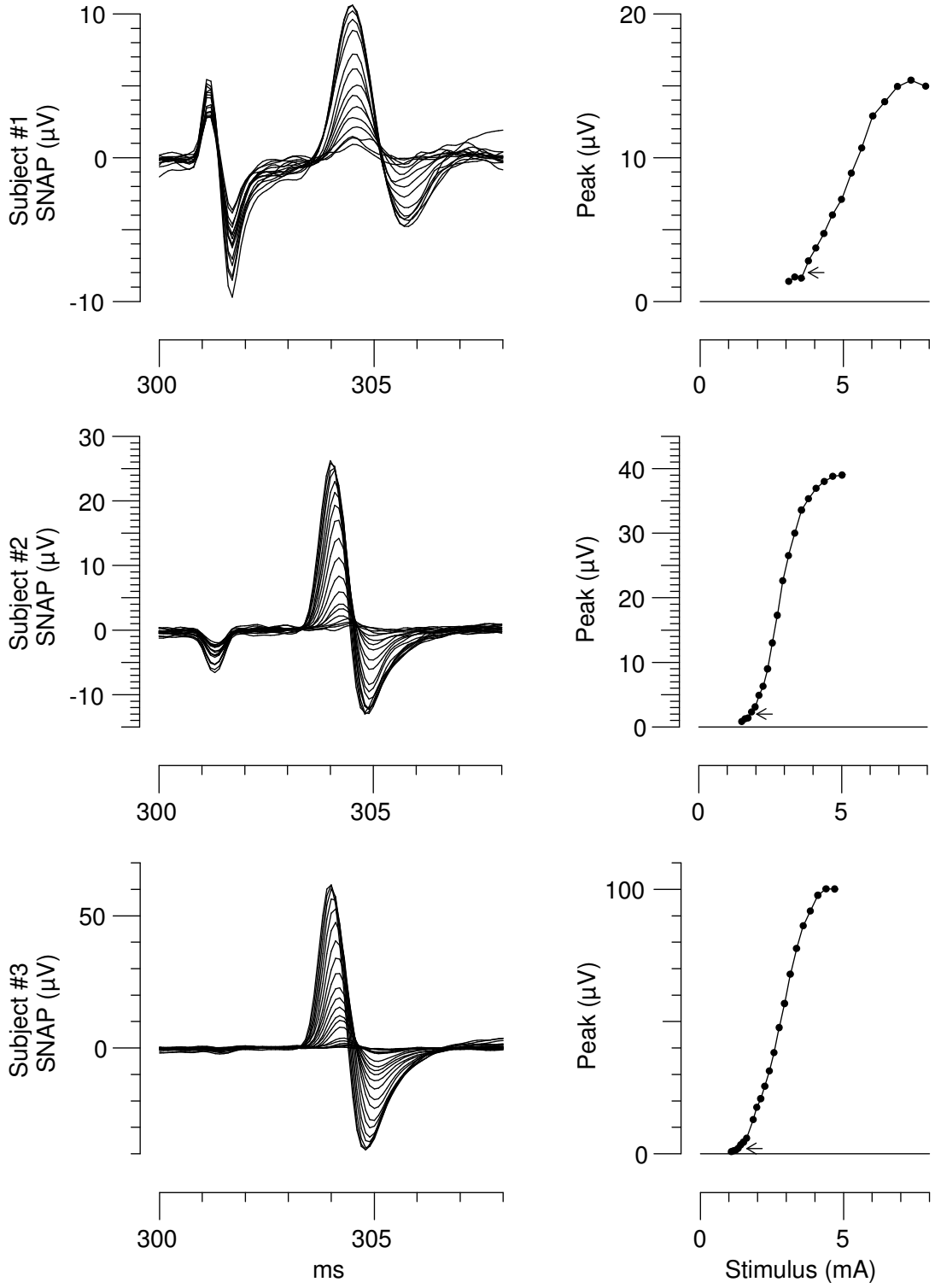

Figure 3.5. Recovery from stimulus artefact during CSAP recruitment.

Left column. Averaged CSAP response waveforms to six consecutive stimuli (0.5-ms wide) of progressively increasing intensity for three subjects. **Right column.** Peak-to-peak measurements for each of the waveforms in the left column. The arrows indicate the 2-µV target for each subject.

Signal-to-noise measurements *in vivo*

Two passes of the binomial smoothing filter resulted in an additional attenuation of high frequency noise (post-digitisation) with a steep roll off and a -3 dB point at 4.4 kHz (Fig 3.4A, open circles). With the lowest amplitude targets, 10% of CSAP and 2 μV, a measure of the equivalent noise was obtained in one subject (Fig. 3.6) by sampling the waveform in a window of the same width, but prior to the stimulus (arbitrarily 50 ms earlier than the peak measurement). The noise measured this way was 0.8 ± 0.5 μV (mean ± SD; closed circles in Fig. 3.6), not surprisingly the same for both the 10% (~ 4 μV) and 2-μV targets.

The standard deviations for the peak measurements were slightly higher (2 μV, 0.55 μV; 10%, 0.6 μV) reflecting the additional variation in amplitude in response to a tracking stimulus, which is, of necessity, not constant. The vertical bars in Fig. 3.6 show one standard deviation from the mean measurements. The 10% target and noise are separated by approximately three standard deviations from their means, while the 2-μV target and noise are separated by a little more than one standard deviation. The signal-to-noise ratio (SNR) was calculated from these data using the formula:

$SNR = \left(\frac{RMS_{peak}}{RMS_{noise}}\right)^2$ giving 19.2 and 5.0 for the 10% and 2-μV targets, respectively.

Threshold tracking 2-μV sensory action potentials

We found that the smallest practical limit of CSAP size that could be tracked without averaging was 2 μV (except for RC; see Legend to Fig. 3.7 and Discussion). Using 'arithmetic/geometric' tracking of peak[+]-to-peak[-] amplitudes (see Methods), it was possible to obtain all measures of axonal excitability for the 2-μV target in less than 32 min (Fig. 3.7 [Subject #3], see also Fig. 3.6B [Subject #2]).

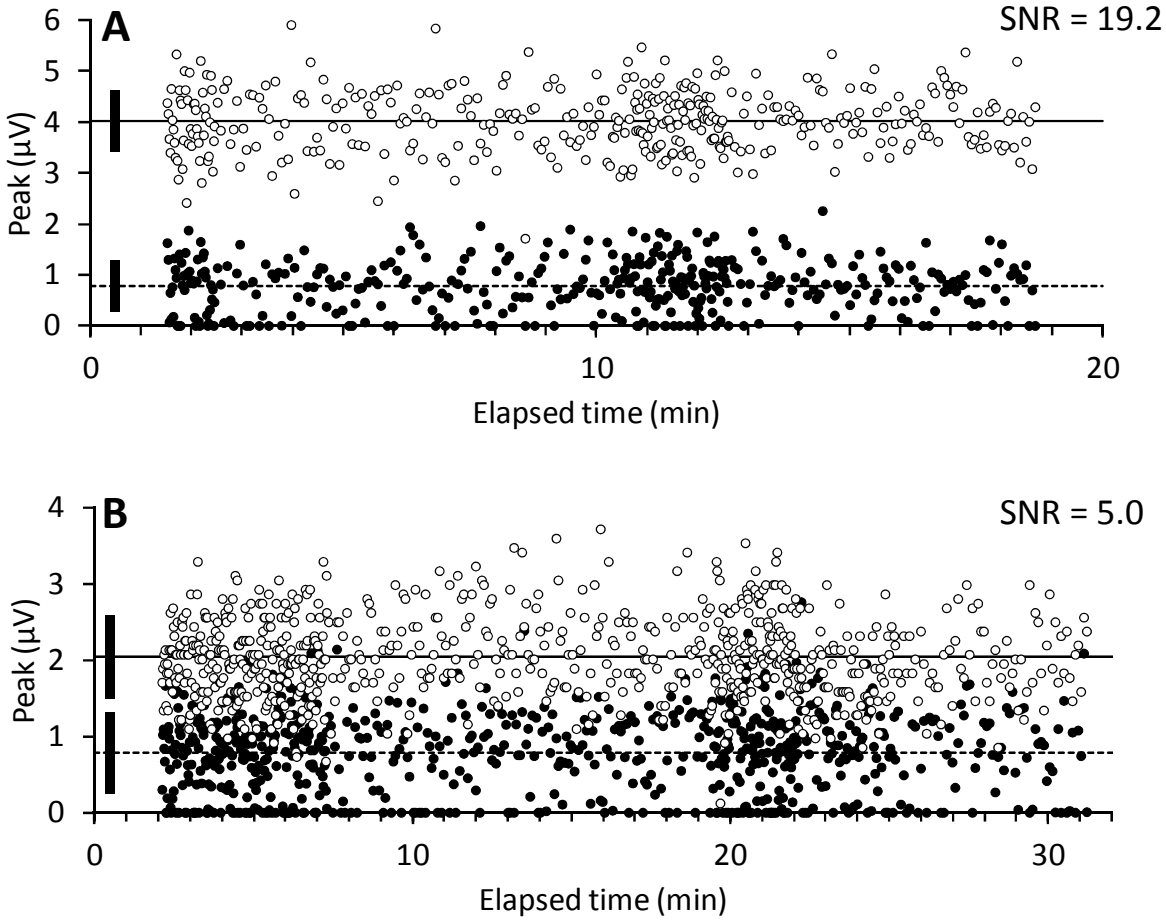

Figure 3.6. Signal-to-noise ratio (Subject #2). The data represents the peak-to-peak amplitudes of the control channel (unconditioned test; open circles) and the equivalent noise (closed circles). The equivalent noise was measured in an earlier window which preceded the test stimulus. The solid lines indicate the mean amplitude and the dashed lines the mean noise. The vertical bars indicate one standard deviation from the mean. **A.** 10% target (~4 µV) of maximal CSAP. **B.** Target 2 µV. Note that some of the variability in the test data (open circles) is because the stimulus was changing to track the threshold for the target CSAP.

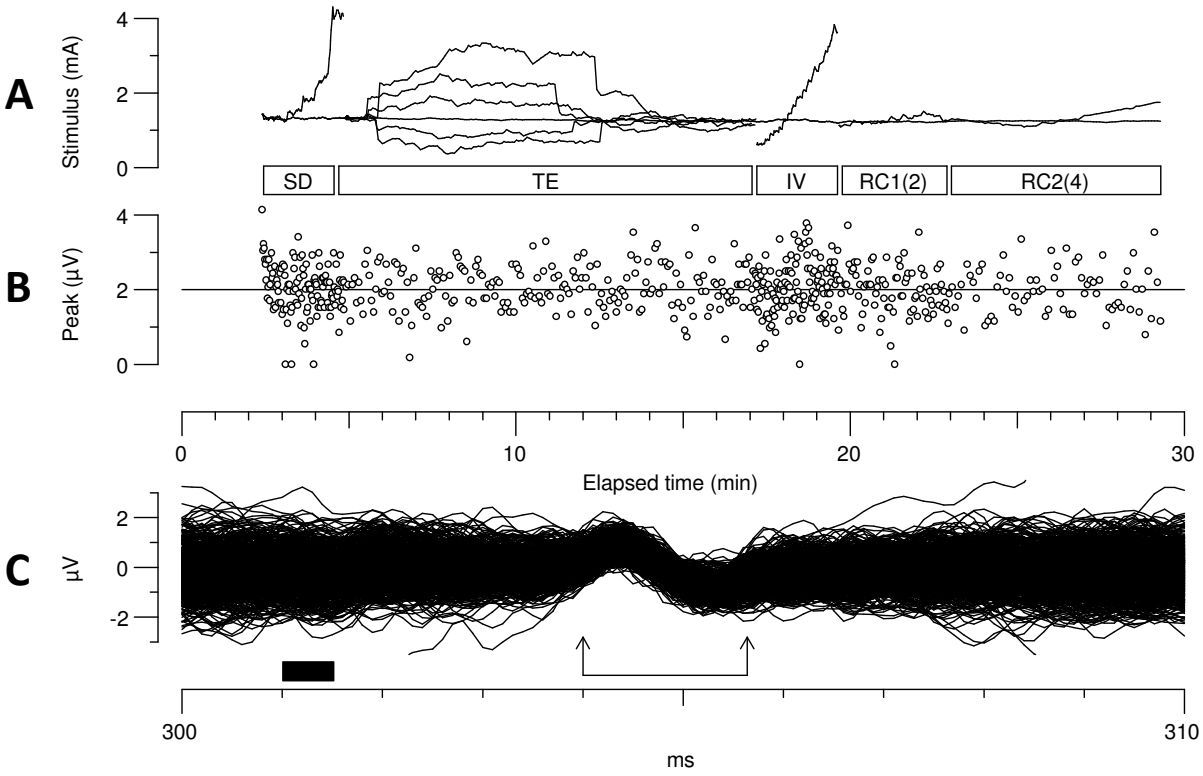

Figure 3.7. Threshold tracking a 2 μV target potential (Subject #3).

The various components of the recording are marked below the data in ***A*****:** SD, strength-duration relationship; TE, threshold electrotonus; IV, current-threshold relationship; RC1, recovery cycle part 1 with 2 averages per measurement; RC2, recovery cycle part 2 with subtraction of the response to the conditioning stimulus and with 4 averages per measurement. **A.** The control stimulus tracked the 2-μV target with a virtually constant value of 1.3 mA for the entire recording. **B.** The peak-to-peak amplitudes for the unconditioned test potential (2-μV target marked by horizontal line). The variability of the CSAP is due to the intrinsic variability of the recording and the variability of the tracking stimulus. **C.** Superimposed responses to the unconditioned test stimulus (timing indicated by the solid bar) for the entire recording. Peak-to-peak measurements of the response were made within the interval marked by the arrows, and correspond to the values displayed in ***B.***

The measures from recordings in the three subjects are shown in Fig. 3.8 (filled circles), and compared with conventional recordings tracking responses 40-50% of maximal in the same subjects (open circles).

The results provide preliminary evidence that in humans, as well as mice (Nodera & Rutkove, 2012a), there is increased inward rectification in low threshold sensory axons.

Repeatability of small-target recordings

Recordings of the 10% target (4.1 ± 0.3 μV) were made in the same subject on five different occasions and are shown in Fig. 3.9. In the charge-duration plot (QT, Fig 3.9A) the slope of the lines represents rheobase, and not surprisingly it differs between the individual recordings with differing application of stimulating electrodes. The strength-duration time constant on the other hand was consistent between the recordings (721 ± 22 μs), but longer than the value reported by Kiernan and colleagues (2001b) of 527 μs, which was obtained at a target level of 40%. Reproducibility of the other excitability recordings was very good, so that the 5 lines for the 5 different recordings can seldom be distinguished. Variability in the recovery cycle recordings is partly due to a reduction in the SNR inherent in the recording technique for the recovery cycle. The response to the supramaximal conditioning stimulus is first subtracted from the conditioned-test response before the peak measurement is made, thereby increasing the noise contribution by √2, halving the SNR.

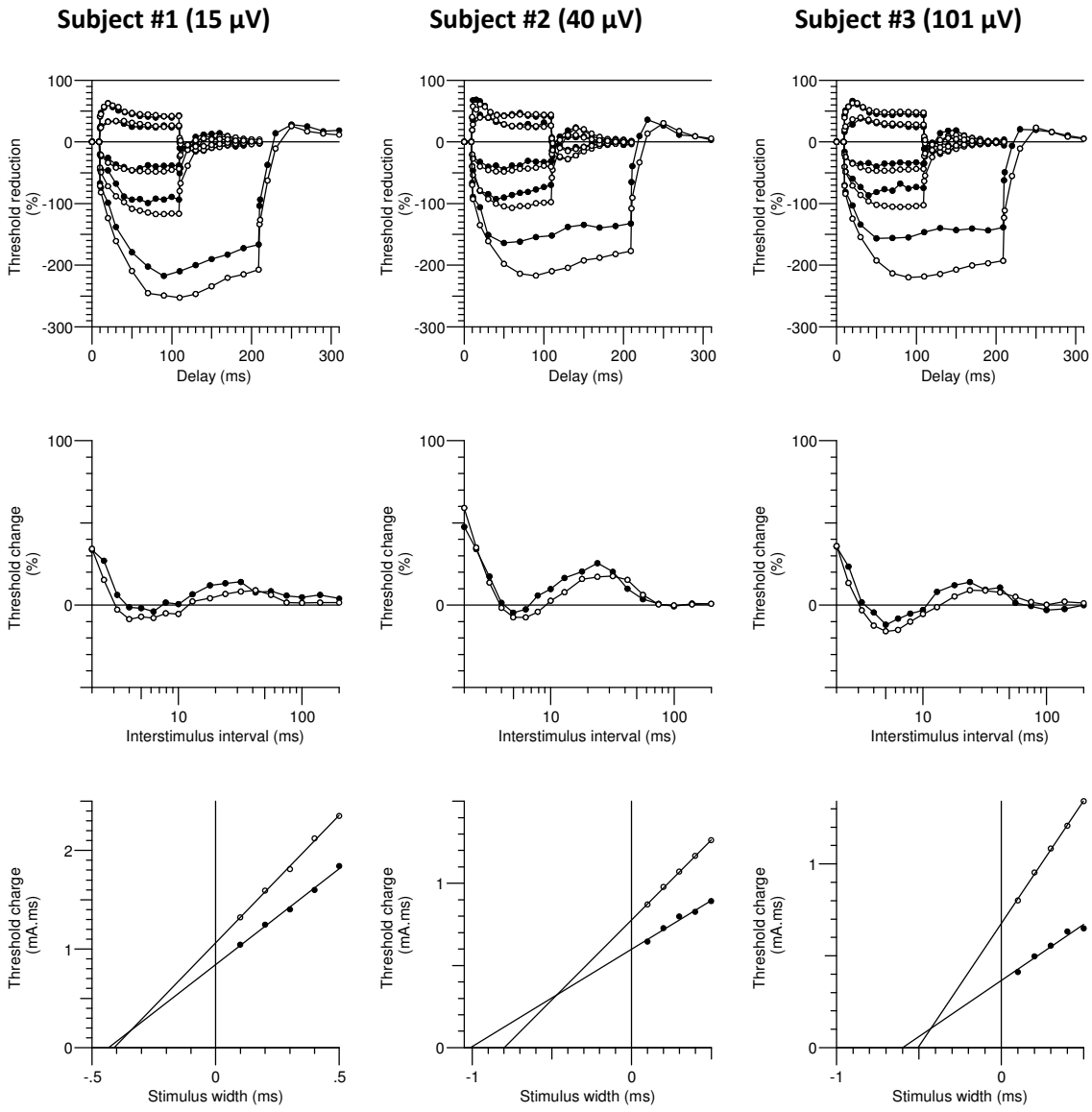

Figure 3.8. Excitability of low-threshold cutaneous afferents. The maximal CSAP is indicated after the subject. The filled circles denote the low target threshold (2 µV) recordings, and the open circles the standard (40-50%) targets. **Extended threshold electrotonus (top row).** The reduction in threshold to conditioning currents of ±20% and ±40% and -70% of the target threshold. **Recovery cycle (middle row).** The recovery of excitability following a supramaximal stimulus. **Strength-duration properties (bottom row).** Plotted here as charge versus stimulus width. The slope represents rheobase, and not surprisingly is steeper for the standard targets. The absolute value of the X-intercept is the strength-duration time constant, which is longer for the 2-µV targets.

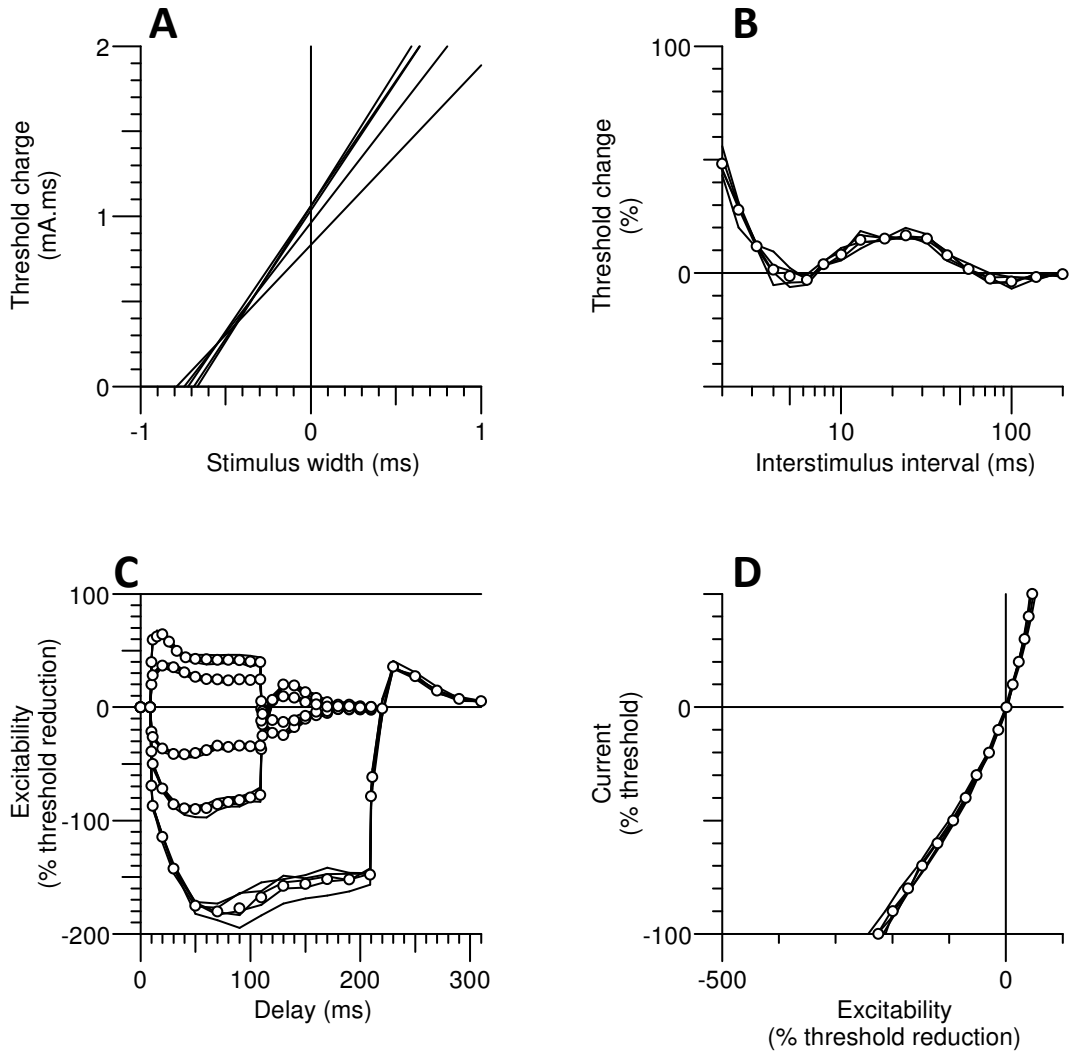

Figure 3.9. Repeatability of small-target recordings (Subject #2). Axonal excitability recordings in the same subject on five different occasions, tracking a 10% CSAP (4.1± 0.3 μV). The open circles represent the mean data and the lines the recordings from different occasions. **A.** Charge-duration plot (QT) of strength-duration properties. The slope of the lines is rheobase, and the X-intercept magnitude corresponds to the strength-duration time constant (SDTC). **B.** The recovery cycle (RC) plots the recovery of an axon following a supramaximal discharge. **C.** Extended threshold electrotonus (TE) recording with conditioning levels of ±20, ±40 and -70% of the unconditioned test threshold. **D.** Current-threshold (IV) relationship plots the threshold reduction versus current strength from +50 to -100% of threshold. *The mean data are not displayed for the QT plot (A), because that may lead to the erroneous interpretation of the X-intercept magnitude as the mean SDTC.*

Orthodromic measurement of distal excitability properties

Distal measurements of the excitability of cutaneous afferents were made on the proximal phalanx of digit 2 using orthodromic stimulation. The maximal orthodromic CSAPs for the three subjects were 7, 14 and 20 µV, resulting in tracking targets of 2.8, 7 and 9.4 µV respectively. Figure 3.10 compares the measurements at the wrist (open circles; antidromic) with those at the digit (closed circles; orthodromic). Data for strength-duration time constant are not presented because the different stimulating electrode arrangements mean that any differences cannot be reliably attributed to differences in excitability.

As with the low-threshold axons, axons appear depolarized at distal sites with reduced superexcitability, 'fanned-in' threshold electrotonus and a greater resting 'I/V' slope (Kiernan & Bostock, 2000; Kiernan *et al.*, 2001b). This is particularly apparent in the susceptibility of these axons to inadvertent activation by the 100-ms depolarizing conditioning currents in threshold electrotonus, currents that are meant to be subthreshold (see Burke *et al.*, 2007; Trevillion *et al.*, 2007).

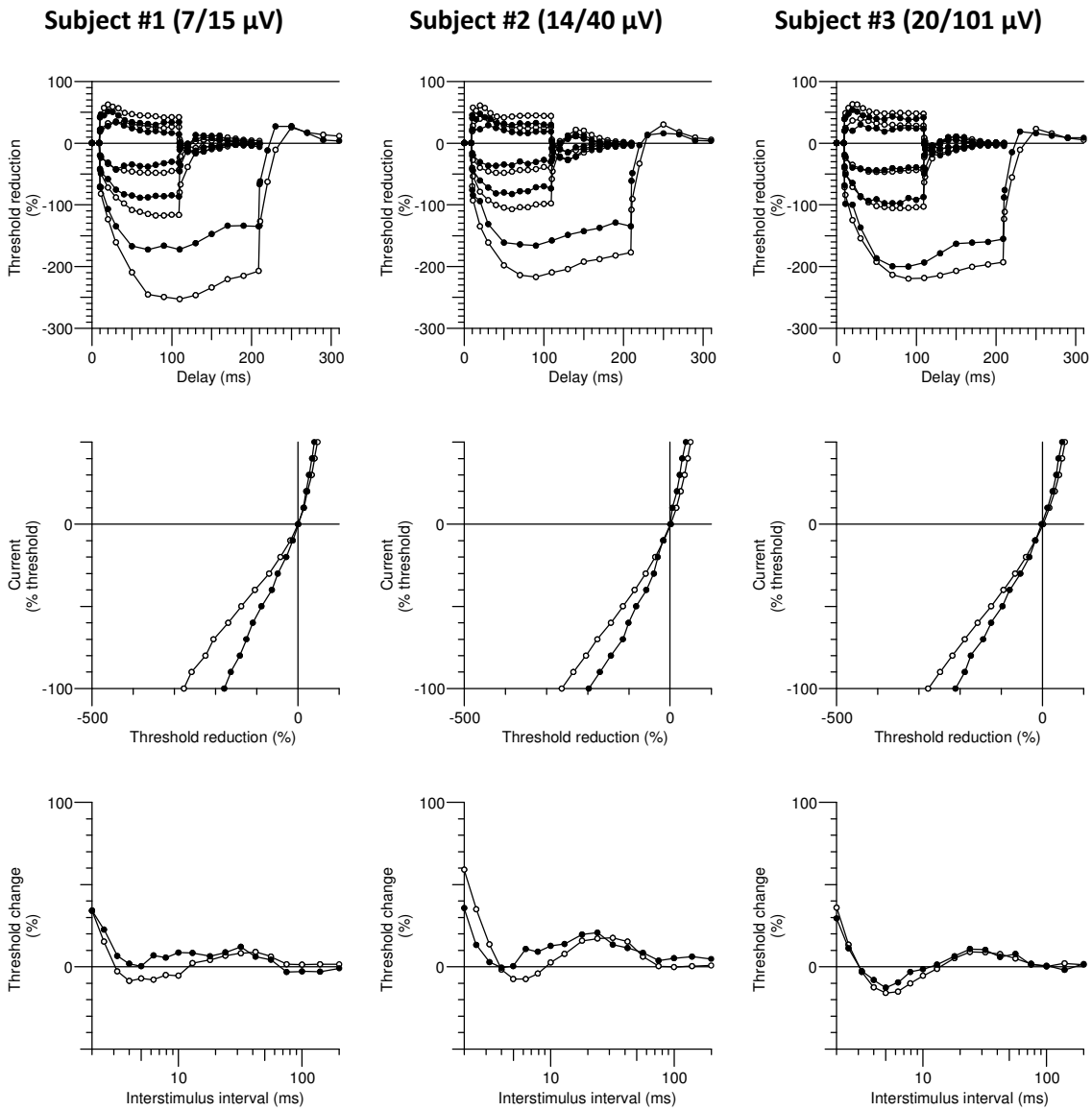

Figure 3.10. Distal measurements of cutaneous afferent excitability. Individual recordings of the excitability of the same cutaneous afferents measured orthodromically (at the digit; filled circles) and antidromically (at the wrist; open circles; same data as in Fig. 3.6). The maximal CSAPs for the orthodromic and antidromic recordings respectively are noted in parentheses. The standard target amplitudes (40 – 50% of the maximal CSAP) were tracked for each recording. **Extended threshold electrotonus (top row).** The threshold reduction to ±20, ±40 and -70% measured before, during and after long lasting conditioning currents. **Current-threshold relationship (middle row).** The threshold reduction (excitability) measured at the end of a 200-ms long conditioning current which varied from -100% to 50% of the target threshold in 10% steps. **Recovery cycle (bottom row).** The recovery of excitability measured at 18 intervals after a supramaximal discharge.

Discussion

This study tackled the difficulty in obtaining reliable measures of the excitability properties of cutaneous sensory axons of low threshold. Using the techniques and amplifier described, low-threshold sensory recordings are presented for the first time in normal human axons, and the results suggest that these cutaneous axons may differ from those of higher threshold. However it is with diseased nerves with pathologically small CSAPs and high thresholds that the true usefulness of the techniques described here may be realised. The discussion will focus on the optimal recording conditions for small CSAPs, the advantages of the amplifier design, and the physiological and clinical need for better recording techniques.

Axonal excitability close to the electrode noise floor

Synchronous mains frequency noise is to some extent always present in raw biosignals, particularly those acquired from the surface. Notch filters distort action potential measurements and in any case they do not remove the higher harmonics. In-line reduction of mains frequency noise can be achieved in hardware by a device such as the HumBug 50/60Hz Noise Eliminator, or in software by sampling a stimulus-free portion of the recording to remove a mains-locked waveform from the response.

Asynchronous noise due to the impedance of the electrode and skin-electrode interfaces or noise due to the amplification system itself all impact on the signal-to-noise ratio. The amplitude of both synchronous and asynchronous noise can be attenuated by careful skin surface preparation at the recording site and an amplifier with both high common mode rejection and low noise.

Because the stimulus artefact tail frequently intrudes into the CSAP, so that it rides on the decaying artefact, the standard *TROND* protocol contains a correction for a sloping baseline in CSAPs by 'clamping' the digitised data during the measurement window.

The sloping baseline is removed by subtracting a straight line that passes through the start and finish of the measurement window at amplitudes corresponding to the mean of the ten samples recorded on either side of the measurement window. This type of clamping assumes that the artefact at the time of the response can be represented as a straight line, whereas it is usually more exponential than linear, so that clamping introduces a systematic and nonlinear distortion of the peak-to-peak measurement. In addition, movement of the CSAP within the measurement window due to changes in its latency alters the amount of distortion. The degree of nonlinearity of the stimulus artefact decay during the measurement window also determines the minimum observable action potential.

Alternatives for removing the stimulus artefact after acquisition include artefact subtraction and localised fitting of the baseline; however for threshold tracking of small amplitude potentials these methods have their drawbacks. Artefact subtraction involves the delivery of a fractional stimulus which is subthreshold; the response is then scaled back up to achieve the stimulus artefact alone. Artefact subtraction can be an effective tool for reducing the stimulus artefact (Trevillion *et al.*, 2010); however it doubles the recording time and halves the SNR. Further, because the artefact does not scale linearly with stimulus intensity, the artefact removal is not complete. Another technique is to fit a curve to the decay of the stimulus artefact (Wagenaar & Potter, 2002). Axonal excitability studies, however, involve conditioning the test stimulus with sub- and supra-threshold pulses, in which the conditioning artefact or response may extend beyond the test stimulus.

The arithmetic/geometric tracking applied to the 2-μV potentials in this study, was slower at tracking sharp transitions in stimulus conditions; on the other hand it was

less susceptible to noise and overall it resulted in faster tracking of low signal-to-noise-ratio potentials.

Recovery cycle measurements in sensory axons with low SNR were further improved with a hybrid recording protocol. For intervals shorter than 30 ms (which allows for possible M-responses and F-waves), the response to the supramaximal conditioning stimulus needs to be subtracted from the conditioned test. To overcome the resultant halving of the SNR, ensemble averaging of 4 responses was performed for these intervals only (see RC2 in Fig. 3.7).

Physiological implications and clinical applications

Trevillion and colleagues (2010) found evidence that the lowest threshold motor axons are depolarized when compared to higher threshold axons, and that this depolarization was probably due to differences in the hyperpolarization-activated cation current (I_h). Such differences may exist in sensory axons. However these sensory axons contain a non-homogeneous population of cutaneous afferents with, in the median nerve at the wrist, axons from four different mechanoreceptors each with different firing patterns (Johansson & Vallbo, 1983). It is a reasonable presumption that the expression of channels and pumps on an axon are optimal to ensure secure conduction with minimal expenditure of energy for the pattern and rate of discharge of that axon. If this is so, studying CSAPs may not reveal the extent of the differences between axons of similar threshold innervating different receptors. Only extensive studies using microneurography would reveal these differences for human subjects. Nevertheless data used to verify these techniques suggest significant differences may be present in sensory axons operating at different resting membrane potentials. Furthermore, the present recordings suggest that these afferents are more depolarized in the digit than at the wrist.

Differences in the membrane potential and the voltage dependence of ion channels need to be considered when explaining differences not only between axons of different modality (sensory and motor; see next chapter) but also axons of different threshold within the same modality (see also Shibuta *et al.*, 2010; Trevillion *et al.*, 2010; Nodera & Rutkove, 2012a, b).

Unlike nerve conduction studies which document the conduction of action potentials along a segment of nerve, threshold tracking studies probe the excitability under the stimulating cathode. Distal measures of excitability may shed further light on the progression of biophysical changes underlying entrapment or length-dependent neuropathies. To date, the excitability of sensory axons in subjects with carpal tunnel syndrome (CTS) has been studied antidromically, that is, proximal to the site of compression (Kiernan *et al.*, 1999; Han *et al.*, 2009; Han *et al.*, 2011). In those studies, subjects with orthodromic CSAPs < 5 μV were excluded on the basis that the antidromically recorded CSAPs would be too small to track. The ability to track CSAPs as small as 2 μV opens up the possibility of studying CTS in more severe cases and distal to the site of compression. Distal excitability studies may also shed some light on polyneuropathies, particularly the 'dying back' neuropathies. For example, it has been reported that sensory nerve excitability studies during early treatment cycles can predict the neuropathic side-effects of oxaliplatin treatment for colorectal cancer in 80% of patients (Park *et al.*, 2009a; Park *et al.*, 2011). Distal sensory measurements may provide an even more sensitive early warning of toxic nerve damage.

Chapter 4

The voltage dependence of I_h in human myelinated axons: a new model of human sensory and motor axons

Work in this chapter was published in Howells J, Trevillion L, Bostock H & Burke D. (2012). The voltage dependence of I_h in human myelinated axons. J Physiol ***590,*** *1625-1640.*

Summary

HCN channels are responsible for I_h, a voltage-gated inwardly rectifying current activated by hyperpolarization. This current appears to be more active in human sensory axons than motor and may play a role in the determination of threshold. Differences in I_h are likely to be responsible for the high variability in accommodation to hyperpolarization seen in different subjects. The aim of this study was to characterise this current in human axons, both motor and sensory. Recordings of multiple axonal excitability properties were performed in ten subjects, with a focus on the changes in threshold evoked by longer and stronger hyperpolarizing currents than normally studied. The findings confirm that accommodation to hyperpolarization is greater in sensory than motor axons in all subjects, but the variability between subjects was greater than the modality difference. An existing model of motor axons was modified to take into account the behaviour seen with longer and stronger hyperpolarization, and a mathematical model of human sensory axons was developed based on the data collected. The differences in behaviour of sensory and motor axons and the differences between different subjects are best explained by modulation of the voltage dependence, along with a modest increase of expression of the underlying conductance of I_h. Accommodation to hyperpolarization for the mean sensory data is fitted well with a value of -94.2 mV for the mid-point of activation ($V_{0.5}$) of I_h as compared to -107.3 mV for the mean motor data. The variation in response to hyperpolarization between subjects is accounted for by varying this parameter for each modality (sensory: -89.2 to -104.2 mV; motor -87.3 to -127.3 mV). These voltage differences are within the range that has been described for physiological modulation of I_h function. The presence of slowly activated I_h isoforms on both motor and sensory axons was suggested by modelling a large internodal leak current and a masking of the Na^+/K^+-ATPase pump activity by a tonic depolarization. In addition to an increased

activation of I_h, the modelling suggests that in sensory axons the nodal slow K^+ conductance is reduced, with consequent depolarization of resting membrane potential and action potential of shorter duration.

Introduction

As discussed in Chapter 1 (pages 23-30) The voltage-gated inwardly rectifying current I_h flows through hyperpolarization-activated cyclic nucleotide-gated (HCN) channels and plays an important role in pace-making and determination of resting membrane potential (Pape, 1996; Biel *et al.*, 2009). Recent studies *in vivo* have suggested a contribution of I_h to the determination of axonal threshold in human motor axons (Trevillion *et al.*, 2010) and to a number of pathologies including diabetes, stroke and porphyria (Horn *et al.*, 1996; Jankelowitz *et al.*, 2007a; Lin *et al.*, 2008). HCN channels are of particular interest as molecular targets for neuropathic pain resulting from traumatic nerve damage or channelopathy (Chaplan *et al.*, 2003; Momin *et al.*, 2008; Momin & McNaughton, 2009; Wickenden *et al.*, 2009).

Sensory axons undergo ectopic activity more readily than motor axons (Erlanger & Blair, 1938; Mogyoros *et al.*, 2000). Bostock and colleagues (1994) suggested that greater expression of I_h in sensory axons than motor was a factor in post-ischaemic paraesthesiae and the greater accommodation of sensory axons to hyperpolarizing currents. This view has been supported by subsequent studies (Lin *et al.*, 2002; Kiernan *et al.*, 2004). Additionally, increased expression of I_h has been suggested as a contributing factor to the greater anode break hyperexcitability seen in sensory axons (Bostock *et al.*, 1994; Stephanova & Mileva, 2000). In a study of motor axons of subjects who had suffered an ischaemic stroke the key difference was a reduction in accommodation to hyperpolarization on the affected side (Jankelowitz *et al.*, 2007a).

Decreased expression of I_h and of the internodal leak conductance accounted for a 77% reduction in the discrepancy between the affected and unaffected sides.

With one exception, previous studies have focused on the average response of a group of subjects, and have ignored the possibility of differences between subjects. Tomlinson and colleagues (2010a) applied longer and stronger hyperpolarization to the motor axons of 15 subjects, performed repeated measures, and found a high degree of variability in response to hyperpolarization between subjects, but not within the same subject. They attributed these findings to the possibility that there was more than one isoform of HCN channels and/or to differences in metabolic factors such as cAMP which are known to modulate the voltage activation of I_h. In a recent study exploring the ionic basis of threshold to electrical stimulation (Trevillion *et al.*, 2010), greater inward rectification was found in low-threshold motor axons, and this could be modelled by a near doubling of the expression of I_h and leak conductance across the internodal axolemma.

In the present study the responses of sensory axons to strong long-lasting hyperpolarization are contrasted with those of motor axons in the same subjects. A mathematical model of human sensory axons is developed and used to provide insight into the mechanisms underlying the differences between axons of different modality. The findings emphasize the importance of differences in channel gating in addition to differences in channel expression and provide evidence for the possibility of HCN isoforms with a slow time constant on both motor and sensory axons.

Methods

Thirty experiments were performed in 10 healthy subjects with no evidence of a peripheral neuropathy. The research conformed to the *Declaration of Helsinki* and

local ethics approval was obtained from The University of Sydney's Human Research Ethics Committee. All subjects provided informed written consent prior to commencement of the study.

The sensory and motor studies in each subject were performed in the same session with the same stimulating electrode setup. Apart from a larger ground electrode, the recording arrangement was as outlined in Chapter 2 (see Fig. 2.1). The cathode was placed in line with the median nerve at the proximal wrist crease and the anode approximately 10 cm proximal on the radial edge of the forearm. Compound muscle action potentials (CMAPs) were measured with disposable ECG electrodes (ClearTrace REF1700-030; ConMed, Utica, NY, USA) over the thenar eminence and the reference electrode over the proximal phalanx of digit one. A self-adhesive electrosurgical plate (#1180; 3M Healthcare, St Paul, MN, USA) was cut down, coated with Redux Creme (Parker Laboratories; Fairfield, NJ, USA) and placed over the palm to provide a large reliable ground electrode. Compound sensory action potentials (CSAPs) were recorded with self-adhesive disposable ring electrodes (RE-D; Electrode Store, Enumclaw, WA, USA), with the active electrode at the proximal end of digit two and the reference 4 cm distal. Temperature was measured continuously with a thermistor close to the site of stimulation. The forearm was wrapped in a towel, and studies commenced only when the temperature was stable and greater than 32°C.

The CMAPs and CSAPs were amplified (x200 for motor; x10k for sensory) and bandpass filtered (2 Hz – 2 kHz) using a purpose-built battery-powered isolated amplifier with low noise and high common mode rejection (as described in Chapter 3). The amplified signals had mains frequency noise removed using a HumBug 50/60Hz Noise Eliminator (Quest Scientific; North Vancouver, BC, Canada) and were then digitised with a 16-bit data acquisition system (NI-USB6251; National Instruments; Austin, Texas, USA).

Stimulation was delivered by a DS5 Isolated Bipolar Constant Current Stimulator (Digitimer; Welwyn Garden City, UK). Both the stimulation and data acquisition were controlled by the QtracS software (as described in Chapter 2).

Excitability protocols

A stimulus-response curve was recorded so that the amplitude of the target potential could be defined. For both motor and sensory recordings the target potential was set to be 50% of maximal amplitude. The threshold for the target potential was tracked using a 1-ms test stimulus. In the present study it was important to optimise the comparison between sensory and motor recordings, and the same test stimulus was therefore used for both sensory and motor axons. However, most studies on sensory axons use a test stimulus width of 0.5 ms, to minimise the effects of temporal dispersion (Kiernan *et al.*, 2001b) so that additional sensory recordings were made with 0.5-ms test stimuli. For two excitability measures, threshold electrotonus and the current-threshold relationship, the strength of the conditioning polarizing currents was set as a percentage of the threshold of the target potential (that is, control threshold).

The strength-duration time constant (SDTC) was calculated by plotting the threshold stimulus charge against stimulus duration for test stimuli of five different durations. The stimulus widths used in the motor recordings were 0.2, 0.4, 0.6, 0.8 and 1.0 ms, and in the sensory recordings were 0.1, 0.2, 0.3, 0.4 and 0.5 ms.

Current-threshold (IV) relationships were recorded by measuring the threshold for the target potential at the end of a 200-ms polarizing current (standard duration). The strength of the polarizing current was adjusted in 10% steps from +50% of control threshold (depolarizing) to -100% of control threshold (hyperpolarizing). A current-threshold relationship was also recorded using a 100-ms polarizing current (shorter duration) adjusted in strength as described for the 200-ms polarizing current. The

threshold changes induced by the shorter duration conditioning current were recorded in order to obtain greater detail about the time course of accommodation to hyperpolarization.

The standard threshold electrotonus protocol using currents ±20% and ±40% of threshold was modified. Depolarizing currents of +40% are often not subthreshold for sensory axons, especially with 0.5-ms test stimuli (Burke *et al.*, 2007; Trevillion *et al.*, 2007), and regularly produce an artefact on the threshold electrotonus waveform. As a result, a 100-ms long +30% depolarizing current was also used in the sensory studies. Activation of I_h was explored using two additional hyperpolarizing currents, -70% for 200 ms and -100% for 300 ms (Tomlinson *et al.*, 2010a).

The recovery cycles of motor and sensory axons were recorded using eighteen different conditioning-test intervals from 2 to 200 ms. The strength of the conditioning stimulus was set to be three times the control threshold to ensure that it was supramaximal. Measurements of the conditioned potential were made after subtraction of the conditioning potential.

Mathematical modelling

An existing mathematical model (the Bostock model; Fig. 4.1) of the human motor axon (Bostock *et al.*, 1991b; Kiernan *et al.*, 2005; Bostock, 2006; Jankelowitz *et al.*, 2007a; Lin *et al.*, 2008; Trevillion *et al.*, 2010) was modified to interpret the measured responses to extended hyperpolarization and, in particular, the contribution of I_h to accommodation. The Bostock model lends itself well to the simulation of axonal excitability studies, which stimulate superficial nerves with relatively large surface electrodes (effectively space-clamped stimulation). For modelling the behaviour of human axons this model reproduces axonal excitability with detailed ionic contributions and simplified axonal geometry.

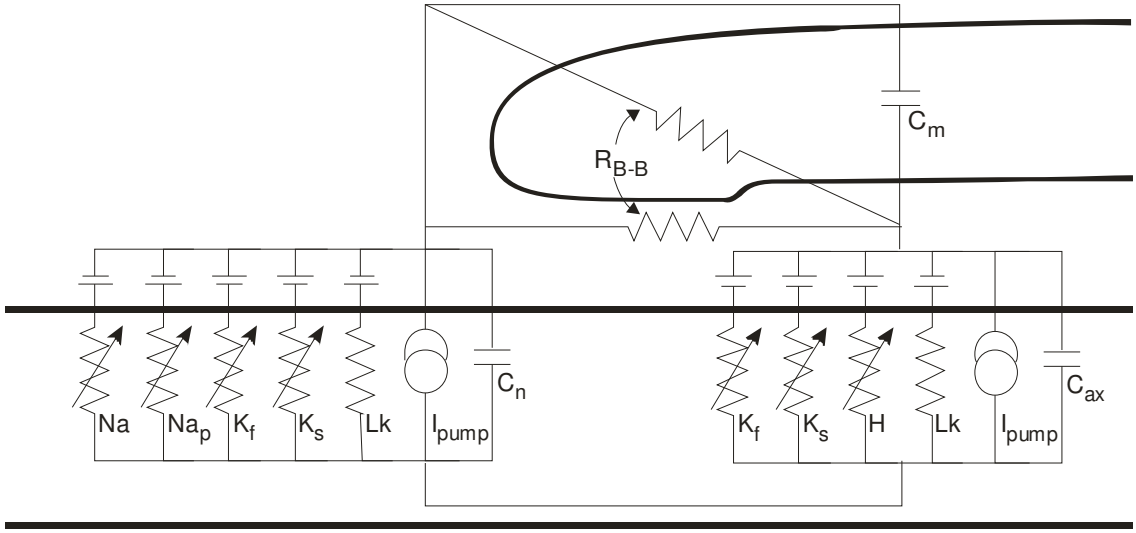

Figure 4.1. The Bostock model of the human motor axon.

Schematic description of the key nodal and internodal features of the mathematical model. Voltage-gated channels: sodium (transient [Na] and persistent [Na_p]); potassium (fast [K_f] and slow [K_s]); HCN [H]. Na^+/K^+-ATPase pump [I_{pump}]. Ohmic leak conductance [Lk]. Capacitance of: axolemma (internodal [C_{ax}], nodal [C_n]); myelin sheath [C_m]. Barrett-Barrett conductance [R_{B-B}] through and under the myelin sheath.

The Bostock model has evolved from the Barrett & Barrett (1982) model of depolarizing afterpotentials in lizard and frog axons, with ionic conductances initially determined by intracellular and extracellular studies of rat spinal root myelinated axons (Baker *et al.*, 1987) and by current- and voltage-clamping of the human node of Ranvier (Scholz *et al.*, 1993; Schwarz *et al.*, 1995; Reid *et al.*, 1999). Later studies of latent addition in human motor and sensory axons led to the inclusion of persistent Na^+ channels in the model (Bostock & Rothwell, 1997). The relevant values are listed in Table 4.1, left column, as modified in the present study to reproduce the extended hyperpolarization for motor axons introduced recently (Tomlinson *et al.*, 2010a).

This space-clamped, two-compartment model consists of a node and internode linked by the paranodal Barrett-Barrett pathways through and under the myelin sheath (Barrett & Barrett, 1982; Mierzwa *et al.*, 2010), and has the key components of: transient and persistent Na^+ channels, fast and slow K^+ channels, a single HCN isoform, Na^+/K^+-ATPase pump, membrane and myelin capacitances, and leak conductances across the axolemma. Stephanova and Bostock (1996) further compartmentalized the internode of this model and found that the increased morphological complexity added no greater insight into axonal function.

The model was run in an unclamped mode, which allowed secondary changes due to the polarization of resting membrane potential (RMP), caused by changes in conductances or pump currents. No restriction was placed on the direction of flow of the constant amplitude (DC) 'pump' currents, so it is possible that these 'pump' currents are actually a composite of Na^+/K^+-ATPase activity and other unspecified tonic and slowly-gated conductances (see Discussion).

Parameter	*Description*	*Motor*	*Sensory*
PNaN ($cm^3s^{-1}x\ 10^{-9}$)	Permeability of Na^+ channels at the node	4.35	4.35
PNaP% (%)	% of Na^+ channels that are persistent	1.07	1.07
GKsN (nS)	Max. conductance of slow K^+ channels at the node	**56.7**	**29.1**
GKsI (nS)	Max. conductance of slow K^+ channels at the internode	0.57	1.74
GKfN (nS)	Max. conductance of fast K^+ channels at the node	18.2	19.4
GKfI (nS)	Max. conductance of fast K^+ channels at the internode	207	205
GH (nS)	Max. conductance of I_h	**2.95**	**4.1**
GLkN (nS)	Leak conductance at the node	1.97	1.69
GLkI (nS)	Leak conductance at the internode	4	3.65
GBB (nS)	Barrett-Barrett conductance	35.9	40.3
Aam (ms^{-1}) †	Activation rate of transient Na^+ channels	**6.54**	**6.25**
Aah (ms^{-1}) †	Inactivation rate of transient Na^+ channels	**0.126**	**0.153**
Aq (ms^{-1}) †‡	Activation rate of I_h channels	5.22×10^{-3}	5.22×10^{-3}
Bq (mV)	Voltage of half-activation of I_h channels	**-107.3**	**-94.2**
Cq (mV) ‡	Voltage activation slope factor of I_h channels	-12.2	-12.2
EIR (mV)	Internodal resting membrane potential *(internodal pump current; nA)**	**-84.6** ***(-7.86 x 10^{-3})***	**-81.3** ***(-4.3 x 10^{-3})***
ENR (mV)	Nodal resting membrane potential *(nodal pump current; nA)**	**-84.4** ***(-3.33 x 10^{-2})***	**-80.3** ***(-5.44 x 10^{-2})***

Table 4.1. Modelled parameters producing the greatest error reduction.

Key differences between motor and sensory axons are highlighted in bold.

† Activation rates at 36°C

‡ These values of Aq, Cq are presented here for completeness. They are not substantially different from the earlier Bostock model (4.30×10^{-3} ms^{-1} and -13.2 mV respectively) and over this range they do not appreciably alter the final model fits.

* The Na^+/K^+-ATPase pump current itself is hyperpolarizing and is masked here by a tonic depolarization (shown by the negative pump currents).

The MEMFIT function (Bostock, 2006) within the QtracP software was used to fit objectively the model parameters to the motor excitability data. The parameters of this model were altered iteratively to reproduce the extended motor data recorded in this study. The fitting of this extended excitability data presented some unique challenges that needed to take into account the large variation between subjects in the responses to strong hyperpolarization. The model optimisation uses a least squares approach which aims to minimise the error between the model and the average data. A goodness of fit measure of the 'discrepancy' between the model and the recordings was obtained by weighting the errors of the four components of the excitability data as follows: strength-duration data, 0.5; threshold electrotonus, 3; recovery cycle, 1; current-threshold, 1. The optimisation procedure normally takes into account the variation of data within each component by inversely weighting each data point according to its standard deviation, but because of the observed variation in the hyperpolarizing electrotonus data, the optimisation employed here ignored the standard deviations and thereby fitted the mean data as closely as possible.

Having optimised the model to fit the motor excitability data, the model was then adapted to fit optimally the extended sensory (1-ms test width) excitability data. The validity of the new sensory model was then further tested against the 0.5-ms sensory data.

Results

Thirty recordings of nerve excitability with extended electrotonus and current-threshold relationships were obtained in 10 subjects in the same session with stable temperatures (motor 33.9 ± 0.2°C; sensory [1-ms test width] 34.0 ± 0.2°C; sensory [0.5-ms test width] 33.9 ± 0.2°C). There were no significant differences in temperature between any of the recordings ($p > 0.7$).

Sensory excitability

Accommodation to hyperpolarization

In conventional threshold electrotonus recordings, it may not be appreciated that there is accommodation to a 100-ms long 40% hyperpolarizing current because the increase in threshold does not reverse. This was also the case for the 200-ms long 70% hyperpolarization in the present study (Figs 4.2A and 4.3A).

In eight out of the ten recordings accommodation appeared complete at the end of a 300-ms 100% hyperpolarization (Fig. 4.3A). The greatest hyperpolarizing change in threshold occurred 100 to 110 ms after the conditioning onset and was -359 ± 12% (mean ± SEM; Fig. 4.2A) with a range of -425% to -304% (Fig. 4.3A). The extent of accommodation was quite variable, ranging from 57% to 104% (Fig. 4.3A) with a mean of 85 ± 5% (Fig. 4.2A), and was not correlated with the hyperpolarizing change in threshold (Pearson product moment correlation, $p = 0.44$).

Fig. 4.2C shows mean sensory data for the current-threshold relationship at the end of 100-ms (left closed circles) and 200-ms (right closed circles) conditioning stimuli. Excitability (measured as a threshold reduction) is the threshold analogue of membrane potential, and the slope of the current-threshold relationship (Fig. 4.2D) is therefore an analogue of conductance. Both the 100-ms and 200-ms conditioning stimuli resulted in a hyperpolarization-activated conductance which did not appreciably grow with further hyperpolarization (left-most data points Figs 4.2D, 4.4D and 4.5B).

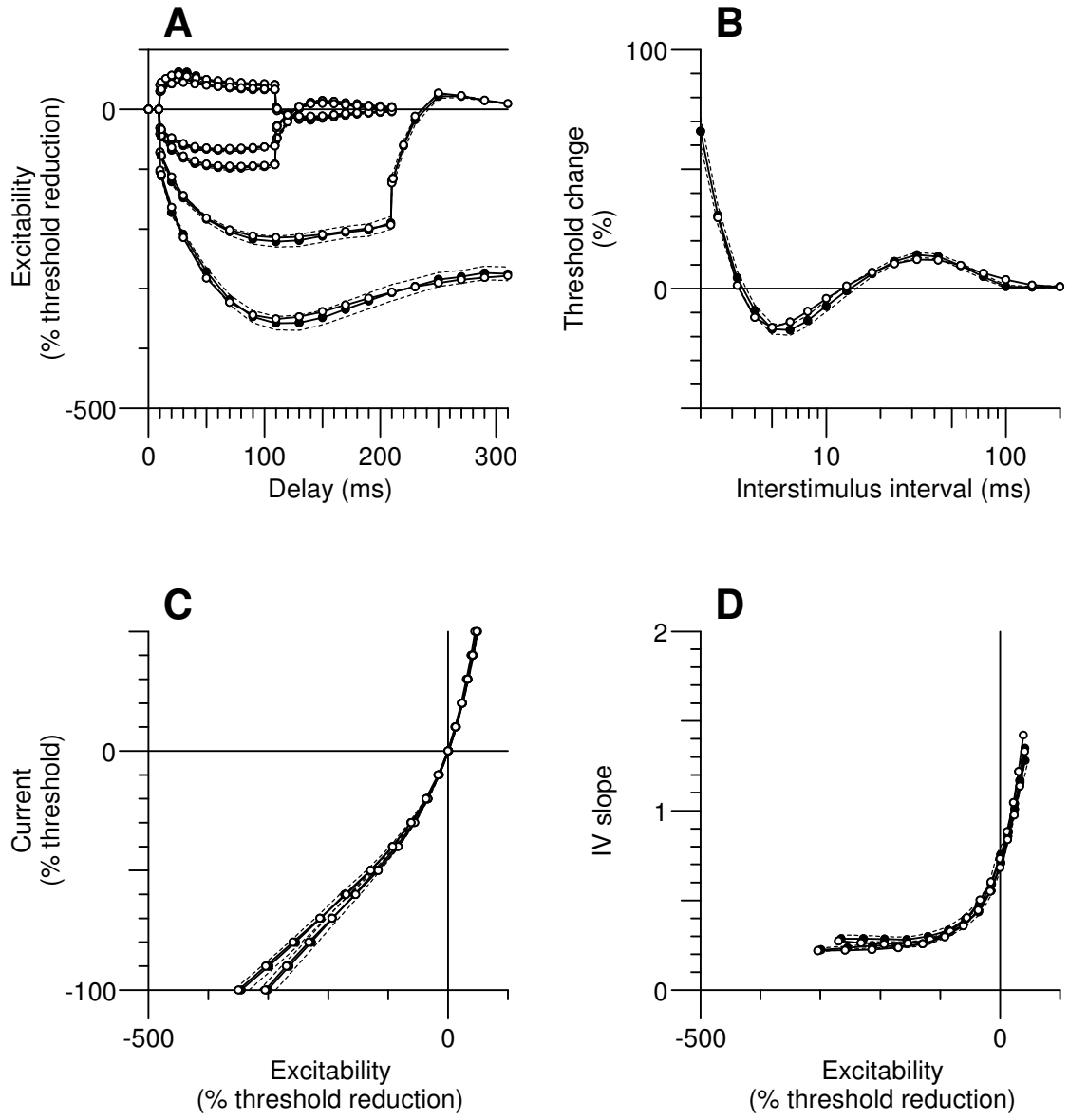

Figure 4.2. Mean sensory nerve excitability data and best-fit from the mathematical model. Extended excitability data for sensory axons (●; n = 10; mean ± SEM [dashed lines]) and the mathematical model simulation (○). **A.** Threshold electrotonus for conditioning levels of ±30%, ±40%, -70% and -100% of control threshold. **B.** Recovery cycle. **C.** Current-threshold (I/V) relationship for 100-ms and 200-ms conditioning stimuli. **D.** I/V slope (threshold conductance) for the data presented in ***C***.

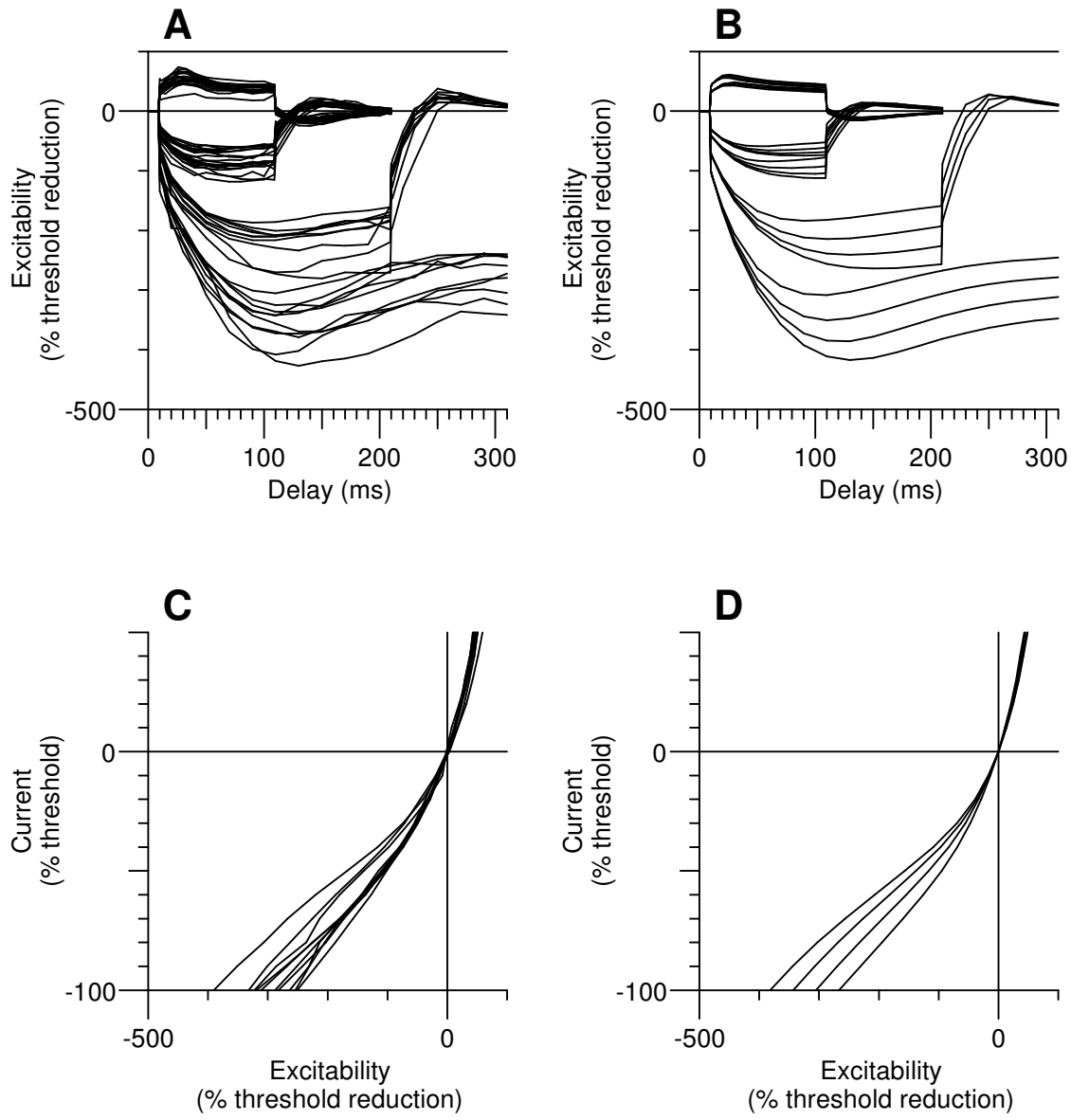

Figure 4.3. Individual sensory nerve recordings and sensory model.

Individual sensory nerve recordings (n = 10; 1-ms test stimulus) of extended threshold electrotonus, **A** (conditioning levels of ±30%, ±40%, -70% and -100% of unconditioned threshold), and current-threshold (I/V), **C** (for clarity, only the 200-ms conditioning stimulus data is displayed). Threshold electrotonus, **B**, and I/V, **D**, as generated by the sensory axon model with variation of $V_{0.5}$ for I_h from -89.2 to -104.2 mV in 5 mV steps.

The recovery cycle

The recovery of excitability after an action potential, tested here with 1-ms stimuli, did not differ significantly from the normative values established by Kiernan and colleagues (2001b) using 0.5-ms stimuli. Refractoriness at 2.5 ms was 31 ± 4%, the relative refractory period was 3.5 ± 0.1 ms and superexcitability was -16 ± 2% (Fig. 4.2B).

Strength-duration time constant

The mean strength-duration time constant of 561 ± 49 μV for sensory axons in the present study is in good agreement with the value of 527 μV obtained by Kiernan and colleagues (2001), and these data are compared in Figure 4.6.

Comparison with conventional sensory recordings

As expected control thresholds were lower with 1-ms test stimuli, 2.9 ± 0.3 mA, than with the conventional 0.5-ms studies, 3.7 ± 0.4mA ($p < 0.008$). The amplitude of the maximal CSAPs produced by supramaximal stimuli were not significantly different (1 ms, 78.3 ± 13.9 μV; 0.5 ms, 79.9 ± 13.7 μV; $p = 0.37$), suggesting that differences in dispersion of the CSAPs were minor. Not surprisingly, the latency to half-peak was longer for the 1-ms recordings (1 ms, 3.6 ± 0.1 ms; 0.5 ms, 3.4 ± 0.1 ms, $p < 2x10^{-6}$).

Motor excitability

Motor axons were studied here in the same session using the 1-ms test stimulus width (except for measurements of SDTC as stated above) and with the extended hyperpolarizing conditioning stimuli.

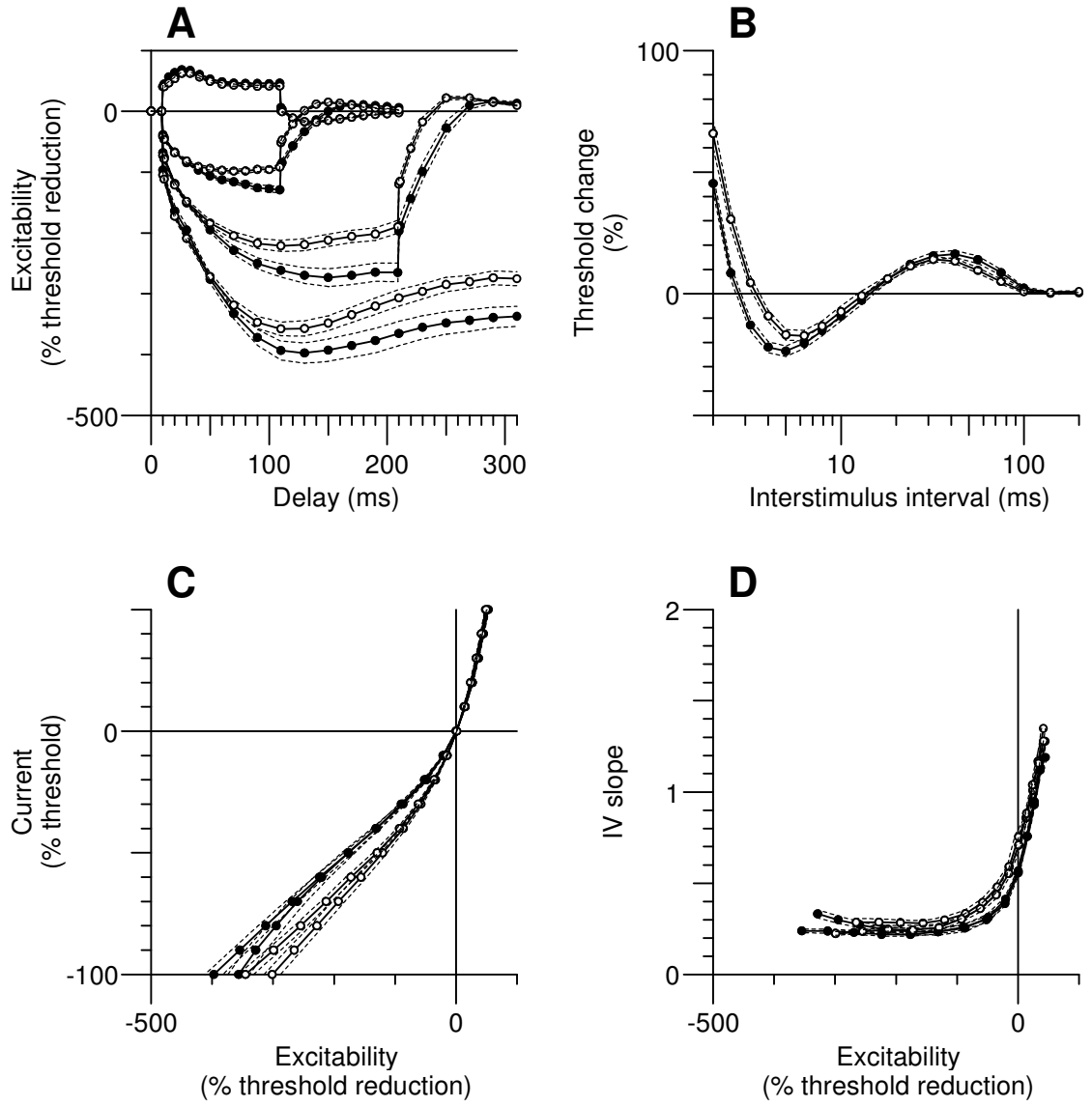

Figure 4.4. Mean motor and sensory nerve excitability.

Extended excitability data for motor (●) and sensory (○; same data as in Fig. 4.2) axons (n=10; mean ± SEM [dashed lines]), both recorded using 1-ms test stimuli. A. Threshold electrotonus for conditioning levels of ±40%, -70% and -100% of control threshold. B. Recovery cycle. C. Current-threshold (I/V) relationship for 100-ms and 200-ms conditioning stimuli. The 100-ms conditioning stimuli resulted in a larger decrease in excitability at -100% as less accommodation to hyperpolarization developed over the shorter time span. **D.** I/V slope (threshold conductance) for the data presented in **C**.

Note the greater accommodation of sensory axons in **A**, **C** and **D**. Also note that in motor axons the longer polarizing currents produce a delayed increase in accommodation (**C**) and increase in I/V slope (threshold conductance; **D**), comparable with that of sensory axons.

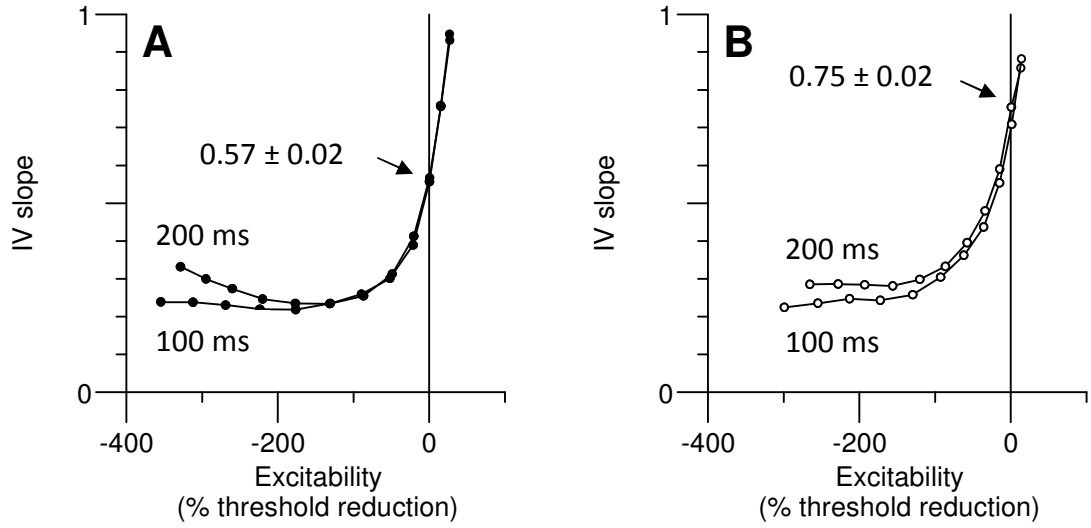

Figure 4.5. Detailed comparison of I/V slope (threshold conductance) for motor and sensory axons

Detail of the most hyperpolarized portion of the current-threshold relationship data in Figure 4.4D. **A.** I/V slope (threshold conductance) for motor axons (●; mean data; n = 10) for 100-ms and 200-ms conditioning stimuli. **B.** Threshold conductance for sensory axons (○; mean data; same subjects as in **A**). Mean values of resting I/V slope indicated by the arrows.

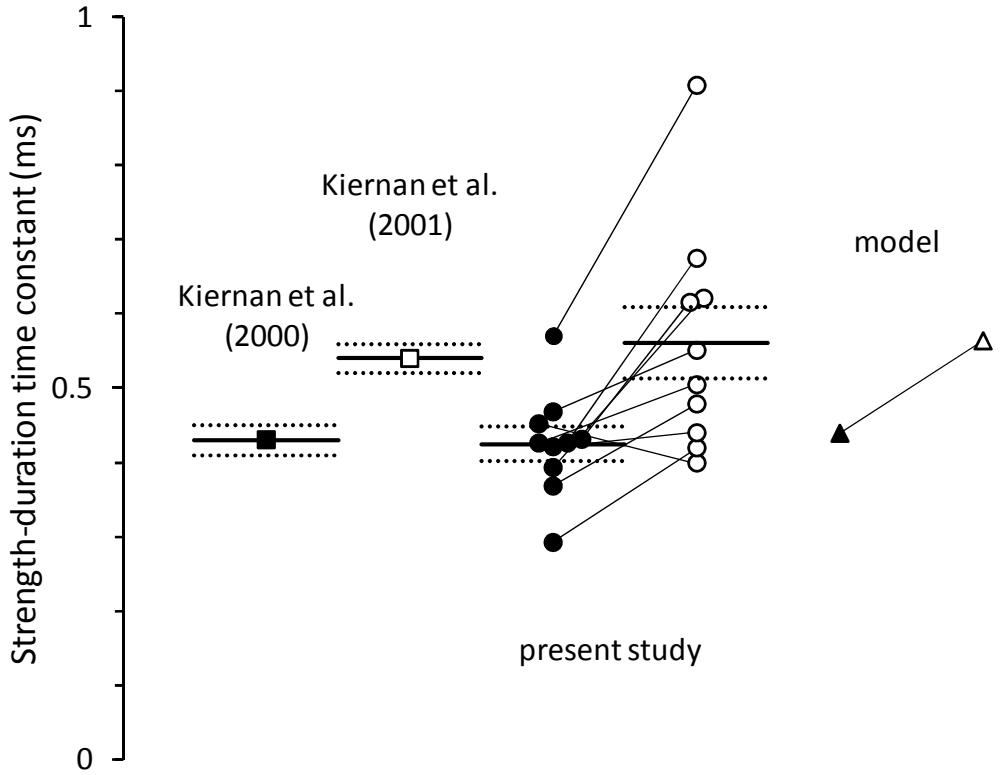

Figure 4.6. Strength-duration time constant.

Strength-duration time constants for motor (filled symbols) and sensory (open symbols) studies. Mean (solid lines) ± SEM (dotted lines). Data from the first published normal control studies are presented for comparison (squares). Data from the 10 subjects in the present study (circles; lines link the same subject). Strength duration time constants as estimated by the mathematical model for sensory and motor axons (triangles).

Accommodation to hyperpolarization

Previous studies have assumed that the difference in accommodation to hyperpolarization between motor and sensory axons is due to a lower expression of HCN channels in motor axons (Bostock *et al.*, 1994; Lin *et al.*, 2002; Tomlinson *et al.*, 2010a). This difference in accommodation is clearly seen in the mean threshold electrotonus data presented in Fig. 4.4A. The current-threshold relationship, however, suggests an additional (slower) conductance. This becomes apparent at the most hyperpolarized levels of the 200-ms conditioning stimulus as a steepening of the curve in Fig. 4.4C, seen more clearly in the I/V slope plot (Fig. 4.4D). Figure 4.5 compares the hyperpolarizing portion of the current-threshold relationship for sensory and motor axons, where, for motor axons, an additional conductance appears for conditioning levels hyperpolarized by more than 40%.

Excitability measures sensitive to membrane potential

The studied measures of axonal excitability are sensitive to changes in membrane potential (Kiernan & Bostock, 2000). The most reliable parameters that are sensitive to polarization are: TEd90-100 (threshold reduction at the end of a 100-ms depolarization); resting I/V slope (an analogue of the resting input conductance); and superexcitability (largely due to the effect of the depolarizing after potential). Motor axons had significantly greater TEd90-100 (motor, 45.7 ± 0.7%; sensory, 41.3 ± 1.2%, $p < 0.002$); significantly lower resting I/V slope (motor, 0.57 ± 0.02; sensory, 0.75 ± 0.07, $p < 0.02$, indicated by the arrows in Fig. 4.5); and greater superexcitability (motor, -22.0 ± 2.2%; sensory, -16.0 ± 2.2%, $p < 0.002$). A factor in these differences could be that sensory axons are probably more depolarized than motor axons (see Modelling, below).

Other excitability measures

The present study confirmed earlier findings of a shorter strength-duration time constant in motor axons (425 ± 23 µs, $p < 0.005$; Fig. 4.6; see Mogyoros *et al.*, 1996; Kiernan *et al.*, 2000; Kiernan *et al.*, 2001b). There were significant differences in the recovery of excitability following discharge (Fig. 4.4B). Refractoriness was significantly lower (8.5 ± 2.9% at 2.5 ms, $p < 0.0004$) and the relative refractory period significantly shorter (2.8 ± 0.1 ms; $p < 3 \times 10^{-5}$) in motor than sensory axons. Although there was greater superexcitability in motor axons (-22 ± 2%; $p < 0.002$; as in Kiernan *et al.*, 1996), late subexcitability was not found to be significantly different (16 ± 1%; $p = 0.12$; unlike Kiernan *et al.*, 1996) between motor and sensory axons.

Modelling

The adaptation of the Bostock model to the extended data for motor axons required neither additional ion channel types nor any changes to those properties primarily reflecting axon morphology. Further, no such changes were required when the model was modified to fit the sensory data. The equations underlying the model are given below, and the key parameters giving the greatest error reduction are listed in Table 4.1.

Model equations

Membrane potential:

$$\frac{dE}{dt} = -\frac{(I_{Na} + I_{Kf} + I_{Ks} + I_{Lk} + I_{pump} + I_{external} + I_{BB})}{C_n + C_{myelin}}$$

$$\frac{dE^*}{dt} = -\frac{I_{Kf^*} + I_{Ks^*} + I_h + I_{pump^*} + I_{Lk^*} - I_{BB} - C_{myelin}\frac{dE}{dt}}{C_{ax}}$$

Capacitance:

$$C_n = 1.4, \qquad C_{myelin} = 1.55, \qquad C_{ax} = 327\ pF$$

Ion concentrations:

$$[Na]_i = 9, \qquad [Na]_o = 144.2, \qquad [K]_i = 155, \qquad [K]_o = 4.5\ mM$$

Sodium current:

$$I_{Na} = P_{Na}(m^3 h) z(Na)$$

$$I_{NaP} = P_{Na}\left(\frac{P_{Na_P}}{100} m_p^3\right) z(Na)$$

$$z(Na) = \frac{EF^2}{RT}\left(\frac{Sel_{Na}\left\{[Na]_o - [Na]_i \exp\left(\frac{EF}{RT}\right)\right\} + (1 - Sel_{Na})\left\{[K]_o - [K]_i \exp\left(\frac{EF}{RT}\right)\right\}}{1 - \exp\left(\frac{EF}{RT}\right)}\right)$$

Fast potassium current:

$$I_{Kf} = G_{Kf} n^4 (E - E_{Kf})$$

$$I_{Kf^*} = G_{Kf^*}\, n^{*4} (E^* - E_{Kf})$$

Slow potassium current:

$$I_{Ks} = G_{Ks} s (E - E_{Ks})$$

$$I_{Ks^*} = G_{Ks^*} s^* (E^* - E_{Ks})$$

Leak current:

$$I_{Lk} = G_{Lk}(E - E_r)$$

$$I_{Lk^*} = G_{Lk^*}(E^* - E_r^*)$$

Barrett-Barrett current:

$$I_{BB} = G_{BB}(E - E^*)$$

Current through HCN channels:

$$I_h = G_h q (E^* - E_h)$$

Equilibrium potentials:

$$E_x = \frac{RT}{F} \ln\left(\frac{[K]_o + Sel_x[Na]_o - Sel_x[K]_o}{[K]_i + Sel_x[Na]_i - Sel_x[K]_i}\right)$$

for $x = K_f, K_s, h$

$Sel_{Na} = 0.9,\ \ Sel_{Kf}, Sel_{Ks} = 0,\ \ Sel_h = 0.097$

$$\frac{dm}{dt} = \alpha_m(1-m) - \beta_m m$$

and similarly for $m_p, h, n, s, n^*, s^*, q$

$$\alpha_m, \alpha_{m_p}, \alpha_n, \alpha_s = \frac{A(E-B)}{1-\exp((\mathrm{B}-\mathrm{E})/\mathrm{C})}$$

$$\alpha_h, \beta_m, \beta_{m_p}, \beta_n, \beta_s = \frac{A(B-E)}{1-\exp\left(\frac{E-B}{C}\right)}$$

$$\beta_h = \frac{A}{1+\exp\left(\frac{B-E}{C}\right)}$$

$$\alpha_q = A\exp((E-B)/C)$$

$$\beta_q = A/\exp((E-B)/C)$$

	A (ms^{-1}, at 36°C)	***Q10***	***B (mV)***	***C (mV)***
α_m	**6.54 (6.25)**	2.2	-18.5 (-18.3)	10.3
β_m	**0.302 (0.289)**		-22.8 (-22.6)	9.16
α_{m_p}	3.27 (3.13)		-36.5 (-36.3)	10.3
β_{m_p}	0.151 (0.145)		-40.8 (-40.6)	9.16
α_h	**0.126 (0.153)**	2.9	-115.1 (-113.8)	**15.6 (11.9)**
β_h	**8.60 (10.5)**		-32.9 (-31.6)	**19.0 (14.5)**
α_n	0.0221	3.0	-90.8	7.7
β_n	0.0393		-73.6	7.35
α_s	0.00563		-23.5	12.7
β_s	0.00341		-91.1	11.7
α_q, β_q	0.00522		**-107.3 (-94.2)**	-12.2

Table 4.2. Voltage- and time-dependent parameters for the rate constants, α and β for motor and sensory (bracketed values) axons. The key differences (bold) between sensory and motor axons are: (i) slowing of the Na^+ activation gate (α_m, β_m), (ii) acceleration of the Na^+ inactivation gate (α_h, β_h) and (iii) depolarization of the I_h voltage activation (α_q, β_q).

Motor axons

Increases in the nodal slow K^+ and the internodal fast K^+ conductances over those in the Bostock model contributed the most to the nodal resting membrane potential of -84.4 mV (3.0 mV hyperpolarized). Although not directly measurable, this resting membrane potential is within the range of previous studies on myelinated nerve (Chiu *et al.*, 1979, -80 mV, rabbit; Brismar, 1980, -80 mV, rat; Neumcke & Stämpfli, 1982, -78 mV, rat; Bostock *et al.*, 1991b, -86.7 mV, human; Halter & Clark, 1991, -78 mV, mammalian model; Schwarz *et al.*, 1995, -84 to -86 mV, human; Stephanova & Bostock, 1995, -86.7 mV, human model).

Strong and long-lasting hyperpolarization revealed a lesser role for the modelled I_h conductance and a greater role for the leak conductance across the internodal axolemma than in the Bostock model. The internodal leak conductance probably incorporates a contribution due to slower HCN isoforms, the activity of which would have remained fairly constant, even for the longer conditioning used in this study. All voltage activation and kinetics parameters associated with the I_h conductance were allowed to vary (Table 4.1), and the most sensitive parameter was Bq (the voltage of half-activation, which was more hyperpolarized than in the Bostock model, by 4.2 mV [comparable to the hyperpolarization of the internodal RMP by 3.1 mV]). Variation of Bq from the value obtained for the group data by -20 mV to +20 mV accounted for the variation in response to hyperpolarization seen in the recordings for different subjects (see Fig. 4.7B, 4.7D).

Sensory axons

A model of sensory nerve was achieved by adjusting the parameters of the new motor model in order to minimise the weighted least squares error between the model and the 1-ms sensory data (see Methods).

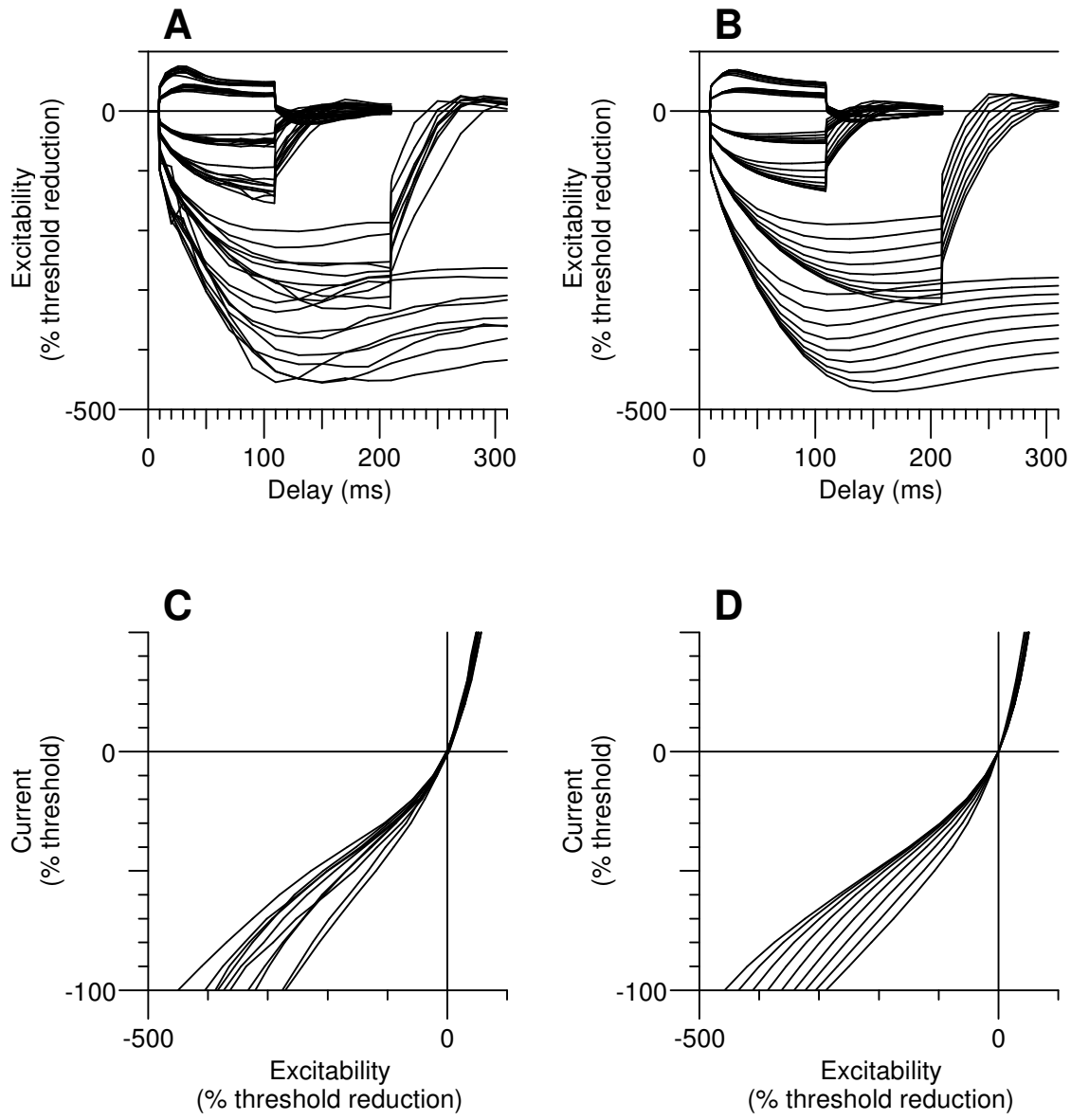

Figure 4.7. Individual motor nerve recordings and motor model.

Individual motor nerve recordings (n = 10) of extended threshold electrotonus, **A** (conditioning levels of ±20%, ±40%, -70% and -100% of unconditioned threshold), and I/V, **C** (for clarity, only the 200-ms conditioning stimulus data is displayed). Threshold electrotonus, **B**, and I/V, **D**, as generated by the motor axon model with variation of $V_{0.5}$ for I_h from -87.3 to -127.3 mV in 5 mV steps.

The overall reduction in discrepancy between the model and the sensory data was 98.8%, made up of reductions in discrepancy of 99.9% for strength-duration time constant, 98.5% for threshold electrotonus, 91.4% for recovery cycle, and 99.6% for current-threshold relationship.

The fit of this new sensory model to the mean data is shown in Fig. 4.2 (open circles) and Fig. 4.5 (right-most filled triangle). Varying Bq (the voltage of half-activation of the I_h conductance) from the value obtained for the group data (by -10 mV to +5 mV), again mirrored the variation in excitability seen in the individual recordings from different subjects (Fig. 4.3).

The sensory model, derived from the 1-ms data, was then tested against the 0.5-ms sensory data recorded in the same session, yielding an overall reduction in discrepancy of 95.8% compared to the motor model. Additionally, the range of responses to hyperpolarization was again suitably modelled by varying Bq by -10 mV to +5 mV.

The time constants of activation were calculated from the modelling and correspond closely to the kinetics of the fastest HCN isoform, HCN1 (motor, 36 ms at -140 mV, 79 ms at RMP; sensory, 12 ms at -140 mV, 162 ms at RMP) confirming earlier findings (Moosmang *et al.*, 2001; Biel *et al.*, 2009).

Unlike earlier studies that proposed a doubling of the expression of I_h between sensory and motor axons (Bostock *et al.*, 1994; Lin *et al.*, 2002), the present study found that the increased activity of I_h in sensory axons is better explained by a combination of a modest increase in the maximal conductance of I_h of 39% and more importantly a 13.1 mV depolarizing shift in Bq, the voltage activation of the conductance underlying I_h (see Table 4.1).

There was a lower expression of nodal slow K^+ channels in the sensory model which alone depolarizes the RMP by 2.1 mV, and this is consistent with earlier studies that have hypothesised that reduced K^+ channel expression contributes to increased susceptibility to ectopic activity in sensory axons (Kocsis *et al.*, 1986; Baker *et al.*, 1987).

The nodal and internodal pump currents are modelled here as constant (DC) currents. The modelled currents are clearly not solely due to hyperpolarizing Na^+/K^+-ATPase activity as they are in the opposite direction, that is, depolarizing (shifting RMP by +1.8 mV). The combined effect of the reduction in slow K^+ channel expression, the increased I_h current and the depolarizing 'pump' current is to depolarize the nodal RMP of sensory above motor axons by +4.1 mV.

The modelling in the present study found no differences between sensory and motor axons in the overall expression of Na^+ channels, nor in the percentage of channels that are in a persistent state, in contrast with the 2.5:1 ratio proposed by Bostock and Rothwell (1997). This may in part be due to the relative depolarization of the resting membrane potential of the sensory model in this study. Differences in the kinetics of the transient (fast) Na^+ channels, namely slower activation and faster inactivation in sensory axons counteract any broadening of the action potential width due to a lower expression of nodal slow K^+, and also support the hypothesis that the reduced superexcitability in sensory axons is due to a narrower action potential (Mitrović *et al.*, 1993; Honmou *et al.*, 1994; Kiernan *et al.*, 2001b; McIntyre *et al.*, 2002).

Can the differences between sensory and motor axons be explained by the consequences of changing a single parameter?

To test whether the difference in RMP was the key factor, the discrepancy between the motor model and the sensory data was assessed with the motor model depolarized by 4.1 mV (Table 4.1). This lengthened the strength-duration time constant (as in sensory axons; error improved by 95%), but the error for all other measures was greater (threshold electrotonus, recovery cycle, and current-threshold relationship; error worse by 22%, 125% and 4%, respectively). Similarly hyperpolarizing the sensory model failed to reproduce the motor findings.

To test whether the difference in slow potassium current (and the consequent difference in resting membrane potential) was the key factor, the nodal slow potassium current (GKsN) was reduced in the motor model from 56.7 nS to 29.1 nS (Table 4.1). Again strength-duration time constant lengthened (94% reduction in discrepancy), but the error for all the other measures was greater (threshold electrotonus, 58%; recovery cycle 52171% [much broader action potential]; current-threshold relationship, 31.6%).

Discussion

This study compared the accommodative responses of sensory and motor axons to strong and long-lasting hyperpolarization for the first time, recorded in the same session, using the same control test stimulus width, and has documented the variability in accommodation seen between subjects. The results indicate that, while sensory axons accommodate to hyperpolarization more efficiently, motor axons can 'catch up' with longer and stronger hyperpolarization. The Bostock model of a motor axon was adapted to incorporate the new I_h data, and a model of human sensory nerve was developed. The modelling was used to quantify differences in various excitability

indices for sensory and motor axons, and suggests that differences in channel gating may be as important as differences in channel expression in explaining the behaviour of sensory and motor axons.

Technical issues

Even though minimising the impedance of the skin electrode interface gave lower conditioning current intensities, unintended stimulation occurred in some axons within the first 20 ms of strong *hyperpolarization*. This often occurs for the strongest hyperpolarization levels in current-threshold relationships (unpublished observations), though its affect on the excitability tested some 200 ms later is most probably small, and is most likely the consequence of virtual cathodic stimulation (Basser & Roth, 2000; Holsheimer, 2003).

Insights from mathematical modelling

The new models of axonal excitability were used to clarify the basis of I_h activity in sensory and motor axons. Figure 4.8A, shows the modelled I_h currents during hyperpolarizing threshold electrotonus. The I_h currents for 40% hyperpolarization, qualitatively agree with the traditional view that sensory axons have a larger I_h conductance (Bostock et al., 1994; Lin et al., 2002). At the end of the 70% hyperpolarization however, the magnitude of I_h is approximately the same for motor and sensory axons, and for the 100% hyperpolarization, I_h in motor axons exceeds that in sensory. I_h is modelled here using a Hodgkin-Huxley formulation style and, in accordance with Ohm's law, the current is simply the product of the instantaneous conductance (Fig. 4.8B) and the electrochemical driving force (Fig. 4.8C) for HCN channels (Hodgkin & Huxley, 1952d). Figure 4.8B suggests that the number of channels conducting I_h in sensory axons is greater than in motor axons, at least for these hyperpolarization levels. Because motor axons hyperpolarize more they are

subjected to a greater electrochemical driving force and thereby a larger I_h current flows with strong hyperpolarization (Fig. 4.8C).

Figure 4.8D demonstrates that the leak current across the internodal axolemma is considerably larger in the motor axons. Much as for I_h, this is due to both a larger maximal conductance *and* a larger driving electromotive force (difference between the instantaneous and resting internodal membrane potentials) in motor axons. It is likely that a component of this leak current is due to slower otherwise unmodelled HCN isoforms. Interestingly, unlike the situation in voltage-clamped studies, the time course of the current flowing through slowly-gated channels is largely determined by the instantaneous membrane potential. If indeed the leak current partially represents 'slow' HCN channels, it can be seen in Figures 4.8A and 4.8D that this current will parallel the degree of hyperpolarization. A similar logic underpinned the suggestion in a previous report that slow K^+ currents make a significant contribution to the extent and duration of refractoriness and of superexcitability following a discharge (Burke *et al.*, 2009).

Similarly, the depolarizing nature of the 'pump' currents as modelled here is likely due to a tonic depolarization not otherwise modelled. Again this is suggestive of a very slowly-gated depolarizing current active at rest, such as one of the slower isoforms of HCN channels.

This study suggests that, leak and pump currents aside, the differences in response to hyperpolarization between motor and sensory axons are best explained by modulation of the voltage activation of the fastest HCN isoform, presumably HCN1. However, the differences in Bq (the voltage of half-activation) between motor and sensory axons and the range of modulation of Bq required to replicate the variability in accommodation seen in different subjects are greater than can be explained by cAMP alone.

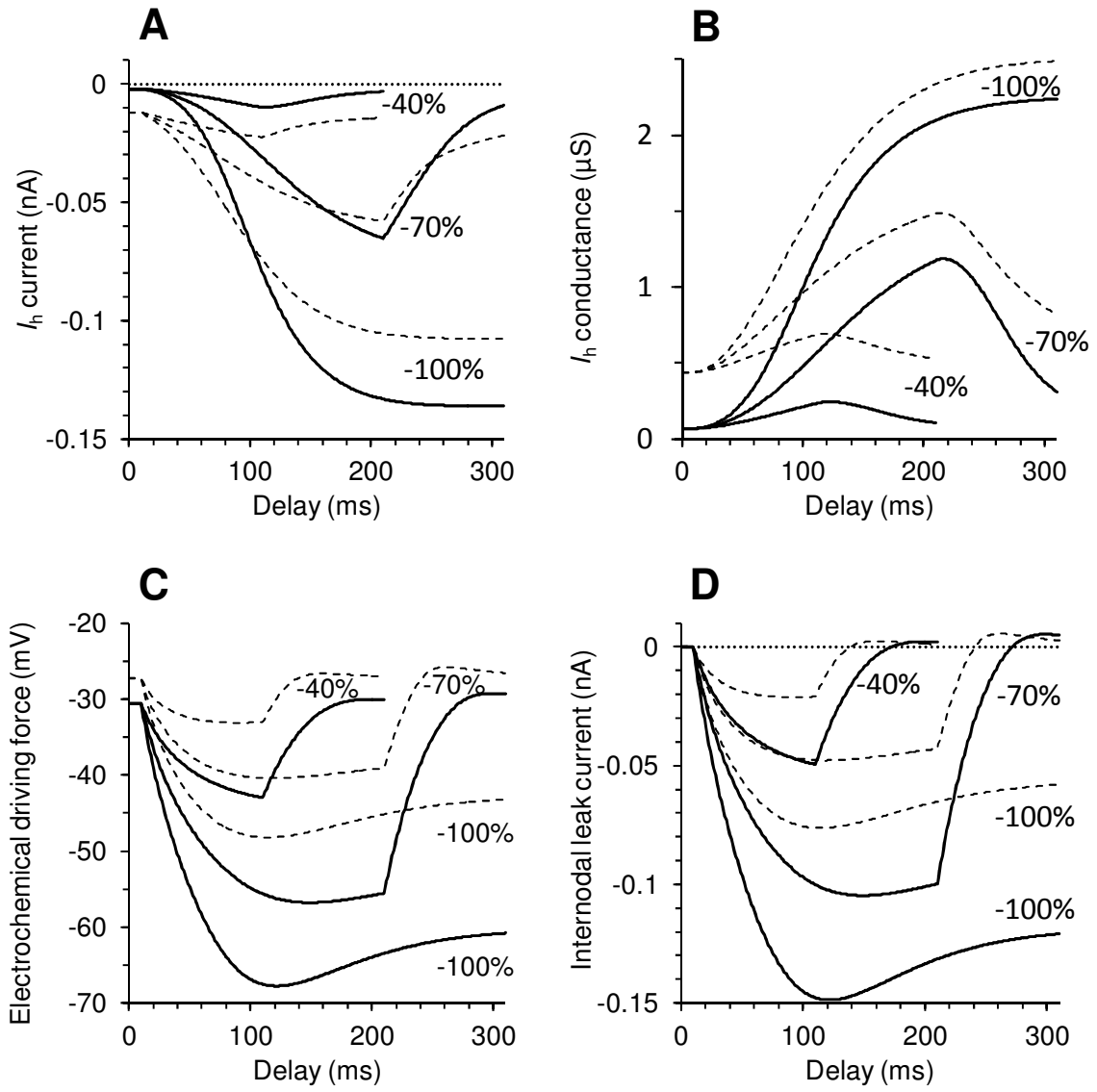

Figure 4.8. Modelled changes in I_h and internodal leak current during hyperpolarization.

Mathematical model simulation of changes in: **A**, I_h; **B**, conductance of HCN channels; **C**, electrochemical driving force for HCN channels (ie., the difference between internodal membrane potential and the equilibrium potential); and **D**, leak current across the internodal membrane, during threshold electrotonus (for conditioning levels of -40%, -70% and -100% of control threshold) in motor (unbroken line) and sensory (dashed line) models.

It is possible that the mechanism behind regulation of I_h function involves an allosteric activator such as the phospholipid PIP2 (phosphatidylinositol 4,5-bisphosphate; Pian *et al.*, 2006; Pian *et al.*, 2007), which may also be required to bring the voltage activation of HCN channels into a physiological range (Zolles *et al.*, 2006).

In summary, more of the 'fast' HCN isoform underlying I_h appears to be open at rest in sensory than in motor axons, and is thus able to participate more readily in limiting further hyperpolarization. In contrast motor axons appear to have a greater internodal leak conductance, which may be due to slowly activated HCN isoforms.

Other mechanisms that influence the action potential and the depolarizing afterpotential

Bostock and Rothwell (1997) concluded that the difference in latent addition between sensory and motor axons is due to a greater persistent Na^+ current in sensory axons, and they modelled this by an increase in the fraction of Na^+ channels functioning in the persistent mode. However, they noted that: "latent addition in depolarized motor fibres was indistinguishable from that in normal sensory fibres, both in our model and *in vivo*, so that although we have modelled the motor-sensory difference by a difference in density of threshold channels, our results are also compatible with the sensory fibres being relatively depolarized …". Persistent sodium currents can be recorded in DRG neurones and motoneurones and in their axons (Baker & Bostock, 1997; Tokuno *et al.*, 2003; Li *et al.*, 2004), but there are no comparative data on the relative numbers of *channels* operating in a persistent mode. The present results favour the alternative suggestion by Bostock and Rothwell (1997), though relative depolarization is insufficient to explain all the differences between sensory and motor axons.

The modelling indicates a reduction in the maximum slow K^+ conductance of sensory axons which would broaden the action potential. However this broadening is more than compensated for by a slowing of the activation of and an acceleration of the inactivation of transient Na^+ channels (Mitrović *et al.*, 1993; Honmou *et al.*, 1994). This overall narrowing of the sensory action potential was suggested by McIntyre and colleagues (2002) as a means of explaining the apparent paradox of reduced superexcitability (after an action potential) despite an increased persistent Na^+ current in sensory fibres. Stephanova and Mileva (2000) proposed an increased expression of *nodal* fast K^+ as a mechanism for a smaller depolarizing afterpotential in sensory axons. In contrast the modelling suggests no difference in the expression or kinetics of fast K^+ channels between modalities. It is worth noting however that this model requires a small stabilising population of 'nodal' fast K^+ channels. Although there is no evidence for their existence at the node, fast K^+ channels could still participate in the dynamics of nodal excitability through pathways which access juxtaparanodally located K^+ channels (Barrett & Barrett, 1982; Kocsis *et al.*, 1986; Mierzwa *et al.*, 2010).

Functional implications

This study supports the view that resting membrane potential is more depolarized in sensory axons, the model suggesting by 4.1 mV. Factors in this depolarizing shift of RMP are: the reduction in nodal slow K^+ (+2.1 mV); a further depolarization of the 'pump' current (+1.8 mV, probably due to slowly-gated HCN channels) and increased expression and depolarization of the voltage dependence of I_h (+0.5 mV). In turn, the relative depolarization can explain the previously reported differences in I_{NaP}, then attributed to a difference in the percentage of Na^+ channels that inactivate slowly, if at all. In addition this shift in resting membrane potential is a factor in the longer strength-duration time constant, decreased superexcitability, increased resting I/V slope and the lower TEd90-100 of sensory axons. However the modelling suggests that

the differences between sensory and motor axons cannot be explained by this change in RMP, or a change in other single properties, and the secondary consequences thereof.

It is often stated that the lower electrical threshold for sensory axons than motor is related to size. The present data provide no support for this view and, instead, suggest that the greater excitability reflects properties such as the currents active at rest (slow K^+, persistent Na^+ and I_h) and their influence on RMP.

There are at present no localisation data on HCN isoforms on human peripheral axons, and scant data for other mammals. The present findings implicate HCN1 in both sensory and motor axons but, in addition, raise the distinct possibility of 'slow' isoforms on both motor and sensory axons.

Chapter 5

Excitability and the safety margin in human axons during hyperthermia

Work in this chapter was published in Howells J, Czesnik D, Trevillion L & Burke D. (2013). Excitability and the safety margin in human axons during hyperthermia. J Physiol ***591,*** *3063-3080.*

Summary

Hyperthermia challenges the nervous system's ability to transmit action potentials faithfully. Neuromuscular diseases, particularly those involving demyelination have an impaired safety margin for action potential generation and propagation, and symptoms are commonly accentuated by increases in temperature. The aim of this study was to examine the mechanisms responsible for reduced excitability during hyperthermia. An additional aim was to determine if motor and sensory axons differ in their propensity for conduction block during hyperthermia. Recordings of axonal excitability were performed at normal temperatures and during focal hyperthermia for motor and sensory axons in six healthy subjects. There were clear changes in excitability during hyperthermia, with reduced superexcitability following an action potential, faster accommodation to long-lasting depolarization and reduced accommodation to hyperpolarization. A verified model of human motor and sensory axons was used to clarify the effects of hyperthermia. The hyperthermia-induced changes in excitability could be accounted for by increasing the modelled temperature by 6°C (and adjusting the maximum conductances and activation kinetics according to their Q10s; producing a 2 mV hyperpolarization of resting membrane potential), further hyperpolarizing the voltage dependence of I_h (motor, 11 mV; sensory, 7 mV) and adding a small depolarizing current at the internode (motor, 20 pA; sensory, 30 pA). The modelling suggested that slow K^+ channels play a significant role in reducing axonal excitability during hyperthermia. The further hyperpolarization of the activation of I_h would limit its ability to counter the hyperpolarization produced by activity, thereby allowing conduction block to occur during hyperthermia.

Introduction

Signalling in axons of the peripheral nervous system has long been known to be sensitive to temperature, and hyperthermia can impact on the ability of axons to faithfully transmit impulses to or from the peripheral nervous system. Cooling increases the duration and amplitude of an action potential and slows conduction velocity, and it has been suggested that this is primarily due to the slowing of Na^+ channel kinetics. Conversely, heating increases conduction velocity and decreases the response amplitude and duration of compound action potentials (Buchthal & Rosenfalck, 1966; Ludin & Beyeler, 1977; Rutkove *et al.*, 1997; Rutkove, 2001). In healthy individuals, the symptoms of fatigue and exhaustion can result from elevations in body temperature. In demyelinating disorders, increases in temperature can produce or exacerbate conduction block at sites of impairment of the safety margin for action potential generation. Experimentally demyelinated single nerve fibres may undergo reversible conduction block with elevations in nerve temperature as small as 0.5°C (Rasminsky, 1973). In a guinea pig model of experimental allergic neuritis, Davis and colleagues (1975) found that the temperature for conduction block is a linear function of conduction velocity (which should be related to the degree of demyelination), confirming their earlier theoretical predictions (Schauf & Davis, 1974).

In the giant squid axon, Hodgkin and Katz (1949) found the resting membrane potential to be practically constant between 3 and 20°C, and then gradually depolarized by 10 to 15 mV up to 35°C. In contrast, they found the shape of an action potential to be much more affected by temperature. The temperature dependence of the falling phase of the action potential was much greater than of the rising phase, for which they postulated that different mechanisms were responsible. To account for the temperature dependence of ion channel gating, Hodgkin and Huxley (1952c, d)

adopted a temperature coefficient (Q10) of 3 for all rate constants. However, subsequent studies in myelinated fibres found Na^+ activation to be less temperature sensitive with a Q10 of ~2 (Frankenhaeuser & Moore, 1963, frog; Schwarz & Eikhof, 1987, rat). To a lesser extent, ion concentrations, Nernst potentials, ion channel permeability, axonal membrane capacity and axoplasmic resistance are also dependent on temperature (Hodgkin *et al.*, 1952; Taylor & Chandler, 1962; Frankenhaeuser & Moore, 1963; Palti & Adelman, 1969).

In vivo threshold tracking techniques have been used to examine the underlying mechanisms of excitability in healthy and diseased human axons (Bostock *et al.*, 1998; Kiernan *et al.*, 2000; Krishnan *et al.*, 2009). Cooling has a marked effect on the excitability of both motor axons and cutaneous afferents (Burke *et al.*, 1999; Moldovan & Krarup, 2004) and even modest changes in temperature can have significant effects (Kiernan *et al.*, 2001a). However, to date the effects of hyperthermia on axonal excitability in human subjects have not been studied, so that the responses of the nervous system during hyperthermia have to be inferred, primarily from studies of cooling.

The present study examined the factors affecting the excitability of peripheral nerve axons when subjected to physiologically high temperatures. It was found that slow potassium (K_s) channels contribute to a dampening of excitability at elevated temperatures, and that this is particularly evident during the recovery of excitability following an action potential. In addition, our modelling suggests that the voltage dependence of the hyperpolarization-activated current (I_h) is further hyperpolarized during hyperthermia. This would limit its ability to counter activity-dependent hyperpolarization and restore resting membrane potential (RMP). These changes would impact on the safety margin for action potential generation, and are likely to be

factors in the conduction failure and fatigue of febrile illnesses, particularly in patients with diseases affecting axonal function, both central and peripheral.

Methods

The research followed the guidelines in the *Declaration of Helsinki* and ethics approval for the studies was obtained from the Human Research Ethics Committee of The University of Sydney, Australia. Experiments were performed on 27 separate occasions on six healthy subjects, all of whom provided written informed consent prior to the commencement of the study.

On each occasion axonal excitability was measured using the extended *TROND* protocol (Tomlinson *et al.*, 2010a; and as in Chapter 4) and a new protocol for studying polarized recovery cycles, first at a normal skin-surface temperature and then during focal hyperthermia. Sensory and motor axons of the median nerve of the six subjects were studied on separate occasions. To test the reproducibility of the results *within subjects*, measurements at normal temperature and during focal hyperthermia were performed on motor axons five times on separate days in two of the six subjects (subjects #1 and #2). The repeatability data for each subject were averaged before inclusion in the group data. The variability *within an experiment* was also tested five times in two subjects (subjects #2 and #3). Temperature was measured continuously near the site of stimulation using a skin-surface thermistor (YSI-409B; YSI Inc., Yellow Springs, Ohio, USA; see Fig. 2.1). Reusable 'click-style' sodium acetate heat pads (Maverick Co., Christchurch, NZ) were applied to the dorsal and palmar aspects of the distal forearm and hand to create focal hyperthermia at the site of stimulation, while the whole arm was wrapped in a blanket to slow temperature loss. The average skin surface temperatures recorded under control conditions were 32.5 ± 0.2°C (mean ± SEM) for motor axons and 32.6 ± 0.1°C for sensory axons. The temperatures recorded

during heating ranged from 39.4 to 43.4°C. After application of the heat pads, measurements began within five minutes, when the skin-surface temperature had stabilized at its peak value (41.7 ± 0.1°C, mean ± SEM). Over the course of the experiment the mean temperature cooled slightly to 40.8 ± 0.1°C, with a maximal drop in any experiment of 2.5°C.

Nerve excitability studies were performed using the QtracS software as described in Chapter 2. Stimuli were applied to the median nerve at the wrist via non-polarizable Ag/AgCl adhesive electrodes (Cleartrace REF 1700-050, ConMed, Utica, NY, USA), with the anode placed 10 cm proximally on the radial edge of the forearm (see Fig. 2.1). Compound muscle action potentials (CMAPs) were recorded using the same Ag/AgCl electrodes with the active electrode over the thenar eminence, the reference electrode distally on the proximal phalanx of the thumb. Compound sensory action potentials (CSAPs) were recorded with disposable Ag/AgCl ring electrodes (RE-D; Electrode Store, EnumClaw, WA, USA) on digit 2 with the active electrode on the proximal phalanx, the reference approximately 4 cm distally. A ground electrode on the palm was used for both motor and sensory recordings. All electrodes were further secured to the skin with surgical tape (Transpore; 3M, St Paul, MN, USA) prior to commencement of the experiments.

A low-noise preamplifier as described in Chapter 3 was used to amplify the compound action potentials (CMAP x200; CSAP x10k) which then had mains-frequency noise removed with a HumBug Noise Eliminator (Quest Scientific, North Vancouver, BC, CA) before being digitized by a data acquisition system (PCI-6221; National Instruments, Austin, TX, USA). QtracS and the data acquisition system provided the command signal for the delivery of stimuli by an isolated linear bipolar current stimulator (DS5; Digitimer, Welwyn Garden City, UK).

Excitability protocols

Excitability studies adjust the intensity of a test stimulus to track a constant fraction of the maximal compound action potential (target potential). The response to graded stimuli was measured first to determine stimulus-response (SR) properties, the size of the target potential and to optimise the tracking. For both motor and sensory studies, 1-ms wide test stimuli were used, allowing simpler comparisons between motor and sensory axons and the use of strong hyperpolarization in sensory axons (Tomlinson *et al.*, 2010a; as in Chapter 4). From the SR relationship, the target response was set to 50% of the maximal response (near the steepest part of the curve).

Routine axonal excitability assessment

The extended nerve excitability protocol (*TrondNF*) was used to study the excitability of axons at normal and hyperthermic temperatures. This protocol consists of five parts: stimulus-response relationship (SR; described above); strength-duration properties, which are plotted as charge versus duration (QT); threshold electrotonus (TE); current-threshold relationship (IV; the threshold analogue of current-voltage) and the recovery cycle (RC).

Strength-duration properties of motor axons were studied by tracking the 50% target potential using stimuli of different widths: 1, 0.8, 0.6, 0.4 and 0.2 ms. There is a linear relationship between stimulus charge (stimulus strength x width) and stimulus width, with the slope and negative intercept on the X-axis representing rheobase and the strength-duration time constant (SDTC), respectively (Mogyoros *et al.*, 1996). The strength-duration properties of sensory axons were made using narrower test widths (0.5, 0.4, 0.3, 0.2 and 0.1) to avoid dispersion of the CSAP that occurs with longer stimuli (as described in Chapter 4).

Threshold electrotonus was tested before, during and after long subthreshold conditioning currents. In addition to the standard conditioning currents of ±20 and ±40% of the unconditioned threshold (see Kiernan *et al.*, 2000), two additional levels of hyperpolarization were included: a 200-ms long hyperpolarizing current which was 70% of the control threshold, and a 300-ms long hyperpolarizing current which was 100% of the control threshold (Tomlinson *et al.*, 2010a; as in Chapter 4).

The ***current-threshold relationship*** quantifies the rectifying conductances, both inward and outward, and the resting input conductance. The test threshold was measured at the end of a 200-ms conditioning current for 16 conditioning strengths from +50% (depolarizing) to -100% (hyperpolarizing) in 10% increments.

The ***recovery cycle*** measures the recovery of excitability following supramaximal stimulation at 18 conditioning-test intervals which change in a logarithmic fashion between 2 and 200 ms. Under normal conditions axons undergo a distinct pattern of excitability following an action potential (Adrian & Lucas, 1912). Initially the axons are inexcitable (absolute refractoriness), followed by reduced excitability (relative refractoriness), the end of which corresponds to the relative refractory period (RRP). After refractoriness axons undergo a period of superexcitability which is associated with the depolarizing afterpotential (Barrett & Barrett, 1982), and then a period of subexcitability ensues, attributed to the after-hyperpolarization.

Polarized recovery cycles

To determine whether changes in membrane potential contribute to the changes in the recovery cycle much as described in Bergmans (1970) and Kiernan and Bostock (2000), recovery cycles were measured in the same way as described above, at rest and during background polarization, at normal and hyperthermic temperatures. The

recovery cycle was measured 200 ms after the onset of long +30% (depolarizing) and -30% (hyperpolarizing) currents which extended beyond the test stimulus.

Mathematical modelling

The Bostock model of the human motor axon (Bostock *et al.*, 1991b), as developed in Chapter 4 for motor and sensory axons, was used to assist in the interpretation of the excitability changes during focal hyperthermia. This space-clamped model is well suited to the simulation of superficially located nerves stimulated with relatively large electrodes, and has been used to model the changes in axonal excitability in tetrodotoxin poisoning (Kiernan *et al.*, 2005), porphyria (Lin *et al.*, 2008), and following stroke and multiple sclerosis (Jankelowitz *et al.*, 2007a; Ng *et al.*, 2008). The model consists of nodal and internodal compartments, which are linked by the Barrett-Barrett conductance, representing paranodal pathways through and under the myelin sheath (Barrett & Barrett, 1982; Mierzwa *et al.*, 2010). To model the effects of focal hyperthermia on axonal excitability, the ion channel rate constants were increased according to their Q10 values (Hodgkin & Huxley, 1952c, d; Frankenhaeuser & Moore, 1963; Guttman, 1971; Hart, 1983; Schwarz & Eikhof, 1987): Na^+ activation 'm', 2.2; Na^+ inactivation 'h', 2.9; K^+ (fast and slow) and HCN channels, 3. As the maximal conductances are affected by changes in passive diffusion, a Q10 of 1.4 was also applied to all voltage-gated ion channel (Hodgkin & Huxley, 1952c, d; Moore, 1958; Hart, 1983; Hille, 1992), leak and Barrett-Barrett conductances. The effect of temperature on capacitance is negligible (Hodgkin *et al.*, 1952; Tasaki, 1955; Taylor & Chandler, 1962; Palti & Adelman, 1969), and capacitances in the model were therefore not adjusted for hyperthermia.

Statistical analysis

Group data are reported as mean (and SEM), except for measures that are better plotted on logarithmic scales to be normally distributed. Here geometric means were calculated and reported as mean [geometric SEM (as a factor)] (Kiernan *et al.*, 2000). The mean values for the two groups (normal and hyperthermic) were compared with Student's t-tests for paired data, and are reported in Table 5.1. The *P*-values of related measures (as indicated by the parentheses in Table 5.1) were adjusted for multiple comparisons using the Holm-Bonferroni method, and the corrected values are reported in the text and Tables.

For statistical analysis the extent of superexcitability was measured as the area below the X-axis following the relative refractory period. Similarly, the extent of subexcitability (which follows superexcitability) was measured as the area above the X-axis.

Results

CMAP recruitment

The latency from the onset of the test stimulus to the peak of the CMAP was 0.36 ms shorter when hyperthermic ($p < 0.02$), though the amplitude of the peak CMAP recorded at the normal and hyperthermic temperatures was not significantly different ($p = 0.24$; Fig. 5.1A and Table 5.1).

	Motor			Sensory		
	Normal	Hyper.	*P* value	Normal	Hyper.	*P* value
Latency to peak (ms)	6.4 (0.3)	6.1 (0.2)	0.02	3.2 (0.1)**	3.1 (0.1)**	0.003
Peak response (mv, μV)*	6.4 [1.22]	6.0 [1.21]	0.24	40.0 [1.16]	46.5 [1.19]	0.12
Stim for 50% max (mA)	4.3 (0.4)	5.1 (0.6)	0.16	3.6 (0.6)	3.9 (0.5)	1
Rheobase (mA)	2.8 (0.3)	3.4 (0.4)	0.20	2.2 (0.3)	2.7 (0.4)	0.6
SR slope*	4.33 [1.09]	4.11 [1.07]	1	1.59 [1.11]	1.70 [1.10]	0.5
SDTC (μs)	517 (54)	506 (30)	0.7	724 (128)	648 (47)	0.8
TEd40(peak; %)	66.4 (2.0)	61.9 (2.1)	0.003	60.3 (1.7)	57.7 (1.5)	0.26
Accomm. half-time (ms)	38.2 (0.7)	29.6 (0.5)	0.004	38.0 (1.9)	31.6 (0.7)	0.2
TEd40(undershoot; %)	-19.5 (1.4)	-10.6 (1.1)	0.007	-17.7 (0.8)	-11.4 (0.6)	0.01
TEd20(peak; %)	38.0 (1.4)	35.8 (1.7)	0.005	33.0 (0.9)	31.4 (0.9)	0.33
TEd20(undershoot; %)	-10.5 (0.7)	-4.9 (0.7)	0.006	-9.0 (0.5)	-6.6 (0.7)	0.28
TEh20(overshoot; %)	8.8 (0.8)	4.0 (0.9)	0.006	7.0 (0.3)	4.9 (0.3)	0.04
TEh40(overshoot; %)	15.8 (1.4)	7.0 (1.2)	0.005	12.1 (0.5)	7.4 (0.4)	0.005
TEh100(260-300 ms; %)	-334 (33)	-366 (37)	0.02	-270 (13)	-292 (11)	0.03
Resting I/V slope	0.61 (0.04)	0.59 (0.06)	0.4	0.71 (0.02)	0.69 (0.03)	0.5
Hyperpol. I/V slope	0.33 (.03)	0.31 (0.02)	0.6	0.31 (0.02)	0.33 (0.02)	1
Refract. at 2 ms (%)	64.0 (15.7)	20.0 (8.0)	0.02	46.5 (9.4)	24.3 (4.1)	0.02
RRP (ms)*	3.1 [1.08]	2.5 [1.08]	0.04	3.1 [1.09]	2.9 [1.07]	0.02
Superexcit. area (%-ms)	-140 (27)	-35 (15)	0.006	-116 (24)	-39 (13)	0.008
Subexcit. area (%-ms)	1124 (142)	952 (284)	0.45	767 (49)	633 (161)	0.50

Table 5.1. Axonal excitability measures at normal and hyperthermic temperatures.

Values are presented as mean and SEM (in parentheses).

P values are from Student t-tests of paired data. Related measures, as indicated by parentheses, were corrected for multiple comparisons using the Holm-Bonferroni method.

*These measures are normally plotted on a logarithmic scale and are reported as the geometric mean and SEM (in square brackets, as a factor).

**Sensory latencies using a 0.5-ms wide test stimulus

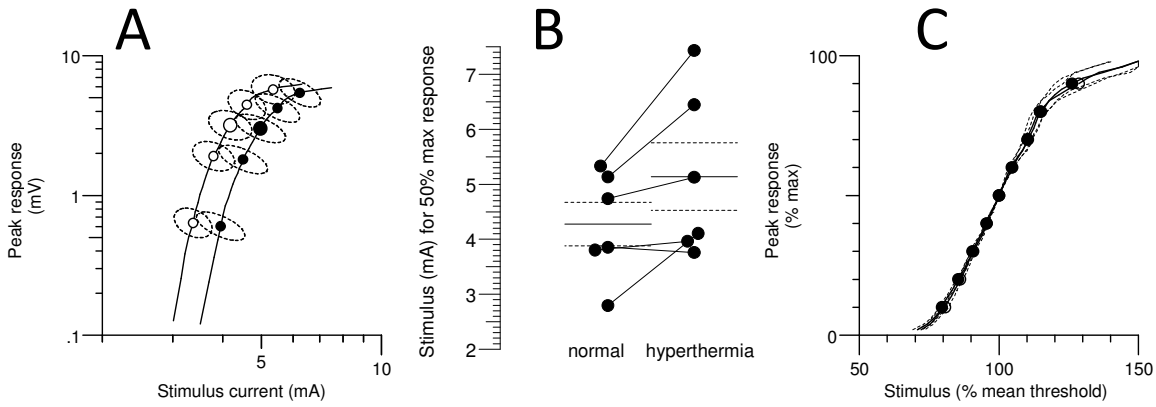

Figure 5.1. Stimulus-response relationship during hyperthermia. Group data (n = 6).

A. Recruitment of CMAP (measured baseline to peak) by gradually increasing stimulus intensity (normal temperature, open circles; hyperthermia, filled circles). **B.** Stimulus required to recruit a half-maximal response at normal and hyperthermic temperatures. The solid and dashed horizontal lines indicate the mean and standard errors (the mean half-maximal stimulus is also indicated by the large circles in A.). **C.** Normalised stimulus-response relationship recorded at normal and hyperthermic temperatures (open and closed circles, respectively). The peak response is normalised to a percentage of maximum and the stimulus is normalised to the stimulus current required for a half-maximal potential, before being averaged.

The stimulus current required for a half-maximal response and rheobase were both higher during hyperthermia but not significantly so after adjustment for multiple comparisons (respectively, 5.1 ± 0.6 mA [hyperthermia] and 4.3 ± 0.4 mA [normal]; and 3.4 ± 0.4 mA [hyperthermia] and 2.8 ± 0.3 mA [normal]; see Fig. 5.1A [large circles], 5.1B and Table 5.1). The stimulus-response slopes and strength-duration time constants were also not significantly different (see Fig. 5.1C and Table 5.1).

Threshold electrotonus and current-threshold relationship in motor axons

Accommodation to depolarizing currents was more rapid during hyperthermia than at normal temperatures (see Fig. 5.2A), such that the maximal threshold reduction was less (with +40%: 61.9 ± 2.1% and 66.4 ± 2%, respectively; with +20%: 35.8 ± 1.7% and 38 ± 1.4%, respectively; see Table 5.1) and accommodation half-time was shorter (the time to the midpoint between the peak threshold reduction and the average level at the end of the polarization; hyperthermia, 29.6 ms; normal, 38.2 ms; see Table 5.1). The undershoot after the 100-ms depolarizing current ended is due to the slow de-activation of accommodative conductances active at the end of the depolarization; the peak undershoot occurred earlier but was smaller for both levels of polarization during hyperthermia ($p \leq 0.007$; see Table 5.1).

In contrast, significant differences in the accommodation to hyperpolarization were only apparent for the strongest hyperpolarizing current and during the hyperpolarizing overshoots (see Fig. 5.2B and Table 5.1). Unexpectedly, the accommodation appeared slower during hyperthermia, and excitability was reduced at the end of the long -100% hyperpolarizing currents (i.e., at the intervals between 260 and 300 ms, 'TEh100(260-300 ms)'; $p = 0.02$).

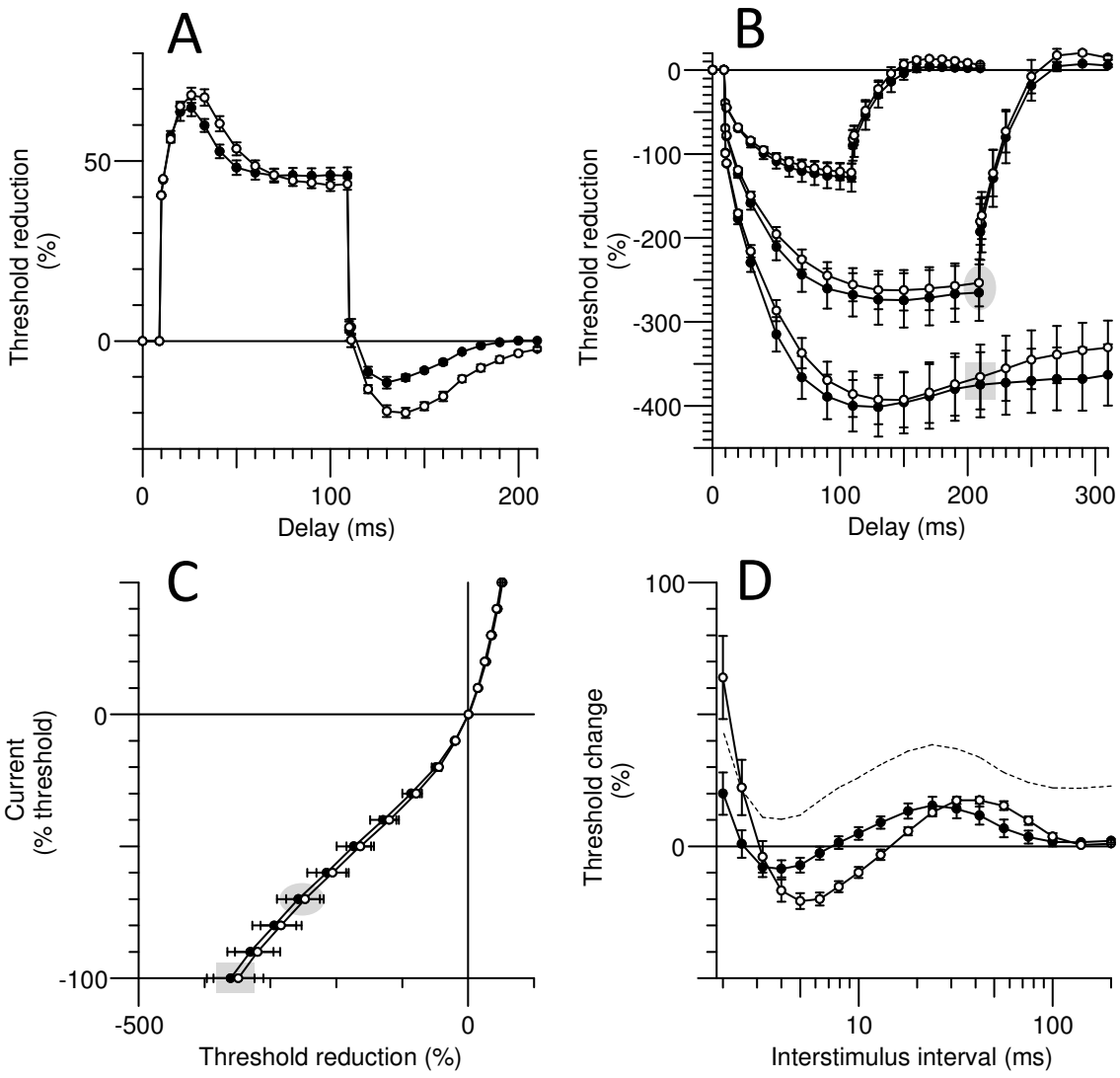

Figure 5.2. Motor axon excitability during focal hyperthermia. Group data (n = 6; mean ± SEM). Measurements of axonal excitability were made at normal resting temperature (open circles) and during focal hyperthermia (filled circles). **A.** Threshold electrotonus for a depolarizing conditioning current of +40% of the unconditioned threshold. **B.** Threshold electrotonus for hyperpolarizing conditioning currents of -40, -70 and -100%. **C.** Current-threshold relationship for 200-ms long conditioning currents from +50% (depolarizing) to -100% (hyperpolarizing) of the control threshold. **D.** The recovery of excitability following a supramaximal discharge. The dotted line represents the recovery of excitability during hyperthermia when normalised to the unconditioned threshold at 'normal' temperature (see Discussion). The corresponding data points in threshold electrotonus (***B***) and the current-threshold relationship (***C***) are highlighted by the shaded ellipses and rectangles for hyperpolarization by -70 & -100%, respectively.

Figure 5.2C shows the current-threshold relationship (a threshold analogue of current/voltage, 'I/V', plots), measured at the end of a 200-ms long conditioning current. Hyperthermia produced no significant differences in the resting and hyperpolarizing I/V slopes ($p = 0.4$ and 0.6, respectively; see Table 5.1).

The fact that the hyperpolarizing portion of the current-threshold relationship appears unaffected by hyperthermia is consistent with the equivalent data in threshold electrotonus (see ellipses and rectangles in Figs 5.2B,C and 5.5B,C), and probably reflects opposing effects on HCN channels which cancel each other out for all but the strongest and longest hyperpolarization (see Modelling and Discussion).

The recovery cycle of motor axons

The hyperthermia-induced changes in excitability of motor axons were particularly obvious in the recovery after a conditioning discharge (Fig. 5.2D and Table 5.1). The recordings during focal hyperthermia were characterized by less refractoriness at 2 ms (20 ± 8% and 64 ± 16%), a shorter relative refractory period (2.5 ± 0.2 ms and 3.1 ± 0.2 ms), with earlier superexcitability of reduced area (-35 ± 15 %-ms and -140 ± 27 %-ms). Similarly, subexcitability occurred earlier during hyperthermia but its area was not significantly different ($p = 0.45$).

Reproducibility

In order to demonstrate the reproducibility within single subjects, all measurements for motor axons were performed five times on separate days in two of the six subjects (subjects #1 and #2; the mean data for each of these two subjects were used in the group data averages). The individual recordings and mean data for one subject (#1) are shown in Figure 5.3. The results were quite reproducible and comparable to the group data. As observed by Tomlinson and colleagues (2010a) and in Chapter 4, the greatest variability was seen for the strongest hyperpolarizing currents in threshold

electrotonus (which is not surprising considering the number of possible modulators of hyperpolarization-activated cyclic nucleotide-gated (HCN) channels). To explore the source of variability further, repeated measurements were made five times in the same experiment in each of two subjects (Subjects #2 and #3). Figure 5.4 compares the variability within an experiment, within a subject and between all subjects, and these data are summarised in Table 5.2. The data shows that the variability within an experiment is considerably lower than within the same subject on different days. It was expected that there would be an increase in excitability during hyperthermia. Based on the within-experiment variability a power analysis using TEh100(260-300 ms) indicated that with six subjects there was sufficient power (80%) to detect a 7.9% increase in excitability at $\alpha = 0.05$. The actual change during hyperthermia was much larger (32%), and in the opposite direction to that hypothesised. The variability *within* an experiment is the relevant measure for the present studies because the normal and hyperthermic studies were done within the *same* experiment.

Parameter	Same subject, within experiment	Same subject, different days	Between subjects (n = 6)
TEd40(peak; %)	0.8 (1.1%)	1.4 (2.2%)	4.8 (7.3%)
TEh100(peak; %)	8.2 (2.4%)	23 (6.8%)	79 (19.8%)
TEh100(260-300 ms; %)	5.5 (1.9%)	18 (6.3%)	81 (24.1%)
RRP (ms; geometric SD)*	1.026	1.06	1.198
Superexcitability (%)	1.2 (5.2%)	1.5 (6.9%)	7.05 (35.8%)
Superexcit. area (%-ms)	-12.5 (8.8%)	-16.4 (12.1%)	-65.4 (46.9%)

Table 5.2. Variability of excitability measures in motor axons.

Figures are for the standard deviation and the coefficient of variation is in parentheses.

* RRP - geometric standard deviation (as a factor)

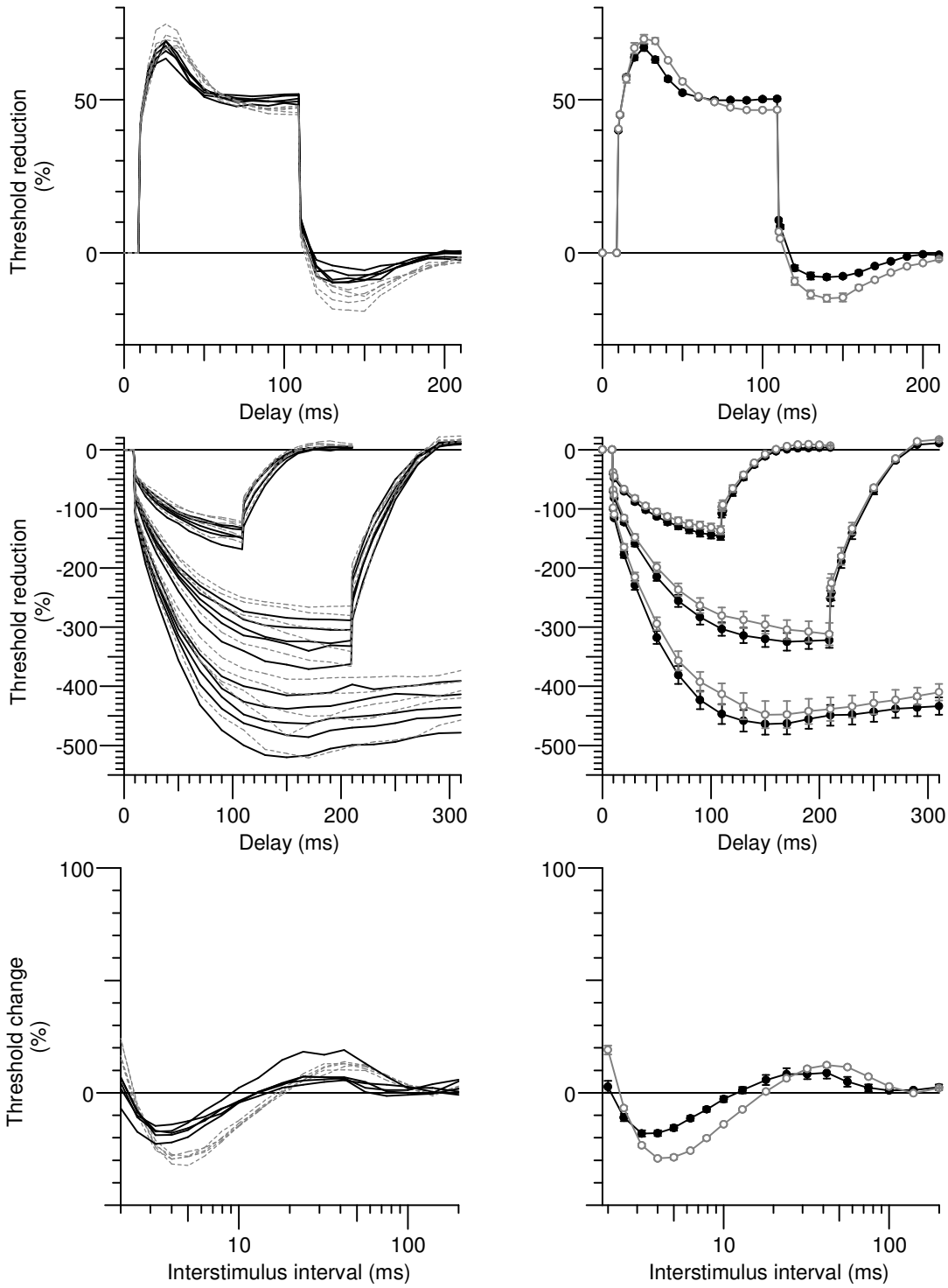

Figure 5.3. Reproducibility of hyperthermia induced changes. Left column. Repeated measurements of axonal excitability in subject #1 on five separate occasions (normal temperature, dashed lines; hyperthermia, solid lines). **Right column.** Mean data (normal temperature, open circles; hyperthermia, filled circles; mean ± SEM). **Top row.** Depolarizing threshold electrotonus (+40%; as in Fig. 5.2A). **Middle row.** Hyperpolarizing threshold electrotonus (-40, -70 and -100%; as in Fig. 5.2B). **Bottom row.** Recovery cycle.

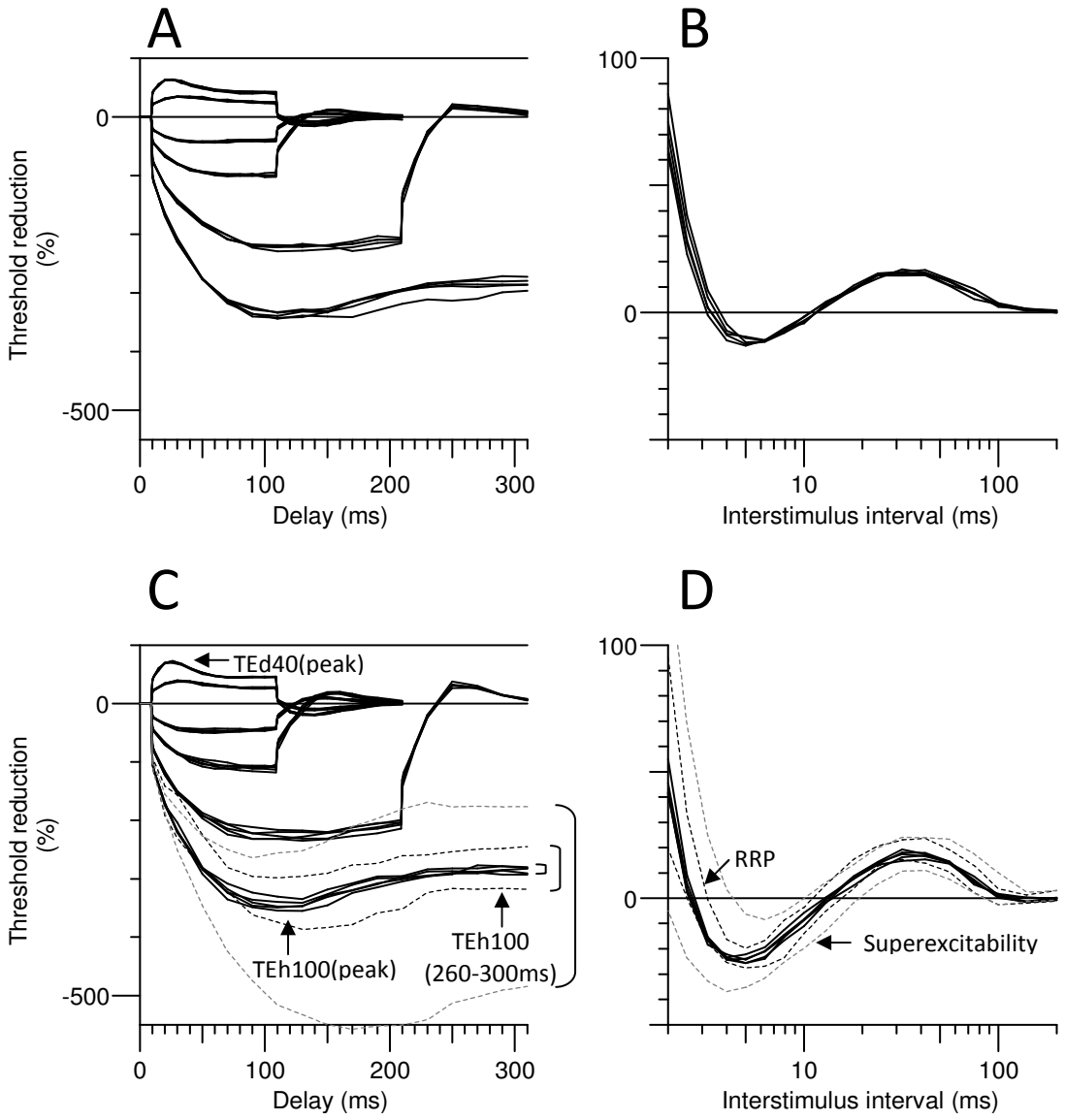

Figure 5.4. Reproducibility of excitability measures within an experiment. Five repeated measurements within the same experiment for subject #3 for threshold electrotonus (***A***) and the recovery cycle (***B***). Five repeated measurements (solid lines) in subject #2 for threshold electrotonus (***C***) and the recovery cycle (***D***). The brackets in ***C*** highlight differences in the variability for the strongest hyperpolarization. The smallest bracket shows the within-experiment variability, the next largest bracket and the inner broken lines indicate the within-subject variability (95% confidence limits) on different days, while the largest bracket and the outer broken lines show the 95% confidence limits for all subjects. Note that the within-experiment variability is the measure relevant to the present studies.

Excitability of sensory axons

The hyperthermia-induced changes in sensory excitability are shown in Figure 5.5 and are summarised in Table 5.1. These changes were qualitatively similar to those described above for motor axons with, in the recovery cycle (Fig. 5.5D), reduced refractoriness (24 ± 4% vs. 46 ± 9%), a shorter relative refractory period (2.9 ± 0.2 ms vs. 3.2 ± 0.3 ms), reduced superexcitability (-8.3 ± 2.4% vs. -17.6 ± 2.8%) and, in threshold electrotonus, reduced undershoot (Fig. 5.5A; -11.4 ± 0.6% vs. -17.7 ± 0.8%) and overshoot (Fig. 5.5B; 7.4 ± 0.4% vs. 12.1 ± 0.5%). Hyperthermia had little effect on hyperpolarizing threshold electrotonus and the current-threshold relationship for sensory axons, except at the end of the strongest hyperpolarization of threshold electrotonus (Fig. 5.5B). The other measures showed trends in the same direction as with motor axons, but the changes were smaller and not significant.

Polarized recovery cycles

To examine the extent to which changes in membrane potential could contribute to the changes in the recovery cycle (the measure most distorted during hyperthermia), recordings were made while injecting depolarizing and hyperpolarizing currents to change membrane potential (Fig. 5.6). The effects of changes in temperature are generally explained by changes in Na^+ currents, but it is probable that an enhanced Na^+ current would produce a left-ward shift in the stimulus-response curve, rather than the trend for a shift to the right shown in Fig. 5.1A.

The reduction in refractoriness could occur with hyperpolarization of RMP, but the reduced superexcitability and early accommodation in depolarizing threshold electrotonus favour depolarization.

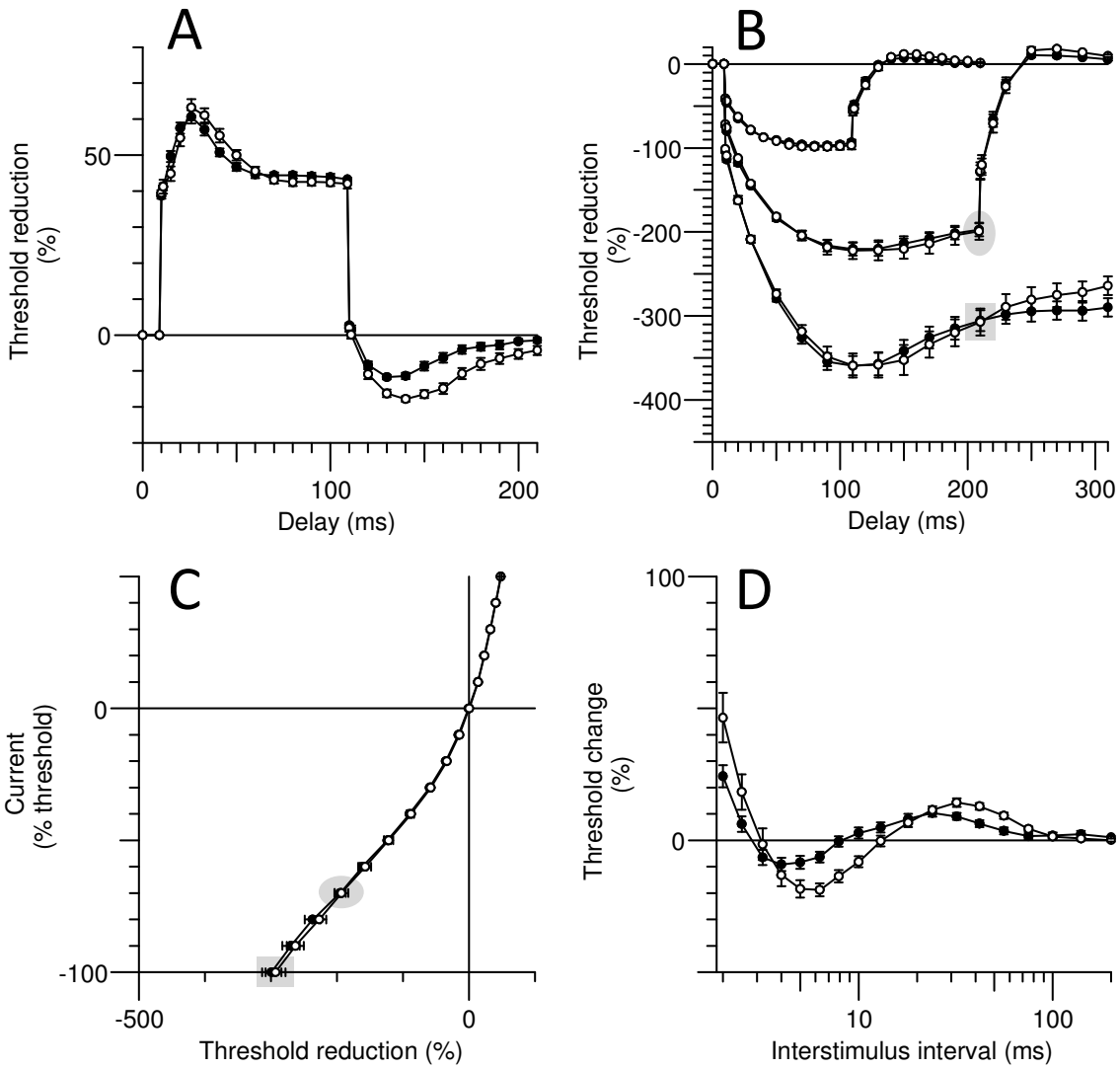

Figure 5.5. Sensory axon excitability during hyperthermia. Group data (n = 6, mean ± SEM), open circles represent measures at normal temperatures and filled circles during hyperthermia.

A. Depolarizing threshold electrotonus with a conditioning current of +40% of the control stimulus. **B.** Hyperpolarizing threshold electrotonus with currents -40, -70 and -100% of the control stimulus. **C.** Current-threshold relationship tested at the end of 200-ms long conditioning currents (+50% to -100% of control threshold). **D.** Recovery cycle after supramaximal stimulation.

The corresponding data points in threshold electrotonus (*B*) and the current-threshold relationship (*C*) are highlighted by the shaded ellipses and rectangles for hyperpolarization by -70 & -100%, respectively.

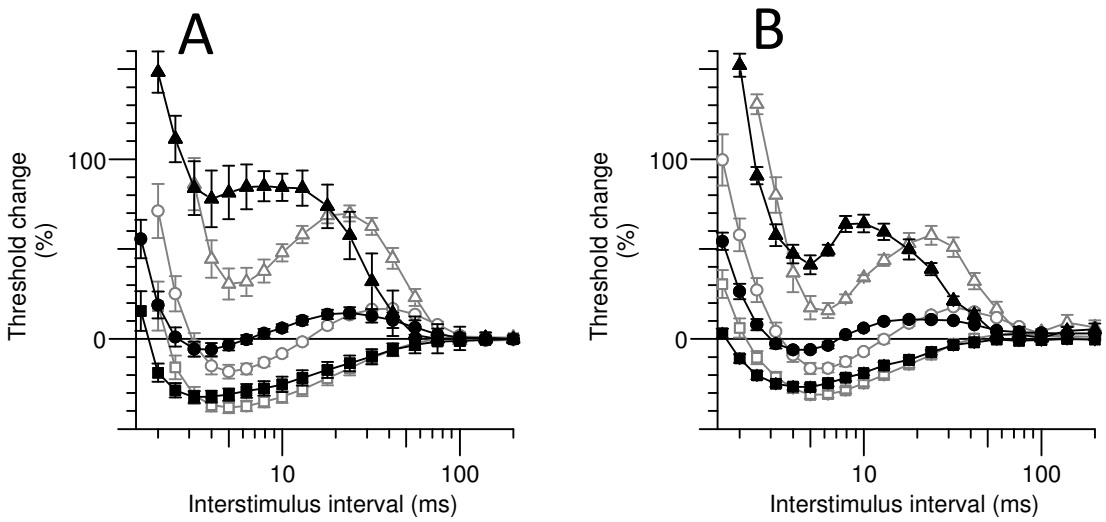

Figure 5.6. Polarized recovery cycles. Group data (n = 6; mean ± SEM). Recovery from activation during polarization (depolarization, triangles; hyperpolarization, squares) and without polarization (circles) at normal temperature (open symbols) and during hyperthermia (closed symbols). **A.** Motor axons. **B.** Sensory axons. The recovery cycle was measured 200 ms after the onset of a long conditioning pulse of strength +30% (depolarization; triangles) and -30% (hyperpolarization; squares) of the unconditioned test stimulus, respectively.

During depolarization (+30% threshold, approximately +1.2 mA for motor axons and 0.5 mA for sensory axons; triangles in Fig. 5.6) superexcitability was abolished in motor axons (Fig. 5.6A), and in five of the six subjects for sensory axons (Fig. 5.6B). The peak of subexcitability occurred earlier, as seen in hyperthermia ($p = 0.002$ for motor axons and $p = 0.04$ for sensory), but unlike hyperthermia, the extent of subexcitability was greater. These findings are similar to those of Kiernan and Bostock (2000). During hyperpolarization (-30% threshold, approximately -1.2 mA for motor axons and -0.5 mA for motor axons; squares in Fig. 5.6), the peak of superexcitability was larger and occurred at much the same conditioning-test intervals, while subexcitability was smaller and later. Hyperpolarization removes resting activation of K_s channels revealing recovery cycles that better represent the true extent of the decay of current through the Barrett-Barrett pathways (compare squares to circles in Fig. 5.6).

Data from recordings at the normal temperature and during hyperthermia (open and closed symbols, respectively, in Fig. 5.6) demonstrate that changes in membrane potential could not restore the normal recovery cycle during hyperthermia.

Modelling

The Bostock model as developed in Chapter 4 was used to interpret the hyperthermia-induced changes in motor and sensory axons. The average increase in skin surface temperature was 8.9°C, but the effects of hyperthermia were better modelled by an increase in nerve temperature of 6°C, the difference being an intuitively reasonable skin-nerve gradient during external heating. The rate constants of the gating processes in this model were increased according to the following Q10 values (Na^+ activation, 2.2; Na^+ inactivation, 2.9; fast K^+, slow K^+, I_h activation, 3) and a Q10 of 1.4 was applied to all of the maximal conductances (i.e. all voltage-gated ion channels, leak conductances and the Barrett-Barrett pathways through and under the myelin sheath).

Motor axons. Increasing the temperature by 6°C lowered the potassium equilibrium potential (E_K; -94.8 mV from -93 mV), and this would have resulted in hyperpolarization of RMP by 1 mV. In combination with the increased conductances (particularly G_{Ks}), the resultant hyperpolarization of RMP was 1.7 mV.

The combined effect of hyperpolarization of E_K and RMP, faster gating and larger conductances modelled well most of the hyperthermia-induced changes in the recovery cycle, accurately replicating the earlier relatively refractory period, earlier and reduced superexcitability and earlier (though reduced) late subexcitability. However the lesser inward rectification during both strong and long hyperpolarization in threshold electrotonus and the current threshold relationship could not be reproduced by these changes alone. The most parsimonious explanation for this unexpected and seemingly paradoxical finding is a reduction in I_h. Accordingly all parameters associated with I_h were varied, and the best fit was obtained with hyperpolarization of the half-activation voltage of I_h (by -11 mV). This additional change in gating has precedent, and its extent compares favourably with the reported temperature sensitivity of the voltage activation of the cardiac isoform (I_f) in sheep Purkinje fibres (Hart, 1983; -8 mV between 27.5 and 36.4°C; see Fig. 8A in that paper).

In addition, a constant (DC) ***depolarizing*** current of 20 pA at the internode improved the fit to hyperpolarizing threshold electrotonus, the current-threshold relationship and the recovery cycle during hyperthermia in motor axons (see Fig. 5.7). This depolarizing influence could reflect greater activity of slow internodally located HCN isoforms (see Chapter 4), and its extent may actually be greater than 20 pA because Na^+/K^+ pump activity probably increases, at least transiently, with elevated temperatures.

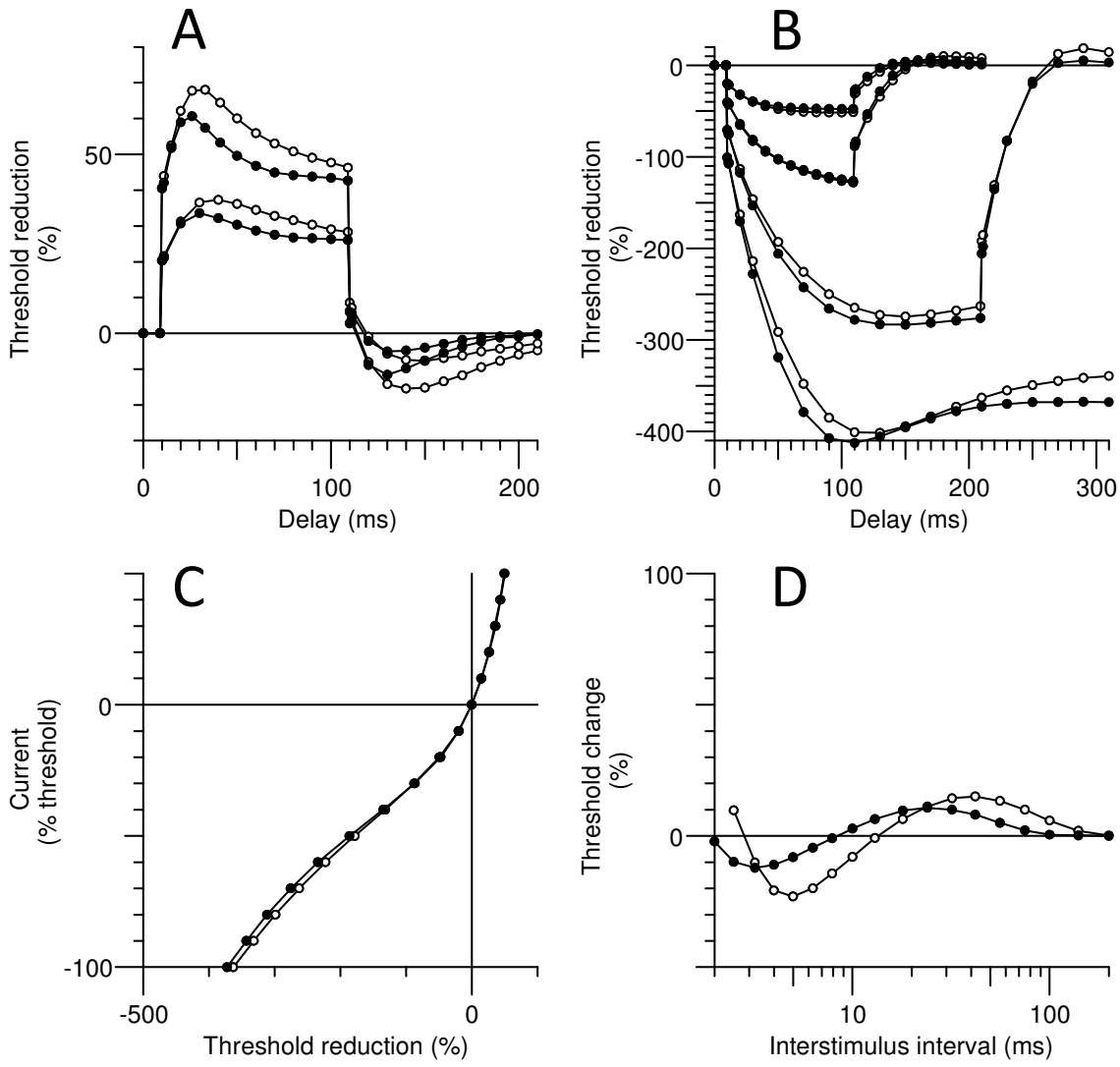

Figure 5.7.

Mathematical model of the hyperthermia-induced changes in excitability of motor axons. The open circles indicate the Bostock motor axon model at normal temperature, and the modelled changes during hyperthermia are shown as closed circles. Hyperthermia was modelled by an increase in temperature of 6°C (with the activation kinetics and maximum conductances increased according to their respective Q10s; see the Methods section), a hyperpolarization of the half-activation voltage of I_h (11 mV) and a small additional depolarizing current at the internode of 20 pA. **A.** Depolarizing threshold electrotonus for +40% and +20% of the control threshold. **B.** Hyperpolarizing threshold electrotonus (-20%, -40%, -70% and -100%). **C.** Current-threshold relationship. **D.** The recovery of excitability after a supramaximal stimulus.

It must be acknowledged however, that this constant depolarizing current is an approximation and, if indeed it does represent slow HCN isoforms, then it is also true that the current through a voltage-gated ion channel should diminish as the membrane potential approaches the equilibrium potential for HCN channels. The modelling suggests that the electrochemical driving force for HCN channels varies three-fold (and as a consequence the current through slowly gated channels) during threshold electrotonus and is ~-23 mV for the 40% depolarization and ~ -77 mV at the peak of the strongest hyperpolarization (-100%). This probably explains why a greater separation of the modelled normal and hyperthermic excitability exists at the end of the depolarizing threshold electrotonus (90-100 ms) than for the observed recordings (compare Figs 5.7A and 5.8A with Figs 5.2A and 5.5A, respectively). This apparent discrepancy provides further support for the possibility of slower isoforms of HCN channels on motor axons.

Sensory axons. Similarly the hyperthermia-induced changes in excitability were modelled well by an increase in temperature of 6°C, increased gating kinetics and maximal conductances (according to the Q10s), hyperpolarization of the voltage dependence of I_h (by -7 mV) and a constant (DC) current of 30 pA (see Fig. 5.8). It is noteworthy that, when normothermic, the voltage dependence of I_h in motor axons is likely to be some 13 mV more hyperpolarized than that of sensory axons (see Chapter 4), and this discrepancy would increase to ~17 mV during hyperthermia. The effect of hyperthermia on inward rectification in sensory axons was only apparent during strong and long hyperpolarization. The modelled hyperpolarization of the voltage dependence of I_h was therefore nearly perfectly balanced with any increase in I_h due to increased diffusion or faster kinetics.

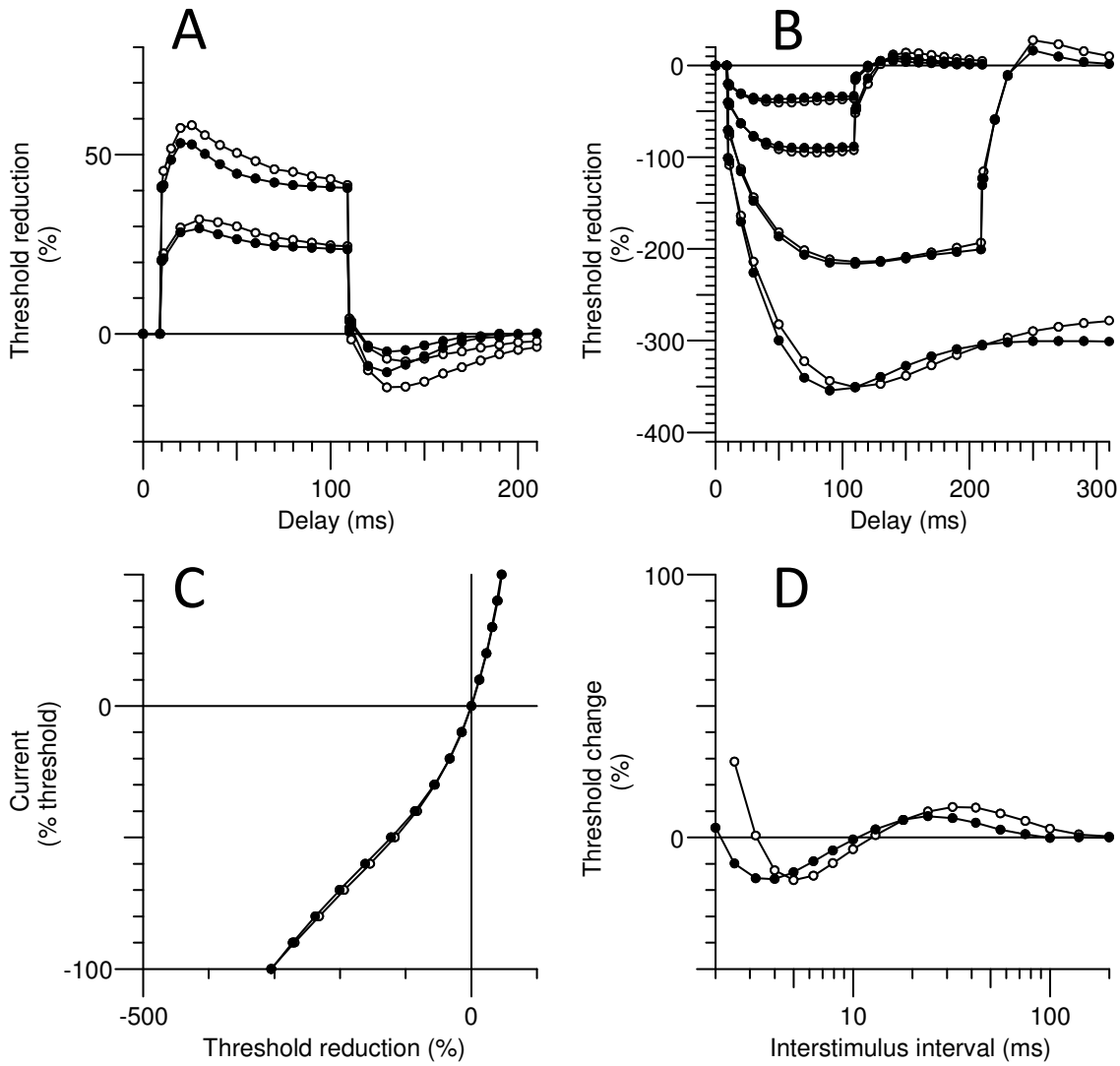

Figure 5.8.

Mathematical model of the hyperthermia-induced changes in excitability of sensory axons. The open circles indicate the Bostock model as modified for sensory axons (Howells *et al.* 2012), and the modelled changes during hyperthermia are shown as closed circles. Hyperthermia was modelled by an increase in temperature of 6°C (with the activation kinetics and maximum conductances increased according to their Q10s; see Methods section), a hyperpolarization of the half-activation voltage of I_h (7 mV) and a small additional depolarizing current of 30 pA. **A.** Depolarizing threshold electrotonus for +40% and +20% of the control threshold. **B.** Hyperpolarizing threshold electrotonus (-20%, -40%, -70% and -100%). **C.** Current-threshold relationship. **D.** The recovery of excitability after a supramaximal stimulus.

Discussion

In this Chapter the effects of focal hyperthermia on the excitability of human peripheral myelinated nerve have been studied for the first time. There are studies of nerve conduction during hyperthermia in human subjects (Rutkove *et al.*, 1997), but studies of the effect of temperature on the excitability of human axons have focussed on either cooling (Burke *et al.*, 1999) or small deviations around normal temperature (Kiernan *et al.*, 2001a; Maurer *et al.*, 2010), while, in the cat, there have been comparable studies of axonal excitability only during cooling (Moldovan & Krarup, 2004).

The action potential of mammalian myelinated axons can be modelled adequately incorporating only Na^+ channels into the model (Schwarz *et al.*, 1995), and the traditional view has been that the predominant effect of changes in temperature is likely due to changes in ion channel kinetics (Hodgkin & Huxley, 1952d; Schwarz & Eikhof, 1987; Burke *et al.*, 1999; Kiernan *et al.*, 2001a), and in particular those of Na^+ channels. This may be so for small changes in axonal temperature. While changes in Na^+ currents may well be the major factor shaping the action potential when temperature is close to normal, it is suggested below that other currents exert a greater influence with marked increases in temperature. These changes would reduce the safety margin for action potential generation and propagation, and would do so more for motor axons than sensory axons, impairing conduction and leading to fatigue in normal subjects and, particularly, in patients with diseases affecting central and peripheral axons.

Mechanisms underlying hyperthermia-induced changes in excitability

Resting membrane potential

Kiernan and Bostock (2000) found the sensitivity of the threshold for the half-maximal CMAP to polarization to be ~8% per mV, which when applied to the small increase in threshold during hyperthermia would suggest a hyperpolarization of 2.2 mV. Applying the same logic to the sensitivity of rheobase to changes in RMP gives a hyperpolarization of 2.1 mV. There is a dearth of literature on Na^+/K^+ pump functions in axons during heating, but a temperature-dependent increase in Na^+/K^+ pump activity could account for some of this hyperpolarization. Nevertheless our modelling suggests that the effects of temperature on the equilibrium potentials (in particular, E_K) and on diffusion through channels open at rest are sufficient to account for 1.7 mV of hyperpolarization.

The hyperpolarization of RMP suggested by the modelling findings needs to be reconciled with the lack of a significant hyperpolarizing change in the threshold, rheobase and shift in the SR curve. These findings are not in conflict: the modelling suggested an offsetting tonic depolarization (which could be due to internodally located slow HCN isoforms) which would rein in the hyperpolarization of RMP to ~0.6 mV. In any case, hyperpolarization by < 2 mV is small, less than the range of holding potentials that result in inactivation of 30% Na^+ channels (a surrogate for RMP) in experiments *in vitro* (e.g., -84 and -86 mV in studies on human sensory axons; Schwarz *et al.*, 1995) and well within the likely difference in RMP for human sensory and motor axons (3 – 4 mV; Chapter 4). A larger sample size may have yielded a statistically significant increase in the *unconditioned* threshold during hyperthermia, but the difference is likely to be small. The inability of polarization to restore normal

recovery cycles during hyperthermia supports the view that a change in RMP was not the primary driver of the observed excitability changes during hyperthermia. The effects of temperature on channel function are more likely to have a greater impact on excitability and the safety margin (see below) than the small change in RMP.

The recovery cycle

The changes in axonal excitability during hyperthermia affected particularly the recovery cycle, possibly reflecting a disturbance to the finely tuned mechanisms underlying action potential generation and propagation.

Refractoriness. The relative refractory period was shorter and refractoriness was reduced during hyperthermia, findings consistent with studies during cooling (where the opposite changes occur; Burke *et al.*, 1999; Moldovan & Krarup, 2004; Maurer *et al.*, 2010) or around 'normal' temperatures (Kiernan *et al.*, 2001a). Diffusion of Na^+ ions would be greater and activation of Na^+ channels would be faster with heating (Fig. 5.9). These changes would lead to an earlier onset of inactivation, accentuating any changes due to the kinetics of the inactivation gate. The changes in refractoriness are consistent with faster recovery from inactivation of Na^+ channels. However temperature-induced changes in K^+ currents would also affect refractoriness, much as they can superexcitability (see below).

Superexcitability. Superexcitability decreased during hyperthermia, a change unexpected from the earlier studies on human axons. Indeed, when the recovery cycle is normalised to the unconditioned threshold at 'normal' temperatures (dotted line in Fig. 5.2D), there is only a period of 'relative' superexcitability with a peak that is actually an *increase* in threshold by +10.3 ± 8.9%.

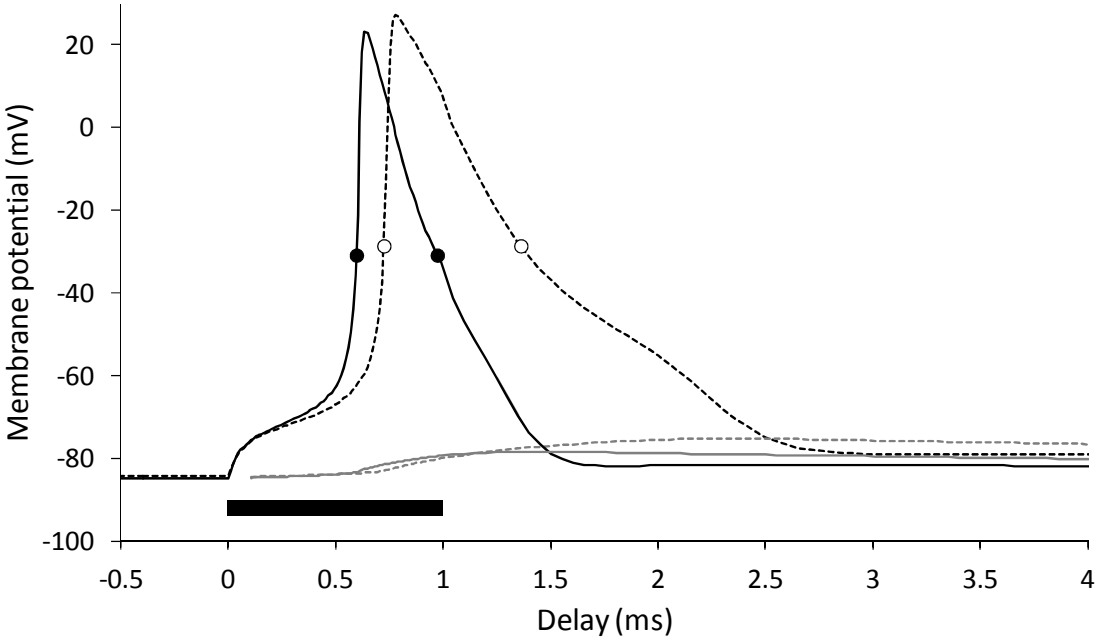

Figure 5.9. Modelled action potential during hyperthermia. Nodal (black) and internodal (grey) membrane potentials during hyperthermia (solid lines) and at normal temperature (dashed). Measurements of the half-maximal action potential width were made and are indicated by circles for hyperthermia (0.38 ms; filled) and normal temperature (0.64 ms; open). The solid bar depicts the stimulus duration.

Increased diffusion through the paranodal seal during hyperthermia would serve to *increase* superexcitability. Decreased superexcitability could be due to a narrower action potential (Fig. 5.9), resulting in reduced charging of the capacitance of the internodal axolemma (Mitrović *et al.*, 1993; Honmou *et al.*, 1994; Vogel & Schwarz, 1995; Kiernan *et al.*, 2001b; McIntyre *et al.*, 2002; Chapter 4), but the modelling suggests that enhanced K^+ currents are more likely to be responsible for the observed changes in superexcitability. By themselves increased diffusion through Na^+ channels (transient and persistent) and their faster kinetics would result in a *wider* action potential, but increases in the potassium currents would provide a dampening effect on the depolarizing after-potential (David *et al.*, 1995), counteracting any increases in the Na^+ current. Figure 5.9 shows the modelled membrane potential changes for a motor axon during hyperthermia in response to a 1-ms test stimulus. The action potential half-width (measured halfway between RMP and the peak of the action potential) decreased from 0.64 ms to 0.38 ms for normal and hyperthermic temperatures, respectively, corresponding to a Q10 of 2.4.

Late subexcitability. The peak of late subexcitability was earlier but its area was not significantly different at hyperthermic temperatures. Late subexcitability reflects after-hyperpolarization due to the decaying activation of K_s channels (Baker *et al.*, 1987; Bowe *et al.*, 1987; Stys & Waxman, 1994; David *et al.*, 1995; Bostock *et al.*, 1998). The earlier peak during hyperthermia is probably due to faster K_s kinetics. The lack of difference in the magnitude of late subexcitability may be due to opposing influences on K_s currents: hyperthermia will increase the K_s conductance, but this would hyperpolarize RMP, resulting in a smaller electrochemical gradient for K^+ currents.

Accommodation to long-lasting depolarization

There was no significant difference in the excitability during the first 10 ms of depolarizing threshold electrotonus during hyperthermia and at normal temperatures (Fig. 5.2A), as would be expected if hyperthermia led to faster activation of K_f channels. However Baker and colleagues (1987) have shown that the fast outward rectification due to K_f currents would occur within the first millisecond at 30°C (see Fig. 5A in Baker *et al.*, 1987) and presumably faster at warmer temperatures. Additionally, a similar increase in the maximal conductances of Na^+ and K_f channels during hyperthermia could cancel any effect during early depolarizing threshold electrotonus. Increased diffusion through, and faster kinetics of, slow potassium (K_s) channels during hyperthermia can be seen in the faster accommodation to depolarizing currents, sufficient to limit the peak depolarization. The reduced peak depolarization would result in a smaller K_s current and correspondingly a smaller threshold undershoot when the polarizing current ends (Schwarz *et al.*, 2006). The primary effect of hyperthermia is on the *kinetics* of K_s, and the current will be enhanced only if the overall depolarization is the same or greater.

The hyperpolarization-activated cation conductance, I_h

Unexpectedly, inward rectification was reduced during hyperthermia (Fig. 5.2B, Table 5.1). If the diffusion through I_h channels and their activation increase with temperature, one would expect greater inward rectification with heating. The reverse was seen. The modelling suggests that this apparent paradox can be resolved by hyperpolarization of the voltage dependence of I_h channels and the addition of a small steady depolarizing current. The effects of temperature on the activation kinetics of voltage-gated ion channels have been well studied, but less is known about the effect of temperature on their voltage dependence. However, Hart (1983) reported a similar temperature dependence of the half-activation voltage of the cardiac isoform, I_f, in

sheep Purkinje fibres. The voltage dependence of other channels could be similarly altered (Thomas *et al.*, 2009), but the present study provides no compelling reasons for postulating such a change. The temperature dependence of HCN channels may involve the voltage sensor directly or indirectly via allosteric activation (Pian *et al.*, 2006; Pian *et al.*, 2007; Börjesson & Elinder, 2008). Some regulators of HCN channels can shift the voltage dependence of HCN channels by up to 50 mV (reviewed in Biel *et al.*, 2009), and it is likely that the potential modulation of HCN channels is greater than occurs with other channels.

The modelling suggests that the reduced inward rectification seen in Figs 5.2 and 5.5 may be accompanied by greater activity of slow internodally located isoforms of I_h. This implies, first, that human axons are likely to express more than one HCN isoform, secondly, that current techniques document the properties of only the faster isoform(s) and, thirdly, that hyperthermia may have different effects on different isoforms. A review of the literature revealed no data to support the latter speculation.

The role of K^+ channels in hyperthermia

Changes in K_s currents appear to be a major factor affecting excitability during hyperthermia, responsible for faster accommodation to depolarizing currents, the reduced super- and earlier late sub-excitability and possibly contributing to the shorter RRP, as discussed above. Sittl and colleagues (2010) tested axonal excitability in myelinated axons of rat sural nerve with the K_v7 (K_s) channel opener flupirtine, and reported increased threshold, reduced refractoriness and increased superexcitability, all consistent with hyperpolarization of RMP. In contrast the present study found reduced superexcitability, probably due to faster activation kinetics of both K_f and K_s channels.

Greater access to K_f channels at the paranode during hyperthermia. Increased diffusion through the paranodal seal to the periaxonal space could have an effect on excitability analogous to that of paranodal demyelination or a loosening of the myelin sheath attachment (Cappelen-Smith *et al.*, 2001; Nodera *et al.*, 2004; Stephanova & Daskalova, 2005). If so this could jeopardize action potential generation, thereby predisposing to conduction block, much as seen in those clinical studies.

Variability of hyperpolarizing threshold electrotonus measures

Tomlinson and colleagues (2010a) examined the inter- and intra-subject variability of measures of hyperpolarizing threshold electrotonus and found that despite these measures appearing variable, that they are actually characteristic of an individual. The data in the present study suggests that the variability of hyperpolarizing threshold electrotonus measures is greater in experiments performed on different days than those in the same session. This is perhaps unsurprising given the number of modulators of HCN channel function, but it does have implications for studies which aim to compare hyperpolarizing threshold electrotonus on different occasions.

Clinical implications

The change in excitability in both sensory and motor axons during hyperthermia is the product of several mechanisms, all of which have implications for the security of conduction.

Safety margin and conduction block. Any reduction in the safety margin for action potential generation during hyperthermia may be of functional significance in healthy motor axons (see below, 'Fatigue'), but is likely to be even more important for already impaired axons. The results of the present study suggest four mechanisms for a deterioration of the safety margin during hyperthermia. First, at rest, motor axons are probably hyperpolarized 3 - 4 mV relative to sensory axons (Chapter 4), and even slight

hyperpolarization during hyperthermia would induce conduction block more readily in motor axons than sensory. Second, the voltage dependence of HCN channels in motor axons is also more hyperpolarized than in sensory axons (Chapter 4), and the further hyperpolarization during hyperthermia, would render them less able to counter activity-dependent hyperpolarization, making motor axons even more vulnerable to conduction block. Third, our modelling suggests that faster channel kinetics during hyperthermia will result in a narrower action potential (Fig. 5.9), such that the time integral of the driving current for the action potential would be reduced. Finally, the narrow action potential would result in reduced charging of the internodal axolemma (Fig. 5.9), affecting superexcitability and the ability to transmit high firing frequencies (see below).

Fatigue. Both central and peripheral mechanisms contribute to the development of fatigue in healthy subjects (Gandevia, 2001) and fatigue can arise from defects at a number of levels in those affected by neuromuscular disease or febrile illness (Friman *et al.*, 1977; Thomas & Zijdewind, 2006).

Todd and colleagues (2005) proposed that during hyperthermia achieving maximal force could impose a greater impulse load because a higher motor unit firing frequency would be required to achieve twitch fusion. This would require greater inward rectification to counter the greater activity-dependent hyperpolarization. However the ability to mobilize at least some HCN isoforms underlying I_h appears to be impaired by hyperthermia. As noted above, the reduction in superexcitability seen in the current study may also contribute to the failure of motor axons to achieve transient high firing rates of 50 – 200 Hz during hyperthermia. This could limit the ability of the motor axon to transmit action potentials at 50 - 200 Hz through branch points into nerve terminals (Adrian & Lucas, 1912; Swadlow *et al.*, 1980; Zhou & Chiu, 2001;

Debanne *et al.*, 2011). Symptoms of fatigue in neuromuscular disease are often exacerbated by elevated temperatures. Exercise and heat are both recognised triggers of fatigue in sufferers of multiple sclerosis with already impaired safety margins (Uhthoff's sign; Guthrie & Nelson, 1995; Vucic *et al.*, 2010), and exercise may accentuate weakness in chronic inflammatory demyelinating polyneuropathy and multifocal motor neuropathy due to the development of activity-dependent conduction block (Cappelen-Smith *et al.*, 2000; Kaji *et al.*, 2000). Even in amyotrophic lateral sclerosis with primarily lower motor neurone involvement, surviving motor axons may suffer from greater activity-dependent hyperpolarization because they are required to maintain an increased impulse load (Vucic *et al.*, 2007).

Fever is a common feature of infectious diseases, such as influenza. Friman and colleagues (1977) reported increased 'jitter' in single-fibre EMG recordings in patients suffering from influenza. They attributed this to hyperthermia-induced blockade of neuromuscular transmission, but the current study provides support for the possibility of branch-point failure due to reduced excitability and a reduction in the safety margin for action potential propagation during hyperthermia.

Chapter 6

I_h and resonance in human axons

The work in this chapter is in preparation for submission to the Journal of Physiology.

Summary

Subthreshold oscillations and resonance underlie essential rhythmic activity in many central neurons. In large myelinated sensory and motor axons of the peripheral nervous system these oscillations can result in paraesthesiae and fasciculations, respectively, particularly following ischaemia and activity. In addition I_h has been implicated in the phenomena associated with neuropathic pain.

The existing evidence points to a greater activity of I_h in sensory axons than in motor, contributing perhaps to the greater susceptibility to paraesthesiae than fasciculations.

The present study has examined the role of I_h in subthreshold oscillations in human motor and sensory axons. A novel application of frequency-domain techniques to human axonal excitability has been used to resolve further the relative contributions of I_h and the slow-potassium current (I_{Ks}). The response to oscillatory input currents was tested between 'DC' and 16 Hz, and a sharp resonant peak at ~ 2 to 2.5 Hz was found in the response of hyperpolarized axons. A smaller and broader response was found in axons at rest demonstrating voltage dependence for the frequency response. The excitability models from Chapter 4 provided a good fit to the frequency response for human axons, and were further used to explore the determinants of resonance. The modelling suggested that the differences between the frequency responses of motor and sensory axons were best explained by the differences documented in Chapter 4: reduced G_{Ks}, up-modulation of I_h and increased I_{NaP} (due to depolarization of RMP) in sensory axons, thereby validating the earlier findings.

Introduction

Axonal excitability studies use threshold-tracking techniques to probe the biophysical determinants of excitability using square pulses that are either subthreshold and long-lasting, or brief and at or above threshold. The contribution of the inwardly rectifying current, I_h, is only seen in these studies with the accommodation to hyperpolarization, and as has been shown in Chapters 4 and 5 requires long and strong hyperpolarization before it can really begin to be appreciated.

The accommodation to hyperpolarization is impacted upon by several conductances. Over the voltage range in which they overlap changes in the rectifying conductances G_{Ks} and G_H have a synergistic effects. Hyperpolarization of the membrane potential leads to a lessening of the hyperpolarizing conductance G_{Ks} and an increase in the depolarizing conductance G_H, with the net effect being a relatively depolarized current countering the hyperpolarization.

The disentanglement of the relative contributions has traditionally focussed on the overall picture of excitability, with the effects of G_{Ks} also present in the accommodation to depolarizing currents and in the slow relaxation of membrane potential in the late subexcitable period following an action potential. To complicate the picture further, it is difficult to separate the leak conductance from these slow-rectifying currents. Nonetheless, this 'whole of excitability' approach has allowed the development of mathematical models which have been successful in describing the biophysical basis of axonal excitability in health and a variety of disease processes.

The primary objective of the present study was to test these models using an independent paradigm, which adds the dimension of frequency to excitability studies. In addition, this study sought to determine whether myelinated human axons exert a frequency preference, and if so the basis of such activity.

The use of frequency as a probe of structure and function is well established. Cole and Curtis (1936) described the impedance of nerve and muscle in terms of an equivalent electrical circuit consisting of a parallel resistance and capacitance, and this model was later extended on functional grounds to include an inductive element to explain the rectifying properties of axon membranes (Cole, 1941; Cole & Baker, 1941).

Puil and colleagues (1986) introduced a frequency probe, which they called the ZAP (Impedance[**Z**] **A**mplitude **P**rofile) as an efficient means to probe the passive and active properties of trigeminal root ganglion neurons in guinea pigs. The ZAP is essentially a small amplitude sinewave current whose instantaneous frequency is continuously increased from start to end. The response voltage to such a current will reflect the functional requirements of the excitable tissue and ultimately will depend upon the particular membrane structure and the composition and state of the ion channels present (Llinás, 1988; Hutcheon & Yarom, 2000).

Using this technique studies have focussed on the low-frequency subthreshold resonance that underlie the θ-rhythms in central neurons (Hutcheon *et al.*, 1996b; Pike *et al.*, 2000; Hu *et al.*, 2002; Wang *et al.*, 2006; Hu *et al.*, 2009a; Zemankovics *et al.*, 2010). Hu and colleagues (2002) found θ-resonances occurred at hyperpolarized and depolarized membrane potentials mediated by HCN and K_S channels,respectively, which they termed H- and M-resonances.

Through the mechanisms of facilitation and depression, synapses act as bandpass filters selectively transferring information from a presynaptic neuron to multiple postsynaptic targets (Markram *et al.*, 1998). Izhikevich and colleagues (2003) have suggested that further trans-synaptic selectivity may be achieved by considering the resonant frequency of the post-synaptic targets. Bursts of action potentials at

frequencies outside the resonant bandwidth are likely to attenuated reducing their likelihood of further transmission.

In the peripheral nervous system subthreshold membrane potential oscillations can contribute to triggering the ectopic discharges in afferents responsible for neuropathic pain (Devor, 2006) and HCN channels have been linked to this pathophysiology (Chaplan *et al.*, 2003; Jiang *et al.*, 2008a; Jiang *et al.*, 2008b; Wickenden *et al.*, 2009).

In the present study a new protocol was developed which allowed the examination of the frequency-dependent response of human axons to subthreshold oscillatory currents. Hyperpolarized motor and sensory axons exhibited a sharp resonant peak at ~2 Hz, with a reduced response to oscillatory inputs at resting membrane potential. The excitability models developed in Chapter 4 provided a good fit to observed data, and were subsequently used to explore the basis of human axons to oscillatory inputs. The differences in frequency response between motor and sensory axons can be best explained by their underlying differences in K_s conductance, up-modulation of I_h and the increase of I_{NaP} (secondary to depolarization of RMP).

Methods

Twenty-four experiments were performed on six subjects. Each experiment lasted ~ 2 hours and they were on separate days. The subjects provided written consent prior to the study, which was approved by the Human Research Ethics Committee of The University of Sydney and conformed to the *Declaration of Helsinki*.

The ZAP protocol was developed in QtracS, and synchronized the delivery of the stimulus command signals with the acquisition of the compound action potentials via a data acquisition system (PCI-6221, National Instruments, Austin, TX). The compound action potentials were amplified using the amplifier developed in Chapter 3, and mains

frequency noise was removed using a Humbug Noise Eliminator (Quest Scientific, Vancouver) before being digitized by the data acquisition system.

The ZAP protocol was applied to motor and sensory axons of the median nerve at the wrist. The pulse protocols in the present study required the delivery of long subthreshold pulses, which necessitated the optimisation of stimulation conditions. Skin surface impedance at the stimulus sites was reduced using abrasive tape (Red Dot Trace Prep, 3M), followed by cleaning with an alcohol swab. The optimal cathode location (at the wrist) was sought using a saline-soaked, gauze-covered electrode before applying the final stimulation cathode. Disposable self-adhesive Ag/AgCl electrodes (Unilect 1010M) were used for stimulation, ground and EMG recording electrodes. The anode was remote from the median nerve, approximately 10 cm proximal to the cathode and toward the radial edge of the forearm. Compound muscle action potentials (CMAPs) were recorded from the thenar eminence, with the reference electrode on the distal phalanx of digit 1. Self-adhesive Ag/AgCl ring electrodes (RE-D, Electrode Store) were used for recording digital compound sensory action potentials (CSAPs), with the active electrode on the proximal phalanx of digit 2, and the reference 4 cm distal (Eduardo & Burke, 1988). The ground electrode was placed on the dorsum of the hand for both motor and sensory recordings. Skin temperature was monitored using a thermistor (YSI-409B) located close to the site of stimulation and recordings began when the temperature was stable and above 32 °C.

'Threshold ZAP' protocol

A threshold analogue of the ZAP technique introduced by Puil and colleagues (1986) was developed for these experiments to enable the *in vivo* study of the frequency response of human axons. This protocol utilises (but does not require) the empirical observation of Bostock and Baker (1988) that the excitability changes to subthreshold

polarization (threshold electrotonus) mirror the underlying changes in electrotonic membrane potential.

The threshold to various conditioning currents was tested using a 1-ms test pulse, with the aim of minimising test stimulus intensities, conditioning currents, and therefore pulse energies. As with other threshold-tracking studies, and as outlined in Chapter 2 the stimulus-response relationship established the tracking target (50% of maximum in this instance) that was used for the rest of the protocol.

The 'threshold ZAP' protocol measures the response to a linear 'chirp' signal (or swept sinewave), whose frequency is increased linearly from DC to 16 Hz over 4000 ms and whose amplitude is a fixed fraction of the unconditioned threshold (see blue curve on left hand side of Figure 6.1), and is described by the equation:

$$ZAP(t) = a \sin\left(\pi \frac{16}{4} \left(\frac{t}{1000}\right)^2\right)$$

where, a is the amplitude of the chirp (-10% in Figure 6.1, beginning downwards) and t is the time in milliseconds.

To examine the role of I_h in the frequency response of human axons, the ZAP signal was superimposed on a hyperpolarizing current of 60% of the control threshold (red curve on the left hand side of Figure 6.1). This was considered the strongest level of hyperpolarization achievable without unintended stimulation of axons by the supposedly subthreshold current (see Chapter 4), and is likely to be strong enough to exclude significant involvement of K_s channels, which might otherwise contribute to low-frequency attenuation (see Fig. 4.7).

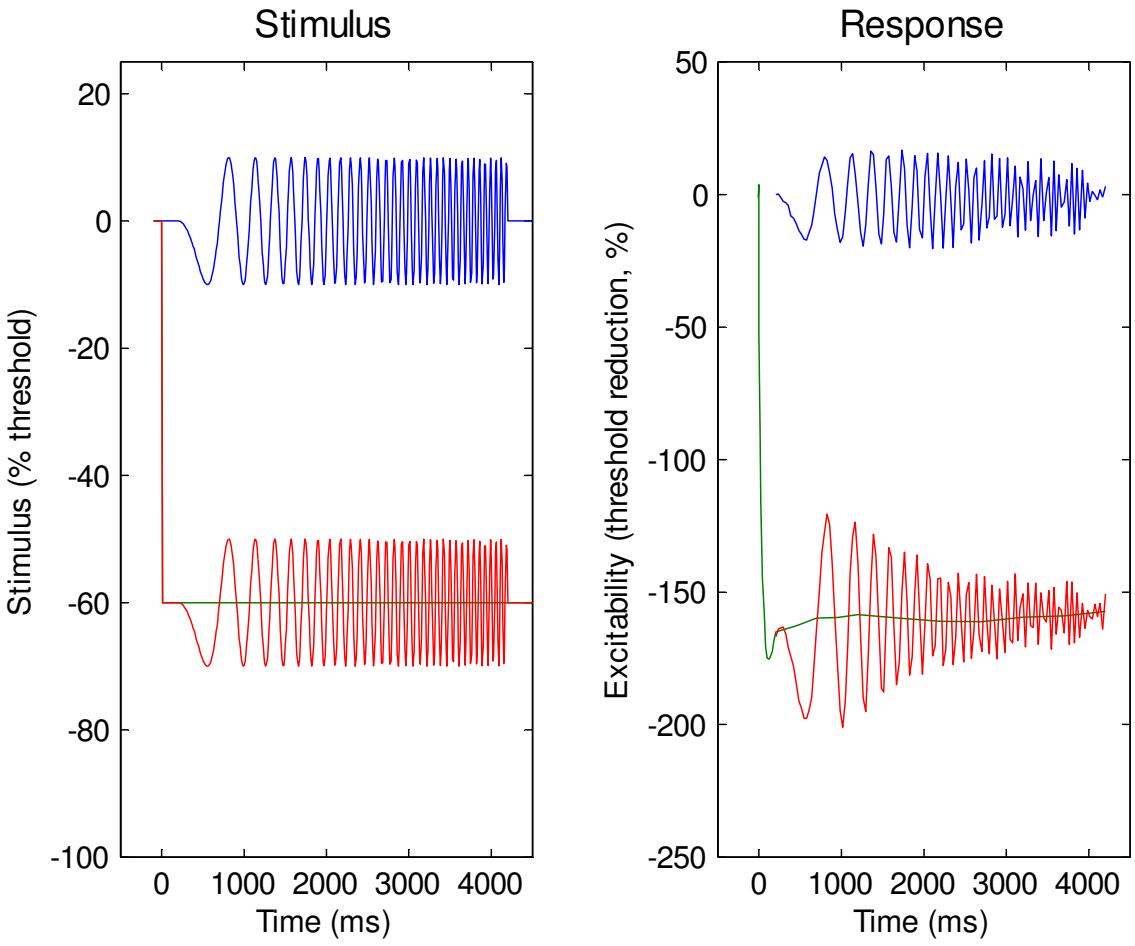

Figure 6.1. ZAP protocol. 4000-ms long sinusoidal conditioning stimuli with linearly increasing frequency and amplitude of 10% were used to study the frequency response at rest (blue) and with 60% hyperpolarization (red). Concurrent measurements of threshold electrotonus were made for the 60% hyperpolarization (green). Small perturbation conditioning currents on the left, and the measured excitability (plotted as a reduction in threshold) on the right.

The ZAP started 200 ms after the onset of the constant polarization. This delay was sufficiently long to be after the majority of the 'fast' accommodation and was chosen because it corresponds to the time delay used by conventional I/V measurements (from which the threshold conductance is estimated, see Chapter 2 and Fig. 2.6).

The amplitude of the ZAP was chosen to be sufficiently large to give a good signal-to-noise ratio (SNR), but small enough to maintain linearity of the response (Koch, 1984).

Preliminary observations using ZAP amplitudes of 10% and 30% of the control threshold gave similar frequency-response curves. The resolution of phase is improved with the 30% amplitude, particularly with high frequencies where the attenuated response lessens the SNR and the frequency approaches the Nyquist limit (half the sampling frequency). The linearity of the underlying membrane potential response was assessed at a hyperpolarization of -60% (of the control threshold) using the mathematical model developed in Chapter 4 and is shown in Figure 6.2. The maximal peak-to-peak deflections were 9.6 and 28.3 mV for the 10% and 30% ZAPs respectively (upper plots in Fig. 6.2).

A measure of the nonlinearity of the response was made by averaging the responses to the negative (green) and positive (red) ZAPs and subtracting the electrotonic response (blue traces in upper plots of Fig. 6.2). The peak nonlinearity occurred between the peak deflections at a time corresponding to 1.9 Hz for both amplitudes and was 0.1 and 1 mV for the 10% and 30% ZAPs respectively (lower plots in Fig. 6.2). Consequently, the 10% ZAP amplitude was chosen for the study as it struck the best balance of nonlinearity and signal-to-noise ratio with modelled peak-to-peak deflections falling below the 20-mV criterion for linearity established by Hutcheon and colleagues (1996b).

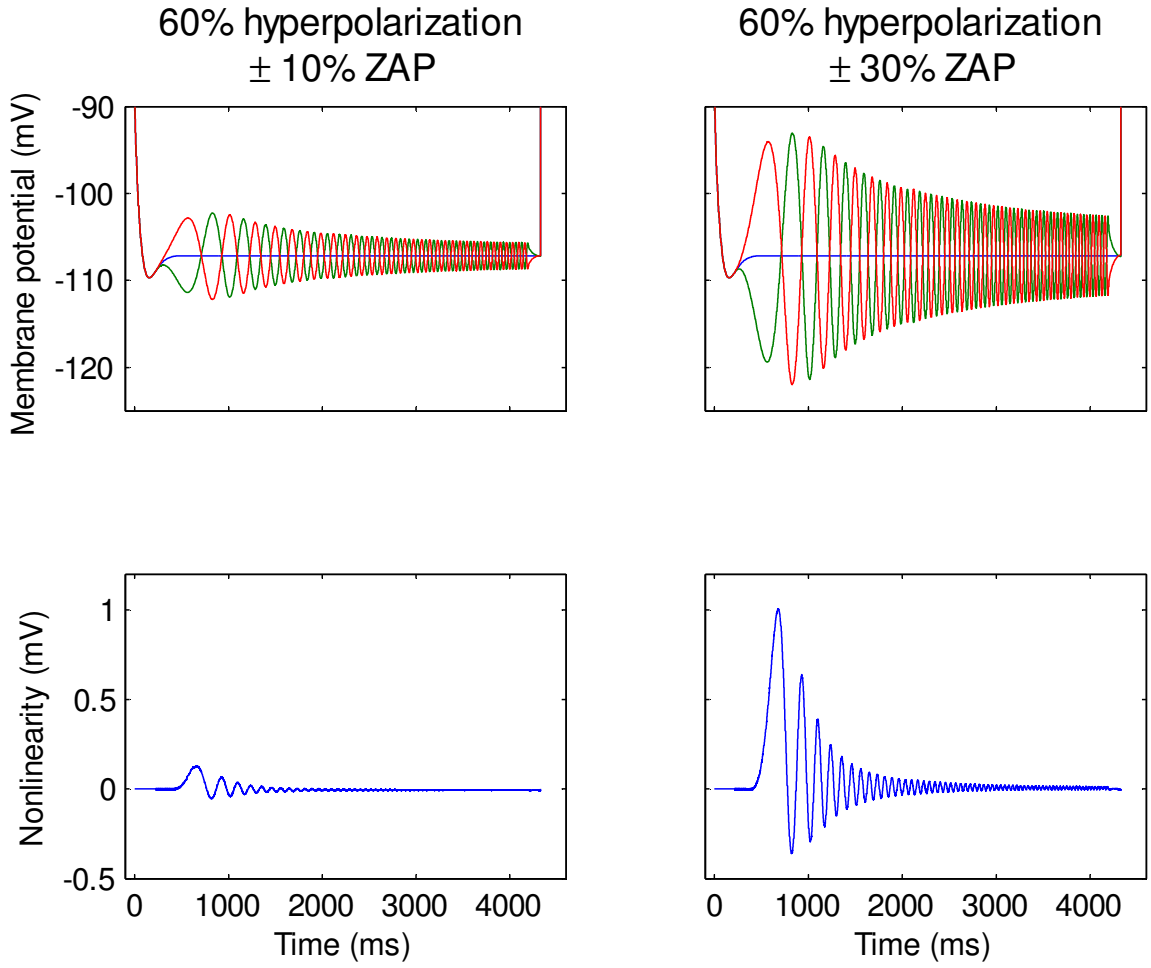

Figure 6.2. Linearity of stimulus protocol. Modelled changes in membrane potential for motor axons with 60% hyperpolarization and two sizes of ZAP amplitude: ±10%, left; and ±30%, right. The nonlinearity was assessed as the difference between the average response of the upward- (red) and downward-going ZAPs and the underlying threshold electrotonus response (blue). For both ZAP amplitudes, the first (positive) peak occurred at 1.8 Hz, and the second (negative) peak occurred at 2.5 Hz.

The underlying threshold electrotonus in response to polarization was recorded in detail during the period of 'fast' accommodation and then more slowly at time points corresponding to every 500 ms during the ZAP current (see green threshold electrotonus response on right hand side of Figure 6.1).

The entire protocol was balanced to prevent polarization of the electrodes and resting membrane potential. On the sweep following every conditioning stimulus an 'anti-stimulus' was delivered which was equal in magnitude but opposite in polarity.

The stimulus threshold was sampled 128 times every 31.25 ms (32 Hz) during the 4000 ms ZAP current, to facilitate the analysis using the Fast Fourier Transform (FFT) technique.

Analysis of Frequency-response curves

In the time domain, the threshold was tracked 128 times at evenly-spaced conditioning test intervals of 31.25 ms throughout the ZAP.

As in the calculation of threshold electrotonus, the excitability at each time point was calculated as the normalised threshold reduction:

$$excitability\ (threshold\ reduction, \%) = \frac{threshold_{control} - threshold_{ZAP}}{threshold_{control}}$$

The analysis of frequency response was performed offline, using a custom script written in Matlab (R2012a). For the recordings made with polarization, the effects of threshold electrotonus were first subtracted from the ZAP response. Any residual trend in the ZAP response was removed prior to conversion to the frequency domain using a FFT.

Typical power spectra for the ZAP stimulus (input) and response (output) are shown in Figure 6.3 and were calculated from the FFTs of the data displayed in Figure 6.1.

In a manner analogous to that introduced by Puil and colleagues (1986), a new measure, $Z_{threshold}$ relating the response (excitability) to input waveforms was constructed as follows:

$$Z_{threshold} = \frac{FFT(excitability)}{FFT(input)}$$

$Z_{threshold}$ is a complex-valued data set with real (resistive) and imaginary (reactive) components, and is the threshold analogue of impedance. The phase of the threshold impedance ($\phi_{threshold}$) represents the difference in phase between the response and input waveforms.

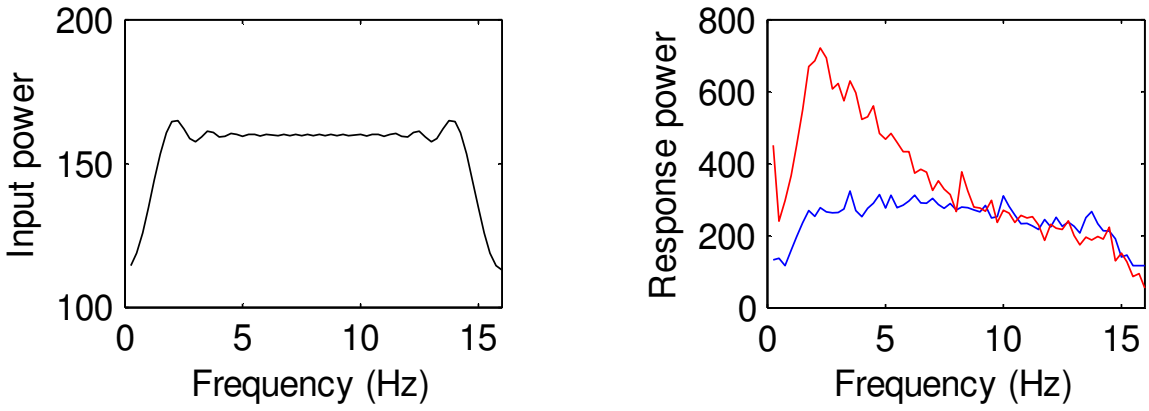

Figure 6.3. Power spectra of input currents and output responses (from data in *Fig. 6.1*). The linearly increasing ZAP input has equal power across its frequency range seen in the plot of input power. The resonant peak during hyperpolarization is seen as a peak in the response power at approximately 2 Hz (red trace). Note the sampling limitations give the false impression that there is a drop off in the input power at both ends of the frequency spectrum.

The frequency response curve was constructed by plotting the magnitude of the threshold impedance ($|Z_{threshold}|$) versus frequency, from which the spectral parameters: $Z_{0.5}$, Z_{max}, f_{max} and Q were calculated. Using the definitions from earlier studies (Hutcheon *et al.*, 1996b; Orio *et al.*, 2009; Zemankovics *et al.*, 2010): $Z_{0.5}$ is defined as the impedance at 0.5 Hz; Z_{max} and f_{max} are the maximum impedance and corresponding frequency; and Q the ratio of Z_{max} to $Z_{0.5}$.

Modelling

The mathematical models of human motor and sensory axons developed in Chapter 4, and used in Chapter 5, were used to examine the basis of the low-frequency response of human motor and sensory axons. The models were subjected to the same ZAP protocol, with the exception that the target threshold was defined as the minimal threshold to generate an action potential.

Excitability clamping

Baseline changes in excitability due to alterations in model parameters were compensated for by clamping the baseline excitability (or threshold reduction). The clamping was achieved by adjusting the strength of the DC hyperpolarizing current to match the baseline excitability recorded using the control model. This procedure is analogous to the manual adjustment of the injected DC current to maintain background membrane potential, particularly when channel blockers are used in cellular studies (Orio *et al.*, 2009; Zemankovics *et al.*, 2010).

Alterations in model parameters which resulted in much larger oscillations of excitability were accounted for by decreasing the ZAP amplitude in order to maintain linearity of the response.

Results

Twenty-four experiments in six subjects were performed on separate occasions using the new resonance protocol, which was well tolerated by all subjects. Even though the protocol was balanced and should not have any long-term effect on axonal excitability, the recordings were made on different days.

In vivo measurement of frequency response in human axons

Balancing the stimulation protocol led to a near doubling of the recording time, but prevented the polarization of the electrodes and damage to the skin. Most protocols were complete within 2 hours, and in recordings with good signal-to-noise ratios the tracking was faster and the studies were complete within 1.5 hours.

Excitability (measured as reduction in threshold) is an effective *in vivo* measure of the response to an input current, but unlike studies of resonance and the frequency preference in cells (Puil *et al.*, 1986; Puil *et al.*, 1988; Puil *et al.*, 1994; Hutcheon *et al.*, 1996b; Hu *et al.*, 2002; Wang *et al.*, 2006; Orio *et al.*, 2009; Zemankovics *et al.*, 2010), the time taken to record each data point is significantly longer, thereby imposing a limit on both the frequency resolution and the maximal frequency recorded. Figure 6.4 shows that despite these challenges a resonant peak was clearly visible in all recordings, and the peak was particularly evident for hyperpolarization (shown in black).

Frequency-response curves

The individual responses to the unpolarized ZAP current are shown in Figure 6.4 (top row, red traces), and their near perfect superimposition shows little variation between subjects in both motor and sensory axons. The response to hyperpolarization however, shows an underlying variation in the baseline or 'threshold electrotonic'

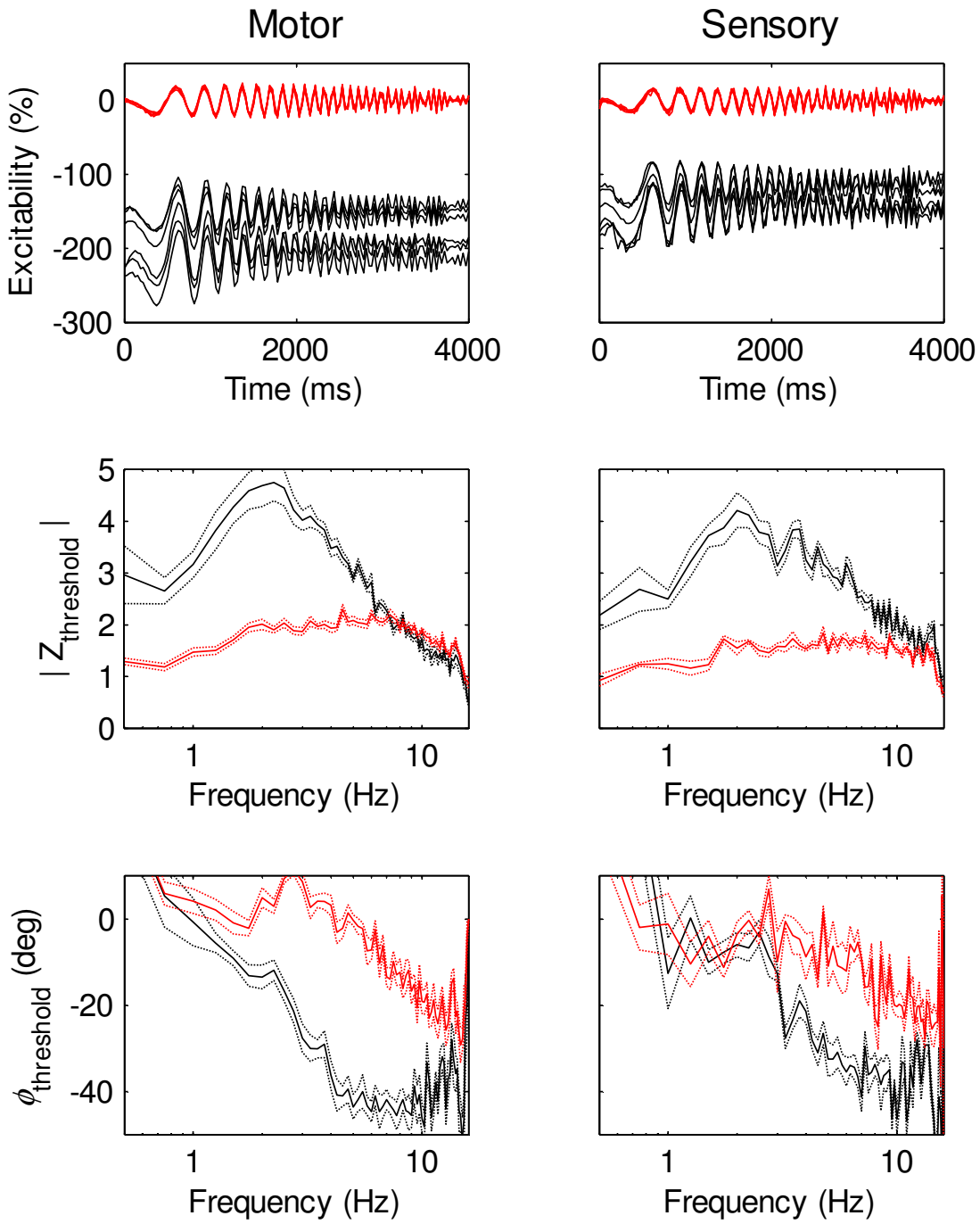

Figure 6.4. Excitability changes in response to ZAP conditioning.

Upper Row. Superimposed responses of the six subjects at rest (red) and with hyperpolarization (black) in motor and sensory axons. **Middle Row.** Mean (± SEM) magnitude of threshold impedance versus frequency (n = 6). **Bottom Row.** Mean (± SEM) phase lag of response behind input (note that between 2 & 4 Hz in motor axons at rest the response appears to lead the input).

response, which was -180 ± 13% (range: -222 to -144) in motor axons and -135 ± 8% (range: -154 to -113) in sensory axons. The lesser hyperpolarization in sensory axons and the variability of the threshold electrotonic baseline confirms earlier findings (Bostock *et al.*, 1994; Lin *et al.*, 2002; Tomlinson *et al.*, 2010a) and the results of Chapters 4 and 5. This enhanced variability with hyperpolarization probably contributes to the greater variability of the resonant peak in the hyperpolarized axons seen in the threshold impedance plots of Figure 6.4 (middle row), and the derived parameter Z_{max} in Table 6.1 (compare variation in Z_{max} at 60% vs 0%).

In the hyperpolarized axons of both motor and sensory nerve a clear resonant peak was observed in all subjects, though the 'noise' between adjacent measurements in the frequency domain also contributed to the variation in the derived spectral parameters

To mitigate this point-to-point variation the spectral parameters were also calculated after first fitting a Pearson Type IV function to the data (Orio *et al.*, 2009). This function fitted the frequency-response curves well (Table 6.1 and Figure 6.5) and, on the whole, reduced the variation in the parameters (see bracketed values in Table 6.1), particularly the frequency corresponding to the maximum impedance (f_{max}).

The resonant response to oscillatory inputs was greater in both motor and sensory axons at hyperpolarized membrane potentials than at rest as evidenced by the greater Z_{max} and Q-values (Fig. 6.4 and Table 6.1) and is comparable to studies of neuronal cells in which the frequency response has been shown to have a voltage dependence (Gutfreund *et al.*, 1995; Hutcheon *et al.*, 1996b; Hu *et al.*, 2002; Wang *et al.*, 2006). The resonant frequency for the hyperpolarized axons occurred at 2.1 ± 0.1 and 2.5 ± 0.2 Hz for the motor and sensory axons, respectively.

In motor axons at rest, the phase of threshold impedance was positive between 2 and 4 Hz, which paradoxically would suggest that the response *leads* the ZAP input current.

Positive impedance phases have been associated with the presence of specific ion channels which behave in an electrical sense as inductive reactances (Puil *et al.*, 1986; Hutcheon & Yarom, 2000; Narayanan & Johnston, 2008; Zemankovics *et al.*, 2010).

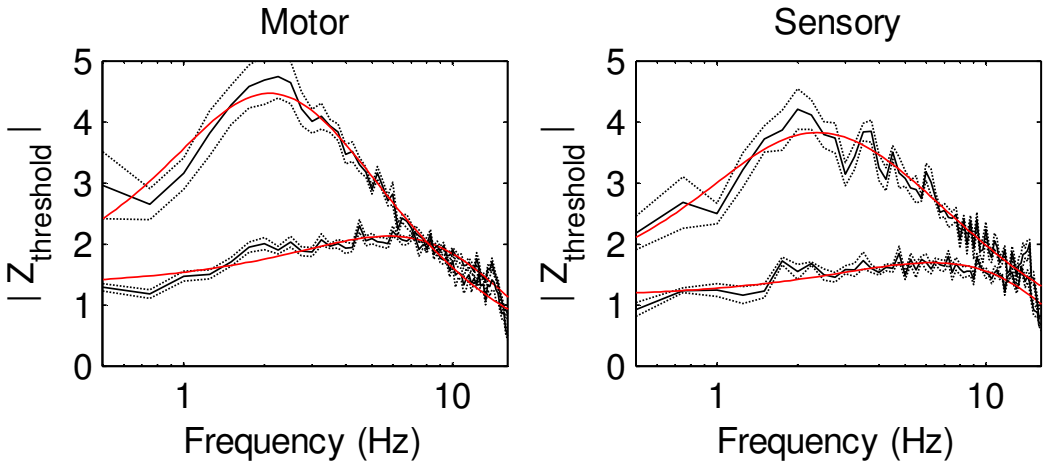

Figure 6.5. Pearson Type IV fits. Mean frequency-response curves (solid black lines; ± SEM [dotted black lines]) and mean fit of Pearson Type IV curve to individual data (red lines).

Subject	$Z_{0.5Hz}$	Z_{max}	Q	f_{max}	Fit (adj.R^2)
			Motor 0%		
1	1.1 [1.6]	2.3 [2.2]	2.1 [1.4]	2.0 [7.2]	0.67
2	1.5 [1.5]	2.4 [2.1]	1.6 [1.4]	7.5 [6.2]	0.65
3	1.2 [1.2]	2.0 [1.9]	1.7 [1.6]	3.5 [5.7]	0.78
4	1.2 [1.5]	2.5 [2.2]	2.1 [1.4]	4.5 [4.9]	0.79
5	1.5 [1.4]	2.5 [2.2]	1.7 [1.5]	3.3 [5.4]	[0.77]
6	1.3 [1.3]	2.7 [2.3]	2.0 [1.8]	7.3 [6.2]	0.79
Mean	**1.3 ± 0.1 [1.4 ± 0.1]**	**2.4 ± 0.1 [2.1 ± 0.1]**	**1.9 ± 0.1 [1.5 ± 0.1]**	**4.7 ± 0.9 [5.9 ± 0.3]**	
			Motor 60%		
1	1.4 [1.7]	3.9 [3.9]	2.8 [2.3]	2.75 [2.4]	0.93
2	1.7 [1.4]	3.7 [3.6]	2.2 [2.6]	2.5 [2.5]	0.96
3	2.0 [1.8]	4.4 [4.1]	2.2 [2.3]	2.25 [2.3]	0.97
4	3.6 [2.9]	5.3 [4.7]	1.5 [1.6]	2.0 [1.8]	0.93
5	5.0 [3.7]	5.8 [5.2]	1.2 [1.4]	2.0 [1.7]	0.89
6	4.1 [3.0]	6.0 [5.5]	1.5 [1.9]	2.25 [2.0]	0.96
Mean	**3.0 ± 0.6 [2.4 ± 0.4]**	**4.8 ± 0.4 [4.5 ± 0.3]**	**1.9 ± 0.3 [2.0 ± 0.2]**	**2.3 ± 0.1 [2.1 ± 0.1]**	
			Sensory 0%		
1	0.5 [1.1]	1.8 [1.5]	3.7 [1.3]	9.25 [7.5]	0.27
2	0.8 [1.1]	2.3 [1.9]	2.9 [1.7]	3.5 [5.7]	0.48
3	1.1 [1.0]	2.1 [1.7]	1.9 [1.6]	4.75 [5.2]	0.27
4	0.9 [1.4]	2.1 [1.8]	2.2 [1.3]	2.0 [6.5]	0.67
5	1.4 [1.3]	2.2 [1.7]	1.6 [1.3]	4.8 [6.8]	0.40
6	0.8 [1.2]	1.8 [1.7]	2.2 [1.4]	9.25 [7.2]	0.67
Mean	**0.9 ± 0.1 [1.2 ± 0.1]**	**2.1 ± 0.1 [1.7 ± 0.1]**	**2.4 ± 0.3 [1.4 ± 0.1]**	**5.6 ± 1.2 [6.5 ± 0.4]**	
			Sensory 60%		
1	1.9 [1.9]	3.6 [3.2]	1.9 [1.7]	4.25 [3.0]	0.77
2	0.8 [1.3]	3.9 [3.3]	4.6 [2.6]	3.5 [2.7]	0.67
3	2.6 [2.2]	5.1 [4.5]	1.9 [2.0]	2.0 [2.2]	0.79
4	2.6 [2.3]	4.7 [4.3]	1.8 [1.9]	2.0 [2.4]	0.90
5	2.3 [2.6]	5.2 [4.4]	2.3 [1.7]	2.0 [1.8]	0.83
6	2.9 [2.4]	4.0 [3.5]	1.4 [1.5]	2.0 [2.8]	0.90
Mean	**2.2 ± 0.3 [2.1 ± 0.2]**	**4.4 ± 0.3 [3.9 ± 0.2]**	**2.3 ± 0.5 [1.9 ± 0.2]**	**2.6 ± 0.4 [2.5 ± 0.2]**	

Table 6.1. Spectral parameters. Derived parameters summarizing the frequency response of motor axons and sensory axons at rest and with a 60% hyperpolarization. Bracketed values were calculated after smoothing the data with a Pearson Type IV function. Group means presented ± SEM.

Computational Model

Assessment of the mathematical models in the frequency domain

In Chapter 4, the 'Bostock' model of a human motor axon was modified to account for the extended excitability data which included stronger and longer hyperpolarization, and a model of the axonal excitability of human sensory nerve was presented for the first time. These models were tested against the new ZAP protocol, and are compared to the group data in Figure 6.6. The motor and sensory models provided an extremely good fit to the changes in excitability in response to the ZAP protocol measured at rest (Fig. 6.6; compare upper red and black traces in the top row). With a 60% hyperpolarization, the motor axon model had a slightly more hyperpolarized baseline than the group data (motor model, -204%; motor data, -180 ± 13%). The sensory axon model however was slightly depolarized when compared to the sensory group data (sensory model, -126%; sensory data, -135 ± 8). These shifts are small and probably reflect the variability of I_h between subjects and on different occasions as observed in Chapters 4 and 5.

In the frequency domain, the modelled excitability data showed the same key features of resonance as the group data both qualitatively and quantitatively, namely a voltage-dependent resonant peak that was greater in motor axons than sensory. The summary statistics of the modelled spectral data are shown in Table 6.2 and apart from an overestimate of the resonant frequency of sensory axons. This is likely due to sampling limitations, and could be overcome by smoothing with a Pearson Type IV function. The fits bear a remarkably good resemblance to the observed data.

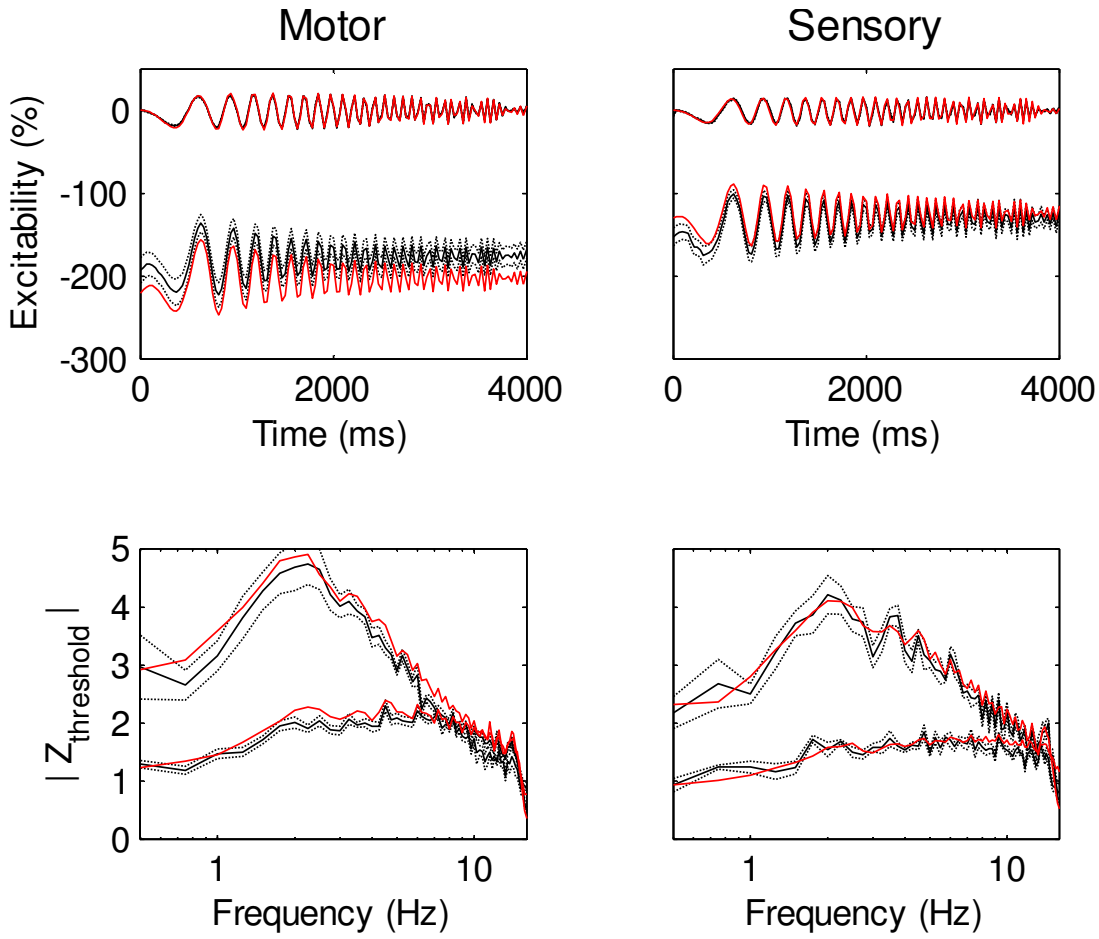

Figure 6.6. Comparison of modelled and observed data.

Observed data (mean [solid black lines] ± SEM [dashed black lines]) and modelled data (red lines). **Top Row.** Response to input ZAP at rest and with 60% hyperpolarization. **Bottom Row.** Magnitude of threshold impedance $|Z_{threshold}|$ versus frequency for the axons at rest and with hyperpolarization.

	$Z_{0.5Hz}$	Z_{max}	Q	f_{max}	Fit (adj.R^2)
Motor 0%	1.2 [1.4]	2.4 [2.3]	1.9 [1.6]	4.5 [4.9]	0.80
Motor 60%	2.9 [2.6]	4.9 [4.6]	1.7 [1.8]	2.3 [2.1]	0.96
Sensory 0%	0.9 [1.1]	1.8 [1.8]	1.9 [1.6]	9.3 [6.5]	0.78
Sensory 60%	2.3 [2.2]	4.1 [3.9]	1.8 [1.8]	2.0 [2.6]	0.93

Table 6.2. Spectral parameters derived from modelled data. Bracketed values were calculated after first smoothing the data with a Pearson Type IV function. Note the improved estimate of the parameter f_{max} (shaded) for sensory axons at rest, which was probably affected by sampling limitations.

The voltage dependence of the frequency response

The voltage dependence of the frequency response was modelled for motor axons at rest (0%) and with background hyperpolarizations of 30, 60 and 90% of the control threshold, and is shown in Figure 6.7.

As described in the methods, the majority of the fast phase of threshold electrotonus was complete by the start of the ZAP protocol, at t=200 ms in Figure 6.7A. The resonant response grows with hyperpolarization, as previously reported (Gutfreund *et al.*, 1995; Hutcheon *et al.*, 1996b; Wang *et al.*, 2006) to a peak which is maximal in the present study with a 60% hyperpolarization (Fig. 6.7B, C). The motor model exhibited a positive phase of threshold impedance, as seen in the observed data (Fig. 6.4), and this 'positivity' diminished with hyperpolarization (Fig. 6.7D).

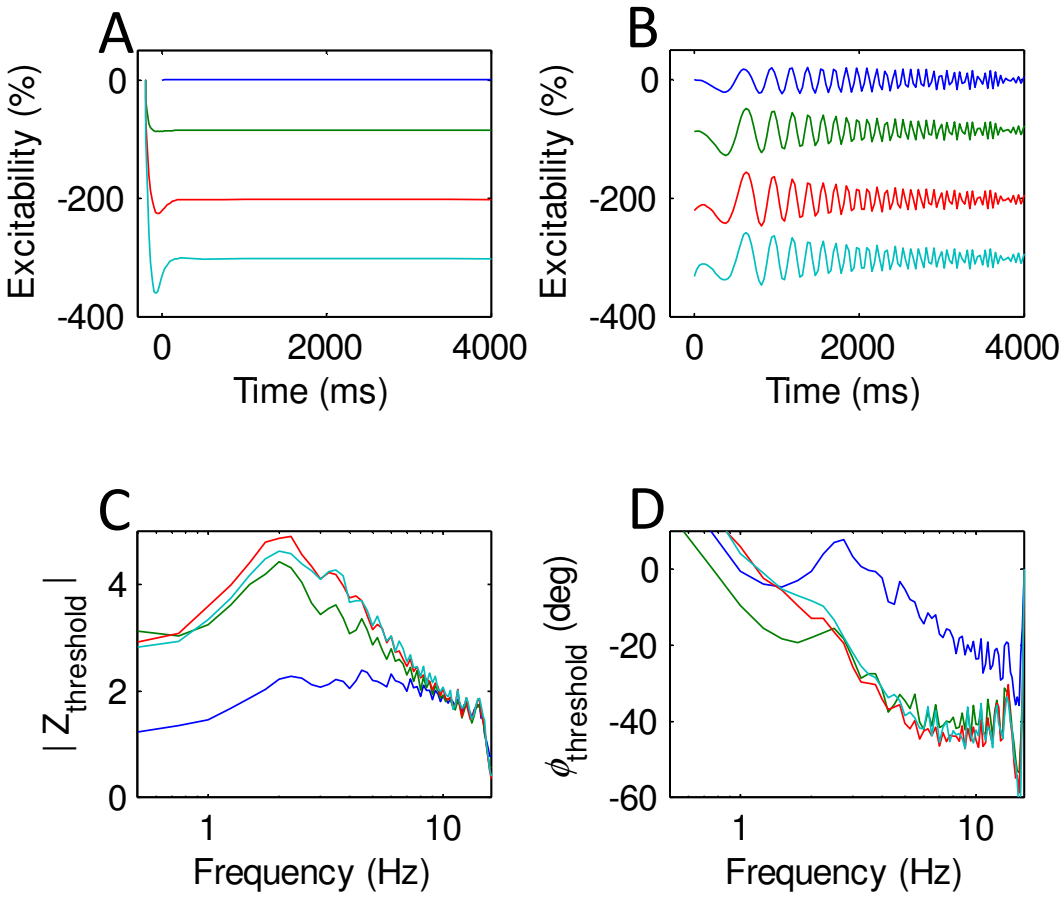

Figure 6.7. Voltage dependence of the frequency response in the model motor axon. **A.** Threshold electrotonic responses at rest (0%, blue) and for 30 (green), 60 (red) and 90% (cyan) hyperpolarizations. **B.** Response to ZAP conditioning superimposed on the hyperpolarizations in ***A***. **C.** Magnitude of the threshold impedance calculated from the responses in ***B***. **D.** Phase of the threshold impedance, corresponding to the lag of response behind input. Note the positive phase around 2.5 Hz for the unpolarized (blue) response.

The contribution of slowly-rectifying conductances to the frequency response.

The effect of blocking I_h was modelled separately for motor and sensory axons and is shown in Figure 6.8 for varying levels of polarization. As described in the Methods, the excitability was clamped by adjusting the polarizing current strength to compensate for the reduction in I_h. Blocking I_h had no effect on the frequency response of modelled axons at rest, but with stronger hyperpolarization both motor and sensory axons progressively lost their low frequency attenuation. The 'high' frequency response ($\gtrsim$3 Hz) was unaffected by blocking I_h at all levels of polarization in modelled axons.

Similarly the effect of blocking I_{Ks} was modelled by setting the conductance (G_{Ks}) to zero and clamping the baseline excitability, and is shown in Figure 6.9. In contrast with blocking I_h, the effect of blocking I_{Ks} was diminished with hyperpolarization, and was negligible below ~60% and ~90% hyperpolarization for motor and sensory axons, respectively. The effect of blocking I_{Ks} was not confined to the low-frequency range, and probably reflects the contribution of slow potassium channels to input conductance at rest.

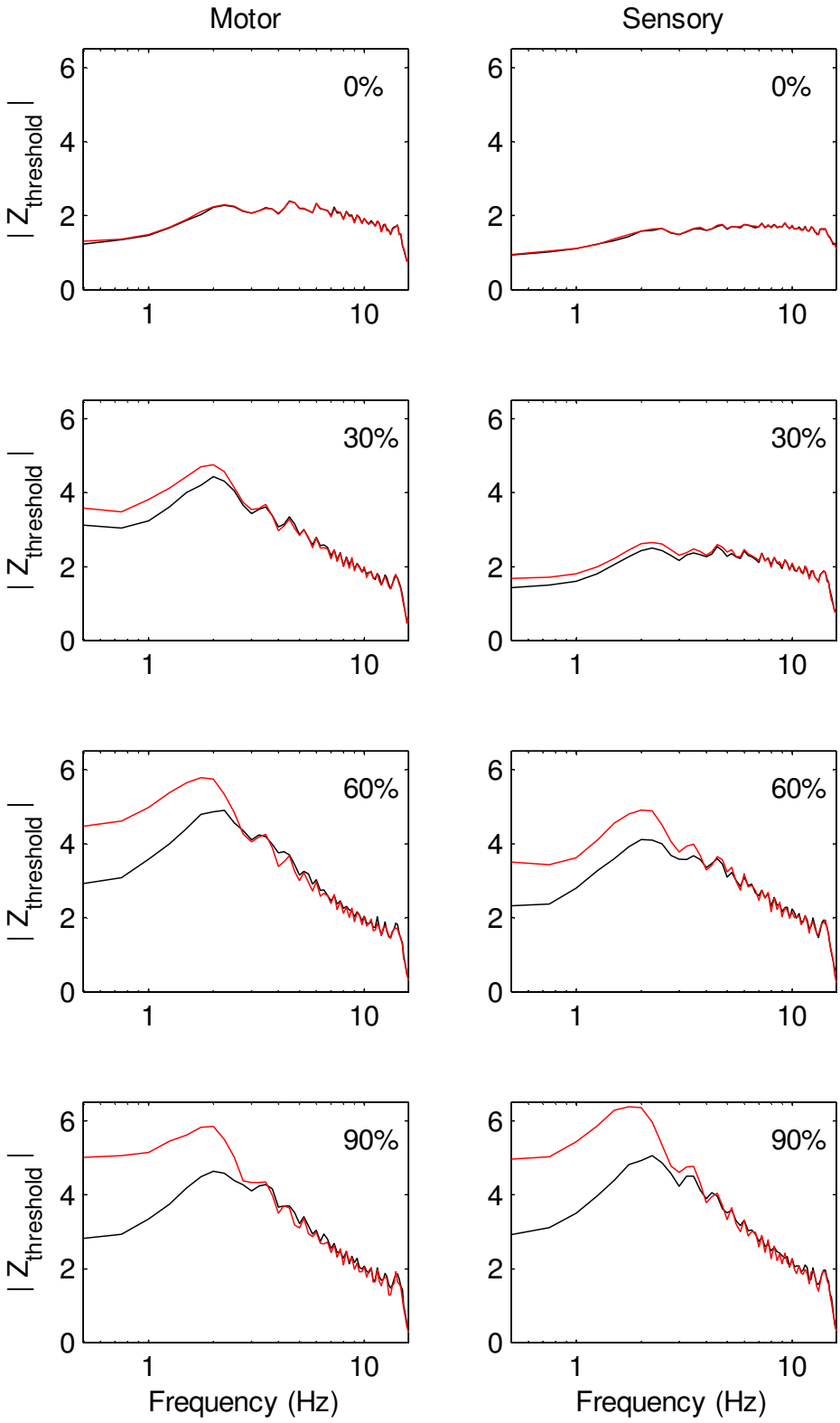

Figure 6.8. I_h attenuates the low-frequency response further with hyperpolarization.

The effect of blocking I_h in the motor and sensory axon models. Comparison of unaltered (control, black) and blocked (red) models for motor and sensory axons at various levels of hyperpolarization.

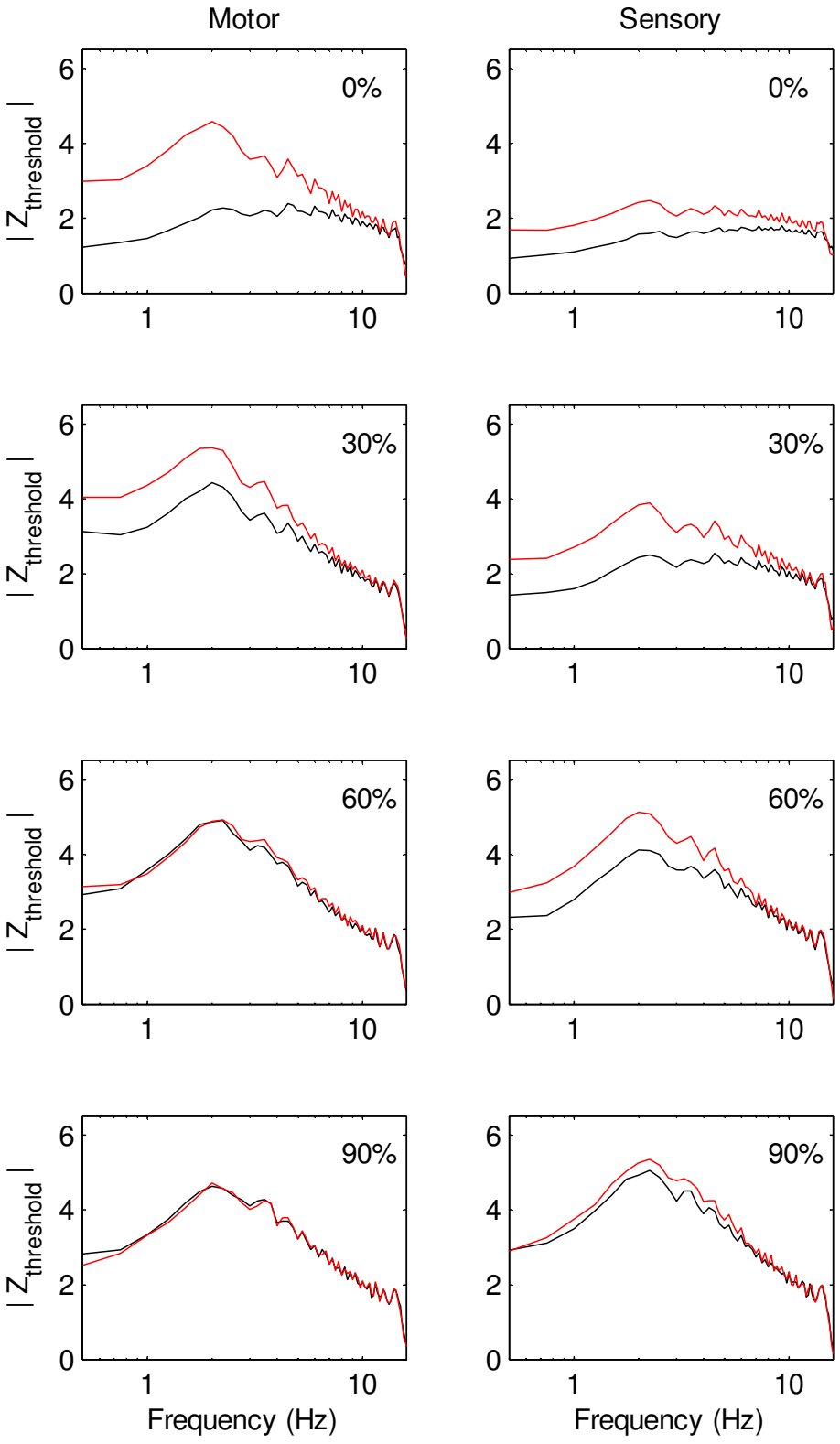

Figure 6.9. G_{Ks} raises the input conductance further with depolarization.

The effect of blocking I_{Ks} in the motor and sensory axon models. Comparison of unaltered (control, black) and blocked (red) models for motor and sensory axons at various levels of hyperpolarization.

Conductances that alter the magnitude of the frequency response

The sensitivity of the leak conductance, G_{Lk} on the magnitude of the frequency response was modelled in motor and sensory axons, and is shown in Figure 6.10. Halving G_{Lk} consistently amplified the resonance, while doubling G_{Lk} consistently reduced the magnitude of resonance. The influence of G_{Lk} was small at rest and increased with hyperpolarization, consistent with an ohmic conductance modelled with a reversal potential near resting membrane potential. The influence of G_{Lk} can be seen purely in terms of its effect on the input conductance, and its ability to 'leak' current across the membrane.

In contrast increases in the fraction of sodium channels operating in a persistent mode *amplify* resonance, and their effect on the frequency-response curves *diminishes* with hyperpolarization, as seen in Figure 6.11. The modelled effects of alterations of Na_p are greater in sensory axons than motor, and most probably reflect the relatively depolarized membrane potential of the sensory model.

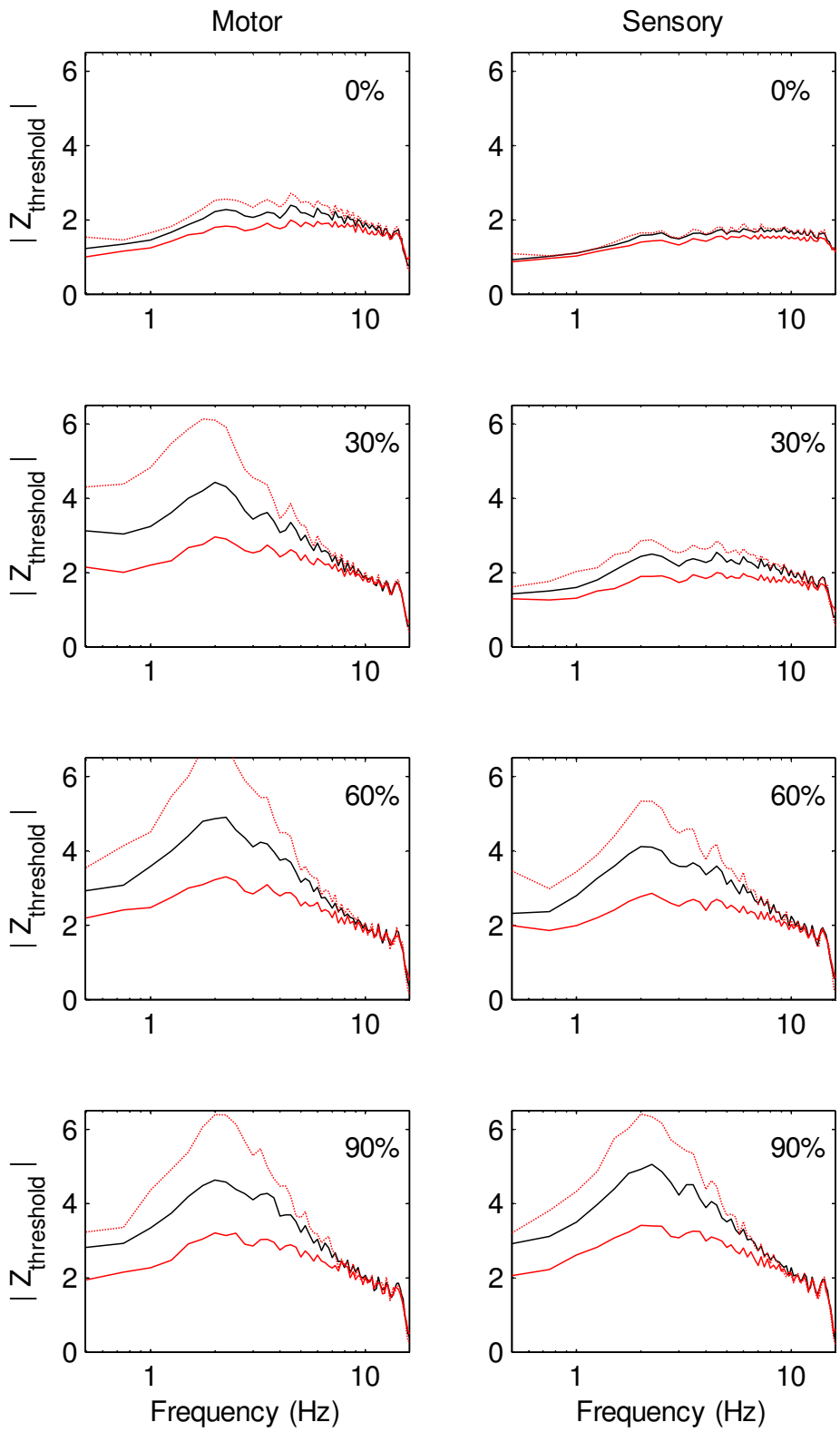

Figure 6.10 G_{Lk} raises the input conductance with hyperpolarization from rest. The effects of G_{Lk} on the magnitude of resonance. Comparison of unaltered (control, black) and alterations of G_{Lk} (doubled, solid red lines; halved, dotted red lines) models for motor and sensory axons at various levels of hyperpolarization.

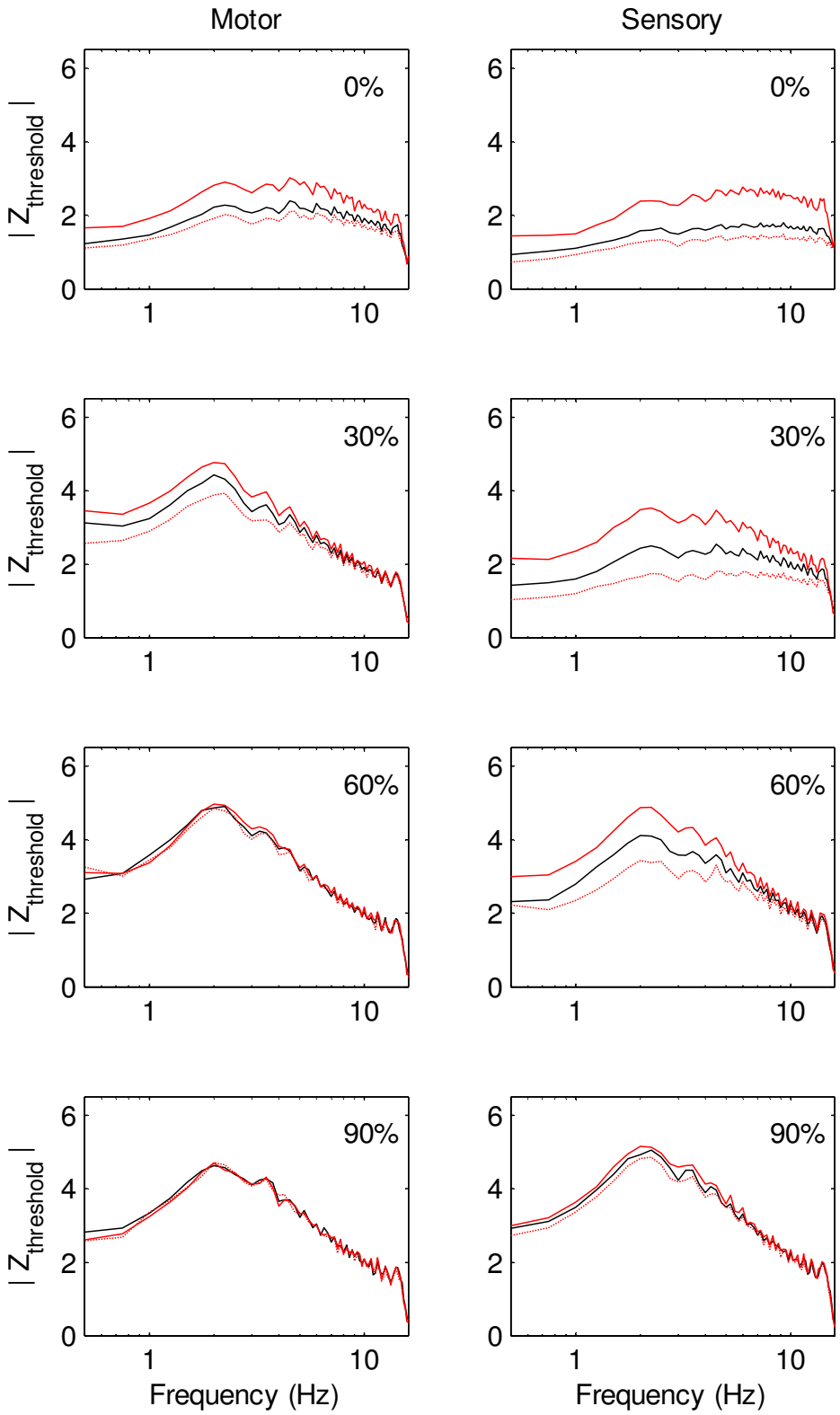

Figure 6.11 Na_p amplifies resonance with further depolarization. Comparison of unaltered (control, black) and alterations of the fraction of Na^+ channels operating in a persistent mode (doubled, solid red lines; halved, dotted red lines) models for motor and sensory axons at various levels of hyperpolarization.

Discussion

The studies in this chapter have examined the low-frequency preference and resonance of human axons *in vivo* using a novel application of frequency domain and threshold tracking techniques. Studying the response to subthreshold oscillatory input currents at different membrane potentials allows the separation of ion channel contributions to axonal excitability based upon their voltage dependence and gating kinetics.

Traditional threshold tracking techniques probe the slowly-gated inwardly-rectifying conductance G_H using long-lasting hyperpolarizing square-wave conditioning currents, but the interpretation of the response must consider the contributions of voltage-dependent (G_{Ks}), and ohmic (G_{Lk}) conductances. This new protocol attempts to address these limitations by adding frequency domain techniques to further distinguish these conductances.

The models developed in Chapter 4 were subjected to this new frequency probe, and adequately described the response to oscillatory inputs. These models were then used to examine the factors responsible for generating and amplifying (or attenuating) resonance in human axons.

Comparison with the current-threshold relationship.

The threshold impedance data presented in this chapter can be related to the threshold conductance derived from the current-threshold relationship. The reciprocal of the slope of the current-threshold relationship gives the threshold impedance, albeit in response to a 200-ms square pulse (giving a period for the first harmonic of 400 ms), which will have a fundamental frequency of 2.5 Hz (similar to but slightly greater than the resonant frequencies for the hyperpolarized axons presented in this Chapter). Using the data from Chapter 4 and shown in Figure 4.5, the threshold

impedances would be: Motor 4.06 (60%), 1.75 (0%); Sensory 3.56 (60%), 1.33 (0%). These values compare favourably to the data shown in Figure 6.4.

Verification of the motor and sensory axon models

The results in this Chapter presented an alternative dataset to test the capability of the models developed in Chapter 4. The ZAP protocol provided the opportunity to test the models against a different stimulus paradigm, and also to test the model in the frequency domain. Without further modification, the models provided a remarkably good fit to the ZAP data (Fig. 6.6), providing independent verification of the dynamics of the modelled conductances of motor and sensory axons.

Factors contributing to resonance in motor and sensory axons

Two mechanisms are required to generate a frequency preference or resonance in axons. The combination of suitable low-pass and high-pass filters allows such a resonance to occur, and this is realised electrically in tuned (RLC) circuits which consist of the parallel combination of a **R**esistor, inductor(**L**) and **C**apacitor (Hutcheon & Yarom, 2000). The input conductance and membrane capacitance form the necessary low-pass filtering, limiting the rate at which membrane potential changes can occur in response to input stimuli according to the membrane time constant (RC). The high-pass filtering is achieved by the so-called 'inductive' reactances which slowly oppose changes in membrane potential, so-called because inductors are not actually a feature of biological membranes.

The regulation and interaction of these low- and high-pass filters determines the size of the membrane potential change in response to a stimulus current.

Low-frequency attenuation

In human axons, the slow rectifying conductances, G_H and G_{Ks} provide the 'inductive' attenuation of output responses at low frequencies. The modelling in this study provided support for the idea that G_{Ks} and G_H play complementary roles. G_{Ks} contributes to the low-frequency attenuation at membrane potentials above 60% and 90% hyperpolarization in motor and sensory axons, respectively, while G_H attenuates the low-frequency response for hyperpolarizations below rest. Whereas the modelling demonstrated that the action of I_h was confined to frequencies below ~ 3 Hz, blocking of I_{Ks} affected all studied frequencies. This suggests that I_{Ks} also contributes to the high-frequency attenuation by augmenting the input conductance.

High-frequency attenuation

As previously discussed the low-pass filtering of the membrane is due to the parallel combination of the nodal capacitance and input conductance. As the membrane capacitance is essentially constant, the low-pass filtering is altered by changes in the input conductance which itself is the parallel combination of all open channels. For the axons in the present study these are predominantly G_{Lk} and G_{Ks}. G_{Lk} increases and G_{Ks} decreases with hyperpolarization from rest, providing a complementary control over the input conductance and thereby the low-pass filtering of the membrane.

Amplifiers and suppressors of resonance

In contrast to the effects of I_{Lk} on the frequency response, I_{NaP} potentiates the response of human axons to oscillatory input currents as seen by the modelled changes in Figure 6.11. This confirms previous studies which have examined the effect of TTX on the frequency-response curve and which showed a significant decrease in the magnitude of the resonant peak, particularly at depolarized membrane potentials (Gutfreund *et al.*, 1995; Hutcheon *et al.*, 1996b; Hu *et al.*, 2002; Wang *et al.*, 2006).

Differences between motor and sensory axons.

It is tempting to attribute the observed differences in the frequency response of motor and sensory axons to differences in their resting membrane potentials. Figure 6.12 shows that depolarizing the motor model by an amount equivalent to a 3-mV depolarization of resting membrane potential does indeed improve both the resonant response and the derived frequency-response curves (compare discrepancy between the blue and red traces in the lower plot to the black and red traces in the middle plot). On closer examination however, the low-frequency attenuation for the hyperpolarized axons is not improved by depolarization, and there is a suggestion that at higher frequencies depolarization attenuates the responses of motor axons further. It can be concluded that, while the difference in membrane potential contributes to the difference in the responses of sensory and motor axons, other factors are important.

The key differences seen in the motor and sensory models presented in Chapter 4 are likely to contribute to the differential frequency responses; namely the near halving of nodal G_{Ks} in sensory axons, the up-modulation of I_h and the increase in I_{NaP} (secondary to depolarization of resting membrane potential).

Functional consequences

This study has examined the preference to oscillation at low frequencies in hyperpolarized human axons *in vivo*, and the modelling suggests that this resonance is facilitated by I_h. It is likely however, that there is also a frequency preference at higher frequencies in *depolarized* axons, mediated by the interaction of K_s and Na_p currents, similar to the so-called 'M-resonance' observed in central neurons (Hu *et al.*, 2002; Peters *et al.*, 2005; Hu *et al.*, 2009a). If an 'M-resonance' exists in depolarized axons then it may contribute to spontaneous oscillations or ectopic activity.

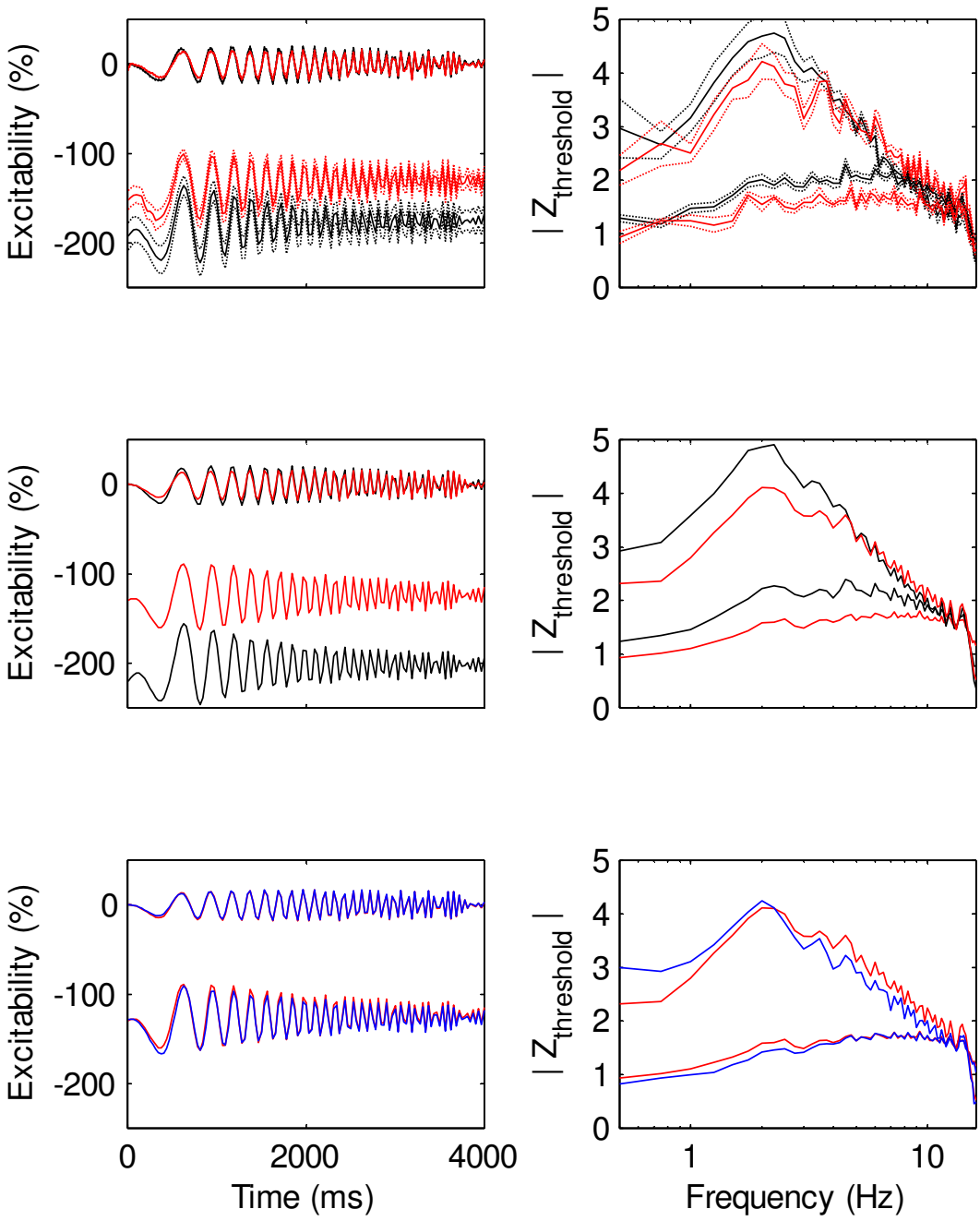

Figure 6.12. Do sensory axons behave as relatively depolarized motor axons?

Top row. Observed responses (mean ± SEM) to ZAP function and frequency-response curves for motor (black) and sensory (red) axons at rest and with a 60% hyperpolarization. **Middle row.** Modelled responses: motor model (black), sensory model (red). **Bottom row.** Depolarized motor model (blue) & sensory model (red).

The primary motivation for studying the low-frequency resonance of human axons in this study was to resolve the contributions of I_h, I_{Ks} and I_{Lk} to excitability. Conventional excitability studies using steady DC currents such as threshold electrotonus can provide only limited insight into the relative contributions of the activity of different channels at different membrane potentials. The fact that a low-frequency resonance was found in healthy axons of peripheral nerve raises the question: Are there functional consequences of this resonance in healthy axons of peripheral nerve, or is it merely an expected consequence of the time-domain properties of ion channels?

The low-frequency preference was not substantially different in the hyperpolarized axons of motor and sensory nerve. Considering the different functional requirements of these axons, perhaps the basis of such a resonance is common and relates to the activation of I_h during activity-dependent hyperpolarization.

It would be pleasing to be able to relate the resonance explored here to ectopic firing axons, but this is not simple, except perhaps with fasciculation. Ectopic activity can occur in sensory and motor axons when they hyperpolarize following release of ischaemia or the cessation of prolonged (tetanic) stimulation (Bostock *et al.*, 1991a; Bostock *et al.*, 1991b; Bostock *et al.*, 1994; Mogyoros *et al.*, 1997; Lin *et al.*, 2002). The resonant frequencies of axons in this study ($\gtrsim$ 2 Hz) could contribute to the interburst interval but probably not to the discharge rate within bursts (Culp *et al.*, 1982). Subthreshold oscillations have been linked to the initiation of burst firing (Carnevale & Wachtel, 1982), and in demyelinated axons, exposure to TTX removes both the subthreshold oscillation and ectopic activity (Kapoor *et al.*, 1997). Baker and Bostock (1992), found that G_{Ks} played a pacemaking role for ectopic activity in demyelinated spinal root axons of rat.

Given the present results, it is timely to reinterpret the conclusions of Bostock and colleagues (1991a; 1991b) where it was suggested that hyperpolarization beyond the equilibrium potential for K^+ could result in a regenerative inward current, leading to oscillatory behaviour during which fasciculations were triggered. This explanation received some support from the recordings of David and colleagues (1993) and Kapoor and colleagues (1993). However the present studies suggest that the 'triggering' may involve HCN channels in addition to K_s and that their relative contributions are likely to be voltage dependent.

The connection between these subthreshold oscillations and ectopic activity may be more important in diseased axons such as in neuropathic pain, where alterations in or modulation of HCN and other relevant ion channels is known to occur (Chaplan *et al.*, 2003; Jiang *et al.*, 2008a; Jiang *et al.*, 2008b; Momin *et al.*, 2008; Momin & Wood, 2008; Momin & McNaughton, 2009; Wickenden *et al.*, 2009; Cregg *et al.*, 2010; Moldovan *et al.*, 2013).

Does resonance have a role other than setting the rate of neural activity, whether it is natural or spontaneous? The frequency dependence of synaptic inhibition and facilitation has been proposed as a filtering mechanism which allows selective communication between an axon and its post-synaptic targets in the central nervous system (Markram *et al.*, 1998; Izhikevich *et al.*, 2003). While it is conceivable that such a mechanism may operate at the neuromuscular junctions of a single motor unit, it would require differences in the transmitter release mechanisms at individual neuromuscular junctions within that motor unit. It is not clear if such differences occur in healthy nerve, but differential alterations in the function of individual neuromuscular junctions may occur in disease.

Does I_h have a role other than restoring membrane potential and its contribution to resonance? Vaidya and Johnston (2013) have provided evidence for the active contribution of HCN channels to dendritic synchrony in CA1 pyramidal neurons. They showed that a gradient of HCN channels provides an inductive reactance which counters the length dependent delays of the membrane time constant. It is unlikely however that fine precision is necessary in motor axons with muscle fibres which are two orders of magnitude slower. Such synchronisation could be utilised in cutaneous afferents, provided that there was a specialised distribution of HCN channels in different branches of the axon arbor. Though there are no data on the issue, this is a reasonable possibility.

Conclusions

Regardless of whether the low-frequency resonance described here in hyperpolarized axons has a functional role, this Chapter presents a technique that (i) allows the contributions of different ion channels to axonal behaviour to be explored in human subjects, and (ii) provides independent validation of the model of the human motor and sensory axons developed in Chapter 4 which largely used steady DC currents.

Chapter 7

Summary and Conclusions

This thesis has focussed on the contributions of the hyperpolarization-activated current, I_h to the excitability of the large myelinated axons of human peripheral nerve. To support this aim new equipment, measurement techniques and protocols have been developed. The 'Bostock' model of a human motor axon has been adapted to account for the extended excitability measurements, and a new model of the excitability of sensory axons has been developed.

The HCN channels that underlie I_h are not necessary for the generation or propagation of action potentials *per se*, but importantly they modulate membrane excitability indirectly through their role in the maintenance of resting membrane potential, particularly following sustained activity and, in some cells, they play a pacemaker role. HCN dysfunction and dysregulation has been reported in a number of neurological disorders, and as a result of subtype-nonselective HCN blockade, and has been implicated in neuropathic pain. This provided the motivation for a better understanding of the contribution of HCN channels in healthy axons, and the development of better techniques for probing their function.

The study of small amplitude sensory nerve action potentials

The studies in this thesis have examined the excitability of small sensory nerve action potentials, and required a preamplifier with low noise and high common-mode rejection. At the start of this thesis there were no such amplifiers commercially available, and although there are some promising products now on the horizon, that is still the case. The preamplifier presented in Chapter 3 has allowed the tracking of compound targets as small as 2 μV without the conventional clamping which tends to distort measurements of amplitude and without additional filtering or waveform

averaging. The common-mode rejection properties allowed the recording of sensory action potentials using 1-ms stimulus widths, which by their very nature encroach upon the response. These advances were tested by recording the excitability of low-threshold cutaneous afferents (with a target as small as 2% of the maximal CSAP), and the first axonal excitability measurements of orthodromically recorded CSAPs. Though the purpose of these measurements was to demonstrate the capability of the low-threshold recording system, the studies indicated that antidromically-recorded low-threshold cutaneous afferents and the orthodromically-recorded cutaneous afferents may be relatively depolarized when compared to conventional measurements of sensory axons. These initial findings open up the possibility of studying the excitability of afferents more distally in polyneuropathies, and those studies are now underway.

New models of human motor and sensory axons

The voltage dependence of I_h of motor and sensory axons was studied in recordings using long and strong hyperpolarization.

Modelling of the data required no differences in morphology of the axons, nor in the configuration or types of ion channels present.

The data in Chapter 4 support earlier findings that sensory axons have greater persistent Na^+ and hyperpolarization-activated currents. The modelling suggests however, that the differences *do not* require a greater expression of HCN channels in sensory axons than motor. Similarly, these results show *no need* to invoke a greater percentage of persistent Na^+ channels in sensory axons. The differences in accommodation to hyperpolarization between motor and sensory axons are best

explained by an up-modulation of the voltage dependence of I_h in sensory axons, and the results also suggest the contribution of slower HCN isoforms in axonal excitability.

The results of Chapter 4 suggest that the resting membrane potential of sensory axons is depolarized by ~4 mV when compared to motor, and that half of this is due to a halving of the nodal slow K^+. This depolarization is sufficient to explain the greater persistent Na^+ current in sensory axons.

The impact of focal hyperthermia on axonal excitability

Axonal excitability is known to be impaired during hyperthermia, and this is of particular relevance in axons with impaired safety margins (Guthrie & Nelson, 1995; Vucic *et al.*, 2010). The studies in Chapter 5 present for the first time the effects of focal hyperthermia in human motor and sensory axons. The effects of hyperthermia were most conspicuous in the recovery of excitability following activation, and rather unsurprisingly the timing of the recovery cycle during hyperthermia was faster, as would be expected with faster ion channel kinetics. What was not expected however, at least from earlier studies (Burke *et al.*, 1999; Kiernan *et al.*, 2001a; Moldovan & Krarup, 2004; Maurer *et al.*, 2010), was the significant reduction in the amplitude of superexcitability during hyperthermia.

The results from long-lasting polarization however led to mixed results. Congruent with the faster channel kinetics during the recovery cycle, the accommodation in depolarizing threshold electrotonus was faster, a result expected on the grounds of faster slow K^+ kinetics. However, in response to hyperpolarization, reduced accommodation was seen, which would not be expected with faster closure of K_s and faster opening of HCN channels. The simplest explanation for this paradoxical observation was a hyperpolarization of the voltage dependence of I_h during

hyperthermia. This explanation has precedent in the literature with a favourable comparison with the temperature sensitivity of the cardiac current, i_f in sheep Purkinje fibres (Hart, 1983).

This study suggests that the impacts of hyperthermia on fatigue are predominantly due to changes in K_s channels. The modelled 2:1 ratio of K_s conductance in motor and sensory axons may contribute to a differential susceptibility to conduction block.

Subthreshold oscillations and resonance in human axons

Chapter 6 introduces a new technique to threshold-tracking studies to help distinguish ion channels by their combined properties of voltage dependence and activation kinetics. Frequency domain techniques have been used in animal studies which focussed on the connection between frequency preference and rhythmic activity in central neurons.

The use of frequency-domain techniques here was driven primarily by the desire to resolve the overlapping contributions of K_s and HCN channels to the accommodation to hyperpolarization.

The response to oscillatory currents was tested between DC and 16 Hz in motor and sensory axons at rest and during hyperpolarization, and a clear resonant peak was observed in the hyperpolarized axons. The models developed earlier were tested against this new stimulus paradigm and fitted the data well without additional modification, providing further independent verification of their validity. Hu and colleagues (2002) demonstrated two forms of low-frequency resonance, which he termed: 'M-resonance' mediated by K_s channels, and 'H-resonance' mediated by HCN channels. The results in Chapter 6 would indicate that 'H-resonance' exists in human axons, and 'M-resonance' is likely. Clarifying whether 'M-resonance' occurs in human

axons was not a prime motivation for the present experiments, but future studies could be undertaken at more depolarized membrane potentials.

The results of Chapter 6 have implications for traditional threshold electrotonus studies, suggesting that the optimal hyperpolarization level for studying I_h is probably around 60 – 70%, with lesser degrees of hyperpolarization affected the contribution of G_{Ks} and stronger hyperpolarizations affected by a progressively greater leak conductance. Again it is noted that the leak conductance could contain unmodelled components of I_h, particularly due to isoforms with slower time constants.

Future Work

The development of the low-noise amplifier and the early observations of orthodromically recorded axonal excitability of cutaneous afferents provides the opportunity of studying axons closer to the site of their receptors. More detailed studies of distal excitability in healthy axons are underway, and studies in disease groups are planned.

Unlike motor axons which form a relatively homogeneous population, the cutaneous afferents studied in this thesis serve four different types of mechanoreceptors, each with different firing patterns (Johansson & Vallbo, 1983). It would be interesting to study the excitability of functionally identified cutaneous afferents. It is tempting to speculate that their biophysical properties would be different, in support of the view that axonal properties are adapted to the activity patterns of their mechanoreceptors.

It is likely that the activity of I_h as studied in this thesis is largely mediated by the fastest HCN isoform. The slower HCN isoforms will however require much longer protocols or new techniques to resolve their contributions to axonal excitability.

The advances made in this thesis are directly applicable to disease processes particularly those that involve HCN channels such as: diabetes mellitus, stroke, porphyria (Horn *et al.*, 1996; Jankelowitz *et al.*, 2007a; Lin *et al.*, 2008) and perhaps neuropathic pain (Chaplan *et al.*, 2003; Momin *et al.*, 2008; Maher *et al.*, 2009; Wickenden *et al.*, 2009). Studies are planned to explore the alterations in excitability of HCN-channelopathies.

References

Adrian ED. (1912). On the conduction of subnormal disturbances in normal nerve. *J Physiol* **45,** 389-412.

Adrian ED. (1917). Physiological basis of electrical tests in peripheral nerve injury. *Arch Radiol Electrother* **21,** 379-393.

Adrian ED & Lucas K. (1912). On the summation of propagated disturbances in nerve and muscle. *J Physiol* **44,** 68-124.

Altomare C, Terragni B, Brioschi C, Milanesi R, Pagliuca C, Viscomi C, Moroni A, Baruscotti M & DiFrancesco D. (2003). Heteromeric HCN1-HCN4 channels: a comparison with native pacemaker channels from the rabbit sinoatrial node. *J Physiol* **549,** 347-359.

Alzheimer C, Schwindt PC & Crill WE. (1993). Modal gating of Na+ channels as a mechanism of persistent Na+ current in pyramidal neurons from rat and cat sensorimotor cortex. *J Neurosci* **13,** 660-673.

Aman TK, Grieco-Calub TM, Chen C, Rusconi R, Slat EA, Isom LL & Raman IM. (2009). Regulation of persistent Na current by interactions between beta subunits of voltage-gated Na channels. *J Neurosci* **29,** 2027-2042.

Applegate C & Burke D. (1989). Changes in excitability of human cutaneous afferents following prolonged high-frequency stimulation. *Brain* **112,** 147-164.

Arnold R, Pussell BA, Pianta TJ, Grinius V, Lin CSY, Kiernan MC, Howells J, Jardine MJ & Krishnan AV. (2013). Effects of hemodiafiltration and high flux hemodialysis on nerve excitability in end-stage kidney disease. *PLoS One* **8,** e59055.

Arroyo EJ, Xu YT, Zhou L, Messing A, Peles E, Chiu SY & Scherer SS. (1999). Myelinating Schwann cells determine the internodal localization of Kv1.1, Kv1.2, Kvbeta2, and Caspr. *J Neurocytol* **28,** 333-347.

Baker M & Bostock H. (1992). Ectopic activity in demyelinated spinal root axons of the rat. *J Physiol* **451,** 539-552.

Baker M, Bostock H, Grafe P & Martius P. (1987). Function and distribution of three types of rectifying channel in rat spinal root myelinated axons. *J Physiol* **383,** 45-67.

Baker MD & Bostock H. (1997). Low-threshold, persistent sodium current in rat large dorsal root ganglion neurons in culture. *J Neurophysiol* **77,** 1503-1513.

Barrett EF & Barrett JN. (1982). Intracellular recording from vertebrate myelinated axons: mechanism of the depolarizing afterpotential. *J Physiol* **323,** 117-144.

Barrett EF, Morita K & Scappaticci KA. (1988). Effects of tetraethylammonium on the depolarizing after-potential and passive properties of lizard myelinated axons. *J Physiol* **402,** 65-78.

Baruscotti M, Bucchi A & Difrancesco D. (2005). Physiology and pharmacology of the cardiac pacemaker ("funny") current. *Pharmacol Ther* **107,** 59-79.

Basser PJ & Roth BJ. (2000). New currents in electrical stimulation of excitable tissues. *Annu Rev Biomed Eng* **2,** 377-397.

Benatar M, Wuu J & Peng L. (2009). Reference data for commonly used sensory and motor nerve conduction studies. *Muscle Nerve* **40,** 772-794.

Benoit E & Dubois JM. (1987). Properties of maintained sodium current induced by a toxin from Androctonus scorpion in frog node of Ranvier. *J Physiol* **383,** 93-114.

Bergmans J. (1970). The physiology of single human nerve fibres. University of Louvain, Vander.

Berthold C, Fraher J, King R & Rydmark M. (2005). Microscopic anatomy of the peripheral nervous system. In *Peripheral neuropathy*, 4th edn, ed. Dyck PJ & Thomas PK, pp. 35-91. Elsevier Saunders, Philadelphia.

Berthold CH & Rydmark M. (1983). Electrophysiology and morphology of myelinated nerve fibers. VI. Anatomy of the paranode-node-paranode region in the cat. *Experientia* **39,** 964-976.

Berthold CH & Rydmark M. (1995). Morphology of normal peripheral axons. In *The Axon: Structure, Function and Pathophysiology*, ed. Waxman SG, Kocsis JD & Stys PK, pp. 13-48. Oxford University Press, New York.

Bezanilla F. (2005). Voltage-gated ion channels. *IEEE Trans Nanobioscience* **4,** 34-48.

Biel M, Wahl-Schott C, Michalakis S & Zong X. (2009). Hyperpolarization-activated cation channels: from genes to function. *Physiol Rev* **89,** 847-885.

Blight AR. (1985). Computer simulation of action potentials and afterpotentials in mammalian myelinated axons: the case for a lower resistance myelin sheath. *Neuroscience* **15,** 13-31.

Börjesson SI & Elinder F. (2008). Structure, function, and modification of the voltage sensor in voltage-gated ion channels. *Cell Biochem Biophys* **52,** 149-174.

BoSmith RE, Briggs I & Sturgess NC. (1993). Inhibitory actions of ZENECA ZD7288 on whole-cell hyperpolarization activated inward current (If) in guinea-pig dissociated sinoatrial node cells. *Br J Pharmacol* **110,** 343-349.

Bostock H. (1983). The strength-duration relationship for excitation of myelinated nerve: computed dependence on membrane parameters. *J Physiol* **341,** 59-74.

Bostock H. (1995). Mechanisms of accommodation and adaptation in myelinated axons. In *The Axon: Structure, Function and Pathophysiology*, ed. Waxman SG, Kocsis JD & Stys PK, pp. 68-96. Oxford University Press, New York.

Bostock H. (2006). MEMFIT: A computer program to aid interpretation of multiple excitability measurements on human motor axons. *Clin Neurophysiol* **117,** S85.

Bostock H & Baker M. (1988). Evidence for two types of potassium channel in human motor axons in vivo. *Brain Res* **462,** 354-358.

Bostock H, Baker M, Grafe P & Reid G. (1991a). Changes in excitability and accommodation of human motor axons following brief periods of ischaemia. *J Physiol* **441,** 513-535.

Bostock H, Baker M & Reid G. (1991b). Changes in excitability of human motor axons underlying post-ischaemic fasciculations: evidence for two stable states. *J Physiol* **441,** 537-557.

Bostock H & Bergmans J. (1994). Post-tetanic excitability changes and ectopic discharges in a human motor axon. *Brain* **117,** 913-928.

Bostock H, Burke D & Hales JP. (1994). Differences in behaviour of sensory and motor axons following release of ischaemia. *Brain* **117,** 225-234.

Bostock H, Cikurel K & Burke D. (1998). Threshold tracking techniques in the study of human peripheral nerve. *Muscle Nerve* **21,** 137-158.

Bostock H & Grafe P. (1985). Activity-dependent excitability changes in normal and demyelinated rat spinal root axons. *J Physiol* **365,** 239-257.

Bostock H, Lin CS, Howells J, Trevillion L, Jankelowitz S & Burke D. (2005). After-effects of near-threshold stimulation in single human motor axons. *J Physiol* **564,** 931-940.

Bostock H & Rothwell JC. (1997). Latent addition in motor and sensory fibres of human peripheral nerve. *J Physiol* **498,** 277-294.

Bostock H & Sears TA. (1978). The internodal axon membrane: electrical excitability and continuous conduction in segmental demyelination. *J Physiol* **280,** 273-301.

Bostock H, Sears TA & Sherratt RM. (1983). The spatial distribution of excitability and membrane current in normal and demyelinated mammalian nerve fibres. *J Physiol* **341,** 41-58.

Bostock H, Sherratt RM & Sears TA. (1978). Overcoming conduction failure in demyelinated nerve fibres by prolonging action potentials. *Nature* **274,** 385-387.

Bowe CM, Kocsis JD & Waxman SG. (1987). The association of the supernormal period and the depolarizing afterpotential in myelinated frog and rat sciatic nerve. *Neuroscience* **21,** 585-593.

Boycott AE. (1899). Note on the muscular response to two stimuli of the sciatic nerve (frog). *J Physiol* **24,** 144-154.

Bray GM, Rasminsky M & Aguayo AJ. (1981). Interactions between axons and their sheath cells. *Annu Rev Neurosci* **4,** 127-162.

Brewster AL, Bernard JA, Gall CM & Baram TZ. (2005). Formation of heteromeric hyperpolarization-activated cyclic nucleotide-gated (HCN) channels in the hippocampus is regulated by developmental seizures. *Neurobiol Dis* **19,** 200-207.

Brismar T. (1980). Potential clamp analysis of membrane currents in rat myelinated nerve fibres. *J Physiol* **298,** 171-184.

Brown HF, DiFrancesco D & Noble SJ. (1979). How does adrenaline accelerate the heart? *Nature* **280,** 235-236.

Bucchi A, Tognati A, Milanesi R, Baruscotti M & DiFrancesco D. (2006). Properties of ivabradine-induced block of HCN1 and HCN4 pacemaker channels. *J Physiol* **572,** 335-346.

Buchthal F & Rosenfalck A. (1966). Evoked action potentials and conduction velocity in human sensory nerves. *Brain Res* **3,** 1-122.

Buchthal F & Schmalbruch H. (1980). Motor unit of mammalian muscle. *Physiol Rev* **60,** 90-142.

Burgess DL, Kohrman DC, Galt J, Plummer NW, Jones JM, Spear B & Meisler MH. (1995). Mutation of a new sodium channel gene, Scn8a, in the mouse mutant 'motor endplate disease'. *Nat Genet* **10,** 461-465.

Burke D & Applegate C. (1989). Paraesthesiae and hypaesthesia following prolonged high-frequency stimulation of cutaneous afferents. *Brain* **112,** 913-929.

Burke D, Howells J, Trevillion L, Kiernan MC & Bostock H. (2007). Inflections in threshold electrotonus to depolarizing currents in sensory axons. *Muscle Nerve* **36,** 849-852.

Burke D, Howells J, Trevillion L, McNulty PA, Jankelowitz SK & Kiernan MC. (2009). Threshold behaviour of human axons explored using subthreshold perturbations to membrane potential. *J Physiol* **587,** 491-504.

Burke D, Kiernan MC & Bostock H. (2001). Excitability of human axons. *Clin Neurophysiol* **112,** 1575-1585.

Burke D, Kiernan MC, Mogyoros I & Bostock H. (1997). Susceptibility to conduction block: differences in the biophysical properties of cutaneous afferents and motor axons. In *Physiology of ALS and Related Diseases*, ed. Kimura J & Kaji R, pp. 43-53. Elsevier, Amsterdam.

Burke D, Mogyoros I, Vagg R & Kiernan MC. (1999). Temperature dependence of excitability indices of human cutaneous afferents. *Muscle Nerve* **22,** 51-60.

Caldwell JH, Schaller KL, Lasher RS, Peles E & Levinson SR. (2000). Sodium channel Na(v)1.6 is localized at nodes of ranvier, dendrites, and synapses. *Proc Natl Acad Sci U S A* **97,** 5616-5620.

Campero M, Serra J, Bostock H & Ochoa JL. (2004). Partial reversal of conduction slowing during repetitive stimulation of single sympathetic efferents in human skin. *Acta Physiol Scand* **182,** 305-311.

Cappelen-Smith C, Kuwabara S, Lin CS, Mogyoros I & Burke D. (2000). Activity-dependent hyperpolarization and conduction block in chronic inflammatory demyelinating polyneuropathy. *Ann Neurol* **48,** 826-832.

Cappelen-Smith C, Kuwabara S, Lin CS, Mogyoros I & Burke D. (2001). Membrane properties in chronic inflammatory demyelinating polyneuropathy. *Brain* **124,** 2439-2447.

Carnevale NT & Wachtel H. (1982). "Subthreshold" oscillations underlying burst firing patterns. In *Abnormal nerves and muscles as impulse generators*, ed. Culp WJ & Ochoa JL, pp. 490-512. Oxford University Press.

Catterall WA, Goldin AL & Waxman SG. (2005). International Union of Pharmacology. XLVII. Nomenclature and structure-function relationships of voltage-gated sodium channels. *Pharmacol Rev* **57,** 397-409.

Cestèle S & Catterall WA. (2000). Molecular mechanisms of neurotoxin action on voltage-gated sodium channels. *Biochimie* **82,** 883-892.

Chandler WK & Meves H. (1970a). Evidence for two types of sodium conductance in axons perfused with sodium fluoride solution. *J Physiol* **211,** 653-678.

Chandler WK & Meves H. (1970b). Sodium and potassium currents in squid axons perfused with fluoride solutions. *J Physiol* **211,** 623-652.

Chaplan SR, Guo HQ, Lee DH, Luo L, Liu C, Kuei C, Velumian AA, Butler MP, Brown SM & Dubin AE. (2003). Neuronal hyperpolarization-activated pacemaker channels drive neuropathic pain. *J Neurosci* **23,** 1169-1178.

Chen K, Aradi I, Thon N, Eghbal-Ahmadi M, Baram TZ & Soltesz I. (2001a). Persistently modified h-channels after complex febrile seizures convert the seizure-induced enhancement of inhibition to hyperexcitability. *Nat Med* **7,** 331-337.

Chen S, Wang J & Siegelbaum SA. (2001b). Properties of hyperpolarization-activated pacemaker current defined by coassembly of HCN1 and HCN2 subunits and basal modulation by cyclic nucleotide. *J Gen Physiol* **117,** 491-504.

Chiu SY & Ritchie JM. (1981). Evidence for the presence of potassium channels in the paranodal region of acutely demyelinated mammalian single nerve fibres. *J Physiol* **313,** 415-437.

Chiu SY, Ritchie JM, Rogart RB & Stagg D. (1979). A quantitative description of membrane currents in rabbit myelinated nerve. *J Physiol* **292,** 149-166.

Cole KS. (1933). Electric conductance of biological systems. In *Cold Spring Harbor Symposia on Quantitative Biology*, pp. 107-116. Cold Spring Harbor Laboratory Press.

Cole KS. (1941). Rectification and inductance in the squid giant axon. *J Gen Physiol* **25,** 29-51.

Cole KS & Baker RF. (1941). Transverse impedance of the squid giant axon during current flow. *J Gen Physiol* **24,** 535-549.

Cole KS & Curtis HJ. (1936). Electric impedance of nerve and muscle. In *Cold Spring Harbor Symposia on Quantitative Biology*, pp. 73-89. Cold Spring Harbor Laboratory Press.

Cole KS & Curtis HJ. (1939). Electric impedance of the squid giant axon during activity. *J Gen Physiol* **22,** 649-670.

Craner MJ, Hains BC, Lo AC, Black JA & Waxman SG. (2004). Co-localization of sodium channel Nav1.6 and the sodium-calcium exchanger at sites of axonal injury in the spinal cord in EAE. *Brain* **127,** 294-303.

Cravioto H. (1965). The role of Schwann cells in the development of human peripheral nerves. An electron microscopic study. *J Ultrastruct Res* **12,** 634-651.

Cregg R, Momin A, Rugiero F, Wood JN & Zhao J. (2010). Pain channelopathies. *J Physiol* **588,** 1897-1904.

Culp WJ, Ochoa JL & Torebjörk E. (1982). Ectopic impulse generation in myelinated sensory nerve fibers in man. In *Abnormal nerves and muscles as impulse generators*, ed. Culp WJ & Ochoa JL, pp. 490-512. Oxford University Press.

David G, Barrett JN & Barrett EF. (1993). Activation of internodal potassium conductance in rat myelinated axons. *J Physiol* **472,** 177-202.

David G, Modney B, Scappaticci KA, Barrett JN & Barrett EF. (1995). Electrical and morphological factors influencing the depolarizing after-potential in rat and lizard myelinated axons. *J Physiol* **489,** 141-157.

Davis FA, Schauf CL, Reed BJ & Kesler RL. (1975). Experimental studies of the effects of extrinsic factors on conduction in normal and demyelinated nerve. 1. Temperature. *J Neurol Neurosurg Psychiatry* **39,** 442-448.

Debanne D, Campanac E, Bialowas A, Carlier E & Alcaraz G. (2011). Axon physiology. *Physiol Rev* **91,** 555-602.

Descoeur J, Pereira V, Pizzoccaro A, Francois A, Ling B, Maffre V, Couette B, Busserolles J, Courteix C, Noel J, Lazdunski M, Eschalier A, Authier N & Bourinet E. (2011). Oxaliplatin-induced cold hypersensitivity is due to remodelling of ion channel expression in nociceptors. *EMBO Mol Med* **3,** 266-278.

Devaux JJ, Kleopa KA, Cooper EC & Scherer SS. (2004). KCNQ2 is a nodal K+ channel. *J Neurosci* **24,** 1236-1244.

Devor M. (2006). Sodium channels and mechanisms of neuropathic pain. *J Pain* **7,** S3-S12.

DiFrancesco D. (1981). A study of the ionic nature of the pace-maker current in calf Purkinje fibres. *J Physiol* **314,** 377-393.

DiFrancesco D. (2006). Serious workings of the funny current. *Prog Biophys Mol Biol* **90,** 13-25.

Dodge FA & Frankenhaeuser B. (1958). Membrane currents in isolated frog nerve fibre under voltage clamp conditions. *J Physiol* **143,** 76-90.

Doyle DA, Morais Cabral J, Pfuetzner RA, Kuo A, Gulbis JM, Cohen SL, Chait BT & MacKinnon R. (1998). The structure of the potassium channel: molecular basis of K+ conduction and selectivity. *Science* **280,** 69-77.

du Bois-Reymond E. (1849). *Untersuchungen über thierische Elektricität*, vol. 1. G. Reimer.

Dubois JM. (1981). Evidence for the existence of three types of potassium channels in the frog Ranvier node membrane. *J Physiol* **318,** 297-316.

Dubois JM & Bergman C. (1975). Late sodium current in the node of Ranvier. *Pflügers Archiv* **357,** 145-148.

Duchen LW & Stefani E. (1971). Electrophysiological studies of neuromuscular transmission in hereditary 'motor end-plate disease' of the mouse. *J Physiol* **212,** 535-548.

Dupree JL, Girault JA & Popko B. (1999). Axo-glial interactions regulate the localization of axonal paranodal proteins. *J Cell Biol* **147,** 1145-1152.

Eduardo E & Burke D. (1988). The optimal recording electrode configuration for compound sensory action potentials. *J Neurol Neurosurg Psychiatry* **51,** 684-687.

Eisner DA & Lederer WJ. (1985). Na-Ca exchange: stoichiometry and electrogenicity. *Am J Physiol* **248,** C189-202.

Emery EC, Young GT, Berrocoso EM, Chen L & McNaughton PA. (2011). HCN2 ion channels play a central role in inflammatory and neuropathic pain. *Science* **333,** 1462-1466.

Enyedi P & Czirják G. (2010). Molecular background of leak K+ currents: two-pore domain potassium channels. *Physiol Rev* **90,** 559-605.

Erlanger J & Blair EA. (1938). Comparative observations on motor and sensory fibers with special reference to repetitiousness. *Am J Physiol* **121,** 431-453.

Farrar MA, Park SB, Lin CS & Kiernan MC. (2013). Evolution of peripheral nerve function in humans: novel insights from motor nerve excitability. *J Physiol* **591,** 273-286.

Fitzhugh R. (1962). Computation of impulse initiation and saltatory conduction in a myelinated nerve fiber. *Biophys J* **2,** 11-21.

Frankenhaeuser B & Huxley AF. (1964). The action potential in the myelinated nerve fiber of Xenopus laevis as computed on the basis of voltage clamp data. *J Physiol* **171,** 302-315.

Frankenhaeuser B & Moore LE. (1963). The effect of temperature on the sodium and potassium permeability changes in myelinated nerve fibres of Xenopus laevis. *J Physiol* **169,** 431-437.

French CR, Sah P, Buckett KJ & Gage PW. (1990). A voltage-dependent persistent sodium current in mammalian hippocampal neurons. *J Gen Physiol* **95,** 1139-1157.

Fricke H. (1923). The electric capacity of cell suspensions. *Phys Rev* **21,** 708-709.

Fricke H. (1925). The electric capacity of suspensions with special reference to blood. *J Gen Physiol* **9,** 137-152.

Friman G, Schiller HH & Schwartz M. (1977). Distubed neuromuscular transmission in viral infections. *Scand J Infect Dis* **9,** 99-103.

Gandevia SC. (2001). Spinal and supraspinal factors in human muscle fatigue. *Physiol Rev* **81,** 1725-1789.

Gandevia SC & Burke D. (2004). Peripheral Motor System. In *The Human Nervous System*, 2 edn, ed. Paxinos G & Mai JK, pp. 113-133. Elsevier.

Gasser HS & Grundfest H. (1939). Axon diameters in relation to the spike dimensions and the conduction velocity in mammalian A fibers. *Am J Physiol* **127,** 393-414.

Geddes LA. (1994). The first stimulators-reviewing the history of electrical stimulation and the devices crucial to its development. *IEEE Eng Med Biol Mag* **13,** 532-542.

Geddes LA & Bourland JD. (1985a). The strength-duration curve. *IEEE Trans Biomed Eng* **32,** 458-459.

Geddes LA & Bourland JD. (1985b). Tissue stimulation: theoretical considerations and practical applications. *Med Biol Eng Comput* **23,** 131-137.

George A, Serra J, Navarro X & Bostock H. (2007). Velocity recovery cycles of single C fibres innervating rat skin. *J Physiol* **578,** 213-232.

Gilliatt RW & Willison RG. (1963). The refractory and supernormal periods of the human median nerve. *J Neurol Neurosurg Psychiatry* **26,** 136-147.

Goldman L & Albus JS. (1968). Computation of impulse conduction in myelinated fibers; theoretical basis of the velocity-diameter relation. *Biophys J* **8,** 596-607.

Goldstein SA, Bayliss DA, Kim D, Lesage F, Plant LD & Rajan S. (2005). International Union of Pharmacology. LV. Nomenclature and molecular relationships of two-P potassium channels. *Pharmacol Rev* **57,** 527-540.

Goldstein SA, Bockenhauer D, O'Kelly I & Zilberberg N. (2001). Potassium leak channels and the KCNK family of two-P-domain subunits. *Nat Rev Neurosci* **2,** 175-184.

Gordon TR, Kocsis JD & Waxman SG. (1990). Electrogenic pump (Na+/K(+)-ATPase) activity in rat optic nerve. *Neuroscience* **37,** 829-837.

Gotch F & Burch GJ. (1899). The electrical response of nerve to two stimuli. *J Physiol* **24,** 410-426.

Grafe P, Quasthoff S, Grosskreutz J & Alzheimer C. (1997). Function of the hyperpolarization-activated inward rectification in nonmyelinated peripheral rat and human axons. *J Neurophysiol* **77,** 421-426.

Graham HT. (1935). The subnormal period of nerve response. *Am J Physiol* **111,** 452-465.

Grissmer S. (1986). Properties of potassium and sodium channels in frog internode. *J Physiol* **381,** 119-134.

Gutfreund Y, Yarom Y & Segev I. (1995). Subthreshold oscillations and resonant frequency in guinea-pig cortical neurons: physiology and modelling. *J Physiol* **483,** 621-640.

Guthrie TC & Nelson DA. (1995). Influence of temperature changes on multiple sclerosis: critical review of mechanisms and research potential. *J Neurol Sci* **129,** 1-8.

Gutman GA, Chandy KG, Grissmer S, Lazdunski M, McKinnon D, Pardo LA, Robertson GA, Rudy B, Sanguinetti MC, Stuhmer W & Wang X. (2005). International Union of Pharmacology. LIII. Nomenclature and molecular relationships of voltage-gated potassium channels. *Pharmacol Rev* **57,** 473-508.

Guttman R. (1971). The effect of temperature on the function of excitable membranes. In *Biophysics and physiology of excitable membranes*, ed. Adelman WJJ, pp. 320-336. Van Nostrand, New York.

Hales JP, Lin CS & Bostock H. (2004). Variations in excitability of single human motor axons, related to stochastic properties of nodal sodium channels. *J Physiol* **559,** 953-964.

Halter JA & Clark JW. (1991). A distributed-parameter model of the myelinated nerve-fiber. *J Theor Biol* **148,** 345-382.

Han SE, Boland RA, Krishnan AV, Vucic S, Lin CS & Kiernan MC. (2009). Ischaemic sensitivity of axons in carpal tunnel syndrome. *J Peripher Nerv Syst* **14,** 190-200.

Han SE, Lin CS, Boland RA & Kiernan MC. (2011). Nerve compression, membrane excitability, and symptoms of carpal tunnel syndrome. *Muscle Nerve* **44,** 402-409.

Hart G. (1983). The kinetics and temperature dependence of the pace-maker current i(f) in sheep Purkinje fibres. *J Physiol* **337,** 401-416.

Henneman E & Olson CB. (1965). Relations between structure and function in the design of skeletal muscles. *J Neurophysiol* **28,** 581-598.

Henneman E, Somjen G & Carpenter DO. (1965). Functional significance of cell size in spinal motoneurons. *J Neurophysiol* **28,** 560-580.

Hill AV. (1936). Excitation and accommodation in nerve. *Proc R Soc Lond B Biol Sci* **119,** 305-355.

Hille B. (1967). Selective inhibition of delayed potassium currents in nerve by tetraethylammonium ion. *J Gen Physiol* **50,** 1287-&.

Hille B. (1972). The permeability of the sodium channel to metal cations in myelinated nerve. *J Gen Physiol* **59,** 637-658.

Hille B. (1992). *Ionic channels of excitable membranes*. Sinauer Associates, Sunderland, Mass.

Hodgkin AL. (1937). Evidence for electrical transmission in nerve: Part II. *J Physiol* **90,** 211-232.

Hodgkin AL & Huxley AF. (1947). Potassium leakage from an active nerve fibre. *J Physiol* **106,** 341-367.

Hodgkin AL & Huxley AF. (1952a). The components of membrane conductance in the giant axon of Loligo. *J Physiol* **116,** 473-496.

Hodgkin AL & Huxley AF. (1952b). Currents carried by sodium and potassium ions through the membrane of the giant axon of Loligo. *J Physiol* **116,** 449-472.

Hodgkin AL & Huxley AF. (1952c). The dual effect of membrane potential on sodium conductance in the giant axon of Loligo. *J Physiol* **116,** 497-506.

Hodgkin AL & Huxley AF. (1952d). A quantitative description of membrane current and its application to conduction and excitation in nerve. *J Physiol* **117,** 500-544.

Hodgkin AL, Huxley AF & Katz B. (1952). Measurement of current-voltage relations in the membrane of the giant axon of Loligo. *J Physiol* **116,** 424-448.

Hodgkin AL & Katz B. (1949). The effect of temperature on the electrical activity of the giant axon of the squid. *J Physiol* **109,** 240-249.

Hofmann F, Biel M & Kaupp UB. (2005). International Union of Pharmacology. LI. Nomenclature and structure-function relationships of cyclic nucleotide-regulated channels. *Pharmacol Rev* **57,** 455-462.

Holsheimer J. (2003). Principles of neurostimulation. In *Electrical Stimulation and the relief of Pain*, ed. Simpson BA, pp. 17-36. Elsevier Science, Amsterdam.

Honmou O, Utzschneider DA, Rizzo MA, Bowe CM, Waxman SG & Kocsis JD. (1994). Delayed depolarization and slow sodium currents in cutaneous afferents. *J Neurophysiol* **71,** 1627-1637.

Hoorweg JL. (1892). Ueber die elektrische Nervenerregung. *Pflügers Archiv* **52,** 87-108.

Horn S, Quasthoff S, Grafe P, Bostock H, Renner R & Schrank B. (1996). Abnormal axonal inward rectification in diabetic neuropathy. *Muscle Nerve* **19,** 1268-1275.

Hu H, Vervaeke K, Graham LJ & Storm JF. (2009a). Complementary theta resonance filtering by two spatially segregated mechanisms in CA1 hippocampal pyramidal neurons. *J Neurosci* **29,** 14472-14483.

Hu H, Vervaeke K & Storm JF. (2002). Two forms of electrical resonance at theta frequencies, generated by M-current, h-current and persistent Na+ current in rat hippocampal pyramidal cells. *J Physiol* **545,** 783-805.

Hu W, Tian C, Li T, Yang M, Hou H & Shu Y. (2009b). Distinct contributions of Na(v)1.6 and Na(v)1.2 in action potential initiation and backpropagation. *Nat Neurosci* **12,** 996-1002.

Hursh JB. (1939). Conduction velocity and diameter of nerver fibers. *Am J Physiol* **127,** 131-139.

Hutcheon B, Miura RM & Puil E. (1996a). Models of subthreshold membrane resonance in neocortical neurons. *J Neurophysiol* **76,** 698-714.

Hutcheon B, Miura RM & Puil E. (1996b). Subthreshold membrane resonance in neocortical neurons. *J Neurophysiol* **76,** 683-697.

Hutcheon B & Yarom Y. (2000). Resonance, oscillation and the intrinsic frequency preferences of neurons. *Trends Neurosci* **23,** 216-222.

Huxley AF & Stämpfli R. (1949). Evidence for saltatory conduction in peripheral myelinated nerve fibres. *J Physiol* **108,** 315-339.

Irnich W. (2002). Georges Weiss' fundamental law of electrostimulation is 100 years old. *Pacing Clin Electrophysiol* **25,** 245-248.

Ishii TM, Takano M & Ohmori H. (2001). Determinants of activation kinetics in mammalian hyperpolarization-activated cation channels. *J Physiol* **537,** 93-100.

Izhikevich EM, Desai NS, Walcott EC & Hoppensteadt FC. (2003). Bursts as a unit of neural information: selective communication via resonance. *Trends Neurosci* **26,** 161-167.

Jacobs JM & Love S. (1985). Qualitative and quantitative morphology of human sural nerve at different ages. *Brain* **108,** 897-924.

Jankelowitz SK, Howells J & Burke D. (2007a). Plasticity of inwardly rectifying conductances following a corticospinal lesion in human subjects. *J Physiol* **581,** 927-940.

Jankelowitz SK, McNulty PA & Burke D. (2007b). Changes in measures of motor axon excitability with age. *Clin Neurophysiol* **118,** 1397-1404.

Jiang YQ, Sun Q, Tu HY & Wan Y. (2008a). Characteristics of HCN channels and their participation in neuropathic pain. *Neurochem Res* **33,** 1979-1989.

Jiang YQ, Xing GG, Wang SL, Tu HY, Chi YN, Li J, Liu FY, Han JS & Wan Y. (2008b). Axonal accumulation of hyperpolarization-activated cyclic nucleotide-gated cation channels contributes to mechanical allodynia after peripheral nerve injury in rat. *Pain* **137,** 495-506.

Johansson RS & Vallbo ÅB. (1983). Tactile sensory coding in the glabrous skin of the human hand. *Trends Neurosci* **6,** 27-32.

Jonas P, Brau ME, Hermsteiner M & Vogel W. (1989). Single-channel recording in myelinated nerve fibers reveals one type of Na channel but different K channels. *Proc Natl Acad Sci U S A* **86,** 7238-7242.

Kaji R, Bostock H, Kohara N, Murase N, Kimura J & Shibasaki H. (2000). Activity-dependent conduction block in multifocal motor neuropathy. *Brain* **123,** 1602-1611.

Kapoor R, Li YG & Smith KJ. (1997). Slow sodium-dependent potential oscillations contribute to ectopic firing in mammalian demyelinated axons. *Brain* **120,** 647-652.

Kapoor R, Smith KJ, Felts PA & Davies M. (1993). Internodal potassium currents can generate ectopic impulses in mammalian myelinated axons. *Brain Res* **611,** 165-169.

Kato G. (1924). *The theory of decrementless conduction*. Nankodo, Tokyo.

Kato GI. (1970). The road a scientist followed. Notes of Japanese physiology as I myself experienced it. *Annu Rev Physiol* **32,** 1-20.

Kaupp UB & Seifert R. (2001). Molecular diversity of pacemaker ion channels. *Annu Rev Physiol* **63,** 235-257.

Kay AR, Sugimori M & Llinas R. (1998). Kinetic and stochastic properties of a persistent sodium current in mature guinea pig cerebellar Purkinje cells. *J Neurophysiol* **80,** 1167-1179.

Kiernan MC & Bostock H. (2000). Effects of membrane polarization and ischaemia on the excitability properties of human motor axons. *Brain* **123,** 2542-2551.

Kiernan MC, Burke D, Andersen KV & Bostock H. (2000). Multiple measures of axonal excitability: a new approach in clinical testing. *Muscle Nerve* **23,** 399-409.

Kiernan MC, Cikurel K & Bostock H. (2001a). Effects of temperature on the excitability properties of human motor axons. *Brain* **124,** 816-825.

Kiernan MC, Hales JP, Gracies JM, Mogyoros I & Burke D. (1997a). Paraesthesiae induced by prolonged high frequency stimulation of human cutaneous afferents. *J Physiol* **501,** 461-471.

Kiernan MC, Isbister GK, Lin CS, Burke D & Bostock H. (2005). Acute tetrodotoxin-induced neurotoxicity after ingestion of puffer fish. *Ann Neurol* **57,** 339-348.

Kiernan MC, Lin CS, Andersen KV, Murray NM & Bostock H. (2001b). Clinical evaluation of excitability measures in sensory nerve. *Muscle Nerve* **24,** 883-892.

Kiernan MC, Lin CS & Burke D. (2004). Differences in activity-dependent hyperpolarization in human sensory and motor axons. *J Physiol* **558,** 341-349.

Kiernan MC, Mogyoros I & Burke D. (1996). Differences in the recovery of excitability in sensory and motor axons of human median nerve. *Brain* **119,** 1099-1105.

Kiernan MC, Mogyoros I & Burke D. (1999). Conduction block in carpal tunnel syndrome. *Brain* **122,** 933-941.

Kiernan MC, Mogyoros I, Hales JP, Gracies JM & Burke D. (1997b). Excitability changes in human cutaneous afferents induced by prolonged repetitive axonal activity. *J Physiol* **500,** 255-264.

Kiernan MC, Walters RJ, Andersen KV, Taube D, Murray NM & Bostock H. (2002). Nerve excitability changes in chronic renal failure indicate membrane depolarization due to hyperkalaemia. *Brain* **125,** 1366-1378.

Kiss T. (2008). Persistent Na-channels: origin and function. A review. *Acta Biol Hung* **59 Suppl,** 1-12.

Kleitman N & Bunge RP. (1995). The Schwann cell: Morphology and development. In *The Axon: Structure, Function and Pathophysiology*, ed. Waxman SG, Kocsis JD & Stys PK, pp. 97-115. Oxford University Press, New York.

Koch C. (1984). Cable theory in neurons with active, linearized membranes. *Biol Cybern* **50,** 15-33.

Kocsis JD, Bowe CM & Waxman SG. (1986). Different effects of 4-aminopyridine on sensory and motor fibers: pathogenesis of paresthesias. *Neurology* **36,** 117-120.

Kocsis JD, Waxman SG, Hildebrand C & Ruiz JA. (1982). Regenerating mammalian nerve fibres: changes in action potential waveform and firing characteristics following blockage of potassium conductance. *Proc R Soc Lond B Biol Sci* **217,** 77-87.

Koles ZJ & Rasminsky M. (1972). A computer simulation of conduction in demyelinated nerve fibres. *J Physiol* **227,** 351-364.

Kouranova EV, Strassle BW, Ring RH, Bowlby MR & Vasilyev DV. (2008). Hyperpolarization-activated cyclic nucleotide-gated channel mRNA and protein expression in large versus small diameter dorsal root ganglion neurons: correlation with hyperpolarization-activated current gating. *Neuroscience* **153,** 1008-1019.

Krarup C. (2004). Compound sensory action potential in normal and pathological human nerves. *Muscle Nerve* **29,** 465-483.

Krarup C & Moldovan M. (2009). Nerve conduction and excitability studies in peripheral nerve disorders. *Curr Opin Neurol* **22,** 460-466.

Krishnan AV, Goldstein D, Friedlander M & Kiernan MC. (2005a). Oxaliplatin-induced neurotoxicity and the development of neuropathy. *Muscle Nerve* **32,** 51-60.

Krishnan AV & Kiernan MC. (2005). Altered nerve excitability properties in established diabetic neuropathy. *Brain* **128,** 1178-1187.

Krishnan AV, Lin CS, Park SB & Kiernan MC. (2009). Axonal ion channels from bench to bedside: a translational neuroscience perspective. *Prog Neurobiol* **89,** 288-313.

Krishnan AV, Phoon RK, Pussell BA, Charlesworth JA, Bostock H & Kiernan MC. (2005b). Altered motor nerve excitability in end-stage kidney disease. *Brain* **128,** 2164-2174.

Krishnan AV, Phoon RK, Pussell BA, Charlesworth JA & Kiernan MC. (2006). Sensory nerve excitability and neuropathy in end stage kidney disease. *J Neurol Neurosurg Psychiatry* **77,** 548-551.

Kugelberg E. (1944). Accommodation in human nerves and its significance for the symptoms in circulatory disturbances and tetany. *Acta Physiol Scand* **8 (S24),** 1-105.

Kugelberg E & Skoglund CR. (1946). Responses of single human motor units to electrical stimulation. *J Neurophysiol* **9,** 391-398.

Kuwabara S & Misawa S. (2008). Pharmacologic intervention in axonal excitability: in vivo assessment of nodal persistent sodium currents in human neuropathies. *Curr Mol Pharmacol* **1,** 61-67.

Lai HC & Jan LY. (2006). The distribution and targeting of neuronal voltage-gated ion channels. *Nat Rev Neurosci* **7,** 548-562.

Lapicque L. (1907). Recherches quantitatives sur l'excitation électrique des nerfs traitée comme une polarisation. *J Physiol Pathol Générale* **9,** 567-578.

Lapicque L. (1909). Définition expérimentale de l'excitabilité. *Comp Rend Soc Biol* **67,** 280-283.

Li Y, Gorassini MA & Bennett DJ. (2004). Role of persistent sodium and calcium currents in motoneuron firing and spasticity in chronic spinal rats. *J Neurophysiol* **91,** 767-783.

Lillie RS. (1925). Factors affecting transmission and recovery in the passive iron nerve model. *J Gen Physiol* **7,** 473-507.

Lin CS, Krishnan AV, Lee MJ, Zagami AS, You HL, Yang CC, Bostock H & Kiernan MC. (2008). Nerve function and dysfunction in acute intermittent porphyria. *Brain* **131,** 2510-2519.

Lin CS, Kuwabara S, Cappelen-Smith C & Burke D. (2002). Responses of human sensory and motor axons to the release of ischaemia and to hyperpolarizing currents. *J Physiol* **541,** 1025-1039.

Llinás RR. (1988). The intrinsic electrophysiological properties of mammalian neurons: insights into central nervous system function. *Science* **242,** 1654-1664.

Lorente de Nó R. (1947a). A study of nerve physiology. *Stud Rockefeller Inst Med Res Repr* **132,** 1-548.

Lorente de Nó R. (1947b). A study of nerve physiology. *Stud Rockefeller Inst Med Res Repr* **131,** 1-496.

Lucas K. (1909). The "all or none" contraction of the amphibian skeletal muscle fibre. *J Physiol* **38,** 113-133.

Ludin HP & Beyeler F. (1977). Temperature dependence of normal sensory nerve action potentials. *J Neurol* **216,** 173-180.

Ludwig A, Zong X, Jeglitsch M, Hofmann F & Biel M. (1998). A family of hyperpolarization-activated mammalian cation channels. *Nature* **393,** 587-591.

Maher MP, Wu NT, Guo HQ, Dubin AE, Chaplan SR & Wickenden AD. (2009). HCN channels as targets for drug discovery. *Comb Chem High Throughput Screen* **12,** 64-72.

Männikkö R, Elinder F & Larsson HP. (2002). Voltage-sensing mechanism is conserved among ion channels gated by opposite voltages. *Nature* **419,** 837-841.

Mantegazza M, Curia G, Biagini G, Ragsdale DS & Avoli M. (2010). Voltage-gated sodium channels as therapeutic targets in epilepsy and other neurological disorders. *Lancet Neurol* **9,** 413-424.

Marchand P & Marmet L. (1983). Binomial smoothing filter: A way to avoid some pitfalls of least squares polynomial smoothing. *Review of scientific instruments* **54,** 1034-1041.

Markram H, Wang Y & Tsodyks M. (1998). Differential signaling via the same axon of neocortical pyramidal neurons. *Proc Natl Acad Sci U S A* **95,** 5323-5328.

Maurer K, Wacker J, Vastani N, Seifert B & Spahn DR. (2010). Changes in axonal excitability of primary sensory afferents with general anaesthesia in humans. *Br J Anaesth* **105,** 648-656.

Mayer ML & Westbrook GL. (1983). A voltage-clamp analysis of inward (anomalous) rectification in mouse spinal sensory ganglion neurones. *J Physiol* **340,** 19-45.

McClure KJ, Maher M, Wu N, Chaplan SR, Eckert WA, 3rd, Lee DH, Wickenden AD, Hermann M, Allison B, Hawryluk N, Breitenbucher JG & Grice CA. (2011). Discovery of a novel series of selective HCN1 blockers. *Bioorg Med Chem Lett* **21,** 5197-5201.

McCormick DA & Pape HC. (1990). Properties of a hyperpolarization-activated cation current and its role in rhythmic oscillation in thalamic relay neurones. *J Physiol* **431,** 291-318.

McIntyre CC, Richardson AG & Grill WM. (2002). Modeling the excitability of mammalian nerve fibers: influence of afterpotentials on the recovery cycle. *J Neurophysiol* **87,** 995-1006.

Melchiorre M, Del Lungo M, Guandalini L, Martini E, Dei S, Manetti D, Scapecchi S, Teodori E, Sartiani L, Mugelli A, Cerbai E & Romanelli MN. (2010). Design, synthesis, and preliminary biological evaluation of new isoform-selective f-current blockers. *J Med Chem* **53,** 6773-6777.

Mierzwa A, Shroff S & Rosenbluth J. (2010). Permeability of the paranodal junction of myelinated nerve fibers. *J Neurosci* **30,** 15962-15968.

Miller DJ. (2004). Sydney Ringer; physiological saline, calcium and the contraction of the heart. *J Physiol* **555,** 585-587.

Mitrović N, Quasthoff S & Grafe P. (1993). Sodium channel inactivation kinetics of rat sensory and motor nerve fibres and their modulation by glutathione. *Pflügers Archiv* **425,** 453-461.

Mogyoros I, Bostock H & Burke D. (2000). Mechanisms of paresthesias arising from healthy axons. *Muscle Nerve* **23,** 310-320.

Mogyoros I, Kiernan MC & Burke D. (1996). Strength-duration properties of human peripheral nerve. *Brain* **119,** 439-447.

Mogyoros I, Kiernan MC, Burke D & Bostock H. (1997). Excitability changes in human sensory and motor axons during hyperventilation and ischaemia. *Brain* **120,** 317-325.

Mogyoros I, Kiernan MC, Burke D & Bostock H. (1998). Strength-duration properties of sensory and motor axons in amyotrophic lateral sclerosis. *Brain* **121,** 851-859.

Moldovan M, Alvarez S, Romer Rosberg M & Krarup C. (2013). Axonal voltage-gated ion channels as pharmacological targets for pain. *Eur J Pharmacol* **708,** 105-112.

Moldovan M & Krarup C. (2004). Mechanisms of hyperpolarization in regenerated mature motor axons in cat. *J Physiol* **560,** 807-819.

Momin A, Cadiou H, Mason A & McNaughton PA. (2008). Role of the hyperpolarization-activated current (I(h)) in somatosensory neurons. *J Physiol* **586,** 5911-5929.

Momin A & McNaughton PA. (2009). Regulation of firing frequency in nociceptive neurons by pro-inflammatory mediators. *Exp Brain Res* **196,** 45-52.

Momin A & Wood JN. (2008). Sensory neuron voltage-gated sodium channels as analgesic drug targets. *Curr Opin Neurobiol* **18,** 383-388.

Moore JW. (1958). Temperature and drug effects on squid axon membrane ion conductances. *Fed Proc* **17,** 113-113.

Moosmang S, Stieber J, Zong X, Biel M, Hofmann F & Ludwig A. (2001). Cellular expression and functional characterization of four hyperpolarization-activated pacemaker channels in cardiac and neuronal tissues. *Eur J Biochem* **268,** 1646-1652.

Much B, Wahl-Schott C, Zong X, Schneider A, Baumann L, Moosmang S, Ludwig A & Biel M. (2003). Role of subunit heteromerization and N-linked glycosylation in the formation of functional hyperpolarization-activated cyclic nucleotide-gated channels. *J Biol Chem* **278,** 43781-43786.

Munsch T & Pape HC. (1999). Modulation of the hyperpolarization-activated cation current of rat thalamic relay neurones by intracellular pH. *J Physiol* **519,** 493-504.

Narahashi T, Moore JW & Scott WR. (1964). Tetrodotoxin blockage of sodium conductance increase in lobster giant axons. *J Gen Physiol* **47,** 965-974.

Narayanan R & Johnston D. (2008). The h channel mediates location dependence and plasticity of intrinsic phase response in rat hippocampal neurons. *J Neurosci* **28,** 5846-5860.

Nernst W. (1908). Zur Theorie des elektrischen Reizes. *Pflügers Archiv* **122,** 275-314.

Neumcke B & Stämpfli R. (1982). Sodium currents and sodium-current fluctuations in rat myelinated nerve fibres. *J Physiol* **329,** 163-184.

Ng K, Howells J, Pollard JD & Burke D. (2008). Up-regulation of slow K(+) channels in peripheral motor axons: a transcriptional channelopathy in multiple sclerosis. *Brain* **131,** 3062-3071.

Ng K, Howells J, Pollard JD & Burke D. (2013). Different mechanisms underlying changes in excitability of peripheral nerve sensory and motor axons in multiple sclerosis. *Muscle Nerve* **47,** 53-60.

Nilsson I & Berthold CH. (1988). Axon classes and internodal growth in the ventral spinal root L7 of adult and developing cats. *J Anat* **156,** 71-96.

Nodera H, Bostock H, Kuwabara S, Sakamoto T, Asanuma K, Jia-Ying S, Ogawara K, Hattori N, Hirayama M, Sobue G & Kaji R. (2004). Nerve excitability properties in Charcot-Marie-Tooth disease type 1A. *Brain* **127,** 203-211.

Nodera H & Kaji R. (2006). Nerve excitability testing and its clinical application to neuromuscular diseases. *Clin Neurophysiol* **117,** 1902-1916.

Nodera H & Rutkove SB. (2012a). Accommodation to hyperpolarizing currents: differences between motor and sensory nerves in mice. *Neurosci Lett* **518,** 111-116.

Nodera H & Rutkove SB. (2012b). Changes of the peripheral nerve excitability in vivo induced by the persistent Na+ current blocker ranolazine. *Neurosci Lett* **518,** 36-40.

Notomi T & Shigemoto R. (2004). Immunohistochemical localization of Ih channel subunits, HCN1-4, in the rat brain. *J Comp Neurol* **471,** 241-276.

Ochoa J. (1971). The sural nerve of the human foetus: electron microscope observations and counts of axons. *J Anat* **108,** 231-245.

Orio P, Madrid R, de la Pena E, Parra A, Meseguer V, Bayliss DA, Belmonte C & Viana F. (2009). Characteristics and physiological role of hyperpolarization activated currents in mouse cold thermoreceptors. *J Physiol* **587,** 1961-1976.

Palti Y & Adelman WJ. (1969). Measurement of axonal membrane conductances and capacity by means of a varying potential control voltage clamp. *J Membrane Biol* **1,** 431-&.

Papazian DM, Schwarz TL, Tempel BL, Jan YN & Jan LY. (1987). Cloning of genomic and complementary DNA from Shaker, a putative potassium channel gene from Drosophila. *Science* **237,** 749-753.

Pape HC. (1996). Queer current and pacemaker: the hyperpolarization-activated cation current in neurons. *Annu Rev Physiol* **58,** 299-327.

Park SB, Goldstein D, Lin CS, Krishnan AV, Friedlander ML & Kiernan MC. (2009a). Acute abnormalities of sensory nerve function associated with oxaliplatin-induced neurotoxicity. *J Clin Oncol* **27,** 1243-1249.

Park SB, Lin CS, Krishnan AV, Goldstein D, Friedlander ML & Kiernan MC. (2009b). Oxaliplatin-induced neurotoxicity: changes in axonal excitability precede development of neuropathy. *Brain* **132,** 2712-2723.

Park SB, Lin CS, Krishnan AV, Goldstein D, Friedlander ML & Kiernan MC. (2011). Dose effects of oxaliplatin on persistent and transient Na+ conductances and the development of neurotoxicity. *PLoS One* **6,** e18469.

Pellegrino RG, Spencer PS & Ritchie JM. (1984). Sodium channels in the axolemma of unmyelinated axons: a new estimate. *Brain Res* **305,** 357-360.

Peters HC, Hu H, Pongs O, Storm JF & Isbrandt D. (2005). Conditional transgenic suppression of M channels in mouse brain reveals functions in neuronal excitability, resonance and behavior. *Nat Neurosci* **8,** 51-60.

Pflüger EFW. (1859). Untersuchungen über die Physiologie des Electrotonus. Berlin.

Pian P, Bucchi A, Decostanzo A, Robinson RB & Siegelbaum SA. (2007). Modulation of cyclic nucleotide-regulated HCN channels by PIP(2) and receptors coupled to phospholipase C. *Pflügers Archiv* **455,** 125-145.

Pian P, Bucchi A, Robinson RB & Siegelbaum SA. (2006). Regulation of gating and rundown of HCN hyperpolarization-activated channels by exogenous and endogenous PIP2. *J Gen Physiol* **128,** 593-604.

Pike FG, Goddard RS, Suckling JM, Ganter P, Kasthuri N & Paulsen O. (2000). Distinct frequency preferences of different types of rat hippocampal neurones in response to oscillatory input currents. *J Physiol* **529,** 205-213.

Poliak S & Peles E. (2003). The local differentiation of myelinated axons at nodes of Ranvier. *Nat Rev Neurosci* **4,** 968-980.

Postea O & Biel M. (2011). Exploring HCN channels as novel drug targets. *Nat Rev Drug Discov* **10,** 903-914.

Puil E, Gimbarzevsky B & Miura RM. (1986). Quantification of membrane properties of trigeminal root ganglion neurons in guinea pigs. *J Neurophysiol* **55,** 995-1016.

Puil E, Gimbarzevsky B & Spigelman I. (1988). Primary involvement of K+ conductance in membrane resonance of trigeminal root ganglion neurons. *J Neurophysiol* **59,** 77-89.

Puil E, Meiri H & Yarom Y. (1994). Resonant behavior and frequency preferences of thalamic neurons. *J Neurophysiol* **71,** 575-582.

Qu Y, Curtis R, Lawson D, Gilbride K, Ge P, DiStefano PS, Silos-Santiago I, Catterall WA & Scheuer T. (2001). Differential modulation of sodium channel gating and persistent sodium currents by the beta1, beta2, and beta3 subunits. *Mol Cell Neurosci* **18,** 570-580.

Quick DC, Kennedy WR & Donaldson L. (1979). Dimensions of myelinated nerve fibers near the motor and sensory terminals in cat tenuissimus muscles. *Neuroscience* **4,** 1089-1096.

Rasminsky M. (1973). The effects of temperature on conduction in demyelinated single nerve fibers. *Arch Neurol* **28,** 287-292.

Rasminsky M & Sears TA. (1972). Internodal conduction in undissected demyelinated nerve fibres. *J Physiol* **227,** 323-350.

Rattay F. (1989). Analysis of models for extracellular fiber stimulation. *IEEE Trans Biomed Eng* **36,** 676-682.

Raymond SA. (1979). Effects of nerve impulses on threshold of frog sciatic nerve fibres. *J Physiol* **290,** 273-303.

Reid G, Scholz A, Bostock H & Vogel W. (1999). Human axons contain at least five types of voltage-dependent potassium channel. *J Physiol* **518,** 681-696.

Ritchie JM. (1995). Physiology of axons. In *The Axon: Structure, Function and Pathophysiology*, ed. Waxman SG, Kocsis JD & Stys PK, pp. 68-96. Oxford University Press, New York.

Ritchie JM & Rogart RB. (1977). Density of sodium channels in mammalian myelinated nerve fibers and nature of the axonal membrane under the myelin sheath. *Proc Natl Acad Sci U S A* **74,** 211-215.

Ritchie JM, Rogart RB & Strichartz GR. (1976). A new method for labelling saxitoxin and its binding to non-myelinated fibres of the rabbit vagus, lobster walking leg, and garfish olfactory nerves. *J Physiol* **261,** 477-494.

Robinson RB & Siegelbaum SA. (2003). Hyperpolarization-activated cation currents: from molecules to physiological function. *Annu Rev Physiol* **65,** 453-480.

Röper J & Schwarz JR. (1989). Heterogeneous distribution of fast and slow potassium channels in myelinated rat nerve fibres. *J Physiol* **416,** 93-110.

Rosenbluth J. (1976). Intramembranous particle distribution at the node of Ranvier and adjacent axolemma in myelinated axons of the frog brain. *J Neurocytol* **5,** 731-745.

Rosenbluth J. (1990). Axolemmal abnormalities in myelin mutants. *Ann N Y Acad Sci* **605,** 194-214.

Rushton WA. (1951). A theory of the effects of fibre size in medullated nerve. *J Physiol* **115,** 101-122.

Rutkove SB. (2001). Effects of temperature on neuromuscular electrophysiology. *Muscle Nerve* **24,** 867-882.

Rutkove SB, Kothari MJ & Shefner JM. (1997). Nerve, muscle, and neuromuscular junction electrophysiology at high temperature. *Muscle Nerve* **20,** 431-436.

Rydmark M. (1981). Nodal axon diameter correlates linearly with internodal axon diameter in spinal roots of the cat. *Neurosci Lett* **24,** 247-250.

Safronov BV, Kampe K & Vogel W. (1993). Single voltage-dependent potassium channels in rat peripheral nerve membrane. *J Physiol* **460,** 675-691.

Schauf CL & Davis FA. (1974). Impulse conduction in multiple sclerosis: a theoretical basis for modification by temperature and pharmacological agents. *J Neurol Neurosurg Psychiatry* **37,** 152-161.

Scholz A, Reid G, Vogel W & Bostock H. (1993). Ion channels in human axons. *J Neurophysiol* **70,** 1274-1279.

Schwarz JR & Eikhof G. (1987). Na currents and action potentials in rat myelinated nerve fibres at 20 and 37 degrees C. *Pflügers Archiv* **409,** 569-577.

Schwarz JR, Glassmeier G, Cooper EC, Kao TC, Nodera H, Tabuena D, Kaji R & Bostock H. (2006). KCNQ channels mediate (I(Ks)), a slow K+ current regulating excitability in the rat node of Ranvier. *J Physiol* **573,** 17-34.

Schwarz JR, Reid G & Bostock H. (1995). Action potentials and membrane currents in the human node of Ranvier. *Pflügers Archiv* **430,** 283-292.

Schwindt PC & Crill WE. (1995). Amplification of synaptic current by persistent sodium conductance in apical dendrite of neocortical neurons. *J Neurophysiol* **74,** 2220-2224.

Shibuta Y, Nodera H, Mori A, Okita T & Kaji R. (2010). Peripheral nerve excitability measures at different target levels: the effects of aging and diabetic neuropathy. *J Clin Neurophysiol* **27,** 350-357.

Siegelbaum SA & Koester J. (2000). Ion Channels. In *Principles of Neural Science*, 4 edn, ed. Kandel ER, Schwartz JH & Jessell TM, pp. 105-124. McGraw-Hill.

Sigworth FJ & Neher E. (1980). Single Na+ channel currents observed in cultured rat muscle cells. *Nature* **287,** 447-449.

Sittl R, Carr RW, Schwarz JR & Grafe P. (2010). The Kv7 potassium channel activator flupirtine affects clinical excitability parameters of myelinated axons in isolated rat sural nerve. *J Peripher Nerv Syst* **15,** 63-72.

Skou JC & Esmann M. (1992). The Na,K-ATPase. *J Bioenerg Biomembr* **24,** 249-261.

Stephanova DI & Bostock H. (1995). A distributed-parameter model of the myelinated human motor nerve fibre: temporal and spatial distributions of action potentials and ionic currents. *Biol Cybern* **73,** 275-280.

Stephanova DI & Bostock H. (1996). A distributed-parameter model of the myelinated human motor nerve fibre: temporal and spatial distributions of electrotonic potentials and ionic currents. *Biol Cybern* **74,** 543-547.

Stephanova DI & Daskalova M. (2005). Differences in potentials and excitability properties in simulated cases of demyelinating neuropathies. Part II. Paranodal demyelination. *Clin Neurophysiol* **116,** 1159-1166.

Stephanova DI & Mileva K. (2000). Different effects of blocked potassium channels on action potentials, accommodation, adaptation and anode break excitation in human motor and sensory myelinated nerve fibres: computer simulations. *Biol Cybern* **83,** 161-167.

Stevens DR, Seifert R, Bufe B, Muller F, Kremmer E, Gauss R, Meyerhof W, Kaupp UB & Lindemann B. (2001). Hyperpolarization-activated channels HCN1 and HCN4 mediate responses to sour stimuli. *Nature* **413,** 631-635.

Stys PK & Ashby P. (1990). An automated technique for measuring the recovery cycle of human nerves. *Muscle Nerve* **13,** 750-758.

Stys PK & Waxman SG. (1994). Activity-dependent modulation of excitability: implications for axonal physiology and pathophysiology. *Muscle Nerve* **17,** 969-974.

Swadlow HA, Kocsis JD & Waxman SG. (1980). Modulation of impulse conduction along the axonal tree. *Annu Rev Biophys Bioeng* **9,** 143-179.

Swedberg K, Komajda M, Bohm M, Borer JS, Ford I, Dubost-Brama A, Lerebours G & Tavazzi L. (2010). Ivabradine and outcomes in chronic heart failure (SHIFT): a randomised placebo-controlled study. *Lancet* **376,** 875-885.

Tasaki I. (1939). The electro-saltatory transmission of the nerve impulse and the effect of narcosis upon the nerve fiber. *Am J Physiol* **127,** 211-227.

Tasaki I. (1955). New measurements of the capacity and the resistance of the myelin sheath and the nodal membrane of the isolated frog nerve fiber. *Am J Physiol* **181,** 639-650.

Taylor RE & Chandler WK. (1962). Effect of temperature on squid axon membrane capacity. *Biophys Soc Abstr* **TD1**.

Tempel BL, Papazian DM, Schwarz TL, Jan YN & Jan LY. (1987). Sequence of a probable potassium channel component encoded at Shaker locus of Drosophila. *Science* **237,** 770-775.

Thomas CK & Zijdewind I. (2006). Fatigue of muscles weakened by death of motoneurons. *Muscle Nerve* **33,** 21-41.

Thomas EA, Hawkins RJ, Richards KL, Xu R, Gazina EV & Petrou S. (2009). Heat opens axon initial segment sodium channels: a febrile seizure mechanism? *Ann Neurol* **66,** 219-226.

Todd G, Butler JE, Taylor JL & Gandevia SC. (2005). Hyperthermia: a failure of the motor cortex and the muscle. *J Physiol* **563,** 621-631.

Tokuno HA, Kocsis JD & Waxman SG. (2003). Noninactivating, tetrodotoxin-sensitive Na+ conductance in peripheral axons. *Muscle Nerve* **28,** 212-217.

Tomlinson S, Burke D, Hanna M, Koltzenburg M & Bostock H. (2010a). In vivo assessment of HCN channel current (I(h)) in human motor axons. *Muscle Nerve* **41,** 247-256.

Tomlinson SE, Tan SV, Kullmann DM, Griggs RC, Burke D, Hanna MG & Bostock H. (2010b). Nerve excitability studies characterize Kv1.1 fast potassium channel dysfunction in patients with episodic ataxia type 1. *Brain* **133,** 3530-3540.

Trevillion L, Howells J, Bostock H & Burke D. (2010). Properties of low-threshold motor axons in the human median nerve. *J Physiol* **588,** 2503-2515.

Trevillion L, Howells J & Burke D. (2007). Outwardly rectifying deflections in threshold electrotonus due to K+ conductances. *J Physiol* **580,** 685-696.

Tu H, Deng L, Sun Q, Yao L, Han JS & Wan Y. (2004). Hyperpolarization-activated, cyclic nucleotide-gated cation channels: roles in the differential electrophysiological properties of rat primary afferent neurons. *J Neurosci Res* **76,** 713-722.

Ulens C & Tytgat J. (2001). Functional heteromerization of HCN1 and HCN2 pacemaker channels. *J Biol Chem* **276,** 6069-6072.

Vaidya SP & Johnston D. (2013). Temporal synchrony and gamma-to-theta power conversion in the dendrites of CA1 pyramidal neurons. *Nat Neurosci* **16,** 1812-1820.

Vogel W & Schwarz JR. (1995). Voltage-clamp studies in axons: Macroscopic and single-channel currents. In *The Axon: Structure, Function and Pathophysiology*, ed. Waxman SG, Kocsis JD & Stys PK, pp. 257-280. Oxford University Press, New York.

Vucic S, Burke D & Kiernan MC. (2010). Fatigue in multiple sclerosis: mechanisms and management. *Clin Neurophysiol* **121,** 809-817.

Vucic S, Krishnan AV & Kiernan MC. (2007). Fatigue and activity dependent changes in axonal excitability in amyotrophic lateral sclerosis. *J Neurol Neurosurg Psychiatry* **78,** 1202-1208.

Wagenaar DA & Potter SM. (2002). Real-time multi-channel stimulus artifact suppression by local curve fitting. *J Neurosci Methods* **120,** 113-120.

Wang WT, Wan YH, Zhu JL, Lei GS, Wang YY, Zhang P & Hu SJ. (2006). Theta-frequency membrane resonance and its ionic mechanisms in rat subicular pyramidal neurons. *Neuroscience* **140,** 45-55.

Webster HD. (2005). Introduction. In *Peripheral Neuropathy*, 4th edn, ed. Dyck PJ & Thomas PK, pp. 3-8. Elsevier Saunders, Philadelphia.

Webster HD, Martin R & O'Connell MF. (1973). The relationships between interphase Schwann cells and axons before myelination: a quantitative electron microscopic study. *Dev Biol* **32,** 401-416.

Weiss G. (1901). Sur la possibilite de rendre comparables entre eux les appareils servant a l'excitation electrique. *Arch Ital Biol* **35,** 413-446.

Wickenden AD, Maher MP & Chaplan SR. (2009). HCN pacemaker channels and pain: a drug discovery perspective. *Curr Pharm Des* **15,** 2149-2168.

Wulff H, Castle NA & Pardo LA. (2009). Voltage-gated potassium channels as therapeutic targets. *Nat Rev Drug Discov* **8,** 982-1001.

Yang Q, Kaji R, Takagi T, Kohara N, Murase N, Yamada Y, Seino Y & Bostock H. (2001). Abnormal axonal inward rectifier in streptozocin-induced experimental diabetic neuropathy. *Brain* **124,** 1149-1155.

Yu FH & Catterall WA. (2004). The VGL-chanome: a protein superfamily specialized for electrical signaling and ionic homeostasis. *Sci STKE* **253,** 1-17.

Yu FH, Yarov-Yarovoy V, Gutman GA & Catterall WA. (2005). Overview of molecular relationships in the voltage-gated ion channel superfamily. *Pharmacol Rev* **57,** 387-395.

Zemankovics R, Kali S, Paulsen O, Freund TF & Hajos N. (2010). Differences in subthreshold resonance of hippocampal pyramidal cells and interneurons: the role of h-current and passive membrane characteristics. *J Physiol* **588,** 2109-2132.

Zhou L & Chiu SY. (2001). Computer model for action potential propagation through branch point in myelinated nerves. *J Neurophysiol* **85,** 197-210.

Zolles G, Klocker N, Wenzel D, Weisser-Thomas J, Fleischmann BK, Roeper J & Fakler B. (2006). Pacemaking by HCN channels requires interaction with phosphoinositides. *Neuron* **52,** 1027-1036.

Zong X, Stieber J, Ludwig A, Hofmann F & Biel M. (2001). A single histidine residue determines the pH sensitivity of the pacemaker channel HCN2. *J Biol Chem* **276,** 6313-6319.